LIMITATIONS ON POINT-SOURCE STOCHASTIC SIMULATIONS IN TERMS OF GROUND-MOTION MODELS

A THESIS SUBMITTED TO
THE GRADUATE SCHOOL OF NATURAL AND APPLIED SCIENCES
OF
MIDDLE EAST TECHNICAL UNIVERSITY

BY

EMRAH YENİER

IN PARTIAL FULFILLMENT OF THE REQUIREMENTS
FOR
THE DEGREE OF MASTER OF SCIENCE
IN
CIVIL ENGINEERING

JANUARY 2009

Approval of the thesis:

LIMITATIONS ON POINT-SOURCE STOCHASTIC SIMULATIONS IN TERMS OF GROUND-MOTION MODELS

submitted by **EMRAH YENİER** in partial fulfillment of the requirements for the degree of **Master of Science in Civil Engineering Department, Middle East Technical University** by,

Prof. Dr. Canan ÖZGEN
Dean, Graduate School of **Natural and Applied Sciences**

Prof. Dr. Güney ÖZCEBE
Head of Department, **Civil Engineering**

Assoc. Prof. Dr. Sinan D. AKKAR
Supervisor, **Civil Engineering Dept., METU**

Examining Committee Members:

Prof. Dr. Polat GÜLKAN
Civil Engineering Dept., METU

Assoc. Prof. Dr. Sinan D. AKKAR
Civil Engineering Dept., METU

Prof. Dr. Haluk SUCUOĞLU
Civil Engineering Dept., METU

Prof. Dr. Reşat ULUSAY
Geological Engineering Dept., Hacettepe University

Dr. Ayşegül ASKAN
Civil Engineering Dept., METU

Date: 06.01.2009

I hereby declare that all information in this document has been obtained and presented in accordance with academic rules and ethical conduct. I also declare that, as required by these rules and conduct, I have fully cited and referenced all material and results that are not original to this work.

Name, Last name: Emrah YENİER

Signature :

ABSTRACT

LIMITATIONS ON POINT-SOURCE STOCHASTIC SIMULATIONS IN TERMS OF GROUND-MOTION MODELS

Yenier, Emrah
M. Sc., Department of Civil Engineering
Supervisor: Assoc. Prof. Dr. Sinan D. Akkar

January 2009, 246 pages

In this study, the limitations of point-source stochastic simulations are investigated in terms of fundamental geophysical parameters. Within this context, a total of 6000 synthetic ground motions are generated for various magnitude ($5.0 \leq M_w \leq 7.5$), source-to-site distance (less than 100 km), faulting style (shallow dipping and strike-slip) and site class (soft, stiff and rock) bins. The simulations are performed in two main stages: (1) the acceleration time series at outcropping very hard rock sites are simulated based on the stochastic method proposed by Boore (1983, 2003) and (2) they are modified through 1-D equivalent linear site response analysis to generate the free-field motions at soft, stiff and rock sites. Thus, as a part of this study, a probability-based soil profile model that considers the random variation of S-wave slowness as a function of depth is derived. The synthetic ground motions are assessed with several recent empirical ground-motion models to constitute the limitations of the simulation procedure. It is believed that the outcomes of this study will realistically describe the limitations of stochastic point-source simulation approach that can be employed further for the studies on improvements of this simulation technique.

Keywords: Stochastic, point-source, simulation, ground motion, site response, S-wave slowness, soil profile model.

ÖZ

NOKTASAL-KAYNAK STOKASTİK SİMÜLASYONLARIN YER HAREKETİ MODELLERİNE GÖRE SINIRLAMALARI

Yenier, Emrah
Yüksek Lisans, İnşaat Mühendisliği Bölümü
Tez Yöneticisi: Doç. Dr. Sinan D. Akkar

Ocak 2009, 246 sayfa

Bu çalışmada, noktasal-kaynak stokastik simülasyonların sınırlamaları temel jeofiziksel parametreler bakımından incelenmiştir. Bu bağlamda, çeşitli deprem büyüklüğü ($5.0 \leq M_w \leq 7.5$), kaynak-istasyon mesafesi (100 kilometerden az), faylanma mekanizması (eğim atımlı ve doğrultu atımlı) ve zemin sınıfı (yumuşak, sıkı ve kaya) kümeleri için toplam olarak 6000 sentetik yer hareketi üretilmiştir. Simülasyonlar iki ana aşamada gerçekleştirilmiştir: (1) Boore (1983, 2003) tarafından önerilen stokastik yönteme göre ivme zaman serileri sert kaya zeminlerde üretilmiş ve (2) bu kayıtlar 1-B eşdeğer-doğrusal (lineer) zemin davranış analizleri yardımıyla yumuşak, sıkı ve kaya zeminlerdeki serbest-yüzey hareketlerine dönüştürülmüştür. Bu suretle, bu çalışmanın bir parçası olarak, S-dalgası yavaşlıklıklarının rastgele değişimini derinliğin bir fonksiyonu olarak dikkate alan olasılığa dayalı zemin profil modelleri türetilmiştir. Simülasyon yönteminin sınırlamalarını belirlemek amacıyla, üretilen sentetik yer hareketleri bazı güncel ampirik yer hareketi modelleri ile karşılaştırılmıştır. Bu çalışmaya ait sonuçların noktasal-kaynak stokastik simülasyon yaklaşımının sınırlamalarını gerçekçi olarak ifade edeceği ve bu simülasyon tekniğinin geliştirilmesine yönelik çalışmalarda kullanılabileceği düşünülmektedir.

Anahtar Kelimeler: Stokastik, noktasal kaynak, simülasyon, yer hareketi, zemin davranışı, S-dalgası yavaşlığı, zemin profil modeli.

To My Family

ACKNOWLEDGMENTS

I would like to express my deepest gratitude to my supervisor Dr. Sinan D. Akkar for his support, guidance, advice, criticism, encouragement and insight throughout the study.

I also would like to express my faithful thanks to Dr. B. Sadık Bakır for providing ProShake software and for his support and guidance in site response analyses.

I wish to express my sincere thanks to Dr. David M. Boore and Prof. Julian J. Bommer who made valuable comments on the technical improvement of the study.

I also would like to express my sincere thanks to Dr. John Douglas for providing “japsyn4_1.exe” software that is used for the generation of non-stationary synthetics.

This work is supported by Scientific Research and Technical Council of Turkey (TÜBİTAK) under Award No. 105G016. The funding provided by TÜBİTAK is gratefully acknowledged.

I am grateful to Özgür Erdoğan, Abdullah Sandıkkaya and İlker Kazaz for their friendship, assistance and encouragement during the thesis study. I also owe thanks to my friends Murat Erdoğdu, Mete Kurtoğlu, Özkan Kale and Bekir Özer Ay for their friendship and support.

Finally, endless thanks to my father M. Şerif Yenier, my mother Mebrure Yenier, my brothers Erkan and Enes and my sister Sebahat for their encouragement, confidence in me, support and for their love.

TABLE OF CONTENTS

CHAPTERS

APPENDICES

LIST OF TABLES

TABLES

LIST OF FIGURES

FIGURES

CHAPTER 1

INTRODUCTION

1.1 General

Earthquakes have been one of the natural disasters causing great losses of life and property along the history of humankind. Since 1930s, with increasing awareness of earthquake disaster, strong-motion networks have been established along the seismically active regions around the world to understand and monitor the earthquake kinematics. The ground-motion records have also been in use by engineers to understand their likely effects on structures in order to mitigate the earthquake hazard. Although the ground-motion records have started to be common in earthquake related studies, current strong-motion databases are still limited in terms of uniform and trustworthy magnitude, distance, site class and faulting style distribution. A typical case is presented in Figure 1.1 that shows the scatter plot of "usable" records of recently compiled Turkish strong-motion database (Erdoğan, 2008). The term "usable" describes the high quality records having reliable moment magnitude, site class, faulting style and source-to-site distance information. Figure 1.1 indicates that Turkish strong-motion database contains a fairly good amount of records between $3.5 \leq M_w \leq 6.5$ and $M_w \geq 7.0$. However, there is a certain magnitude gap between 6.5 and 7.0. Also note that there is small number of records with $R_{JB} \leq 20$ km and $M_w \geq 5.5$. When the site class is of concern, it is observed that the Turkish database is dominated by ground motions recorded at NEHRP C and D sites. The number of ground motions recorded at NEHPR B sites is very few.

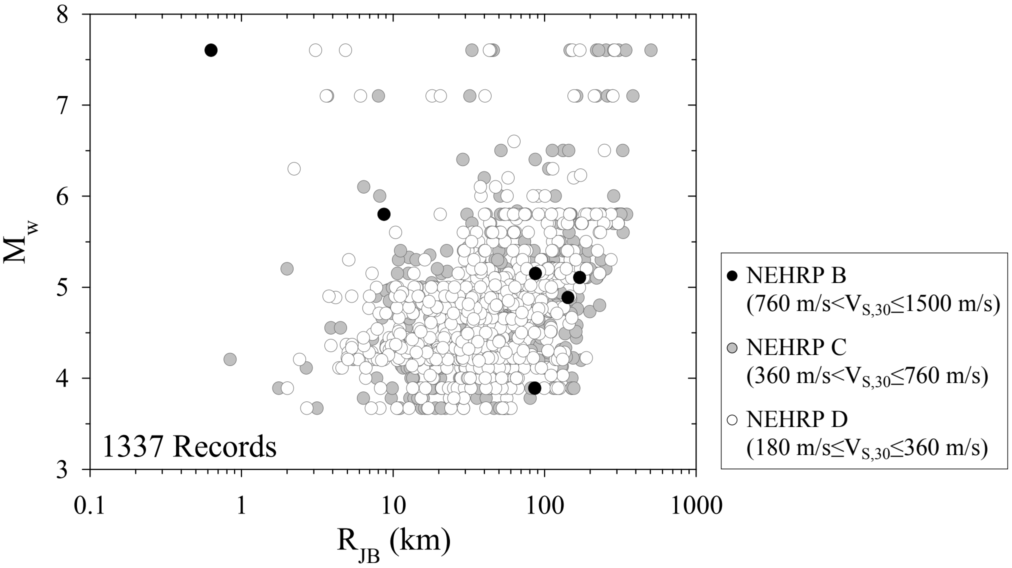

Figure 1.1 M_w-R_{JB} scatter of the recently compiled Turkish strong-motion database that includes main, fore- and after-shocks (M_w refers to moment magnitude; R_{JB} is the closest distance measured from the site to the vertical projection of the fault rupture). The scatter data is classified according to the NEHRP site class definitions (BSSC, 2003). $V_{S,30}$ denotes the travel-time weighted average of S-wave velocities for the top 30 m of the site. The reader is referred to Erdoğan (2008) and Sandıkkaya (2008) for a full discussion on the general features of Turkish strong-motion database.

Similar limitations are also observed in the strong-motion databases of other regions as well as global databases (e.g. European strong-motion database (http://www.isesd.cv.ic.ac.uk/ESD/frameset.htm), COSMOS strong-motion database (http://www.cosmos-eq.org), etc.). The lack of reliable data is due to the absence of nearby recording stations to the events or because of the site being in a low to moderate seismicity region (Pousse et al., 2006) as well as other deficiencies such as lack of site class information of strong-motion stations and source parameters. The long recurrence period of large earthquakes constitutes another reasoning of this deficiency (Boore, 1986). Furthermore, some of the ground motions recorded by analogue instruments are problematic and removal of these recordings decreases the number of strong-motion data that are suitable for earthquake related studies.

To overcome the difficulties arising from the lack of strong-motion data, either the ground motions obtained from other seismic regions are used or synthetic time series are generated. The use of actual ground motions from different seismic regions requires the recordings to be scaled from host regions to the target region. However, proper scaling of ground-motion records requires sound knowledge on the source, path and site characteristics of both host and target regions. Therefore, ground-motion simulation procedures are commonly employed as they can provide the specific seismological features of ground motions for engineering studies.

The ground-motion simulations are also useful for data rich regions because they provide a conceptual framework for understanding some of the fundamentals underlying the physical parameters that control the observed ground-motion amplitudes and their variability (Atkinson and Silva, 2000). Additionally, synthetics can be used to guide the empirical ground-motion prediction equations (GMPEs) in extending the estimations to the magnitude and distance ranges that are not well constraint by the actual data (Atkinson and Silva, 1997). This is a particularly important issue for seismic hazard analysis because the empirical ground-motion relations are commonly applied over a range of magnitudes and distances that is much wider than that covered by the underlying empirical database (Atkinson and Silva, 2000). The ground-motion simulations have also been used in conducting linear and nonlinear dynamic analysis of structures. Thus, the simulated accelerograms must have realistic energy, duration, and frequency content, representing the physical conditions of actual ground-motion time series (Pousse et al., 2006).

The major objective of this study is to determine how well the stochastically simulated point-source ground motions represent the actual ground-motion records. Within this context, the limitations of the synthetics are investigated in terms of various magnitude, distance, faulting style and site class bins. This is performed by comparing the peak motions and spectral displacements obtained from simulations and those estimated from recently developed GMPEs. It is believed that the outcomes of this study will realistically describe the limitations of stochastic point-source synthetic approach that can be employed further for the studies on improvements of this simulation technique. Furthermore, as part of this study, the depth-dependent probabilistic S-wave slowness models for soft, stiff and rock sites are derived. These models can be used as part of a probabilistic methodology to account for the variability of slowness.

1.2 Literature Survey

Many ground-motion simulation methods have been proposed in the literature and these procedures can be classified as deterministic and stochastic methods. Low-frequency ground motions, which show a deterministic character in terms of their phase contents and arrivals, can be generated using deterministic methods. The empirical Green’s function (EGF) method and the ray-theory method are two of the contemporary deterministic simulation approaches (Atkinson and Somerville, 1994; Bolt, 1995; Irikura, 1986; Irikura and Kamae, 1994). In EGF method, identical empirical Green’s functions that define the wave generated by a small impulse traveling through an elastic medium are derived from small seismic events and are superimposed with short time lags to generate accelerograms of much larger events based on established scaling laws. Although the EGF method is simple to implement, it mainly generates low-frequency ground motions. Thus, it requires representative real seismic events in order to account for high frequency components. Moreover, suitable empirical Green's functions are not always available to define the scenario (Lam et al., 2000). In the ray-theory method, a theoretical Green's function synthesized by ray-theory is convolved with an empirical or theoretical source time function that is based on the assumed fault geometry and focal depth to simulate the ground-motion acceleration time series.

However, the method requires the source and crustal structure of the hypothetical event to be studied in detail (Lam et al., 2000).

Numerical solution of elastic wave equation with a kinematic source is another way of ground motion simulation technique (Graves 1996, Pitarka 1998). In order to solve the elastic wave equation, finite-difference or finite-element schemes are employed by making use of point-sources as well as extended faults. These numerical approaches enable the simulation of ground motions in regions of heterogeneous crustal structure. Akcelik et al. (2003) incorporates the solution of a three-dimensional predictive and physical model of the elastic wave propagation problem for the simulation of low-frequency ground motions.

In some circumstances, the elastic design spectrum is the only information available to the design engineer. The spectrum-compatible ground-motion simulation approaches are commonly employed in such cases to obtain artificial acceleration time series (Kaul, 1978; Vanmarcke, 1979; Gasparini and Vanmarcke, 1979). SIMQKE (Gasparini and Vanmarcke, 1979) and RASCAL (Silva and Lee, 1987) are the commonly employed software to generate spectrum-compatible artificial accelerograms. The approach employed in SIMQKE is to generate a power spectral density function from the smoothed response spectrum, and then to derive sinusoidal signals having random phase angles and amplitudes (Bommer and Acevedo, 2004). The sinusoidal motions are summed and the match with the target spectrum is iteratively improved based on the ratio between target and actual response spectra. The fundamental deficiency of the spectrum-compatible approaches is that the resultant synthetics present too many cycles of strong motion and hence they possess unreasonably high energy content (Bommer and Acevedo, 2004; Lam et al., 2000). Naiem and Lew (1995) demonstrated the inefficiency of using such artificial records for nonlinear analyses. Furthermore, the spectrum-compatible synthetics will be unrealistic if the target design spectrum is a uniform hazard spectrum. This type of spectrum is not event-based since it envelopes the ground motions from several seismic sources such as small, local earthquakes and distant, large magnitude events (Bommer and Acevedo, 2004).

Another well-known and commonly used ground-motion simulation method is the stochastic approach. It identifies the important factors affecting the characteristics of the earthquake ground motion and distills these factors into a few key parameters (Boore, 1983; Boore, 2003; Lam et al., 2000). The procedure typically consists of an amplitude spectrum defining the frequency content and a set of random phase angles defining the phase arrivals (Vanmarcke, 1977). The amplitude spectrum is modeled by convolving the source, path, and site effect with the engineering notion (Hanks, 1979; Hanks and McGuire, 1981; Boore, 1983; Boore, 2003). The source models range from point-source stochastic simulations through their extension to finite sources, to fully-dynamic models of stress release (Bommer and Acevedo, 2004).

With the advent of computers, stochastic ground-motion simulation methods have become popular (Lam et al., 2000). They have provided a simple and effective framework for guiding and interpreting empirical ground-motion relations (Atkinson and Siva, 1997). Using a point-source model, Atkinson and Boore (1995) and Toro et al. (1997) derived stochastic based GMPEs for eastern North America (ENA) where the strong-motion data is limited. For the same region, Atkinson and Boore (2006) developed earthquake ground-motion relations including the estimates of their aleatory uncertainty based on stochastic finite-fault modeling.

The stochastic simulations not only applied for regions where the actual strong-motion data is limited but also they are implemented for data rich regions. Atkinson and Silva (1997) analyzed the strong-motion database of California to determine the source spectra, the average regional attenuation, and the average response of soil sites relative to rock sites. Based on the point-source and finite-source stochastic simulations, they indicated that the single-corner point-source approximation does not work well for large earthquakes. Atkinson and Silva (2000) developed GMPEs for California using a stochastic method. They indicated that a point-source model can mimic the salient effects of finite-fault models through appropriate specification of an equivalent point-source representation. The stochastic method has also been implemented for a variety of regions other than North America, such as Greece (Margaris and Boore, 1998), Italy (Rovelli et al., 1991, 1994; Berardi et al., 1999) and Russia (Sokolov, 1997).

Campbell's hybrid empirical approach (2003, 2004) is another recent simulation approach that employs strong-motion prediction methods for regions where the strong-motion data is limited. Campbell (2003, 2004) presents a methodological framework to transfer the empirical ground-motion models developed for one region to use in another region. The method uses response-spectral transfer function that accounts for the differences in regional characteristics (source, average stress drop, attenuation, geometrical spreading, etc) to adjust the ground-motion relations. The transfer function is generally calculated from the analysis of stochastically simulated ground motions. Scherbaum et al. (2006) calculated equivalent stochastic host-region models for several empirical GMPEs that can be used for the calculation of the response-spectral transfer function.

The stochastic method is a simple and powerful tool that has been considered to be as successful as more sophisticated methods in predicting ground-motion amplitudes (Atkinson and Boore, 2000). There are several studies examining the validity of the simulations in the literature (e.g. Atkinson and Sommerville, 1994; Silva et al., 1997; Beresnev and Atkinson, 1998; Hartzell et al., 1999; Atkinson and Silva, 2000). Atkinson and Sommerville (1994) compared the stochastic and ray-theory simulation methods with the actual recordings and assessed the applicability of the methods in terms of spectral frequency. Atkinson and Sommerville (1994) stated that the stochastic method underpredicts 1 Hz response spectra by 20 to 40%. However, it was indicated that the ray-theory method underpredicts 1 Hz response spectra by 10 to 40%. Both methods accurately predict response spectra for higher frequencies. The stochastic method accurately predicts peak ground acceleration and velocity but the ray-theory method overpredicts peak ground acceleration and velocity by 10 to 40%.

A more recent study performed by Atkinson and Silva (2000) examined the applicability of the stochastically derived GMPE for California. The influence of magnitude and distance was taken into account while assessing the GMPE against the observed data. It was found that the two-corner stochastic estimates of ground motions are accurate to within 20% on average, for earthquakes of $M_w \geq 6.0$, at distances $R_{JB} \leq 50$ km of the fault, and for spectral frequencies from 0.2 to 10 Hz. However, for events $M_w < 6.0$, the stochastic model underpredicts the ground motion amplitudes at low spectral frequencies ($f < 1$ Hz) by about 20%. When the source-to-site distance is of concern, it was observed that for distances less than 10 km, the simulations overpredict the ground-motions at spectral frequencies larger than 2 Hz by about 50%.

Advances in earthquake engineering studies and consequently, increase in the necessity of reliable ground-motion estimations require the simulated time series to be assessed in detail. Although the validity of the stochastic methods was investigated by a number of researchers, the studies are generally limited to a specific region or earthquake. Additionally, in some of these studies, the simulations were examined against the empirical prediction equations that were derived from relatively limited strong-motion data. Thus, the assessment of stochastic simulations against recently developed GMPEs can provide more realistic and updated information on the limitations of simulated records to researchers. It should be noted that the validity of synthetics has generally been investigated in terms of a few independent parameters: magnitude and distance. Nevertheless, the consideration of the site class and faulting style influence on the limitations of simulations can provide additional information for their effective use by the end users.

1.3 Object and Scope

The major objective of this study is to determine the limitations of stochastic point-source simulations by considering the magnitude, distance, faulting style and site class influence. To accomplish this objective, a total of 6000 synthetic ground motions are generated randomly for various magnitude ($5.0 \leq M_w \leq 7.5$), distance ($1 \text{ km} \leq R_{JB} \leq 100 \text{ km}$), faulting style (shallow dipping – grossly represents normal and reverse dipping faults – and strike-slip) and site class (soft, stiff and rock) bins. The simulation process consists of two main steps (Figure 1.2). Firstly, the acceleration time series at outcropping very hard rock (VHR) sites are simulated based on the stochastic method proposed by Boore (1983, 2003). In the second stage, the stochastically simulated outcropping VHR motions are modified by performing site response analyses to generate the free-field motions at soft, stiff and rock sites. The outcropping VHR motions are deconvolved to the bedrock and concolved to the surface via ProShake v1.12 software (2007). The performance of the simulated ground-motions is assessed with several recently developed GMPEs to constitute the limitations of the simulations.

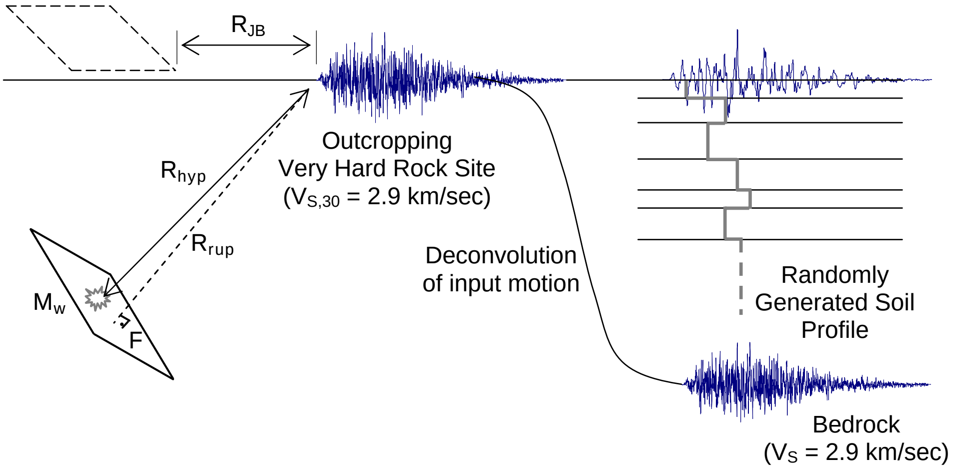

Figure 1.2 Simulation process

The thesis starts with introducing the random generation of important seismological parameters (i.e. magnitude and distance values) for the synthetic ground motions (Chapter 2). In Chapter 3, the first stage of the simulation process is discussed in detail. The components of stochastic simulation process are presented. The outcropping VHR motions are generated using random ground-motion parameters presented in Chapter 2.

Chapter 4 describes the second stage of the ground-motion simulation process. In this stage, the stochastically simulated outcropping VHR motions (Chapter 3) are combined with 1-D equivalent linear site response analyses (Schnabel et al., 1972) to generate the free-field motions at soft, stiff and rock sites. Soil profiles are randomly generated based on the statistical evaluation of the datasets compiled from USGS(1), Turkish NSMP(2) and NGA(3) databases. The details of random soil profile generation process and the statistical analysis of the compiled datasets are also presented in this chapter.

In Chapter 5, the simulated ground motions are evaluated for several recently developed GMPEs to determine the performance of the simulation procedure. The simulations are also compared with another set of simulations generated by a non-stationary procedure proposed by Pousse et al. (2006) to identify the differences between the stationary and non-stationary stochastic simulation approaches.

In Chapter 6, the simulation process and the outcomes of this study are summarized. The report ends with a detailed appendix that contains additional figures that are not presented in the main body of the thesis.

---

(1) USGS refers to the United States of Geological Survey. The soil profiles are downloaded from http://quake.wr.usgs.gov/~boore/data_online.htm

(2) Turkish NSMP is the abbreviation of “Compilation of Turkish strong ground-motion database in accordance with international standards” project financially granted by the Scientific and Technological Research Council of Turkey under the Award No. 105G016.

(3) NGA refers to “Next Generation of Ground-Motion Attenuation Models” project (http://peer.berkeley.edu/products/nga_project.html) coordinated by the Lifelines Program of the Pacific Earthquake Engineering Research Center (PEER).

CHAPTER 2

SIMULATION DATA SET

2.1 General

This chapter describes the generation of important seismological parameters for the synthetic ground motions. The ground motions are simulated based on randomly generated moment magnitude (M_w) and Joyner-Boore (R_{JB}) distances (Joyner and Boore, 1981) using the Monte Carlo simulation technique. The magnitude ranges for the synthetic accelerograms is $5.0 \leq M_w \leq 7.5$ whereas the distance is between 1 km $\leq R_{JB} \leq$ 100 km. Though the details will be given in the next chapters, the synthetics are first computed for outcropping very hard rock (VHR) sites and then scaled for different site classes (soft, stiff and rock). Although, R_{JB} is regarded as the reference distance metric throughout the study, the outcropping VHR motions are generated using hypocentral distance (R_{hyp}) due to its better performance in simulated ground motions (Scherbaum et al., 2006). Therefore, the chapter ends with the detailed descriptions about the computation of R_{hyp} as well as R_{rup} (rupture distance) that is used in Chapter 5 for the evaluation of the simulated ground motions.

2.2 Random Generation of M_w and R_{JB} Values

As the complexity in engineering problems increases, the formulation of analytical models starts to become extremely difficult (Ang and Tang, 1984). In such cases, solutions may be obtained through Monte Carlo simulations. The Monte Carlo simulation method is a procedure that relies on the use of randomly sampled input parameters in a stochastic approach to replicate the observations in real life. In this study, the seismological parameters of artificial ground-motion time series are simulated via Monte Carlo simulation technique. The simulations are performed at soft, stiff and rock sites for a number of earthquake magnitude, distance and faulting style bins. Table 2.1 presents the simulation bins considered in this study.

Table 2.1 Simulation bins

Magnitude Bins	Distance Bins	Faulting Styles
$5.0 \leq M_w < 5.5$	$1\text{ km} \leq R_{JB} < 10\text{ km}$	Shallow dipping
$5.5 \leq M_w < 6.0$	$10\text{ km} \leq R_{JB} < 25\text{ km}$	Strike-slip
$6.0 \leq M_w < 6.5$	$25\text{ km} \leq R_{JB} < 50\text{ km}$	
$6.5 \leq M_w < 7.0$	$50\text{ km} \leq R_{JB} \leq 100\text{ km}$	
$7.0 \leq M_w \leq 7.5$		

In stochastic ground-motion simulations, the principal factors affecting the ground motion characteristics are generally combined with a random phase spectrum to generate the ground-motion time series. In this sense, the earthquake magnitude and source-to-site distance are accepted as the fundamental ground-motion parameters for generating VHR motions. In this study, 50 pairs of M_w and R_{JB} values are randomly generated for each magnitude - distance - faulting style bin combination and a total of 2000 M_w-R_{JB} pairs are generated. All parameters are assumed to be log-normally distributed within the intervals presented in Table 2.1. For a random parameter X, the mean ($\mu_{X,i}$) and the standard deviation ($\sigma_{X,i}$) of the i^{th} simulation bin are computed using Equations (2.1) and (2.2), respectively (Ang and Tang, 1984). Note that the log-normally distributed random parameter X denotes either M_w or R_{JB} in these equations.

$$\mu_{X,i} = \exp\left(\lambda_{X,i} + \frac{1}{2}\xi_{X,i}^{\,2}\right) \tag{2.1}$$

$$\sigma_{X,i} = \mu_{X,i} \cdot \sqrt{\exp\left(\xi_{X,i}{}^{2}\right) - 1} \tag{2.2}$$

In Equations (2.1) and (2.2), $\lambda_{X,i}$ and $\xi_{X,i}$ are the mean and standard deviation of ln(X), respectively. The parameters $\lambda_{X,i}$ and $\xi_{X,i}$ are defined in Equations (2.3) and (2.4), respectively where $X_{L,i}$ and $X_{U,i}$ are the upper and lower bounds of X that are listed in Table 2.1. Random variables (M_w and R_{JB}) are generated such that $P(X_{L,i} \leq X \leq X_{U,i}) = 99.5\%$.

$$\lambda_{X,i} = \frac{\ln(X_{U,i}) + \ln(X_{L,i})}{2} \tag{2.3}$$

$$\xi_{X,i} = \frac{\ln(X_{U,i}) - \ln(X_{L,i})}{6} \tag{2.4}$$

The realizations for M_w and R_{JB} are performed in continuous space. In engineering seismology and earthquake engineering applications, moment magnitudes are generally expressed in two significant digits. Therefore, the generations for M_w are rounded to two significant digits whereas no modification is done in R_{JB} generations. Although, the generated M_w and R_{JB} values are within the ±3 standard deviation interval, they are checked for possible outliers. Whenever a bin contains outlier realizations, the procedure is repeated until all the generations are within the pre-defined ranges.

The generated data is evaluated visually to investigate whether the random number generation process performs well. Figures 2.1 to 2.5 illustrate the distribution of the randomly generated M_w and R_{JB} values for each magnitude bin. Each figure consists of 4 scatter plots that display the generations of shallow dipping and strike-slip faulting styles for different distance ranges. The scatter plots show that all generations lay within the pre-defined simulation intervals. The scatters also indicate that most of the generated data is concentrated around the corresponding mean values ($\mu_{X,i}$) and the number of realizations decreases towards the tails. To graphically assess the match between the generations and the prescribed log-normal probability distributions, the cumulative frequency histograms of the data are compared with the theoretical log-normal cumulative distribution functions (CDF) next to each axis. The actual log-normal CDFs are computed using the corresponding mean ($\mu_{X,i}$) and standard deviation ($\sigma_{X,i}$) values determined from Equations (2.1) and (2.2), respectively. Note that the probability distribution comparisons for M_w are performed in discrete space. The agreement between the actual CDFs and the cumulative frequency histograms suggests that the generations follow the prescribed log-normal probability distributions fairly well.

2.3 Generation of R_{hyp} and R_{rup} Values

The Joyner-Boore distance (R_{JB}) is one of the most commonly used source-to-site distance metrics in ground-motion simulations. However, Scherbaum et al. (2006) stated that the use of hypocentral distance (R_{hyp}) for the simulation of ground motions provides the lowest-misfit stochastic models for most of the empirical equations. Therefore, the synthetic outcropping VHR motions are simulated based on R_{hyp}. Since, the generated synthetic motions are evaluated using several GMPEs that either use the closest rupture distance (R_{rup}) or R_{JB} (Chapter 5), the randomly generated R_{JB} values are converted to R_{hyp} and R_{rup} distances.

Using regression analysis on the simulated data, Scherbaum et al. (2004) established explicit distance conversion relations for various distance metrics. In the study performed by Scherbaum et al. (2004), R_{JB} was chosen as the reference distance metric and a number of different distance measures were expressed in terms of R_{JB} for generic, shallow dipping and strike-slip faulting styles for $5.0 \leq M_w \leq 7.5$ and $0 \leq R_{JB} \leq 100$ km ranges. The conversion relationships proposed by Scherbaum et al. (2004) use models based on gamma distribution to express the shape of the residual functions. The relationships between R_{hyp} vs. R_{JB} and R_{rup} vs. R_{JB} proposed by Scherbaum et al. (2004) are presented in Equations (2.5) and (2.6), respectively.

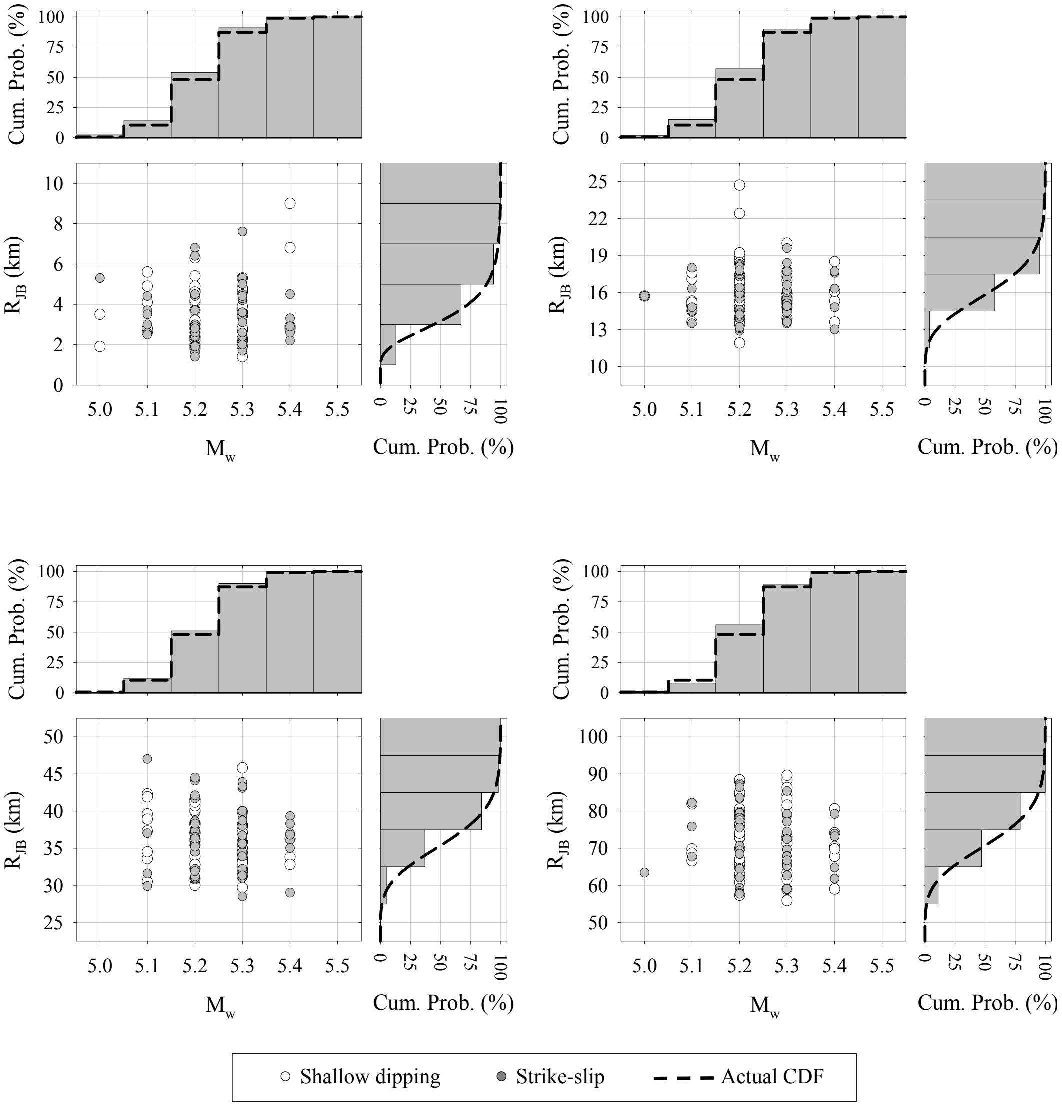

Figure 2.1 Distribution of randomly generated M_w and R_{JB} values for $5.0 \leq M_w < 5.5$

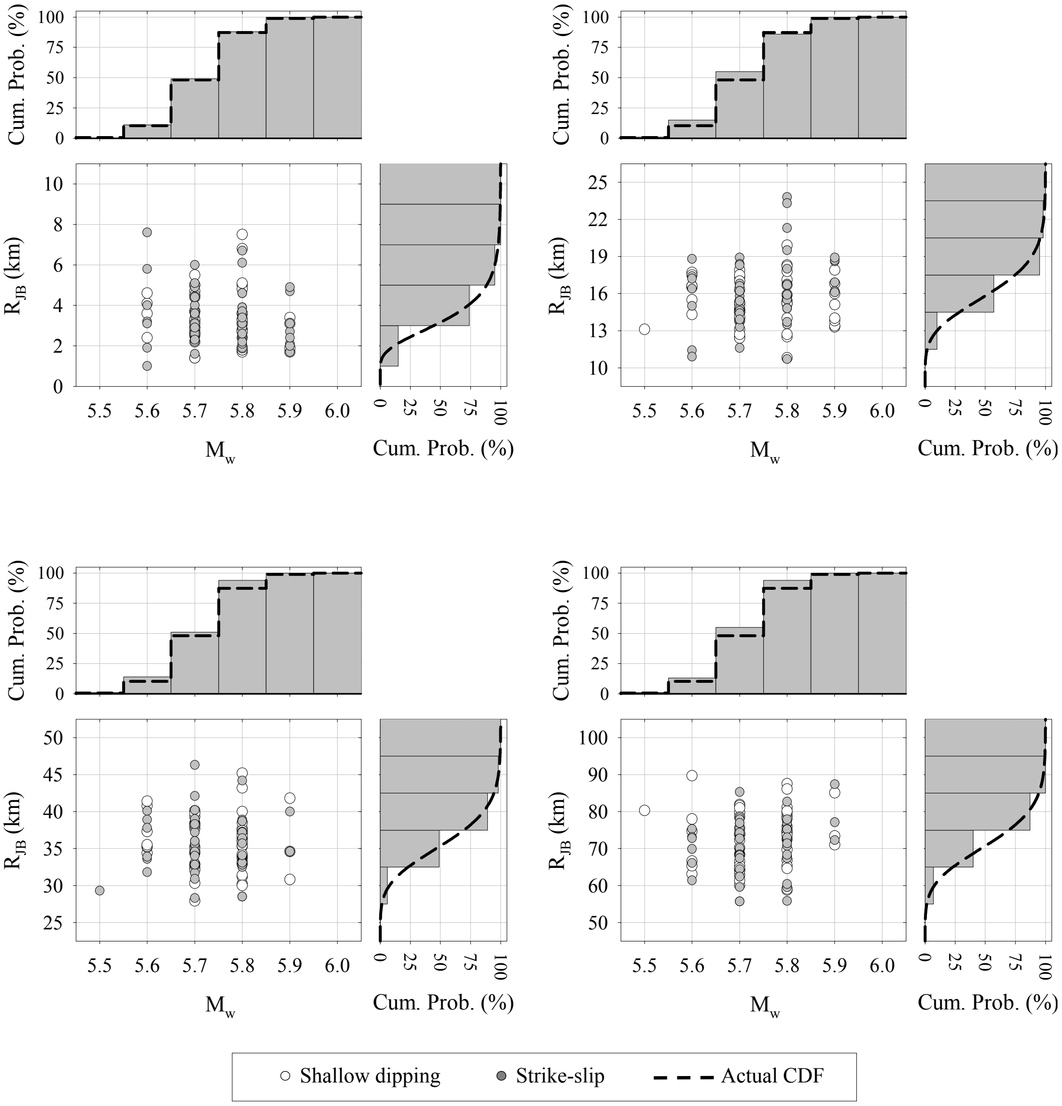

Figure 2.2 Distribution of randomly generated M_w and R_{JB} values for $5.5 \le M_w < 6.0$

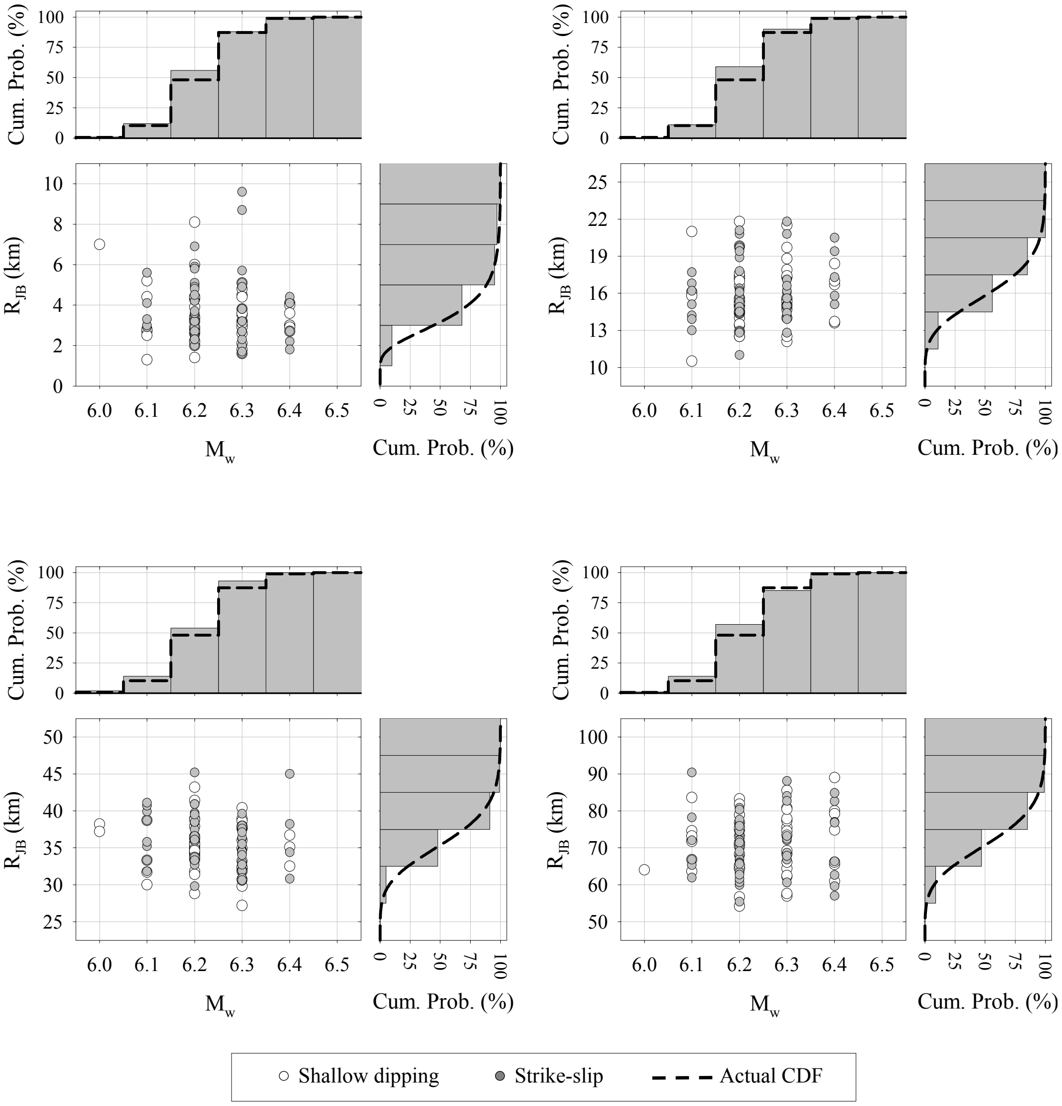

Figure 2.3 Distribution of randomly generated M_w and R_{JB} values for $6.0 \le M_w < 6.5$

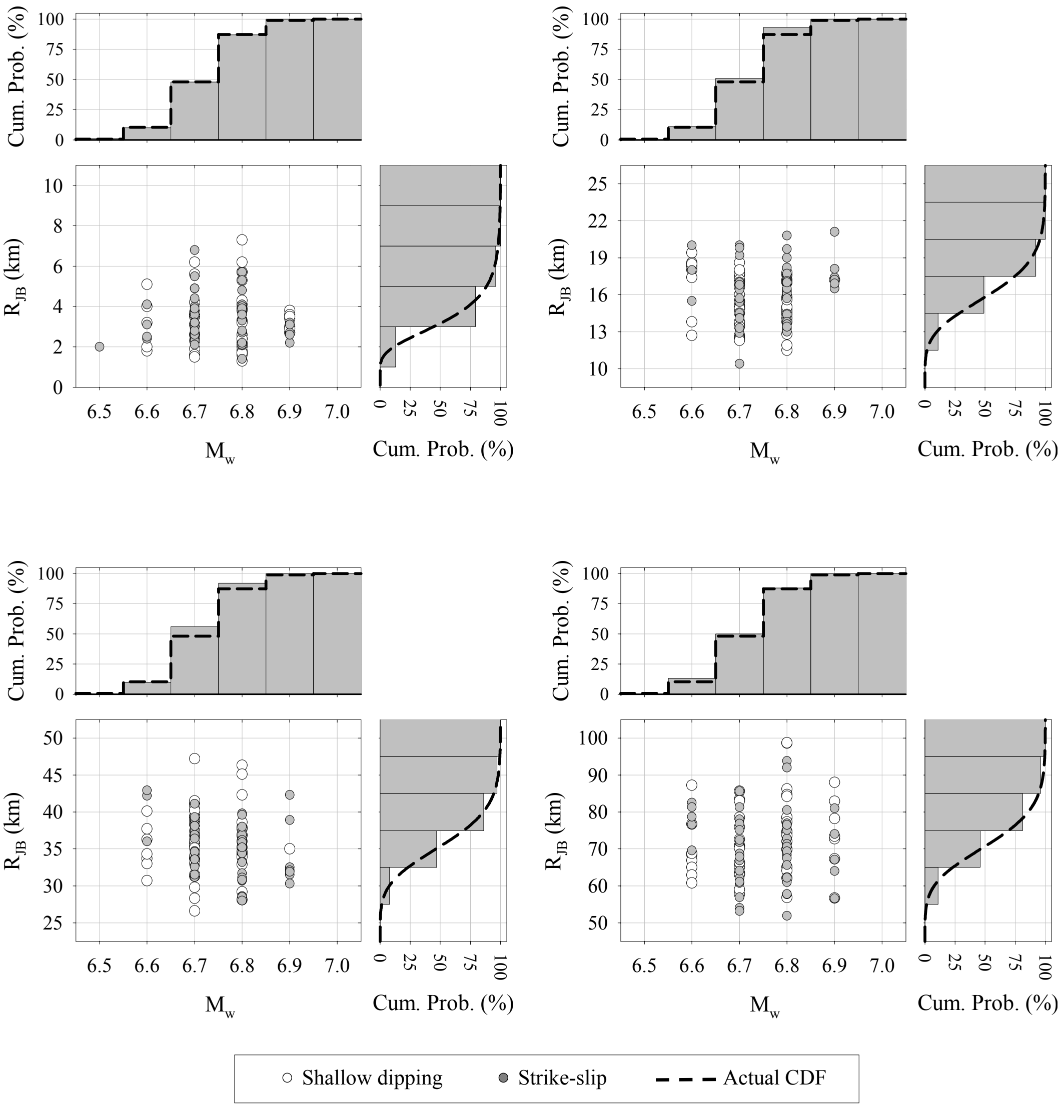

Figure 2.4 Distribution of randomly generated M_w and R_{JB} values for $6.5 \le M_w < 7.0$

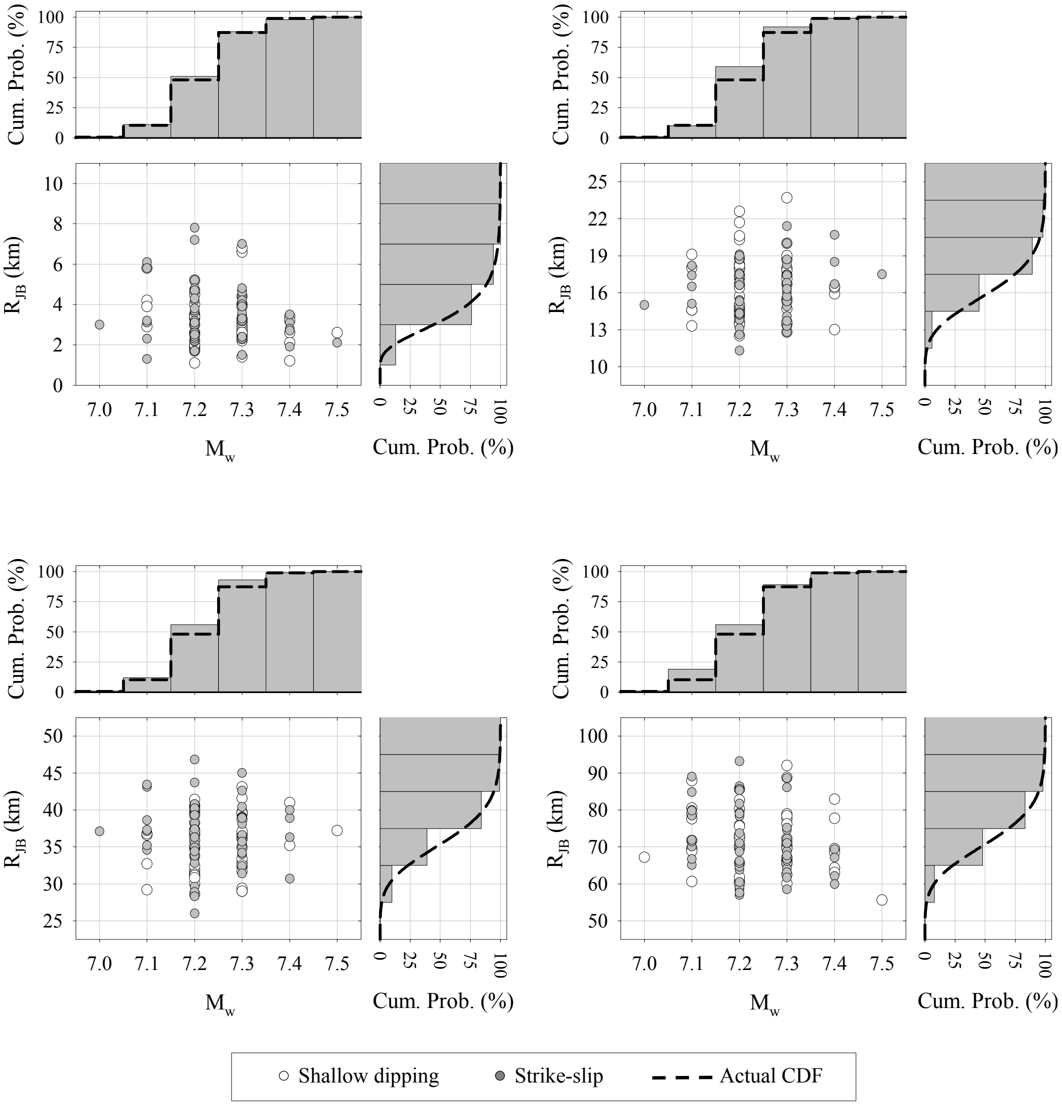

Figure 2.5 Distribution of randomly generated M_w and R_{JB} values for $7.0 \leq M_w \leq 7.5$

$$R_{hyp} = \varepsilon_{JBhyp} + \sqrt{R_{JB}^{2} + h_{seis}^{2}} \qquad (2.5)$$

$$R_{rup} = \varepsilon_{JBrup} + R_{JB} \qquad (2.6)$$

where ε_{JBhyp} and ε_{JBrup} denote to the residual models used for converting R_{JB} to R_{hyp} and R_{rup}, respectively. h_{seis} is the depth of the top level of the seismogenic zone considered by Scherbaum et al. (2004) (h_{seis} = 3 km). The residual models are gamma-distributed random variables and their means and standard deviations are expressed in terms of magnitude- and distance-dependent polynomials. The coefficients of the polynomials differ for each fault type.

In this study, R_{hyp} and R_{rup} are randomly sampled according to the procedure proposed by Scherbaum et al. (2004) using previously generated M_w-R_{JB} pairs. The closest rupture distance (R_{rup}) samplings are constrained by R_{hyp} values (i.e. $R_{rup} \leq R_{hyp}$) to avoid unrealistic realizations. Scatter plots of R_{JB}-R_{hyp} pairs for each magnitude bin are presented in Figure 2.6. The scatters show that R_{hyp} always attains larger values than R_{JB}, as expected. The difference between these two distance metrics is large at close distances and it decreases with increasing distance due to geometrical features of the fault. The scatter plots also indicate that the discrepancy between R_{JB} and R_{hyp} increases with increasing magnitude. The increase in fault dimensions for large earthquakes is the main reason for the amplified difference between these two distance metrics. Similar observations can be also made for R_{JB} vs. R_{rup} comparisons (Figure 2.7). However, the discrepancy between these two distance metrics is not as large as it is observed in the R_{JB}-R_{hyp} pairs. This is due to the difference in the definitions of R_{hyp} and R_{rup}. The geometrical orientation of fault plane is accounted for in both R_{JB} and R_{rup} definitions. However, R_{hyp} is only related to the location of hypocenter with respect to the site. Consequently, R_{rup} always attains closer values to R_{JB} than R_{hyp}.

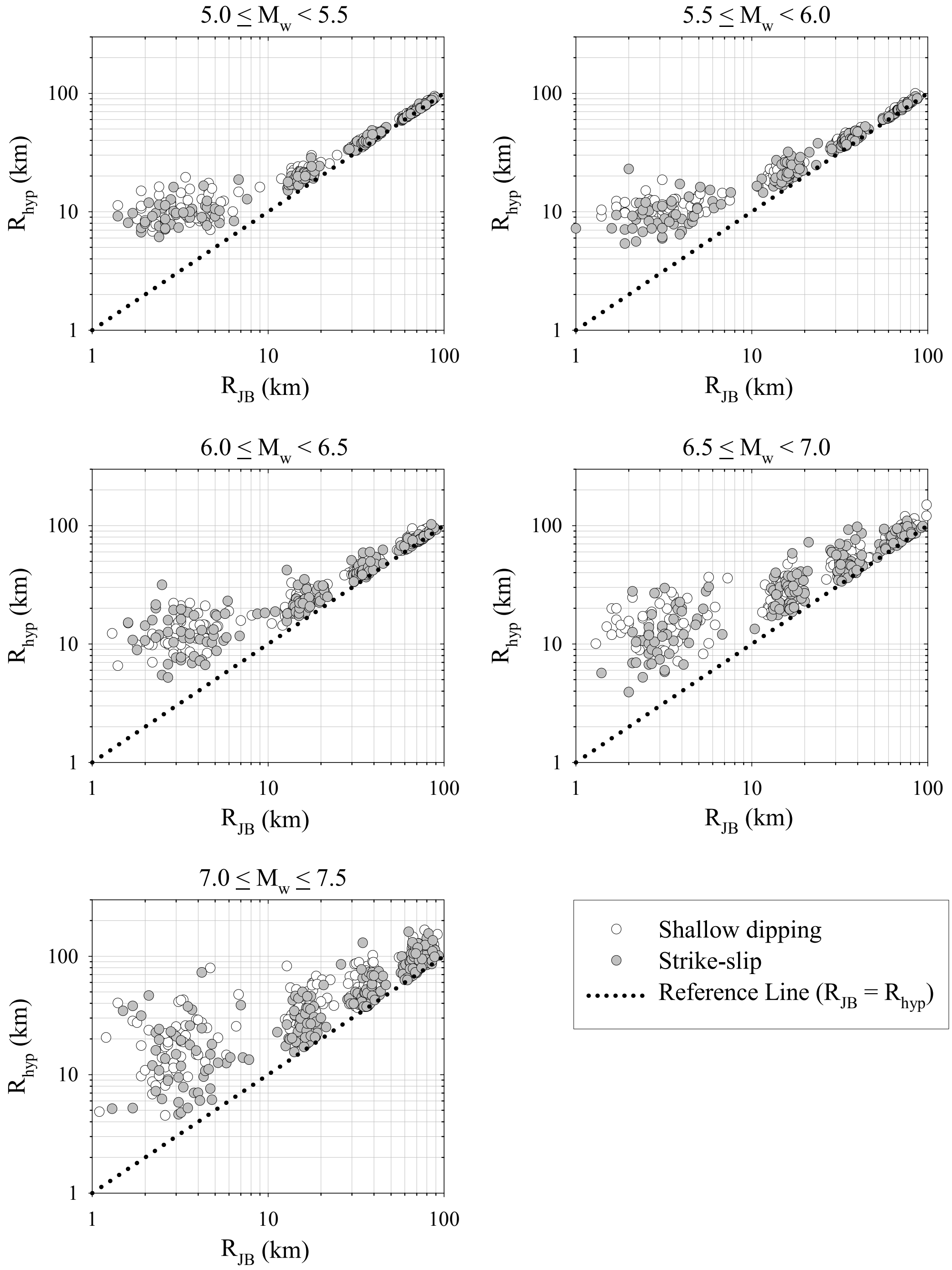

Figure 2.6 Scatter plots for R_{JB}-R_{hyp} pairs

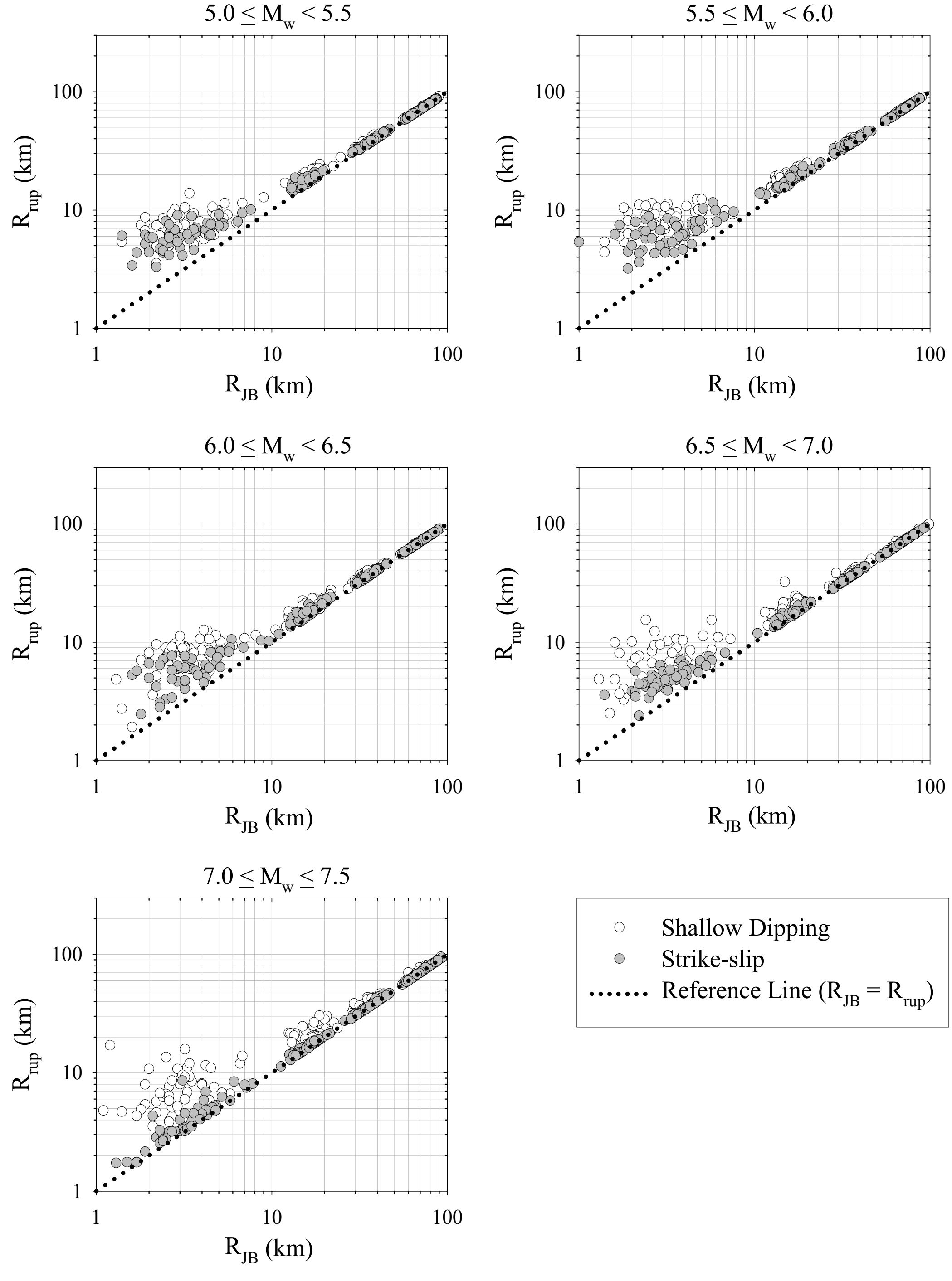

$5.0 \leq M_w < 5.5$

$5.5 \leq M_w < 6.0$

$6.0 \leq M_w < 6.5$

$6.5 \leq M_w < 7.0$

$7.0 \leq M_w \leq 7.5$

Figure 2.7 Scatter plots for R_{JB}-R_{rup} pairs

When the faulting style is of concern, it is depicted from Figure 2.7 that shallow dipping events diverge from strike-slip events with increasing earthquake magnitude. The discrepancy is observed especially at close distances. The influence of dipping angle and depth-to-top of rupture on R_{rup} is the main cause of this divergence. Fault rupture for large earthquakes tends to reach to the ground surface, whereas for small earthquakes the rupture is mostly below the ground (Abrahamson and Silva, 2008). Therefore, for large magnitude and vertically-dipping strike-slip events $R_{rup} \approx R_{JB}$ since the rupture plane is closer to the surface. However, for shallow dipping events, the dipping angle (δ) plays an important role in the calculation of R_{rup} and this leads $R_{rup} > R_{JB}$. At moderate-to-large distances, this discrepancy tends to vanish due to the diminishing of rupture depth and fault dipping effects.

Figure 2.8 shows the R_{hyp}-R_{rup} scatters for each magnitude bin to explore whether their variations are rational. It is depicted from the scatters that R_{rup} always attains equal or smaller values than R_{hyp} and the difference between these two distance metrics increases with increasing magnitude and decreasing source-to-site distance. Consequently, the scatter plots presented in Figures (2.6) to (2.8) suggest that the randomly sampled distance metrics exhibit the physically expected rational variations.

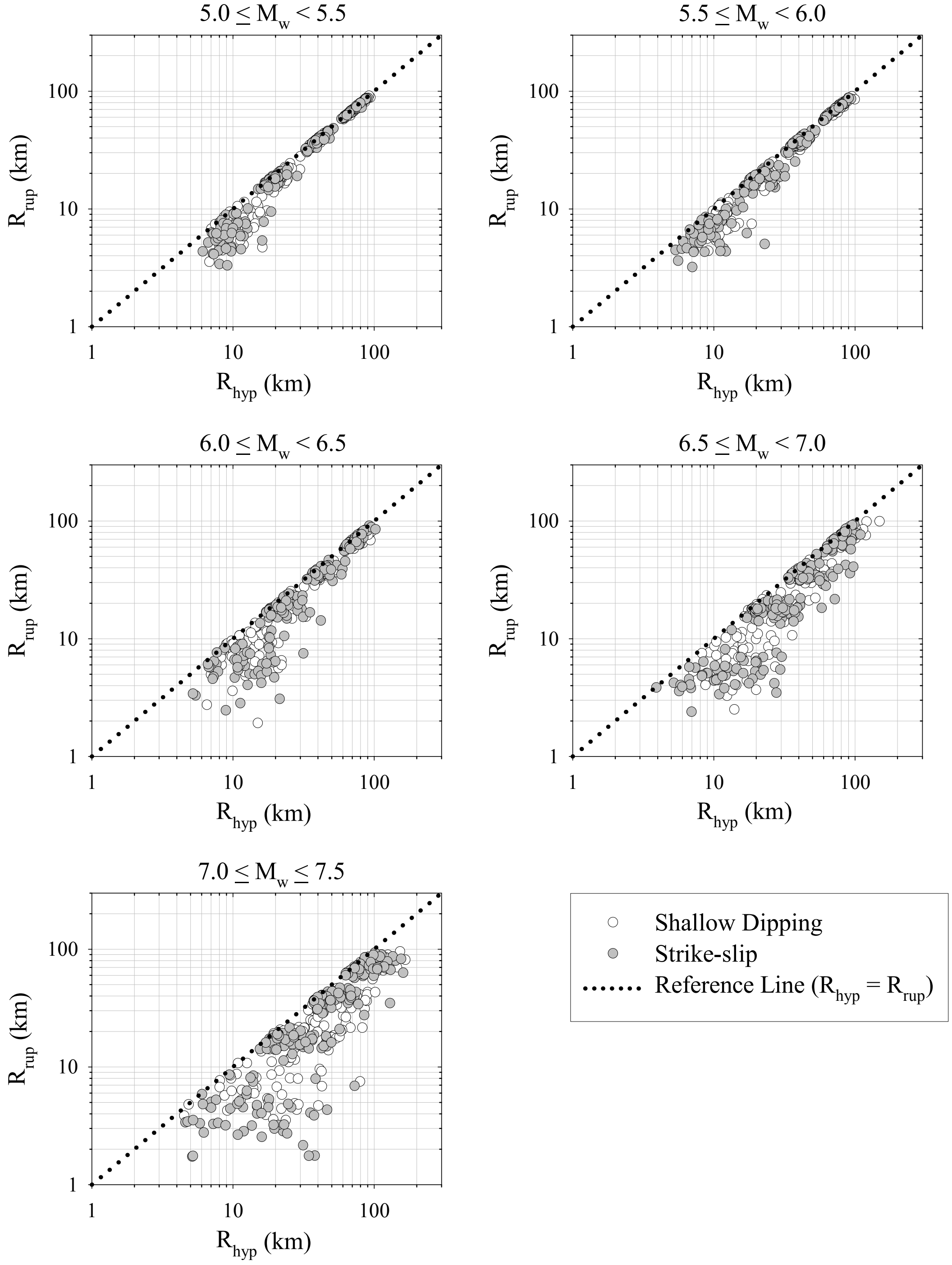

Figure 2.8 Scatter plots for R_{hyp}-R_{rup} pairs

CHAPTER 3

SIMULATION OF GROUND MOTIONS AT OUTCROPPING VERY HARD ROCK SITES

3.1 General

In this chapter, the simulation of ground motions at outcropping very hard rock (VHR) sites is discussed. The ground-motion time series are simulated based on the well-known point-source stochastic method of Boore (1983, 2003). The double-corner point-source spectrum proposed by Atkinson and Silva (2000) is used in the simulation process. The source spectrum is attenuated by the empirical travel-path attenuation functions derived by Raoof et al. (1999) and amplified by the site amplification factors for VHR sites proposed by Boore and Joyner (1997). A total of 2000 ground motions are generated at outcropping VHR sites for moment magnitude $5.0 \leq M_w \leq 7.5$ and distance 1 km $\leq R_{JB} \leq 100$ km ranges, for shallow dipping and strike-slip events. The simulations are performed using randomly generated ground-motion parameters via Monte Carlo simulation technique (Chapter 2). The components of stochastic simulation process are discussed in the following sections.

3.2 Simulation Method

Stochastic simulation procedures typically consist of two essential components: (i) a ground-motion amplitude spectrum defining the frequency content and (ii) a set of random phase angles characterizing the phase arrivals (Vanmarcke, 1977). The ground-motion amplitude spectrum is the essential ingredient and it describes the physics of the earthquakes and wave propagation through the crust (Boore, 2003). The amplitude spectrum is defined as the product of the key factors affecting the ground motion characteristics (i.e. source, path and site). The amplitude spectrum is then combined with a random phase spectrum such that the artificially generated motion is distributed over a duration related to the earthquake magnitude and the source-to-site distance (Boore, 2003).

In this study, the stochastic method introduced by Boore (1983, 2003) is used to simulate the ground-motion time series. It is based on the studies performed by Hanks and McGuire (Hanks, 1979; Hanks and McGuire, 1981; McGuire and Hanks, 1980). The procedure assumes that the ground motions are stationary in frequency content. The method considers only the contribution of S-wave motions and it is stated as successful in predicting the important features of ground motions as the S-waves contain most of the ground-motion energy that is directly related to seismic hazard (Boore, 2003).

The VHR simulations are performed via SMSIM software (Boore, 2005). The steps of the ground-motion simulation process are illustrated in Figure 3.1. The algorithm starts with the generation of a band-limited Gaussian white noise for a duration related to the earthquake magnitude and source-to-site distance (Figure 3.1.a). Next, the generated noise is windowed (Figure 3.1.b) and transformed to the frequency domain (Figure 3.1.c). The purpose of windowing is to give a realistic shape to the artificial acceleration time series. The spectrum of the windowed noise is normalized by the square-root of its mean square amplitude spectrum (Figure 3.1.d). Then, the normalized spectrum is multiplied by the ground-motion amplitude spectrum (Figure 3.1.e). Finally, the resulting spectrum is transformed back to the time domain that yields the final ground-motion time series (Figure 3.1.f). In this manner, the simulation procedure accomplishes two essential conditions: time series with (i) a finite duration and (ii) a specified amplitude spectrum (Boore, 1983).

The ground-motion amplitude spectrum is predicted as the product of the source spectrum, E, path effect, P, site effect, G, and the type-of-motion parameter, I (Boore, 2003). The generic expression of amplitude spectrum, Y, is given in Equation (3.1).

$$Y(M_0,R,f) = E(M_0,f)\cdot P(R,f)\cdot G(f)\cdot I(f) \tag{3.1}$$

where M_0 is the seismic moment, R is the source-to-site distance and f is the frequency. As noted previously, the source spectrum, path and site effects are the key components influencing the characteristic of the earthquake ground motion. The type-of-motion parameter specifies the type of time series (i.e. acceleration, velocity or displacement) to be generated. In complex Fourier domain, it is expressed as

$$I(f) = (2\pi f i)^n \tag{3.2}$$

where $i = \sqrt{-1}$ and n = 0, 1 and 2 for ground displacement, velocity and acceleration, respectively.

3.2.1 Source Model

The source spectrum designates the Fourier amplitude spectrum of the displacements developed at the source due to the generated S-waves. As presented in Boore (2003) most of the source models described in the literature have a functional form of

$$E(M_0,f) = C\cdot M_0\cdot S \tag{3.3}$$

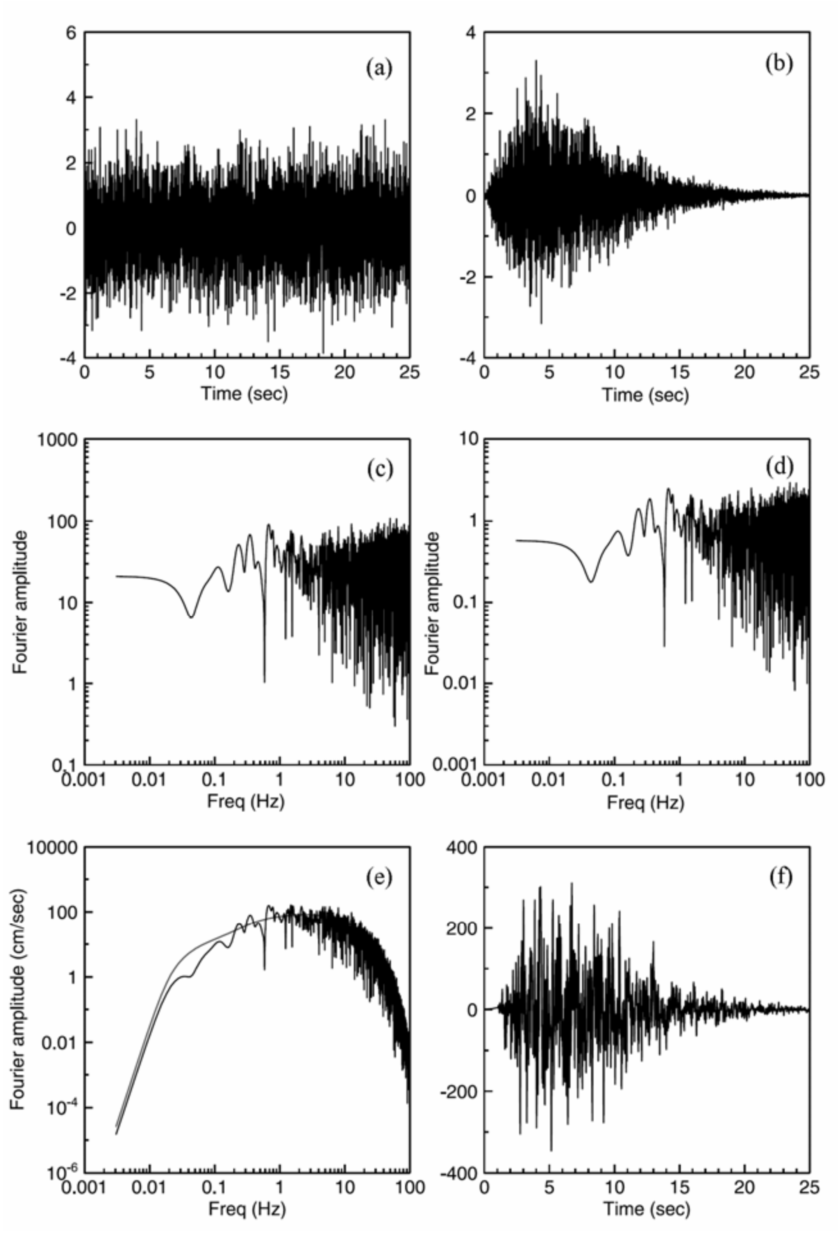

Figure 3.1 Illustration of the steps followed in the stochastic simulation process (courtesy of Boore, 2003)

where C is a scaling constant and S is the displacement source function. The constant, C, is expressed as

$$C = \frac{< R_{\Theta\phi} > VF}{4\pi\rho_s\beta_s^3 R_0} \tag{3.4}$$

where $< R_{\Theta\phi} >$ denotes the radiation pattern averaged over a suitable range of azimuths and take-off angles, V (= $1/\sqrt{2}$) represents the partitioning of the total S-wave energy into its horizontal components, and F (= 2) accounts for the free surface effect. ρ_s and β_s are the density and S-wave velocity at the source, respectively. In this study, ρ_s and β_s are taken as 2.8 g/cm^3 and 3.5 km/sec, correspondingly. The source-to-site distance and faulting style dependent radiation coefficients proposed by Boore and Boatwright (1984) are used in this study (Table 3.1).

Table 3.1 Radiation coefficients, $< R_{\Theta\phi} >$, used in this study

	Shallow dipping	Strike-slip
1 km ≤ R_{JB} < 25 km	0.64	0.50
25 km ≤ R_{JB} ≤ 100 km	0.48	0.60

The displacement source function, S, is the most important component used for establishing the source spectrum, E (M_0, f). One of the well-known and commonly used models is Brune (1970) spectrum, which is a single-corner point-source model. It was generated assuming that the S-waves radiate from a point-source located at the center of a circular fault plane (Brune, 1970). The shape and amplitudes of Brune spectrum are controlled by two parameters. The seismic moment, M_0, is one of these parameters and it is related to the size of the earthquake. The other parameter is the constant stress drop, $\Delta\sigma$, which expresses the energy released during an earthquake. $\Delta\sigma$ controls the high-frequency amplitudes of the ground motions. The displacement source function proposed by Brune (1970) is given as

$$S_{\text{Brune}} = \frac{1}{1+\left(f/f_c \right)^2} \tag{3.5}$$

where f_c is the corner frequency that is inversely proportional to the duration of the fault rupture. It is given by the following equation

$$f_c = 4.9 \times 10^6 \beta_s \left(\frac{\Delta\sigma}{M_0} \right)^{1/3} \tag{3.6}$$

where β_s is expressed in km/sec, $\Delta\sigma$ is in bars and M_0 is in dyne-cm.

The use of Brune spectrum for the stochastic simulations successfully predicts the ground-motion amplitudes at high frequencies ($f \geq 2$ Hz). However, at low-to-intermediate frequencies (0.1 – 2 Hz), the amplitudes of ground motions for moderate-to-high magnitude earthquakes are overpredicted (Atkinson and Silva, 1997; 2000). This inconsistency increases with increasing magnitude. Atkinson and Silva (1997) indicated that the observed discrepancy between the single-corner point-source simulations and the empirical data could be due to the failure of the point-source approximation for large ruptures. The implicit circular fault assumption of Brune model may be another cause of this discrepancy because the fault planes are typically rectangular for large magnitudes and the frequency content at the source can be influenced considerably by the fault geometry (Lam et al., 2000).

The comparisons of empirical source spectra with the predictions obtained from Brune's point-source and the finite-fault simulations indicated that the finite-fault simulations can imitate the observed spectra better (Beresnev and Atkinson, 1997; Atkinson and Silva, 1997). Consequently, Atkinson and Silva (2000)(4) presented an equivalent point-source spectrum generated from the finite-fault modeling to mimic the salient finite-fault effects.

In this study, the ground motions at outcropping VHR sites are simulated using the source model of Atkinson and Silva (2000). The displacement source function of Atkinson and Silva (2000), S_{AS00}, is given as

$$S_{AS00} = \frac{1-\varepsilon}{1+(f/f_a)^2} + \frac{\varepsilon}{1+(f/f_b)^2} \tag{3.7}$$

where f_a and f_b are the corner frequencies and ε is a relative weighting parameter. The expressions proposed by Atkinson and Silva (2000) for f_a, f_b and ε are presented below.

$$\log(f_a) = 2.181 - 0.496M_w \tag{3.8}$$

$$\log(f_b) = 2.41 - 0.408M_w \tag{3.9}$$

$$\log(\varepsilon) = 0.605 - 0.255M_w \tag{3.10}$$

---

(4) In Atkinson and Silva (2000), the length and width of the fault plane were computed from the magnitude-dependent expressions proposed by Wells and Coppersmith (1994) and the fault plane was modeled by an array of sub-faults. The seismic wave radiation from each sub-fault was modeled as a Brune's point-source model. The time series were simulated at many azimuths placed at equidistant observation points around the fault. The simulations for an observation point were generated by adding the seismic waves radiated from sub-faults, appropriately shifted in time. The Fourier spectra of the simulated time series at a reference near-source distance were averaged over all azimuths for each magnitude. The mean Fourier spectra were employed to define the shape and amplitude of an equivalent point-source spectrum that reflects the salient finite-fault effects.

The lower corner frequency, f_a, is related to the size of the finite fault and correlated with the source duration. However, the higher corner frequency, f_b, is related to the sub-fault size and it is defined as the frequency at which the spectrum reaches half of the high frequency amplitude level. The relative weighting parameter, ε, lies between 0 and 1. Atkinson and Silva (2000) spectrum is identical to the Brune spectrum when $\varepsilon = 1$.

The randomly generated moment magnitudes that are described in Chapter 2 are used for the simulation of ground motions at outcropping VHR sites. Note that in Equations (3.8) to (3.10), the corner frequencies and the relative weighting parameter are defined in terms of M_w, whereas the source spectrum, E, is expressed in terms of M_0 (see Equation (3.3)). The conversion between M_w and M_0 is performed within SMSIM software using the magnitude scaling relationship proposed by Hanks and Kanamori (1979). This relation is given in Equation (3.11).

$$M_w = \frac{2}{3}\log M_0 - 10.7 \tag{3.11}$$

Figure 3.2 compares the point-source models proposed by Brune (1970) and Atkinson and Silva (2000) in terms of acceleration source spectra for various earthquake magnitudes. The ground-motion amplitudes increase with increasing earthquake magnitude for both source models and both models are in good agreement at high frequencies ($f \geq 2$ Hz). However, as previously noted, Brune's model overpredicts the ground-motion amplitudes at low-to-intermediate frequencies and the discrepancy between the two models increases with increasing M_w.

Not only the amplitude spectrum, but also the ground-motion duration is affected by the source kinematics. Ground-motion duration, T, is predicted as the summation of source duration, T_0, and distance-dependent duration, bR, (Atkinson and Boore, 1995; Atkinson and Silva, 2000; Boore, 2003):

$$T = T_0 + bR \tag{3.12}$$

The source duration, T_0, is defined as the length of time required for the release of accumulated strain energy by the fault rupture. T_0 increases with increasing earthquake magnitude and it is inversely proportional to the corner frequency of the source model. Atkinson and Silva, (2000) employed the expression proposed by Boatwright and Choy (1992) to relate the source duration, T_0, and the lower corner frequency, f_a. This is given in Equation (3.13).

$$T_0 = 1/(2f_a) \tag{3.13}$$

In this study, the source duration is accounted for using the same relationship. Figure 3.3 presents the variation of source duration with the magnitude.

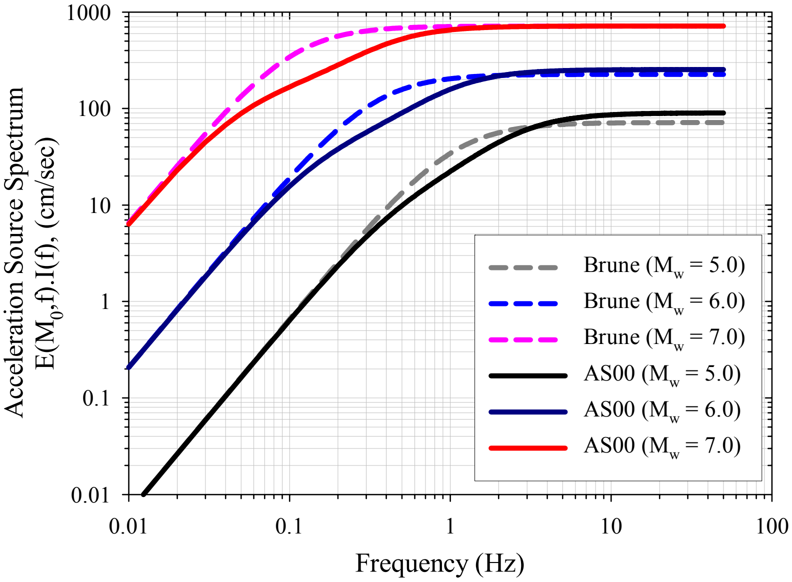

Figure 3.2 Comparison of source models proposed by Brune (1970) ($\Delta\sigma$ = 80 bars) and Atkinson and Silva (2000), AS00, for various earthquake magnitudes. The acceleration source spectra are computed for $< R_{\Theta\phi} > = 0.50$.

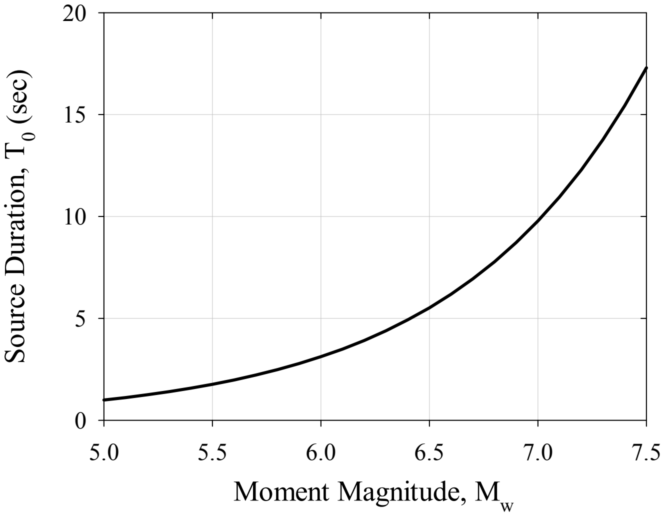

Figure 3.3 Magnitude vs. source duration relationship (Atkinson and Silva, 2000)

As indicated in Equation (3.12), the travel path of the seismic waves influences the ground-motion duration as well. The ground-motion duration increases as the source-to-site distance increases. The variable b in Equation (3.12) is a region-dependent parameter that is either a constant or a function of distance (Atkinson and Boore, 1995). The travel path duration, in this study, is modeled from the study performed by Atkinson and Silva (2000) in which b was assumed to attain a constant value of 0.05.

3.2.2 Path Effect

The path followed by the seismic waves propagating through the crust is another important factor that influences the characteristic of a ground motion. The amplitude spectrum of a ground motion decays with increasing source-to-site distance due to geometrical and anelastic (intrinsic) attenuation. The geometrical attenuation refers to the decay of the ground-motion amplitudes due to spreading of seismic wave energy over a continuously increasing area as a result of expansion of wave fronts. The anelastic attenuation expresses all energy losses that have not been accounted for by the geometrical attenuation except for the local site effects

(Lam et al., 2000). Romero and Rix (2001) define the intrinsic attenuation as the dissipation of seismic energy due to particle interaction.

Boore (2003) describes the total path effect as the product of geometrical and anelastic attenuations. This is given in Equation (3.14).

$$P(R,f) = Z(R) \cdot \exp\left(-\frac{\pi \cdot f \cdot R}{Q(f) \cdot c_Q}\right) \tag{3.14}$$

where R is the source-to-site distance, Z is to the geometrical spreading function, Q denotes the frequency-dependent quality factor and c_Q refers to the S-wave velocity used in the derivation of Q.

The geometrical spreading function, Z, describes the decay of ground-motion amplitudes due to geometrical attenuation. The geometrical attenuation is based on the source-to-site distance and the regional thickness of the earth crust. At close-to-intermediate distances, ground motions are dominated by the directly arriving seismic waves (Atkinson and Mereu, 1992). Within this range of distances, the seismic waves spread spherically that results in a 1/R decay in ground-motion Fourier amplitudes. At far distances, however, the ground motions are controlled by the body waves formed due to the multiple reflections within the earth crust. Lam et al. (2000) stated that the seismic waves spread cylindrically at far distances. Therefore, the geometrical attenuation is, generally, expressed as distance-dependent piecewise continuous series of functions.

The exponential term presented in Equation (3.14) accounts for the anelastic attenuation that indicates the exponential decay of ground-motion amplitudes with number of wave cycles (Lam et al., 2000). The quality factor, Q, represents the regional wave-transmission quality of the propagation medium (Lam et al., 2000). In general, it is determined from the analysis of weak-motion data. The spectral ratio and coda wave methods are two commonly used approaches to determine the quality factor (Atkinson and Mereu, 1992). In the spectral ratio method, the ratios of spectral amplitudes observed at sites with various distances are examined to derive the quality factor. In the coda wave method, the quality factor is determined from the investigation of the amplitude decay of randomly distributed scattered waves with time (Lam et al., 2000).

Trade-offs between the geometrical spreading and anelastic attenuation require the use of same empirical data while deriving the corresponding predictive models (Boore, 2003). In this study, the most important components of total path effect (Z(R) and Q(f)) are modeled by the empirical attenuation functions (predictive models) developed by Raoof et al. (1999). These researchers performed analyses on Z(R) and Q(f) as well as duration and site effects using data from a broadband, digital seismograph network in southern California. Raoof et al. (1999) investigated the variation of Fourier amplitude spectra with distance to derive a geometrical spreading function and a frequency-dependent quality factor. The geometrical spreading function, Z, and quality factor, Q, proposed by Raoof et al. (1999) are presented in Equations (3.15) and (3.16).

$$Z(R) = \begin{cases} \dfrac{1}{R} & \text{for } R < 40 \text{ km} \\ \dfrac{1}{40}\left(\dfrac{40}{R}\right)^{0.5} & \text{for } R \geq 40 \text{ km} \end{cases} \qquad (3.15)$$

$$Q(f) = 180f^{0.45} \qquad (3.16)$$

In this study, the distance metric R is taken as R_{hyp} in Equation (3.15). As indicated in Chapter 2, the outcropping motions of VHR sites are simulated using R_{hyp} due to the recommendation of Scherbaum et al. (2006).

Figure 3.4 presents the total path effect proposed by Raoof et al. (1999) for various ground-motion frequencies. It is shown that the multiplicative path factor decreases as the hypocentral distance increases. It is also observed that the high-frequency components decay more rapidly with distance when compared to the behavior of low-frequency components. This explains why the ground motions recorded at far distances are generally rich in low-frequency components (Boore and Bommer, 2005).

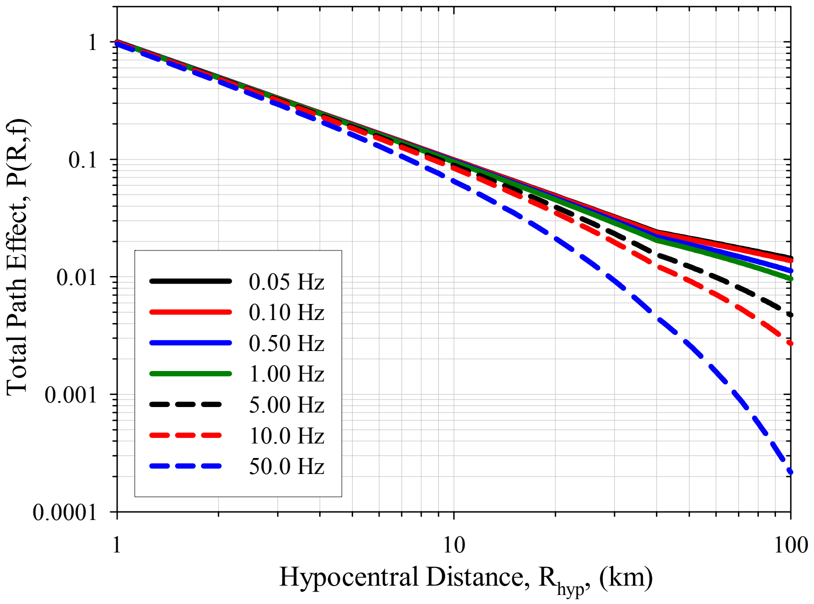

Figure 3.4 Influence of path on the ground-motion amplitudes for various frequencies

3.2.3 Site Effect

The local site conditions can significantly influence the characteristics of the earthquake ground motions. The modification of seismic waves by the surface soils overlying bedrock is, actually, part of the path effect. However, Boore (2003) considers the path and site effects separately as the local site effects are largely independent of distance (except for nonlinear site effects). The stochastic methods are generally implemented to predict ground motions at generic sites. The ground-motion simulation approach proposed by Boore (2003) does not consider the nonlinear site effects. Boore (2003) suggests to compute rock motions using a linear model and account for nonlinear effects as part of an additional site response analysis. The influence of site on the ground-motion amplitude spectrum, G (f), is defined as the product of the unattenuated amplification of the seismic waves relative to the source, A(f), and the path-independent loss of high-frequency energy, D(f) (Boore, 2003).

$$G(f) = A(f)\,D(f) \tag{3.17}$$

The amplitudes of the seismic waves crossing the boundary between two mediums are modified in accordance with the principle of the conservation of energy (Lam et al., 2000). The transmission of the seismic waves from a high-impedance medium (wave propagation velocity multiplied by the density) to a lower impedance causes the amplitudes of the seismic waves to increase.

Generally, the amplification of the seismic waves propagating through the crust, A(f), is derived from the wave-calculation solutions that account for reverberations or impedance contrasts determined from S-wave velocity (V_S) variations with depth (Boore, 2003). Boore and Joyner (1997) used S-wave travel-time measurements obtained from boreholes with the guidance of the studies on P-wave velocities in the crust to derive the variation of S-wave velocity (V_S) with depth. They employed these generated V_S models to compute the site amplifications for generic sites, using quarter-wavelength approximation.

According to the quarter-wavelength approximation, the amplification for a particular frequency is determined as the square root of the ratio of the seismic impedance at the source to the seismic impedance averaged over a depth that is equal to the quarter wavelength of the corresponding frequency (Boore and Joyner, 1997). The amplification factor is

$$A(f(z)) = \sqrt{\frac{\rho_s V_{S,s}}{\overline{\rho}(z)\overline{V}_S(z)}} \tag{3.18}$$

where, ρ_s and $V_{S,s}$ denote the density and S-wave velocity in the vicinity of the source. The parameters $\overline{\rho}(z)$ and $\overline{V}_S(z)$ are travel-time-weighted average of density and S-wave velocity to depth z, respectively. The frequency corresponding to depth z, f(z), is

$$f(z) = \frac{1}{4S_{tt}(z)} \tag{3.19}$$

where $S_{tt}(z)$ refers to the S-wave travel-time from depth z to the ground surface.

The validity of the quarter-wavelength approximation was checked by several studies comparing the approximate and exact theoretical amplifications (Boore and Joyner, 1991; 1997; Silva and Darragh, 1995). It was found that the quarter-wavelength approximation provides a good estimate of the mean values of the response. However, the soil nonlinearity effects are not taken into account by this method. In this study, therefore, it is preferred to simulate the outcropping motions at VHR sites through the stochastic procedure of Boore (2003) where the local site effects are not significant. These artificial ground motions are then modified to generate the surface motions at soft, stiff and rock sites. This subject is treated in detail in Chapter 4.

The amplifications at VHR sites are considered by implementing the frequency dependent discrete functional form proposed by Boore and Joyner (1997). Table 3.2 lists this functional form at discrete frequency points.

Table 3.2 Discrete points of the site amplifications proposed by Boore and Joyner (1997) for VHR sites

Frequency (Hz)	Amplification
0.01	1.00
0.10	1.02
0.20	1.02
0.30	1.05
0.50	1.07
0.90	1.09
1.25	1.11
1.80	1.12
3.00	1.13
5.30	1.14
8.00	1.15
14.00	1.15

The amplitudes of the seismic waves decay independently from distance due to the existence of mediums with low wave-transmission quality at the top of the earth crust (Lam et al., 2000). This path-independent loss of energy is accounted for by the diminution function, D(f), in Equation (3.17). Some studies revealed that this energy loss may not be only due to the site effect but also due to a source effect (Papageorgiou and Aki, 1983) or a combination of these two effects (Atkinson, 1996; Boore, 2003). Filters referred as f_{max} and κ_0 are two of the commonly used multiplicative filters that account for the diminution of high-frequency motions. Boore (2003) defines f_{max} and κ_0 filters as presented in Equations (20) and (21), respectively.

$$D(f) = \left[1 + \left(f/f_{max}\right)^8\right]^{-0.5} \tag{3.20}$$

$$D(f) = \exp\left(-\pi \kappa_0 f\right) \tag{3.21}$$

where f_{max} is the high-cut filter frequency proposed by Hanks (1982) and κ_0 is the zero-distance intercept of the high-frequency decay parameter introduced by

Anderson and Hough (1984). κ_0 filter and the path-dependent anelastic attenuation (the exponential term presented in Equation (3.14)) have similar functional forms. The anelastic attenuation is expressed in terms of distance, wave transmission quality factor and the S-wave velocity at the source. In κ_0 filter, however, the attenuation effect is lumped into a single controlling parameter, κ_0.

In some applications, the influence of the source on the diminution factor is taken into account by relating κ_0 to the earthquake magnitude (e.g. Sokolov et al., 2008). The magnitude dependence of κ_0 is believed to be the result of the nonlinear behavior of the surface layers (Atkinson and Silva, 1997; Lam et al., 2000). In this study, κ_0 is considered to be independent of magnitude as the site effects are not significant for the VHR sites and the soil nonlinearity effects are later taken into account in the site response analyses (Chapter 4). Boore and Joyner (1997) stated that there may be a correlation between the attenuation parameter, κ_0, and mean S-wave velocity, $V_{S,30}$. In general, κ_0 is less than 0.01 sec for VHR sites and increases with decreasing $V_{S,30}$. However, the correlation between κ_0, and $V_{S,30}$ may be region-dependent or the class of geological materials beneath a site can influence this correlation. For instance, Atkinson (1996) found that κ_0 for VHR sites show a variation from $\kappa_0 = 0.004$ sec to $\kappa_0 = 0.011$ sec in southeastern and southwestern Canada, respectively.

In some studies, κ_0 is used to calibrate the ground-motion simulations at high frequencies with respect to the empirical or predicted ground-motion spectra (Boore et al., 1992; Boore and Joyner, 1997). In this study, a preliminary sensitivity analysis is performed to decide on the κ_0 value to be used in the simulations. For various κ_0 values, the spectral displacements computed from the simulated ground motions at soft, stiff and rock sites are compared with the spectral displacement estimations obtained from the ground-motion prediction equations. Based on these analyses, κ_0 is selected as 0.015 sec for the generation of synthetic VHR motions.

f_{max} filter is used to filter out the high-frequency components above the Nyquist frequency (i.e. $f_{max} = f_{Nyquist}$). For the ground-motion simulations, the sampling rate, Δt, is selected as 0.01 sec due to the limitations of ProShake v1.12 software (2007) used in modifying VHR simulations to different site classes (Chapter 4).

Figure 3.5 demonstrates the construction of a ground-motion amplitude spectrum at a VHR site for $M_w = 6$, $R_{hyp} = 25$ km and strike-slip (SS) faulting style. The acceleration source spectrum is multiplied by the path and site effects to generate the ground-motion amplitude spectrum. The figure displays that the path traveled by the seismic waves causes the ground-motion amplitudes to attenuate. As previously noted, the decay of the ground-motion amplitudes due to path effect is more pronounced at high frequencies compared to the attenuation of low-frequency components. When source spectrum combined with the path effect is compared to the total amplitude spectrum, it is observed that the ground-motion amplitudes show almost no difference at low-to-intermediate frequencies ($f \leq 5$ Hz). This is due to the fact that the amplification effect (A(f)) is not significant for VHR sites within this frequency band. The decay in ground-motion amplitudes at higher frequencies is due to the diminution effect of the site that is accounted by D(f). Table 3.3 summarizes the prominent parameters used in this study while generating the outcropping ground motions of VHR sites.

3.3 Examination of the Synthetic VHR Motions

The ground-motion time series at outcropping VHR sites are simulated using the models and parameters discussed in the previous sections. The simulations are performed using randomly generated M_w-R_{hyp} pairs. A total of 2000 outcropping VHR motions are simulated (= 5M x 4R x 2F x 50 simulations, see Table 2.1: 40 different M_w, R_{JB} and faulting style bin combinations and each combination contains 50 simulations). Each realization represents a random horizontal component of a ground motion at a VHR site. Ground motions are generated with a 20 sec of pre-event time (t_{shift} in Table 3.3) to minimize the influence of long-period noise that results in unrealistic drifts in the ground displacements (personal communication with Dr. D. M. Boore, 2008).

The synthetic outcropping VHR motions are investigated to determine whether they mimic the general characteristics of real ground-motion records. Three samples of the simulated motions for various earthquake magnitudes are illustrated in Figure 3.6. The simulations presented in the figure are generated at comparable hypocentral distances for strike-slip events. It is observed that the ground-motion amplitudes and duration of time series increase with increasing earthquake magnitude, as expected. Recall that the ground-motion simulation method proposed by Boore (2003) is based on the generation of S-waves radiated from a point source. As a result, the realizations do not exhibit P-wave arrivals. The significance

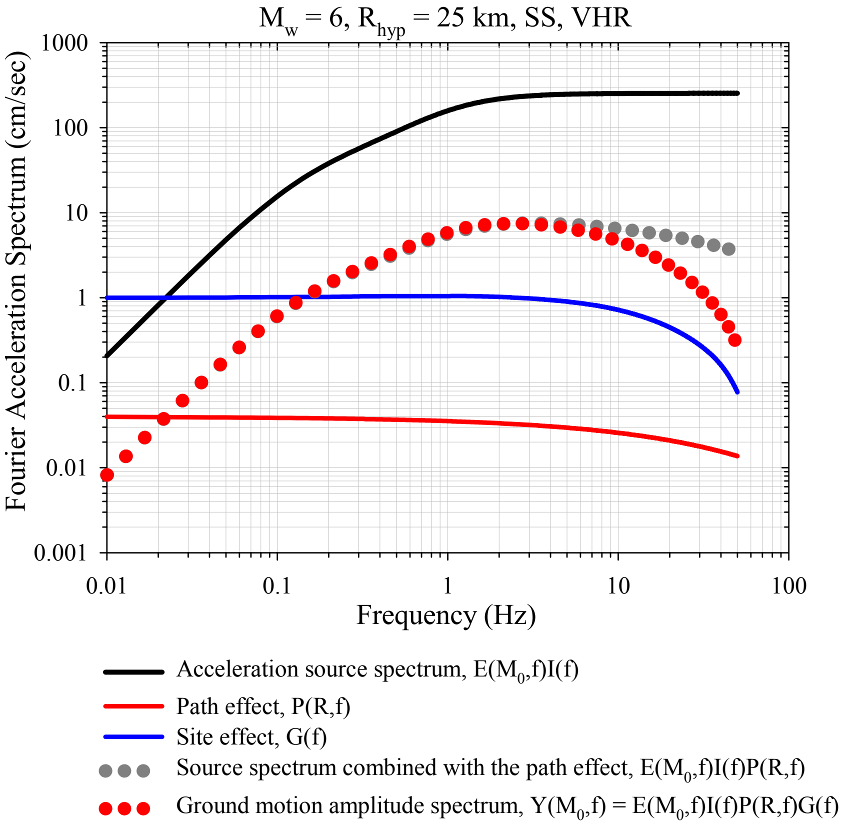

Figure 3.5 Construction of a ground-motion amplitude spectrum

Table 3.3 Summary of the prominent parameters used for the simulation of outcropping ground motions at VHR sites

Parameter	Value
Density in the vicinity of the source, ρ_s	2.8 g/cm^3
S-wave velocity in the vicinity of the source, β_s	3.5 km/sec
Partition factor, V	$1/\sqrt{2}$
Free surface factor, F	2
Radiation pattern, $<R_{\Theta\Phi}>$	Boore and Boatwright (1984)
Source model, S	Atkinson and Silva (2000)
Path effect, P(R,f)	Raoof et al. (1999)
Reference distance metric, R	R_{hyp}
Source duration, T_0	$1/(2f_a)$
Path duration factor, b	0.05
Site amplification factor, A(f)	Boore and Joyner (1997)
Site diminution parameters	f_{max} = 50 Hz κ_0 = 0.015 sec
Gaussian noise windowing type	Exponential window (Boore, 2003)
Other parameters	Δt = 0.01 sec t_{shift} = 20 sec

of stationary simulations (i.e. disregarding the P-wave arrivals) in capturing the important features of real ground motions will be verified later in Chapter 5.

Figure 3.7 presents the velocity and displacement time series obtained by integrating of the acceleration synthetics presented in Figure 3.6. Both velocity and displacement time series presented in this figure become zero when the ground motion ceases. When the ground displacements are of concern, the pre-event buffer (20 sec) displays a stable behavior and does not influence the peak ground displacement (PGD) that governs the long-period behavior of spectral displacements. Therefore, the VHR synthetics seem to be free-of the long-period noise at least for the spectral bands of engineering interest that may originate during the various steps of the simulation procedure.

Figure 3.8 illustrates the Fourier amplitude spectra (FAS) of the simulated ground motions for $7.0 \leq M_w \leq 7.5$ and 10 km $\leq R_{JB} < 25$ km bin for strike-slip events. The mean FAS of the simulated ground motions and the target spectrum are also presented in the same figure. The target spectrum is the average amplitude spectrum computed from Equation (3.1) by using the corresponding randomly generated M_w-R_{hyp} pairs that are generated for the simulation bin under consideration. The plots presented in Figure 3.8 show that the FAS of individual ground-motion simulations oscillate around the target spectrum that is in good agreement with the average of the simulations. Thus, the overall picture in this figure suggests that the simulated outcropping VHR motions can represent the expected characteristics of the real records at VHR sites fairly well.

Figure 3.9 compares the mean FAS of simulated ground motions with the corresponding target amplitude spectrum for 10 km $\leq R_{JB} < 25$ km and strike-slip (SS) events for different magnitude bins. The plot also displays the f^2 trends (dashed lines) to validate the low frequency behavior of the simulated data. It is clear that the agreement between the mean FAS of simulations and the target FAS holds for the entire magnitude range considered in this study. The consistency between the theoretical f^2 trends and the mean FAS suggest that the simulations behave as expected in the low-frequencies. Moreover, the coherency between the f^2 trends and the mean FAS curves once again emphasize that the VHR simulations are not contaminated by the long-period noise for the entire frequency band considered in this study.

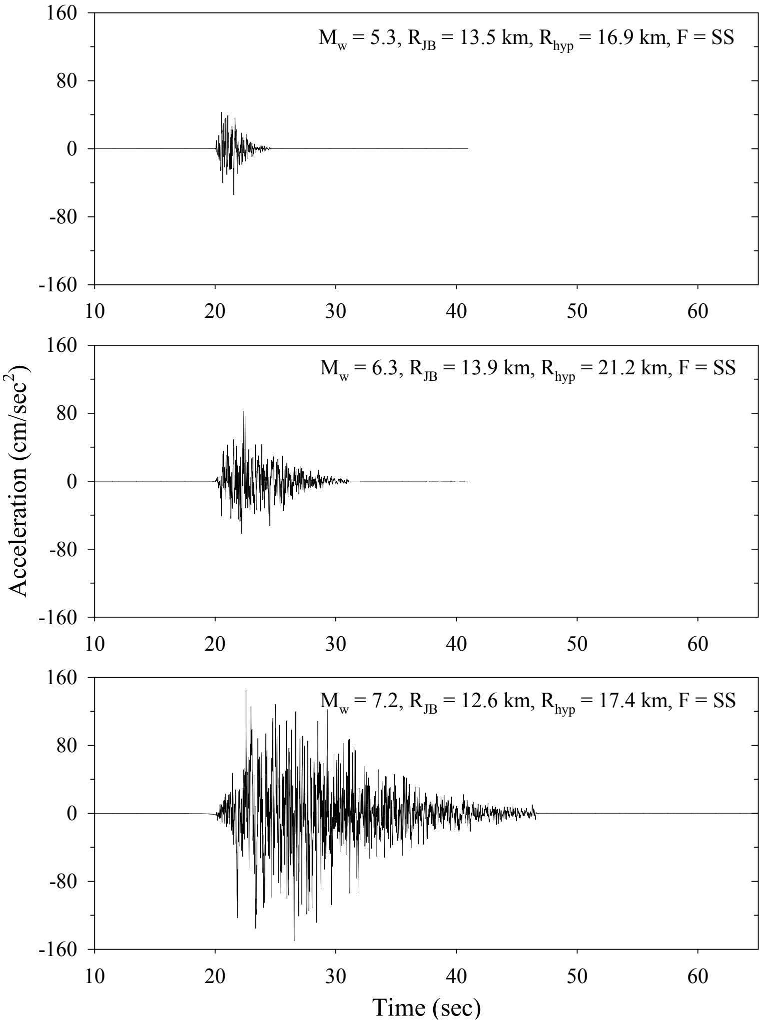

Figure 3.6 Illustrative samples of simulated acceleration time series at VHR sites. The time series are generated with 20 sec pre-event time. The time axis and the ordinate scaling are kept the same for comparative purposes.

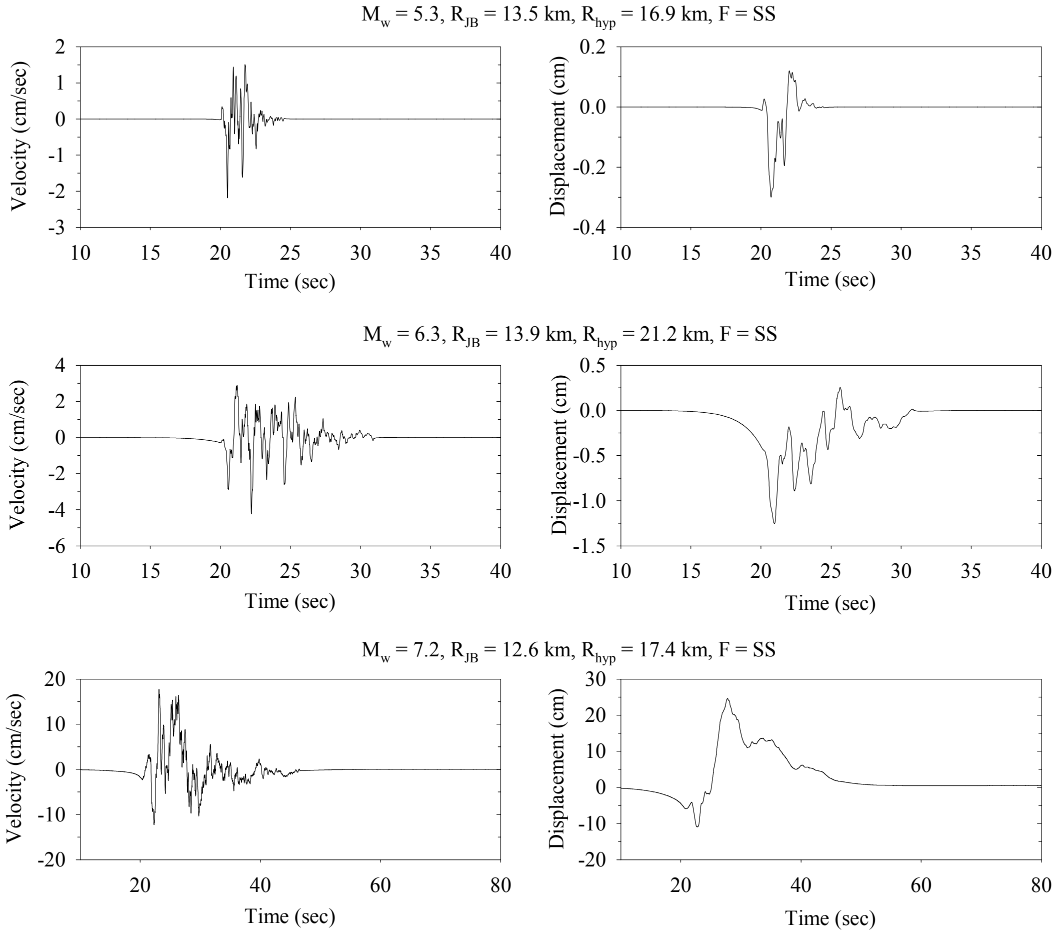

$M_w = 5.3$, $R_{JB} = 13.5$ km, $R_{hyp} = 16.9$ km, F = SS

$M_w = 6.3$, $R_{JB} = 13.9$ km, $R_{hyp} = 21.2$ km, F = SS

$M_w = 7.2$, $R_{JB} = 12.6$ km, $R_{hyp} = 17.4$ km, F = SS

Figure 3.7 Velocity and displacement time series of the VHR simulations presented in Figure 3.6. Note that the ordinate and abscissa scaling of each panel are different.

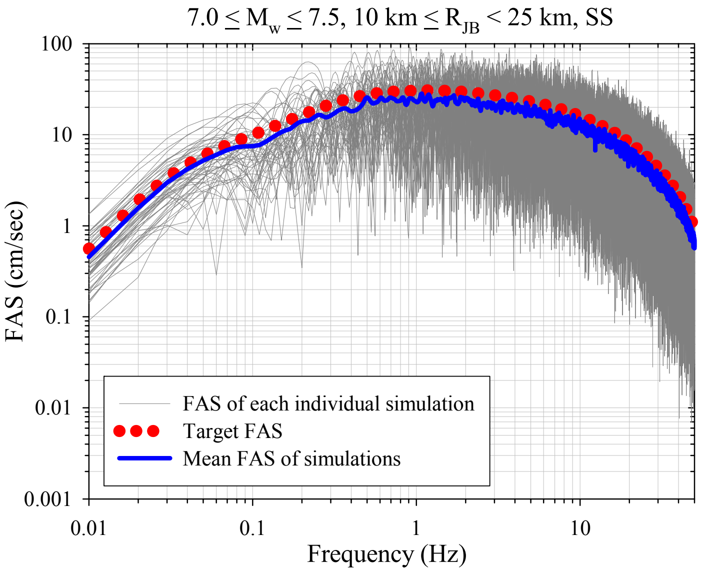

Figure 3.8 A sample case illustrating the comparison of the Fourier amplitude spectra (FAS) of the simulated time series and target amplitude spectrum.

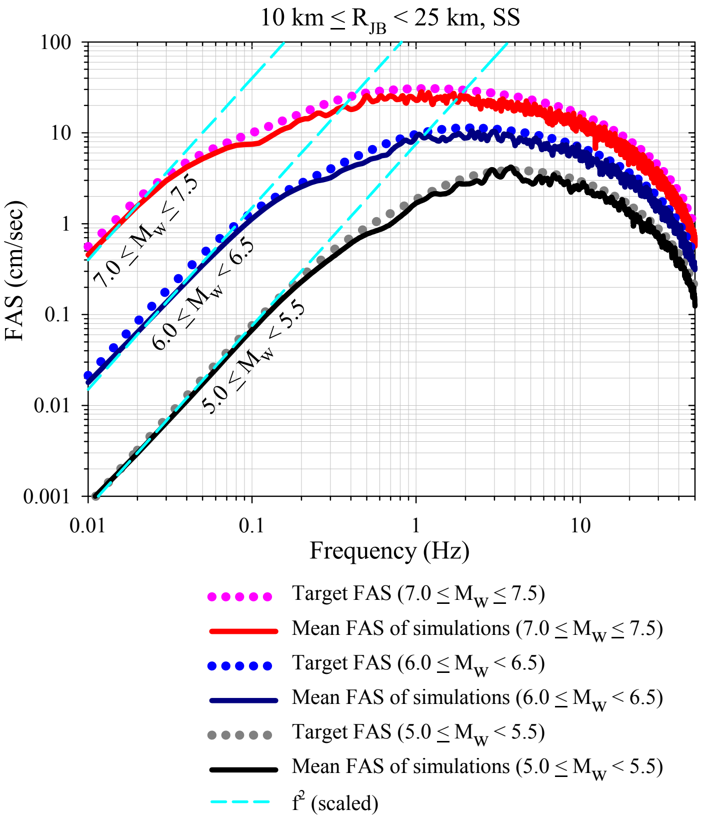

Figure 3.9 Comparisons of the mean FAS of the simulations with the corresponding target FAS for various magnitude intervals

CHAPTER 4

GENERATION OF FREE-FIELD MOTIONS AT SOFT, STIFF AND ROCK SITES

4.1 General

This chapter describes the second stage of the ground-motion simulation process. In this stage, the stochastically simulated outcropping VHR motions (Chapter 3) are modified by performing site response analyses to generate the free-field motions at soft, stiff and rock sites (The site classification is based on the mean S-wave velocity that is discussed in the succeeding sections). The site response analyses are carried out via ProShake v1.12 software (2007) that makes use of 1-D equivalent linear analysis method (Schnabel et al., 1972). Soil profiles are randomly generated based on the statistical evaluation of the soil profiles compiled from the USGS, Turkish NSMP and NGA databases. The details of the random soil profile generation process and the statistical analysis of the compiled datasets are discussed in the following sections.

4.2 Statistical Evaluation of Compiled Datasets

Engineers need to know how the characteristics of ground motions (i.e. amplitude, frequency content, and duration) vary with respect to the local site conditions to predict the peak ground values that are likely to occur at a site (Boore and Thompson, 2007). There are several ways to determine the local site effects: by theoretical ground response analyses, by measurements of actual surface and subsurface motions at the same site, and by measurements of ground surface motions from sites with different subsurface conditions (Kramer, 1996). Of these three methods, the theoretical ground response analysis is the simplest and the effective way of determining local site effects. In this study, 1-D site response analyses are performed to account for the influence of local site conditions in the simulation process. The simulated outcropping VHR motions are used as input motions for the site response analyses.

The theoretical site response analyses require soil profile definitions that are modeled as stacks of horizontal layers in 1-D equivalent linear analysis method. The description of soil profiles should include (i) the total depth of the profile (i.e. depth-to-bedrock), (ii) the number and thickness of layers and (iii) material properties (unit weight/density, S-wave velocity and dynamic material properties) of each layer. In this study, the soil profiles are randomly generated based on the S-wave slowness (inverse of S-wave velocity, V_S) models derived from the rigorous statistical evaluation of 424 soil profiles compiled from the USGS and Turkish NSMP databases. The slowness models account for the variability in depth-to-bedrock using the statistics obtained from the analysis of soil profile depths where V_S attains the value of 2.5 km/sec as presented by the NGA metafile. The compiled soil profiles are also evaluated in terms of number and thickness of layers. For the present study, the number and thickness of layers are randomly generated using the statistics obtained during the compilation of soil profiles. The details of these statistical analyses are presented in the following sub-sections. The unit weight and dynamic material properties are modeled according to the findings presented in the literature which will also be discussed in the succeeding sections of this chapter.

4.2.1 Depth-to-Bedrock

The time series simulated at outcropping VHR sites are used as the input motions for the site response analyses. Therefore, the soil profiles are extended down to depths where the S-wave velocities are comparable to those of VHR sites. The total depth of the profiles are modeled using the basic statistical quantities obtained from the analysis of depths to V_S = 2.5 km/sec (Z2.5) presented by the NGA flatfile. Despite the fact that the variation of depth-to-bedrock is completely random in nature, it can be correlated with the stiffness of the soil column overlying the bedrock. One of the commonly used parameters in expressing the stiffness of a soil structure is $V_{S,30}$ (the travel-time weighted average of S-wave velocities for the top 30 m of the profile). The measured $V_{S,30}$ and corresponding Z2.5 values presented by the NGA metafile are statistically evaluated to investigate the correlation between these two parameters. Figure 4.1 presents the scatter plots for Z2.5 in terms of site classes considered in this study. Note that the site classification is based on $V_{S,30}$. Soft, stiff and rock sites refer to the soils with 180 m/sec ≤ $V_{S,30}$ ≤ 360 m/sec, 360 m/sec < $V_{S,30}$ ≤ 760 m/sec and 760 m/sec < $V_{S,30}$ ≤ 1500 m/sec, respectively. The statistical and visual inspection of these scatters reveals that the data does not show any clear pattern. Thus, only the mean and standard deviation of Z2.5 are computed for further analysis in this study. The site class-dependent mean ($\mu_{Z2.5}$) and standard deviation ($\sigma_{Z2.5}$) statistics computed from the compiled data are listed in Table 4.1. Note that the data is scarce and draws a dispersive behavior for rock sites. The preliminary evaluation of these statistics indicates that Z2.5 has a strong dependence on site class. It can be also interpreted that soft sites are expected to attain V_S = 2.5 km/sec at greater depths when compared to the rock sites.

Figure 4.1 also presents 16% and 84% percentiles for Z2.5 for each site class. In this study, depth-to-bedrock parameter is assumed to be normally distributed and 16% and 84% percentiles are computed based on this assumption. To validate this assumption, the normal probability plots of Z2.5 values for each site class are visually examined (Figure A.1). It is observed that the normal distribution assumption is fairly acceptable for soft and stiff sites. However, the scarce rock site data makes it difficult to derive the same conclusion for this site class. Nevertheless, in this study, the depth-to-bedrock parameter for rock sites is also assumed to be normally distributed for the sake of uniformity.

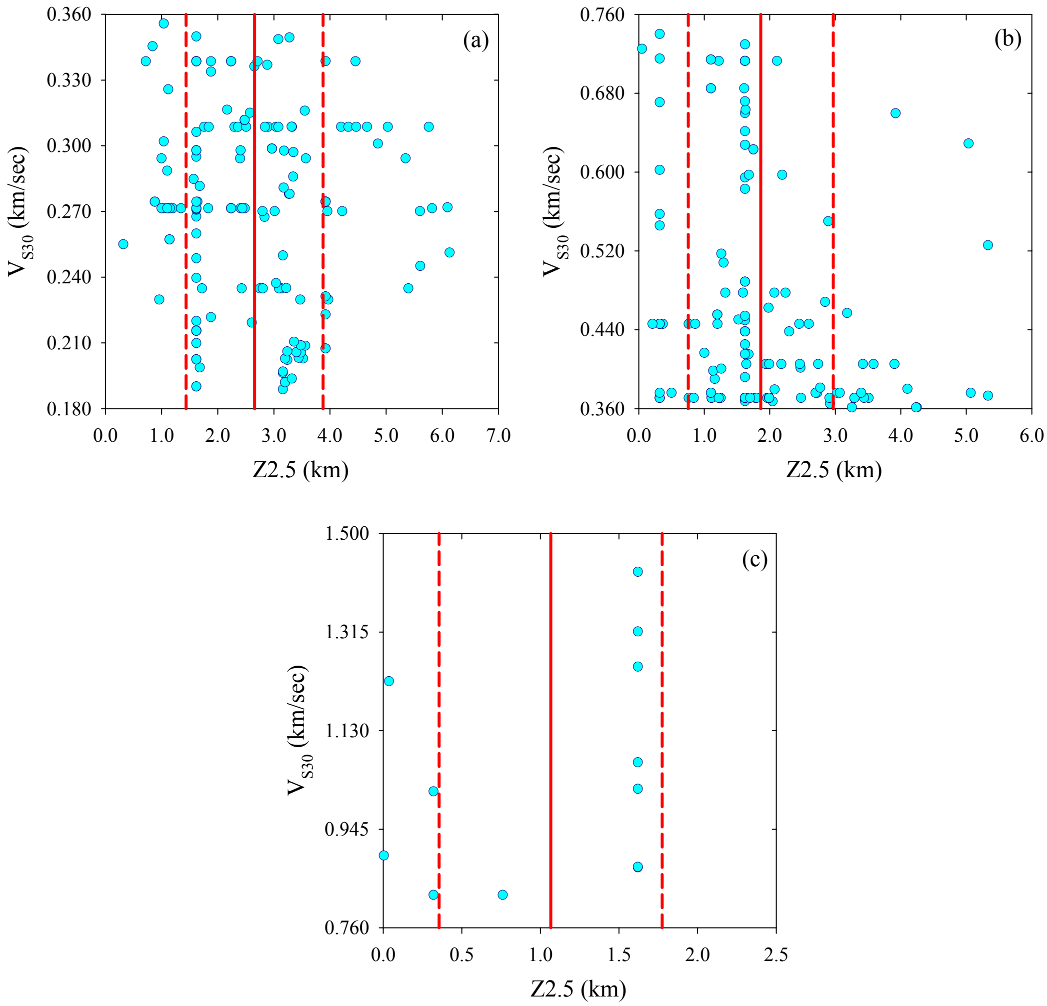

Figure 4.1 Scatter plots of depths to V_S = 2.5 km/sec (Z2.5) presented by the NGA metafile for (a) soft (180 m/sec $\leq V_{S,30} \leq$ 360 m/sec), (b) stiff (360 m/sec $< V_{S,30} \leq$ 760 m/sec) and (c) rock (760 m/sec $< V_{S,30} \leq$ 1500 m/sec) sites. The vertical solid lines display the mean Z2.5 ($\mu_{Z2.5}$) value for each site class. The vertical dashed lines describe the 16% and 84% percentiles for Z2.5 assuming that the scatters are normally distributed (this is a poor assumption for rock site data).

Table 4.1 Mean ($\mu_{Z2.5}$) and standard deviation ($\sigma_{Z2.5}$) statistics for Z2.5 in terms of different site classes

	Soft	Stiff	Rock
$\mu_{Z2.5}$ (km)	2.66	1.86	1.07
$\sigma_{Z2.5}$ (km)	1.22	1.11	0.71

4.2.2 Variation of S-wave Velocity/Slowness with Depth

According to the wave propagation theory, when a body wave strikes a normal boundary between two different materials, part of the wave energy is reflected and part is transmitted across the boundary (Kramer, 1996). Behavior of the wave at the boundary is governed by the ratio of the specific impedances of the materials on either side of the boundary. This impedance ratio determines the amplitudes and polarities of the reflected and transmitted waves. The specific impedance of a material is defined as the product of the material density and the wave propagation velocity. Therefore, the variation of S-wave velocity (or its reciprocal, S-wave slowness, s) with depth is one of the controlling factors of the site response.

In this study, the variation of S-wave velocity with depth is investigated in terms of slowness for each site class by statistically evaluating the actual soil profiles. Slowness is used as the material characteristic of interest, rather than velocity because the comparison of slowness profiles is more appropriate in terms of site response analysis. Boore and Asten (2008) indicated that this parameter is directly related to the site amplification. Additionally, slowness is a more sensitive indicator of material variability near the soil surface when compared to velocity.

A total of 424 S-wave velocity profiles (226 soft, 180 stiff and 18 rock sites) are compiled from the USGS and Turkish NSMP databases. The USGS data is based on the borehole seismic measurements whereas the Turkish database is obtained through the method of multi-channel analysis of surface waves (MASW) (Yılmaz et al., 2008). Note that the uncertainty induced due to the use of soil profiles from different analysis methods (MASW vs. borehole seismic) is not taken into account in this study. However, Boore and Asten (2008) indicated that alternative measurement methods yield slowness models similar to each other and the difference in the site amplifications based on any of these models is within 10% to 20% range.

It should be noted that the compiled data is adequate to compute meaningful descriptive statistics of slowness up to 150 m, 75 m and 30 m depths for soft, stiff and rock sites, respectively. Since the variation of depth-to-bedrock (Table 4.1) is considerably larger than the aforementioned depths, the functional forms that represent the variation of S-wave slowness with depth are constructed in two stages. Figure 4.2 illustrates the structure of S-wave slowness models.

In the first step, the mean (μ_s) and standard deviation (σ_s) of slowness are computed at every 0.5 m interval up to the depths of H = 150 m, 75 m and 30 m for soft, stiff and rock sites, respectively. The functional form presented in Equation (4.1) is used to fit curves on the computed μ_s and σ_s variations.

$$x_s = (a + b \cdot z)^{(-1/c)} \tag{4.1}$$

In Equation (4.1), x_S stands either for μ_s or σ_s (sec/km) at depth z (km).The parameters a, b and c are the regression coefficients. Table 4.2 presents the coefficients obtained form the regression analyses for depths $z \leq H$ (H = 150 m, 75 m, and 30 m for soft, stiff and rock sites, respectively).

In the second stage (i.e. when z > H), the coefficients obtained in Stage I are modified to satisfy the continuity in slowness variation at z = H. The modified coefficients are also constrained such that the functional form attains the value of 0.4 sec/km (i.e. V_S = 2.5 km/sec) at $z = \mu_{Z2.5}$ and $z = \mu_{Z2.5} \pm \sigma_{Z2.5}$ for each site class. This way the functional form presented in Equation (4.1) accounts for the variability in depth-to-bedrock in terms of different site classes, which is one of the prominent features observed in the actual variation of V_S in different soil profiles. The regression coefficients that are computed for Equation (4.1) in the second stage are presented in Table 4.3.

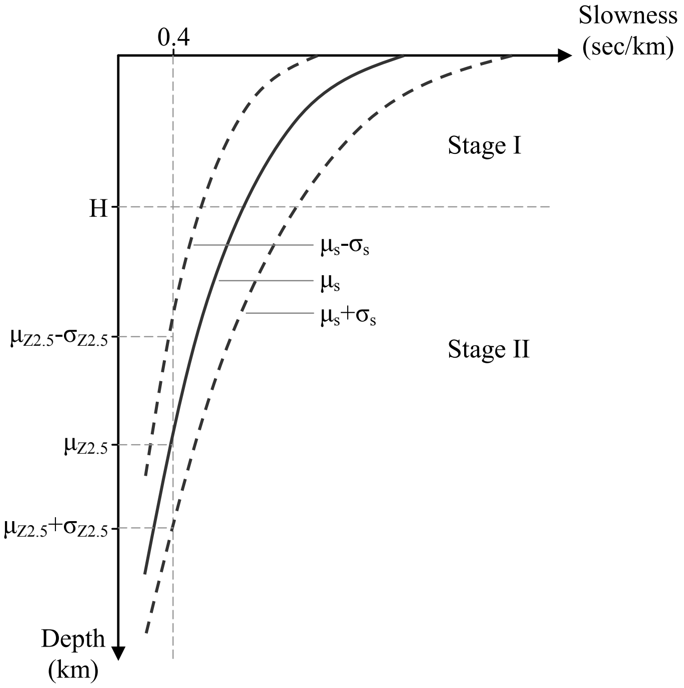

Figure 4.2 Illustration of the construction of S-wave slowness models

The generated S-wave slowness models together with the actual slowness variations for each site class are shown in Figure 4.3. The plots presented in the figure compare the actual profiles with the models in terms of mean and 16% and 84% percentile slowness variations. The 16% and 84% percentiles are computed based on the assumption that S-wave slowness at any depth is normally distributed. The justification of this assumption is discussed in the following paragraph. Figure 4.3 shows that the derived models fit the actual slowness variations fairly well for all site classes. To investigate whether the proposed slowness models mimic the prescribed depth-to-bedrock variations, the cumulative probabilities of Z2.5 obtained from the models and the statistics presented in Table 4.1 are compared (Figure 4.4). Figure 4.4 suggests that both cumulative probabilities are in good agreement for all site classes.

Table 4.2 Regression coefficients of μ_s and σ_s models for $z \leq H$ (Stage I)

	μ_s			σ_s		
	Soft	Stiff	Rock	Soft	Stiff	Rock
a	0.0104	0.0215	0.09	0.2107	0.215	0.7807
b	1.9224	8.7781	70	48.2781	280	150
c	2.5597	2.7037	1.9	2.8997	3.75	0.84

Table 4.3 Regression coefficients of μ_s and σ_s models for $z > H$ (Stage II)

	μ_s			σ_s		
	Soft	Stiff	Rock	Soft	Stiff	Rock
a	0.1327	-0.0841	-306.4360	1.3790	1.7954	11.8
b	1.9420	9.6317	12597.16	7.5905	10.0287	1445
c	1.8182	3.1459	10.3481	1.3315	1.1380	2.0235

As the soil profiles are randomly generated, their probability distributions are required. In this study, the slowness at a given depth z is assumed to be normally distributed with mean, μ_s, and standard deviation, σ_s computed from Equation (4.1). The normal probability plots of the actual slowness profiles are evaluated at certain depths to check the validity of this assumption (Figures A.2 to A.4). It is observed that the normal probability assumption holds except at very low and very high percentiles. Due to the lack of data at depths larger than H = 150 m, 75m and 30 m for soft, stiff and rock sites respectively, this assumption could not be verified for larger depths. However, for the sake of completeness, the slowness variations at depths greater than H are assumed to be normally distributed.

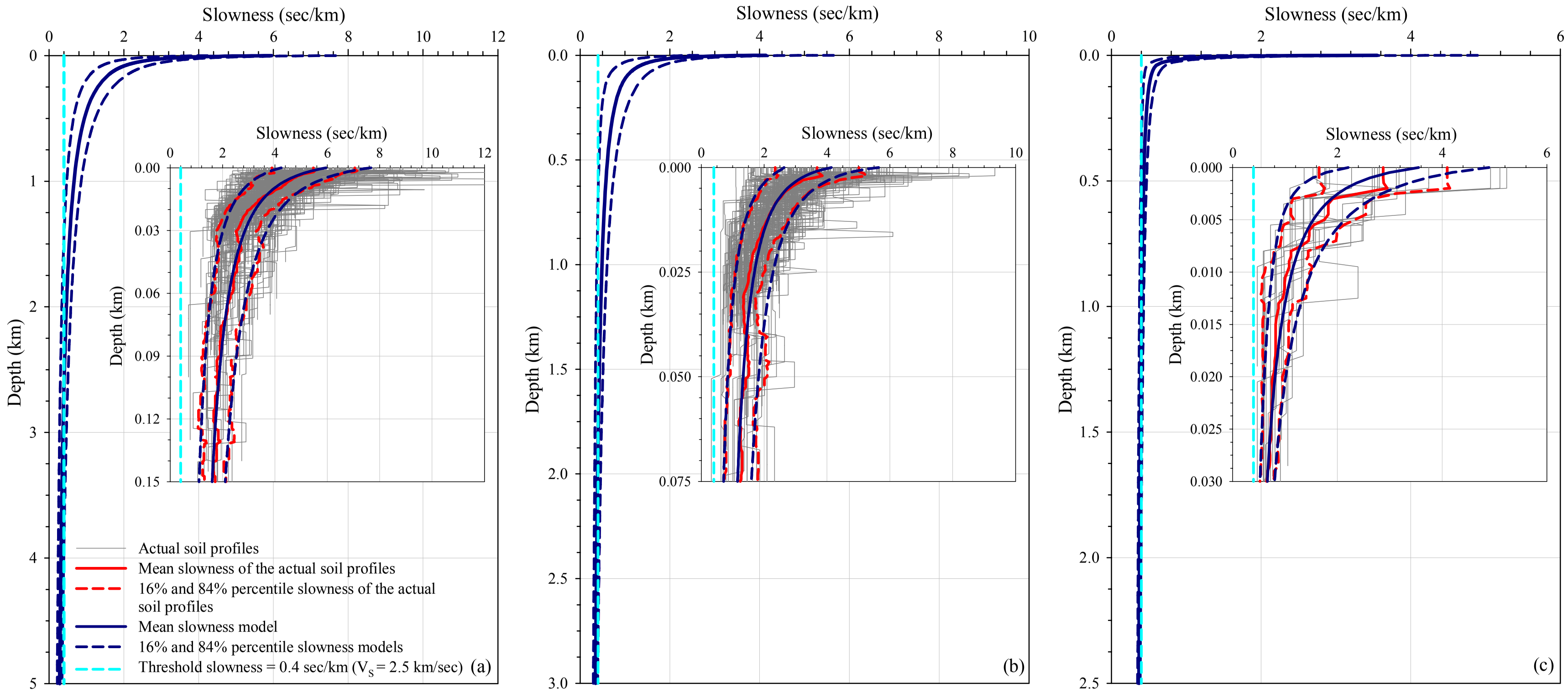

Figure 4.3 S-wave slowness models for (a) soft, (b) stiff and (c) rock sites

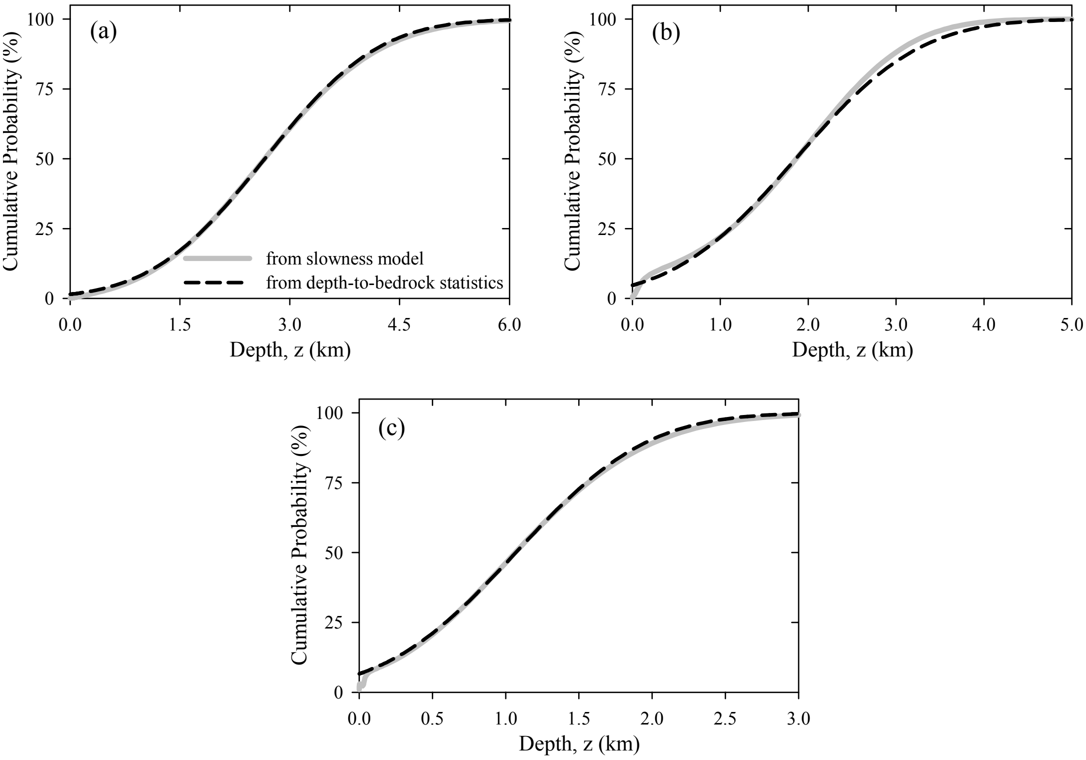

Figure 4.4 Comparisons of cumulative probability plots of Z2.5 computed through slowness models and depth-to-bedrock statistics presented in Table 4.1 for (a) soft, (b) stiff and (c) rock sites

The residual analysis is conducted to assess the performance of the proposed slowness models. Slowness residuals ($e_{i,z}$) are defined as the difference between the observed ($s_{i,z}$) and the estimated slowness of profile "i" at depth z (i.e. $e_{i,z} = s_{i,z} - \mu_s(z)$). Figure 4.5 presents the residual scatters against depth for each site class. The depth-dependent variation of residuals indicates higher uncertainty at depths close to surface. The mean residuals (red circles) computed for pre-defined depth intervals attain values close to zero suggesting fairly unbiased slowness estimations of Equation (4.1). The error bars that describe ± σ_e (standard deviation of residuals for each interval) coincide very well with the standard deviation model ($\sigma_s(z)$) presented as solid cyan line. This observation also suggests that the proposed slowness expression as well as the σ_s can able to capture the variations in actual slowness. The last two observations can arguably verify the validity of normal distribution assumption with zero mean and $\sigma = \sigma_s(z)$ for the slowness residuals. This conclusion can be used further to account for the variability of slowness in a probabilistic methodology.

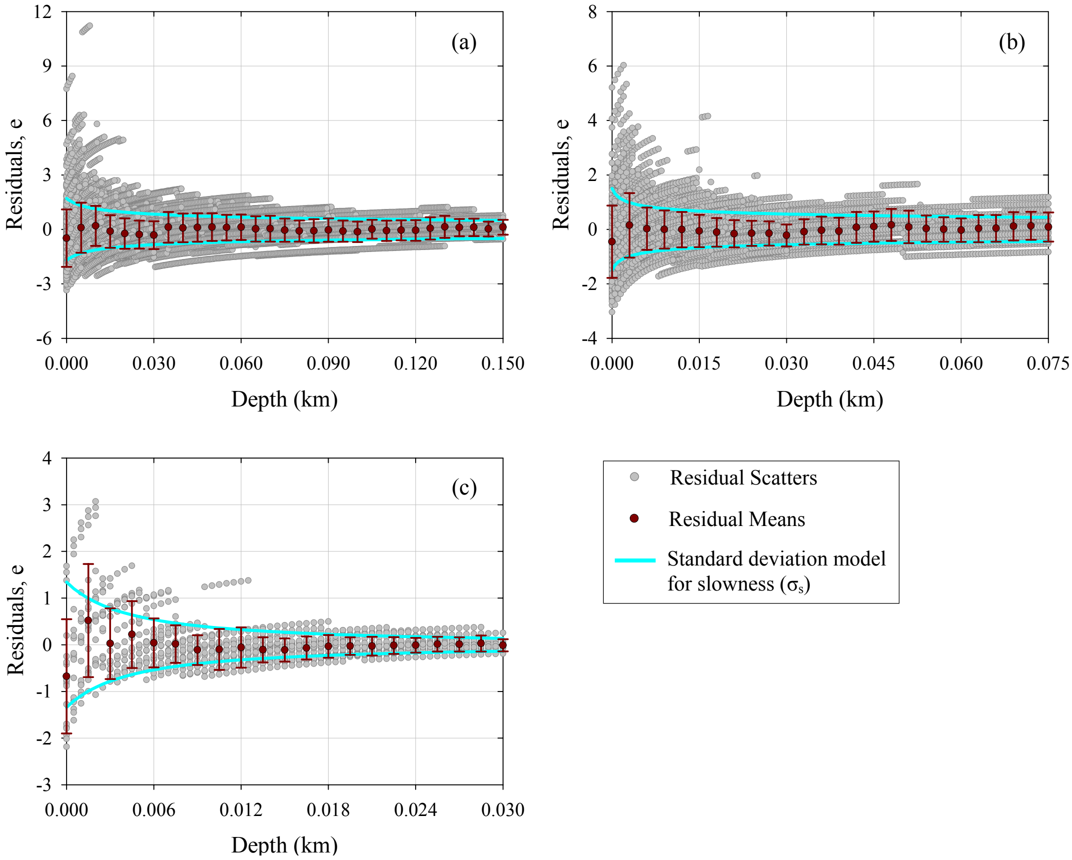

Figure 4.5 Residual scatters of slowness models for (a) soft, (b) stiff and (c) rock sites. Note that the residuals are computed for the limiting depth values for each site class where the empirical data is available. Thus, the slowness model evaluation is performed for Stage I regression.

4.2.3 Number and Thickness of Layers

The number and thickness of the layers are the essential parameters for a complete description of a soil profile. Similar to the other modeling parameters in this study, the S-wave velocity profiles compiled form the USGS and Turkish NSMP databases are investigated statistically to describe the number and thickness of the soil layers. As stated previously, the compiled S-wave velocity data allow reliable computation of soft, stiff and rock site slowness statistics for depths up to 150 m, 75 m and 30 m, respectively. Therefore, this data is evaluated for the top 30 m, 30 m to 75 m and 75 m to 150 m depths, separately. The mean of layer numbers (μ_n) and corresponding standard deviations (σ_n) computed for each depth interval are listed in Table 4.4. In a similar manner, Table 4.5 presents the mean layer thickness' (μ_t) and their standard deviations (σ_t) for the same depth intervals. Note that μ_n and μ_t statistics are fairly consistent with the total thickness of the depth intervals considered.

In this study, the layer thickness' are assumed to be log-normally distributed. This assumption is validated by plotting the normal probability curves of the natural logarithm of the database (Figure A.5). The plots clearly indicate that the log-normal assumption for the layer thickness' is rationale.

Table 4.4 Mean, μ_n, and standard deviation, σ_n, of the layer numbers for the top 30 m, 30 m - 75 m and 75 m - 150 m

	0 - 30 m	30 m - 75 m	75 m - 150 m
μ_n	6	3	3
σ_n	2	1	1

Table 4.5 Mean, μ_t, and standard deviation, σ_t, of the layer thickness' for the top 30 m, 30 m - 75 m and 75 m - 150 m

	0 - 30 m	30 m - 75 m	75 m - 150 m
μ_t (m)	5.1	18.4	28.0
σ_t (m)	4.1	11.3	13.6

4.3 Soil Profile Generation Process

The models and statistical parameters presented in the previous sections are employed for the generation of soil profiles that are used to introduce the site response to the VHR simulations. The soil profile generation process is summarized in the following steps.

Step 1 (layer thickness and layer number related process): Initially, the number and thickness of the layers are generated for a constant depth of 7.5 km that is accepted as the maximum possible profile depth ($P(z \leq 7.5 \text{ km}) = 0.99996$ for soft sites, see Table 4.1). The uppermost 30 m of the soil profile is divided into 6 layers and the depth intervals 30 m - 75 m and 75 m - 150 m are divided into 3 layers (Table 4.4). The layer thickness' within the first 150 m of the soil profiles are randomly sampled assuming that the layer thickness' are log-normally distributed with μ_t and σ_t as presented in Table 4.5. For depths greater than 150 m, the soil profiles are divided into 4, 5, 10 and 24 layers with equal thickness' of 25, 50, 100 and 250 m, respectively.

Step 2 (generation of slowness profiles): The slowness at the mid-depth of a layer is generated randomly assuming that it is normally distributed with mean, μ_s and standard deviation, σ_s computed from Equation (4.1). The computed slowness is assumed to be constant throughout the corresponding layer. The slowness generation process is performed layer-by-layer until the slowness of a layer falls below the threshold slowness of $s = 0.4$ sec/km ($V_S = 2.5$ km/sec). For a given soil profile, whenever the S-wave slowness stays below the threshold level for the first time the corresponding depth is considered as the bedrock depth and the slowness generation process is terminated. Thus, the rest of the previously generated layers in Step 1 that are below the bedrock depth are discarded. The S-wave velocities are computed by taking the reciprocals of the S-wave slowness'. The deposits with $V_S \leq 760$ m/sec are considered to be soil and the layers with $V_S > 760$ m/sec are regarded as rock layers.

To avoid unrealistic V_S variations, some constraints are imposed to the slowness generation process. The investigation of actual slowness profiles shows that the ratio of the slowness of a rock layer ($V_S > 760$ m/sec) to the slowness of the layer below (i.e. $s_{\text{Rock Layer}}/s_{\text{Layer Below}}$) varies between 0.5 and 1.7 (Figure 4.6). The same constraint is implemented during the slowness generation process. The evaluation of actual slowness profiles also indicates that 99.5% of the slowness data is smaller than 11 sec/km (i.e. $V_S > 90$ m/sec). Therefore, the maximum slowness is taken as 11 sec/km, to avoid the generation of very soft layers.

Depths to certain S-wave velocities are as important as V_S variations in soil profiles. For example, depths to $V_S = 1.0$ km/sec (Z1.0) and $V_S = 2.5$ km/sec (Z2.5) are the common parameters that are used to reflect the basin effect on the site response. Thus, the slowness generation process is also constraint by the probability distributions of Z1.0 and Z2.5 that are prescribed in the slowness models.

Figure 4.7 illustrates the randomly generated slowness profiles for a set of 50 samples at soft sites. The scatters for Z2.5 and Z1.0 values that are obtained from the generated slowness profiles are presented in Figures 4.8 and 4.9, respectively. The Z1.0 and Z2.5 values of NGA metafile and those compiled from the soil profiles of Turkish NSMP and USGS databases are also demonstrated in Figures 4.8 and 4.9. The generations in this study seem to represent the distribution of other

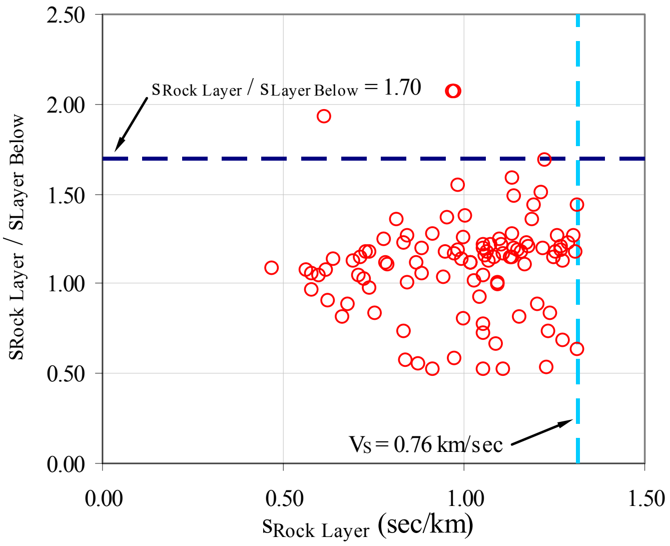

Figure 4.6 Scatter plot of the rock layer slowness normalized by the slowness of the layer below

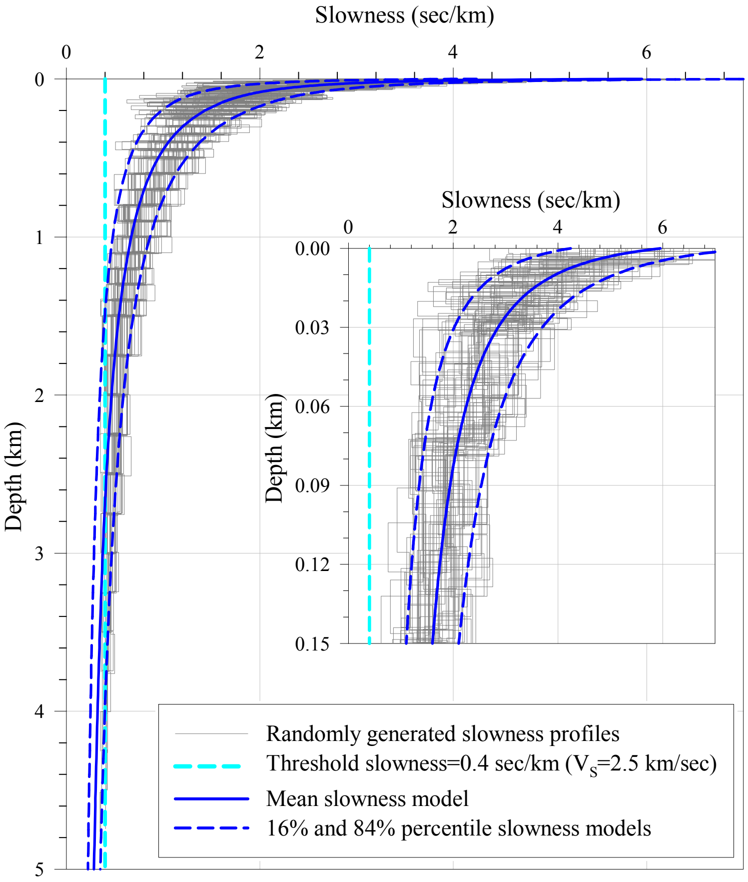

Figure 4.7 Randomly generated S-wave slowness profiles for soft sites

data (i.e. NGA, Turkish NSMP and USGS) fairly well for Z2.5 (Figure 4.8). The scatters in Figure 4.9, however, suggest that the generated soil profiles attain V_S = 1.0 km/sec at relatively shallower depths for soft and stiff sites when compared to the variations in NGA data. For rock sites, Z1.0 simulations of this study are comparable to those compiled from the other databases. Note that the empirical data still scarce for establishing fully rational models for addressing the variations of Z1.0 and Z2.5. Therefore the modeling and evaluations of Z1.0 and Z2.5 of this study should be considered in a limited perspective.

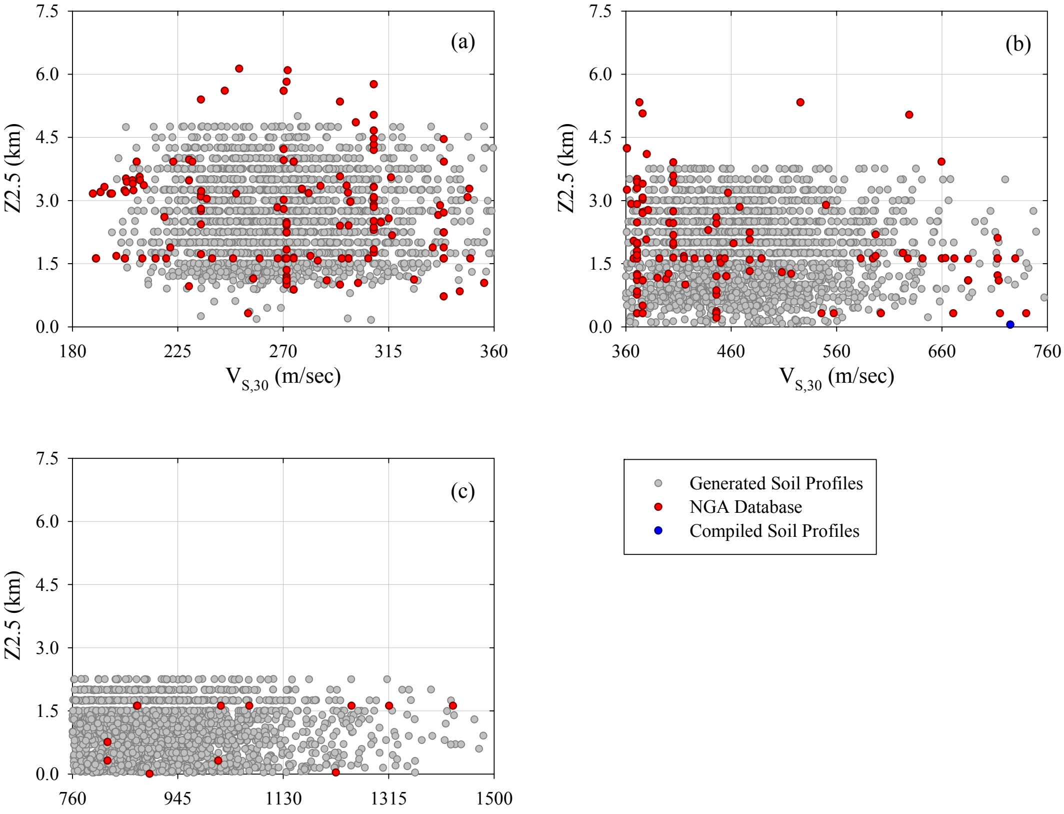

Figure 4.8 Z2.5 scatters for (a) soft, (b) stiff and (c) rock sites

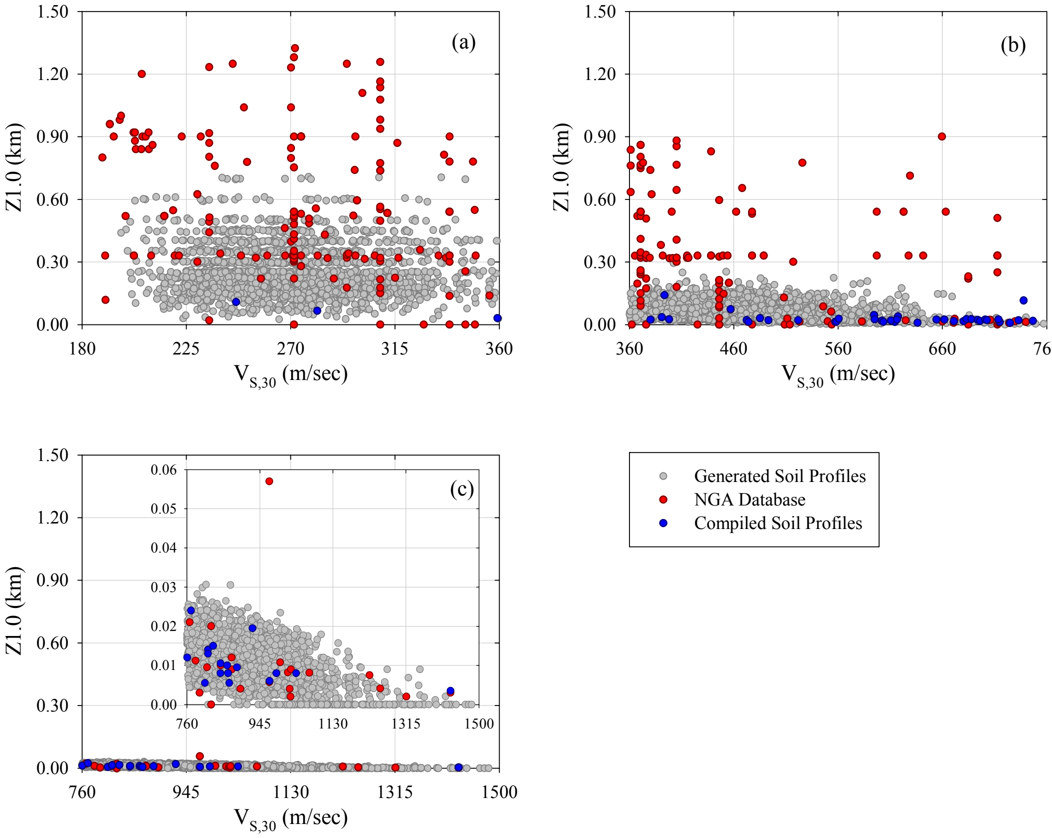

Figure 4.9 Z1.0 scatters for (a) soft, (b) stiff and (c) rock sites

Step 3 (unit weights of soil layers): Unit weights of the randomly generated layers are calculated based on the procedure proposed by Boore (2007). Boore (2007) predicts the density of soils as $\rho = 1.93$ gm/cm^3 if $V_S \leq 0.30$ km/sec. For materials within 0.30 km/sec $< V_S <$ 3.55 km/sec, Boore (2007) uses the relationship between S-wave and P-wave (V_P) velocities proposed by Brocher (2005) in combination with $\rho - V_P$ relationship presented by Gardner et al. (1974). The relationships proposed by Gardner et al. (1974) and Brocher (2005) are given in Equations (4.2) and (4.3), respectively.

$$\rho = 1.74 V_P^{0.25} \ (\mathrm{g/cm^3}) \tag{4.2}$$

$$V_P = 0.9409 + 2.0947 V_S - 0.8206 V_S^2 + 0.2683 V_S^3 - 0.0251 V_S^4 \tag{4.3}$$

Step 4 (dynamic material properties): In equivalent linear site response analysis, nonlinear soil behavior is modeled using strain-dependent shear modulus reduction and hysteretic damping curves. In this study, the modulus reduction and hysteretic damping curves proposed by Ishibashi and Zhang (1993) and Schnabel et al. (1972) are implemented for soil ($V_S \leq 760$ m/sec) and rock ($V_S > 760$ m/sec) layers, respectively. The curves proposed by Ishibashi and Zhang (1993) are expressed in terms of plasticity index and confining earth pressure which are the essential ingredients influencing the nonlinear soil behavior under cyclic loading. The modulus reduction and damping curves proposed by Ishibashi and Zhang (1993) is computed using Equations (4.4) and (4.5), respectively.

$$\frac{G}{G_{\max}} = K(\gamma, I_P)\overline{\sigma}_0^{\,m(\gamma, I_P)-m_0} \tag{4.4}$$

$$\zeta = 0.333\frac{1+\exp\left(-0.0145 I_P^{1.3}\right)}{2}\left[0.586\left(\frac{G}{G_{\max}}\right)^2 - 1.547\left(\frac{G}{G_{\max}}\right)+1\right] \tag{4.5}$$

where G/G_{max} is the modulus reduction factor and ζ is the damping ratio of the soil with plasticity index, I_P and the mean effective confining pressure, $\overline{\sigma}_0$ at the corresponding shear strain, γ. The mean effective confining pressure is defined as $\overline{\sigma}_0 = \frac{\sigma'_v \times (1+2K_0)}{3}$ where K_0 is the coefficient of earth pressure at rest and σ'_v is the effective vertical stress at the mid-height of the layer. The functional forms $m(\gamma, I_P) - m_0$ and $K(\gamma, I_P)$ are presented in Equations (4.6) and (4.7), respectively.

$$m(\gamma, I_P) - m_0 = 0.272\left[1-\tanh\left\{\ln\left(\frac{0.000556}{\gamma}\right)^{0.4}\right\}\right]\exp\left(-0.0145 I_P^{1.3}\right) \tag{4.6}$$

$$K(\gamma, I_P) = 0.5\left[1+\tanh\left\{\ln\left(\frac{0.000102+n(I_P)}{\gamma}\right)^{0.492}\right\}\right] \tag{4.7}$$

where $n(I_P)$ is given as:

$$n(I_P)=\begin{cases}0.0 & \text{for } I_P = 0 \text{ (non-plastic soils)}\\ 3.37\times10^{-6}\,I_P^{\ 1.404} & \text{for } 0 < I_P \le 15 \text{ (low plastic soils)}\\ 7.0\times10^{-7}\,I_P^{\ 1.976} & \text{for } 15 < I_P \le 70 \text{ (medium plastic soils)}\\ 2.7\times10^{-5}\,I_P^{\ 1.115} & \text{for } I_P > 70 \text{ (high plastic soils)}\end{cases} \tag{4.8}$$

Figures 4.10 and 4.11 present the modulus reduction and damping curves proposed by Ishibashi and Zhang (1993) for various I_P and $\bar{\sigma}_0$ values, respectively. The dynamic material properties presented in these figures are computed using Equations (4.4) to (4.8). The modulus reduction and damping curves proposed by Schnabel et al. (1972) for rock layers are shown in Figure 4.12.

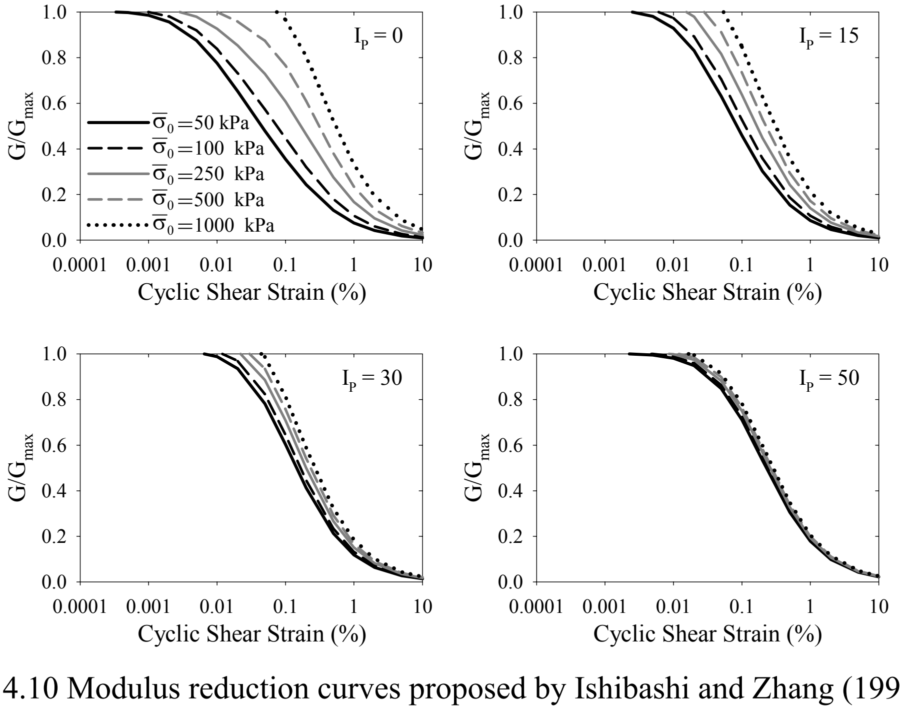

Figure 4.10 Modulus reduction curves proposed by Ishibashi and Zhang (1993), for several plasticity index (I_P) and mean effective confining pressure ($\bar{\sigma}_0$) values. These curves indicate that increasing I_P reduces the difference between the modulus reduction curves. The G/G_{max} values increase with increasing $\bar{\sigma}_0$.

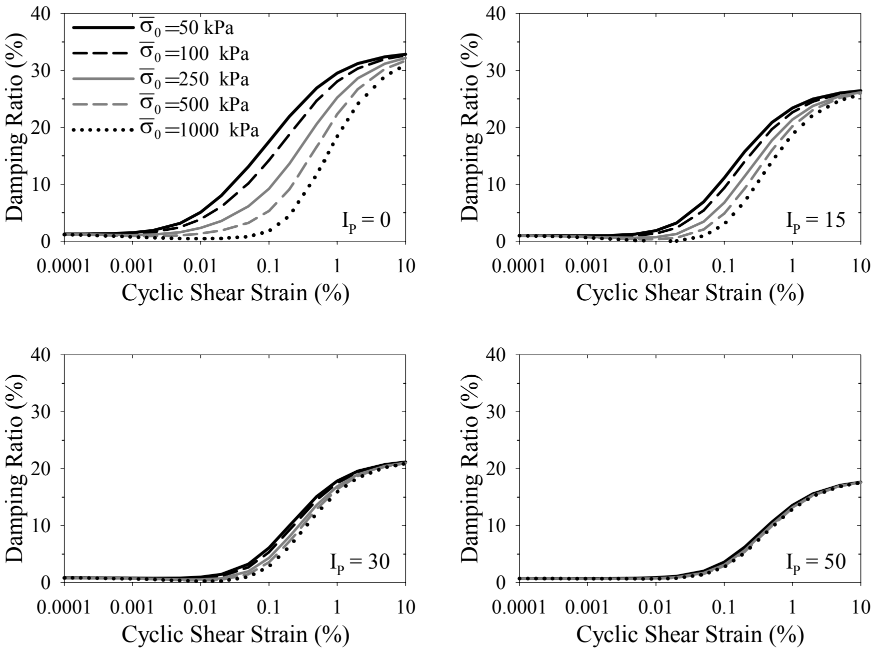

Figure 4.11 Hysteretic damping ratio curves proposed by Ishibashi and Zhang (1993), for several plasticity index (IP) and mean effective confining pressure ($\overline{\sigma}_0$) values. Note that increased $\overline{\sigma}_0$ decreases the damping ratio values.

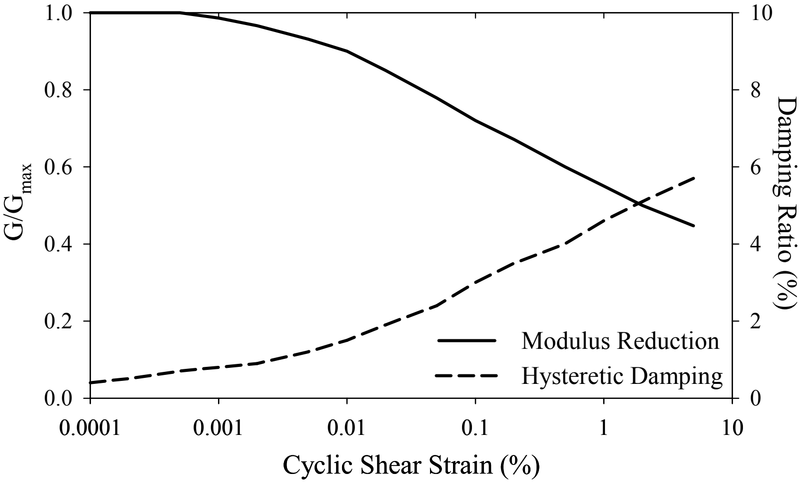

Figure 4.12 Modulus reduction and hysteretic damping ratio curves proposed by Schnabel et al. (1972), for rock layers

In this study, the soil layers are divided into plastic and non-plastic soil sub-classes because the modulus reduction and damping curves proposed by Ishibashi and Zhang (1993) depend on plasticity index. The material plasticity is randomly assigned to the soil layers with equal probabilities (i.e. uniform distribution). The plasticity index, I_P, and coefficient of earth pressure at rest, K_0, that is required to compute the confining earth pressure, are randomly generated according to the ranges and probability distributions presented in Table 4.6. The parameters I_P and K_0 are generated in a similar methodology as explained in Chapter 2.

Table 4.6 Ranges and distributions used in the random generation process of various material properties

Variable	Distribution	Ranges
Material plasticity of a layer	Uniform	Plastic or Non-plastic
Plasticity index for soil layers, I_P	Log-normal	Non-plastic: $I_P = 0$ Plastic: $0 < I_P \leq 50$
Coefficient of earth pressure at rest for soil layers, K_0	Log-normal	Non-plastic: $0.25 \leq K_0 \leq 0.60$ Plastic: $0.40 \leq K_0 \leq 0.70$

The preliminary analyses performed on dynamic material properties indicate that for relatively small cyclic shear strains, the curves proposed by Ishibashi and Zhang (1993) yield unrealistic results (i.e. $G/G_{max} > 1.0$ and $\xi < 0$) at high confining pressures. In this study, the G/G_{max} values set to 1.0 when the actual estimations of Ishibashi and Zhang (1993) are larger than 1.0. This modification is illustrated in Figure 4.13.a. For cases where $\xi < 0$, I_P and K_0 parameters are resampled iteratively until ξ attains values larger than 0 for all cyclic strains. If this iterative procedure is unsuccessful in computing the desired ξ after 50 trials, the damping curve is modified as demonstrated in Figure 4.13.b.

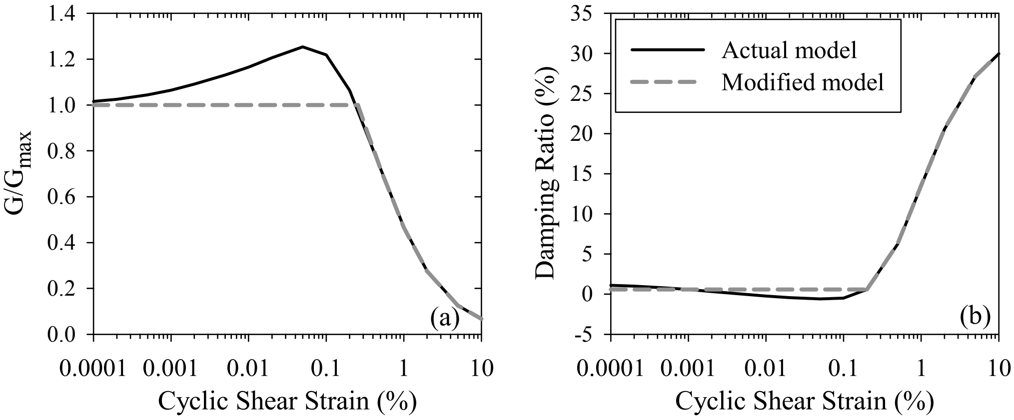

Figure 4.13 Modifications of (a) shear modulus reduction and (b) hysteretic damping curves for the unrealistic estimations of the Ishibashi and Zhang (1993) model. A typical illustration for $I_P = 0$ and $\bar{\sigma}_0 = 2000$ kPa.

4.4 Examination of the Free-Field Motions

A total of 6000 free-field motions are generated for various magnitude, distance, faulting style and site class bins using the procedure summarized in the previous sections. Note that the influence of water table and topographical conditions on site response is not considered in this study.

The simulated free-field motions are examined in terms of various ground motion parameters to exhibit the general characteristics of the final simulations. Figures 4.14 to 4.16 illustrate three sets of ground-motion time series. Each figure presents the soft (first row), stiff (second row) and rock (third row) site ground motions from low (Figure 4.14) to large magnitude (Figure 4.16) events. Note that except for the magnitude values, the other seismological features of the simulations reveal great similarity. In other words, the input VHR motions are from strike-slip faulting with R_{JB} and R_{hyp} approximately equal to 13 km and 17 km, respectively. The second and third columns in each figure represent the integrated velocity and displacement time series. The comparisons of the time series indicate that acceleration and velocity amplitudes consistently increase with increasing magnitude. When the ground displacements are of concern, low-to-moderate magnitude cases (i.e. Figures 4.14 and 4.15) show unphysical linear trends in soft and stiff sites. This long-period noise seems to be introduced during the site response analyses because the input VHR motions do not exhibit such unphysical variations as discussed in Chapter 3 (see Figures 3.9). Figures 4.14 and 4.15 also indicate that the rock site simulations are either not influenced or minimally affected by the long-period noise as there seems to be no abnormal trend in the ground displacements or they return to zero when the motions end. For the large magnitude case-study (Figure 4.16), the long-period noise contamination seems to be not a concern for all site classes since the displacement waveforms do not show any trend that is physically unjustifiable.

The long-period noise issue of simulated records is analyzed further by examining the Fourier amplitude spectra (FAS). Figure 4.17 presents the FAS plots of a set of simulations from soft, stiff and rock sites for various magnitude ranges ($5.0 \leq M_w < 5.5$, $6.0 \leq M_w < 6.5$ and $7.0 \leq M_w \leq 7.5$). Note that all simulations presented in the figure are generated for the same faulting style (strike-slip) and distance range (10 km $\leq R_{JB} <$ 25 km). The figure presents the individual FAS plots as well as the mean (μ) and $\pm\sigma$ bands at certain frequencies. Each FAS plot also presents the theoretical f^2 trends to see the frequency ranges where the long-period noise starts dominating the ground motions. It is depicted from Figure 4.17 that for small magnitude events, the soft site simulations seem to be noise contaminated by long-period noise at frequencies lower than 0.05 Hz. Small magnitude, stiff site simulations also exhibit some amount of deviation from the theoretical f^2 trend at significantly low frequencies. However, this deviation is negligible when compared to the soft site simulations. The plots in Figure 4.17 present that the degree of noise contamination due to site response analysis decreases with increasing magnitude for both soft and stiff sites. Note that the rock site simulations are not influenced from the long-period noise for the magnitude intervals concerned in this study. In essence, it can be stated that the long-period noise that is probably introduced during the site response analysis may limit the use of soft and stiff site simulations

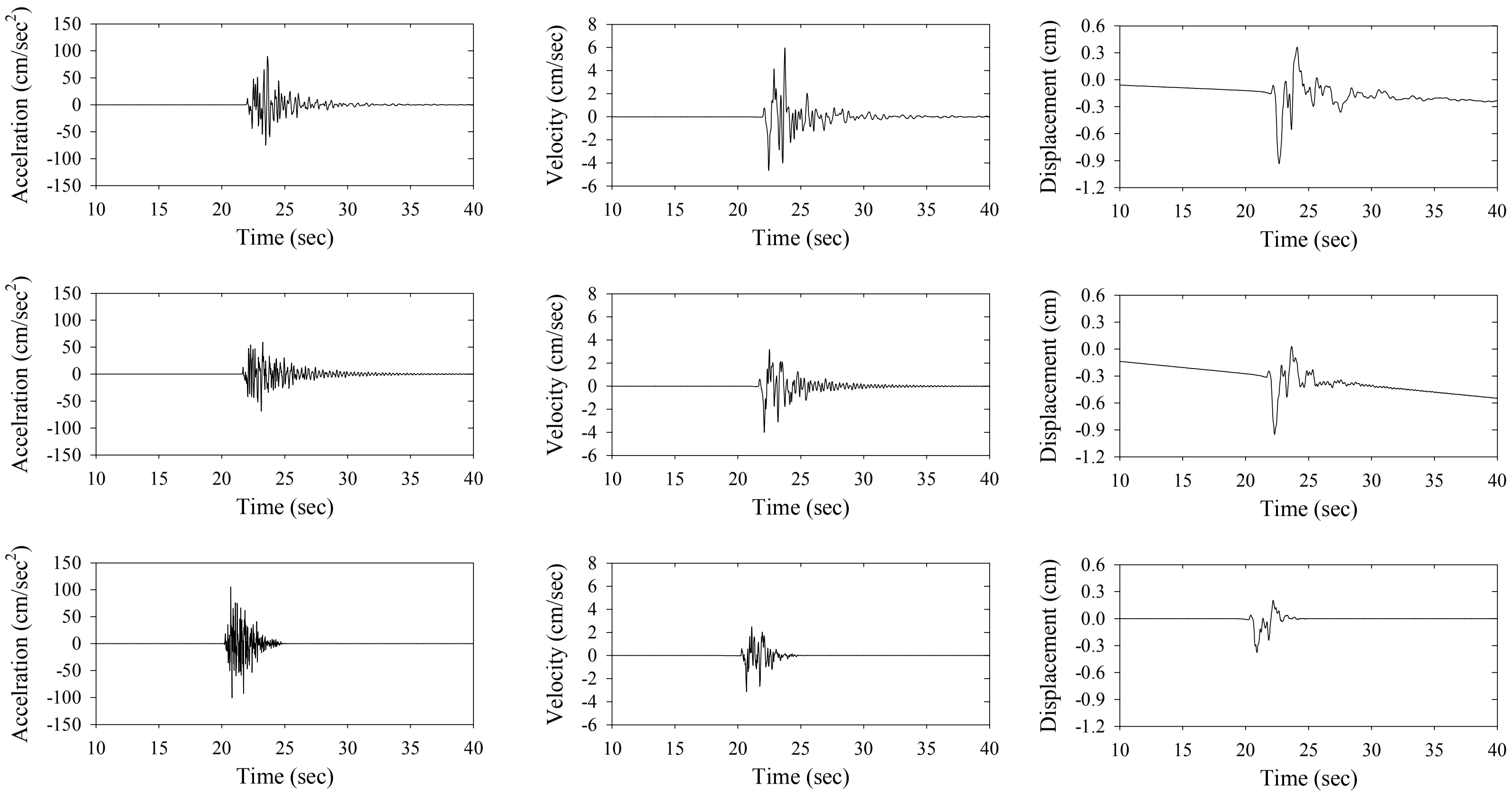

Figure 4.14 Acceleration, velocity and displacement waveforms simulated at soft (first row), stiff (second row) and rock sites (third row). The ground motions are generated using the outcropping strike-slip VHR motion with $M_w = 5.3$, $R_{JB} = 13.5$ km and $R_{hyp} = 16.9$ km.

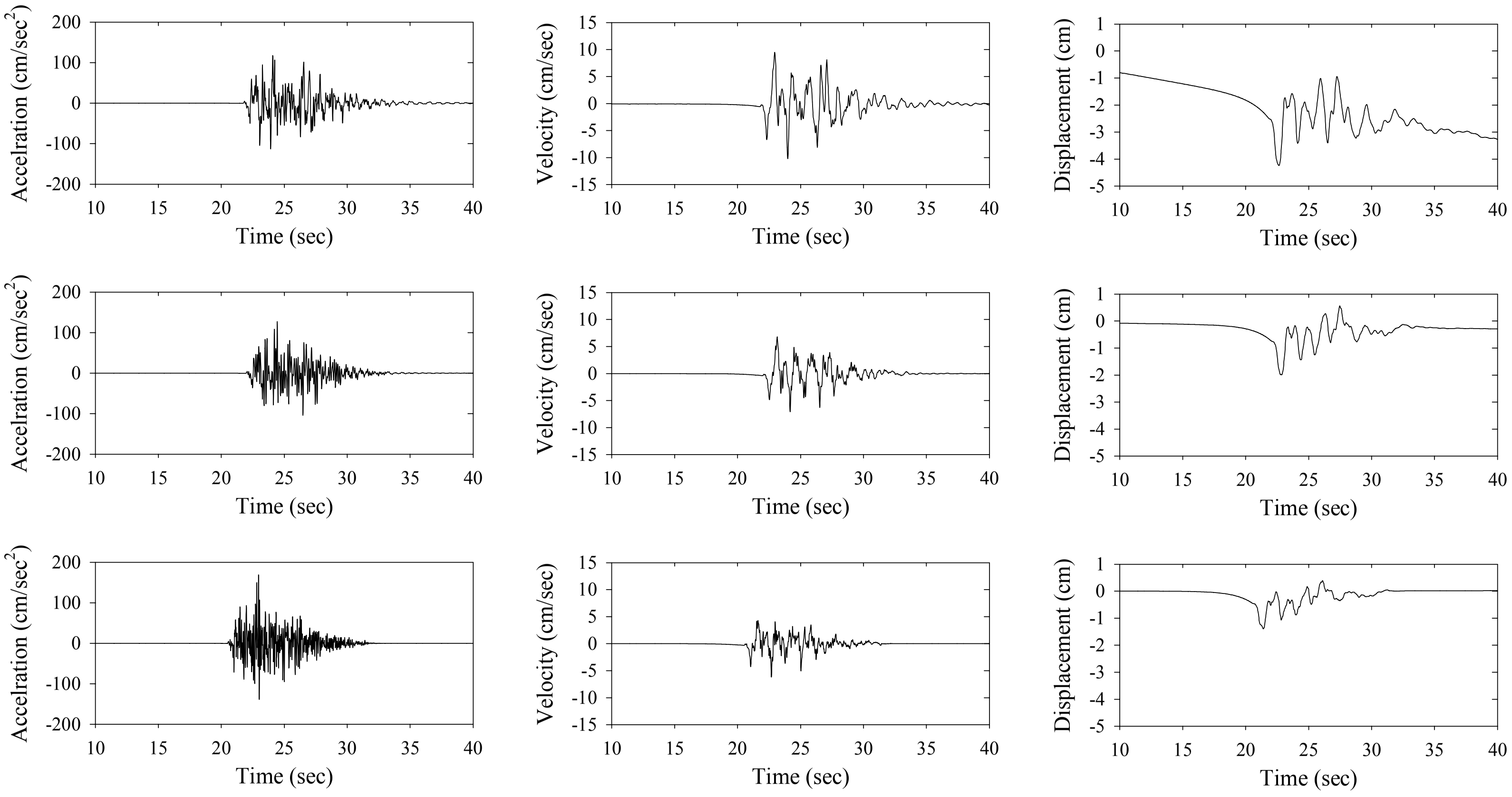

Figure 4.15 Acceleration, velocity and displacement waveforms simulated at soft (first row), stiff (second row) and rock sites (third row). The ground motions are generated using the outcropping strike-slip VHR motion with $M_w = 6.3$, $R_{JB} = 13.9$ km and $R_{hyp} = 21.2$ km.

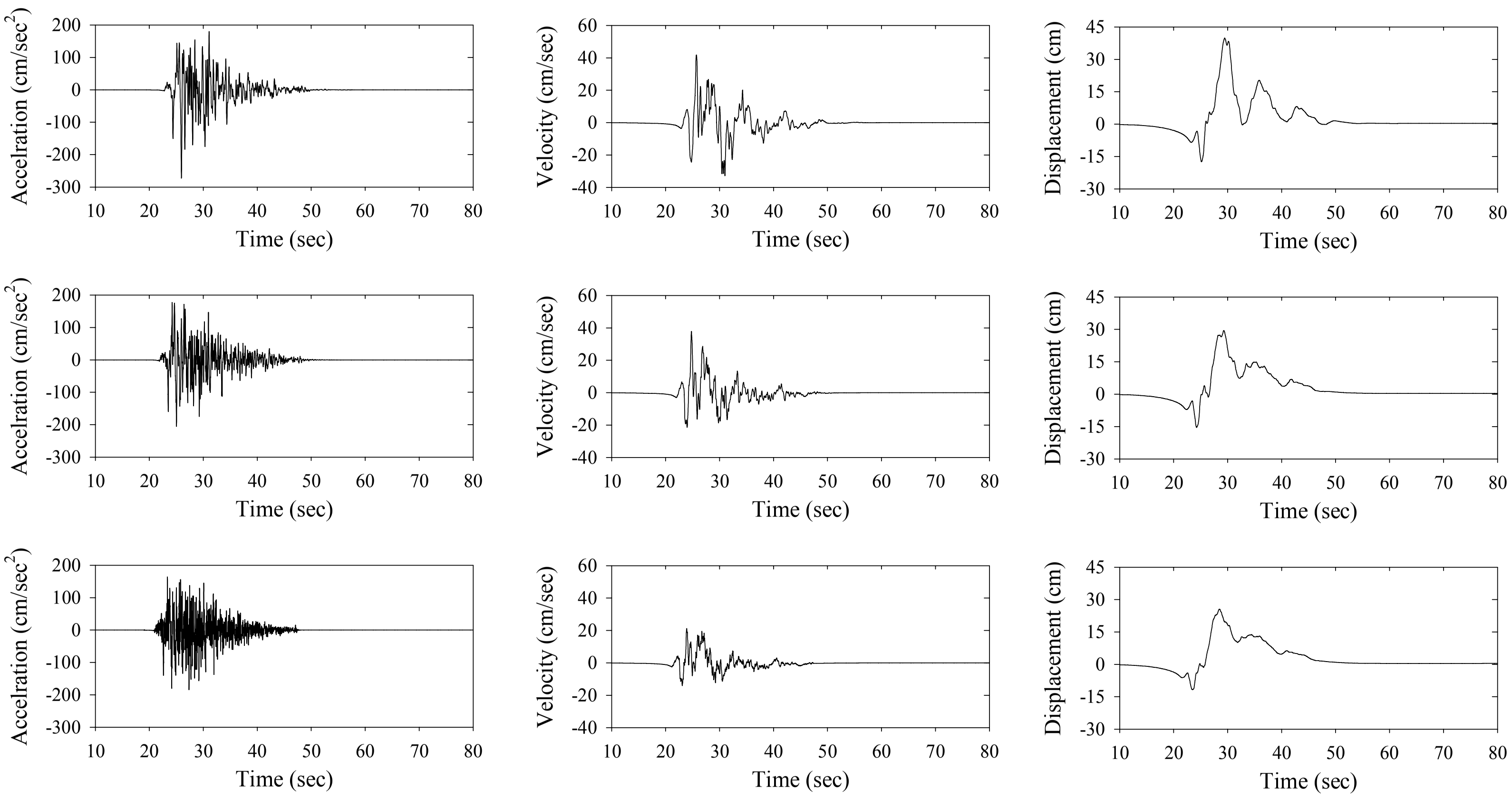

Figure 4.16 Acceleration, velocity and displacement waveforms simulated at soft (first row), stiff (second row) and rock sites (third row). The ground motions are generated using the outcropping strike-slip VHR motion with $M_w = 7.2$, $R_{JB} = 12.6$ km and $R_{hyp} = 17.4$ km.

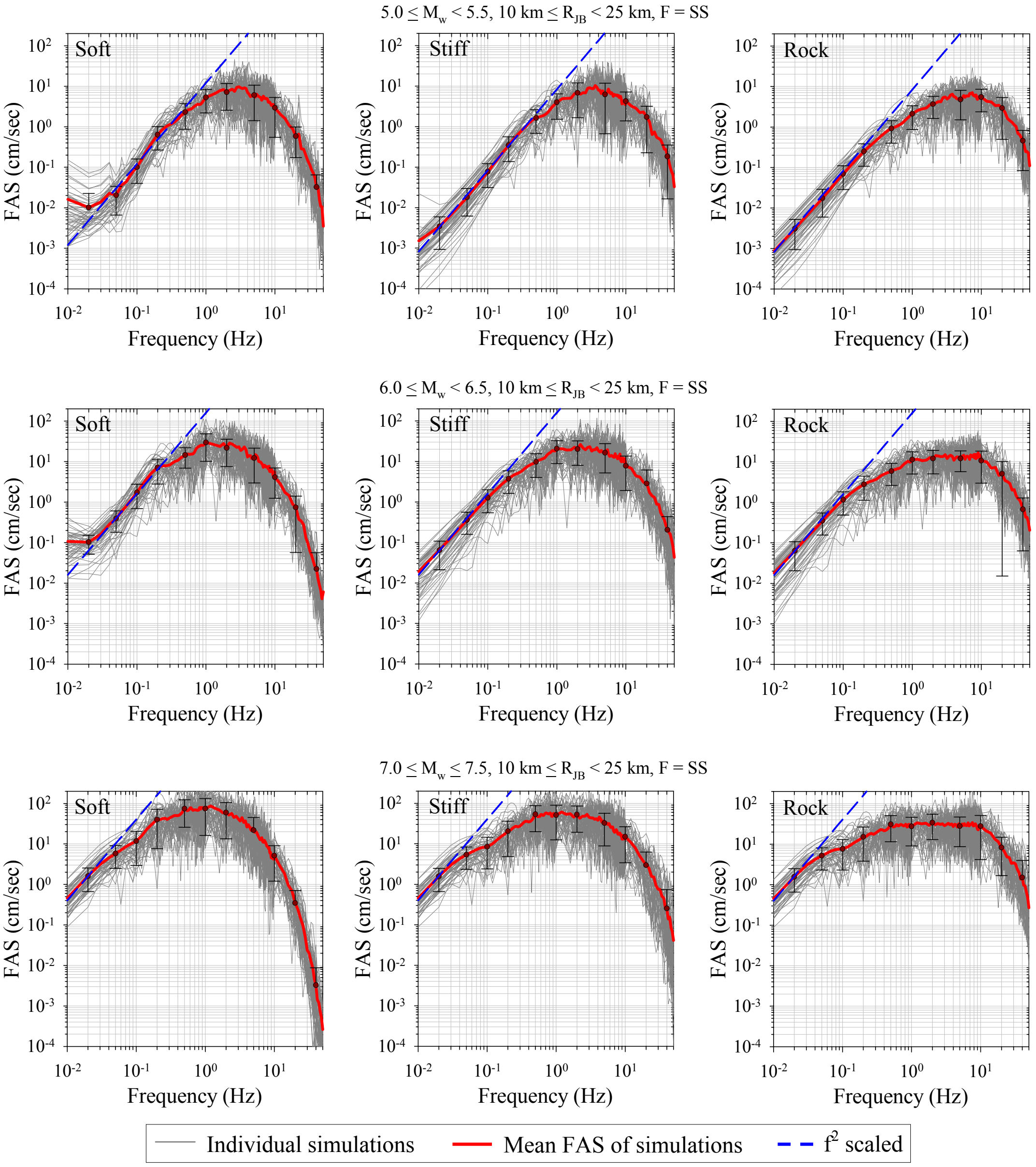

Figure 4.17 Fourier amplitude spectra (FAS) of soft, stiff and rock site simulations for various magnitude ranges. Each row shows the FAS plot for different magnitude bins whereas the columns display results from different site classes. The important seismological features of each simulation bin are presented at the top of each row.

for spectral periods beyond ~20 sec. Based on this observation, the long-period dominant peak ground displacements (PGDs) of the simulations are neither evaluated nor used in this study. However, the other short-to-intermediate period peak ground motion values (i.e. PGA and PGV) as well as the spectral quantities up to 20 sec computed from the simulations are believed to be reliable.

PGA and PGV scatters obtained from the simulated motions are examined in Figures 4.18 and 4.19, respectively. Both figures consist of three scatter plots and each plot pertains to a specific site class. Each scatter plot compares the peak ground motion data as a function of distance for different magnitude bins. The high-frequency peak motion, PGA, is fairly well separated for different magnitude bins at large distances. However, this separation diminishes with decreasing distance and PGA values of the two highest magnitude bins start mixing with the corresponding PGA values of lower magnitude clusters. This observation is very clear in soft sites and can be interpreted as the influence of soil nonlinearity as well as saturation of PGA at high magnitudes. The same trend is not observed in the PGV scatters (Figure 4.19). This suggests that the soil nonlinearity effects are less prominent in PGV that is consistent with the observations of Akkar and Bommer (2007a).

The influence of magnitude and faulting style on the simulated ground motions is presented in Figure 4.20. The comparisons are made in terms of mean Fourier amplitude spectra (FAS). The distance range of the simulations presented in the figure is 1 km $\leq R_{JB} <$ 10 km. Figure 4.20 suggests that the faulting style has minor influence on ground motion amplitudes. The amplitudes of strike-slip events are relatively smaller than the amplitudes of dipping events. Regardless of the site class, an increase in magnitude results in a consistent amplification of the low-to-intermediate frequency components. When the high-frequency components are of interest, it is observed that the rock site simulations present relatively small amplifications with the increase in magnitude. The variations in magnitude are also

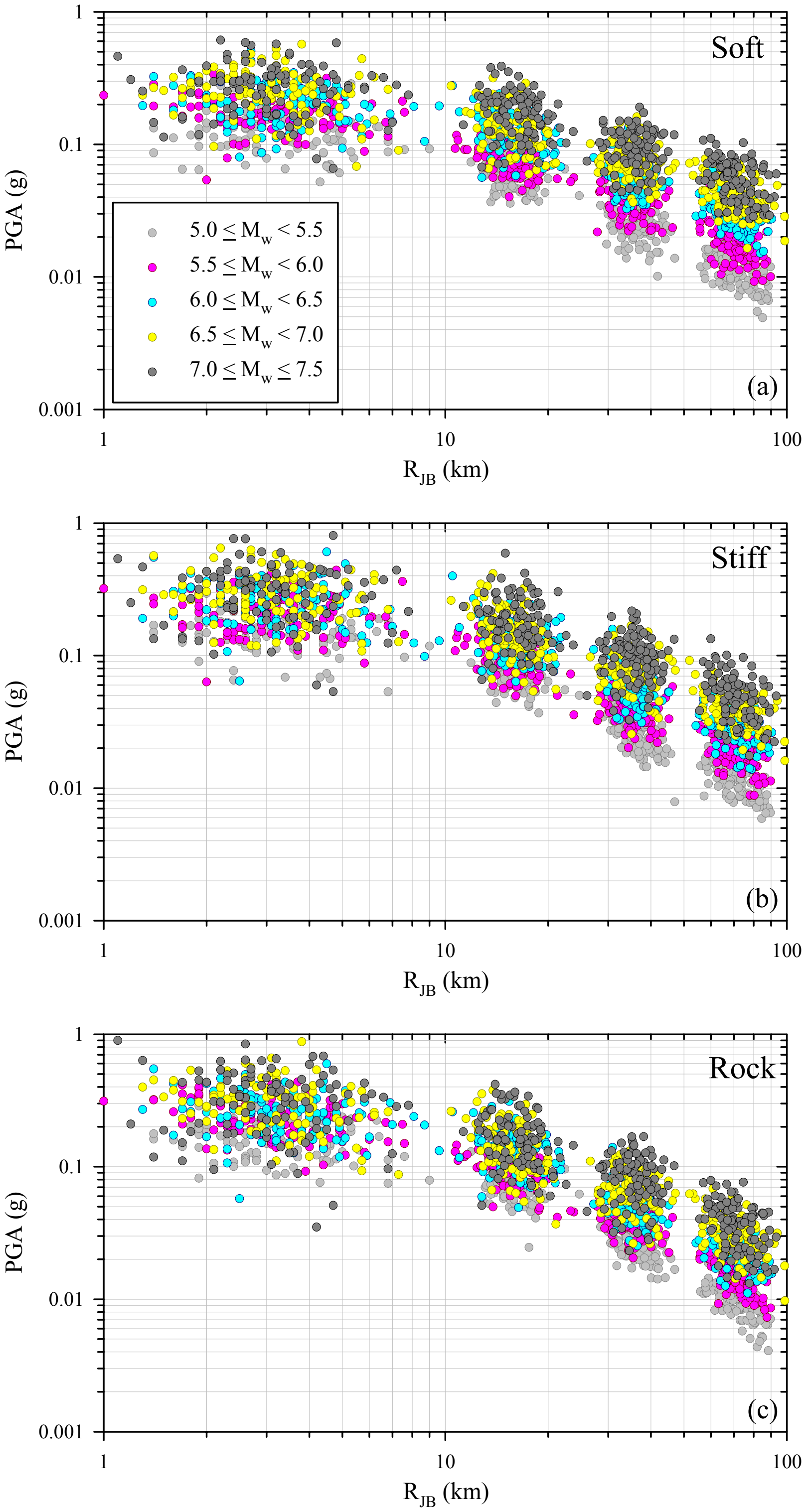

Figure 4.18 Comparison of PGA scatters from the simulated data for (a) soft, (b) stiff and (c) rock sites.

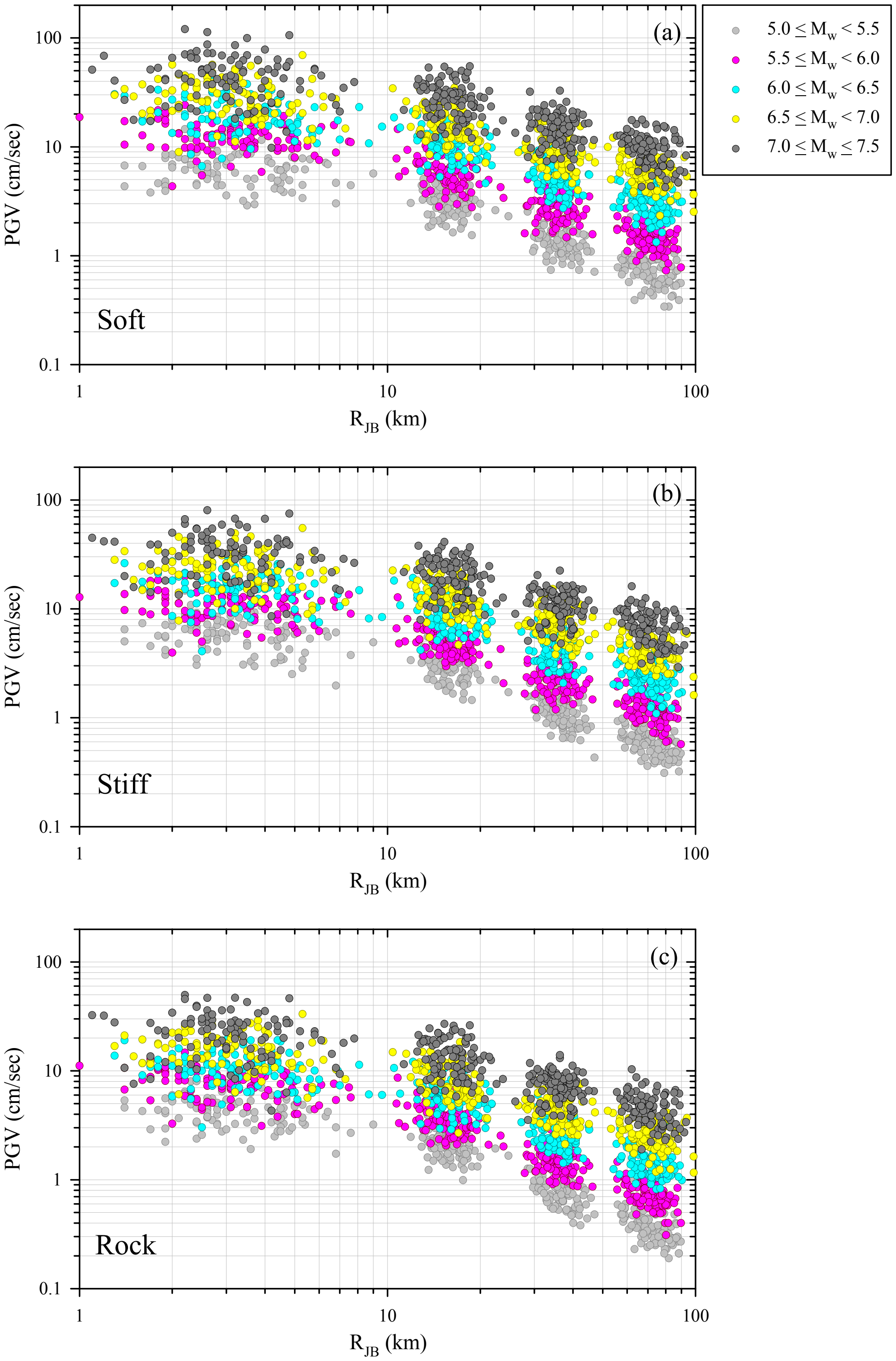

Figure 4.19 Comparison of PGV scatters from the simulated data for (a) soft, (b) stiff and (c) rock sites.

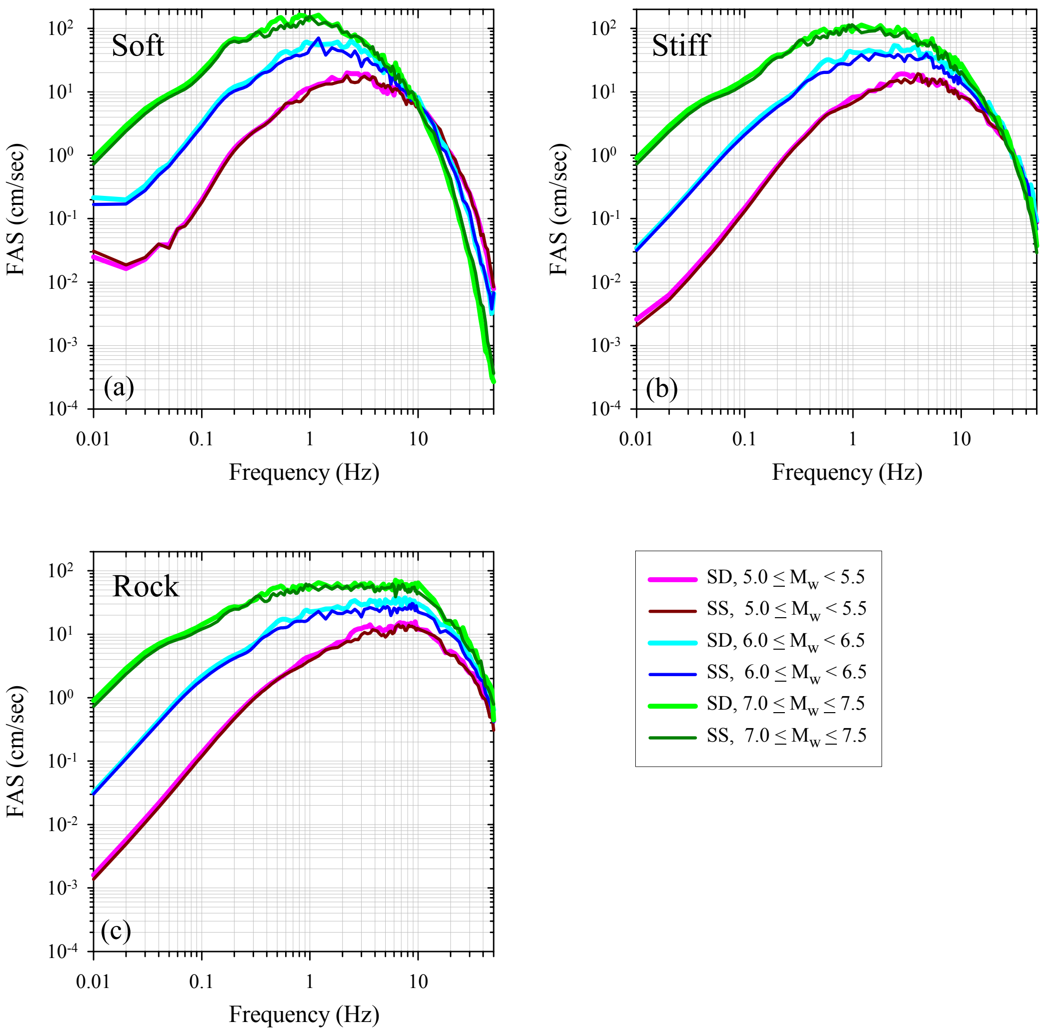

Figure 4.20 Comparison of mean Fourier amplitude spectra (FAS) of the simulated motions at (a) soft, (b) stiff and (c) rock sites for various magnitude bins. Both shallow dipping (SD) and strike-slip (SS) simulations are displayed in the figure. The distance range for the simulations presented in the figure is $1\text{ km} \leq R_{JB} < 10\text{ km}$.

not significant at high frequency components of stiff sites. However, the soft site simulations present considerable decay at high frequencies with increasing magnitude. This may be attributed to the consequential effects of soil nonlinearity. Large amplitudes at high frequencies would result in high shear strains. This results in yielding (nonlinearity) of soft sites and consequently, the high-frequency components attenuate more rapidly at soft sites with respect to other sites.

From this perspective, in order to reinforce the above observations, linear site response analyses are performed for a set of simulations to investigate whether the artificial ground motions generated via the equivalent linear method genuinely mimic the soil nonlinearity effects. For linear site response, the soil profiles are modeled by the strain-independent shear modulus and damping ratio to ensure the linear behavior of all layers. The damping ratio for each soil layer ($V_S \leq 760$ m/sec) is computed from Isihibashi and Zhang (1993) at small shear strains (i.e. 10^{-6} %). However, for rock layers ($V_S > 760$ m/sec), the initial damping proposed by Schnabel et al (1972) is taken into account.

Figure 4.21 compares the mean FAS of the simulations obtained from linear and equivalent linear (nonlinear) site response analyses. It is shown that the simulations reflect the theoretical site effects: softening of the site amplifies the low-to-intermediate frequency components and attenuates the high-frequency amplitudes. This is valid for both site response analyses. The figure clearly shows that consideration of soil nonlinearity makes a significant difference with respect to linear assumption at high frequencies when large magnitude ground motions at soft sites are of interest. For this type of records the decrease in distance increases the rapid decay of high frequency ground-motion components when the soil nonlinearity is taken into account (i.e. when equivalent linear procedure is implemented). Note that for rock site or small amplitude records (due to low magnitude or large distances) the linear assumption supersedes the nonlinear assumption in terms of site response. This is most probably due to the negligible soil nonlinearity in such cases.

Figure 4.22 depicts the similar observations from the site amplification perspective calculated from the soft and stiff response spectra normalized by the rock site response spectra (ratios are based on pseudo-acceleration response spectra). The same simulation set of Figure 4.21 is used for the site amplification plots. The site amplifications are plotted for a period band of 20 sec that is considered as the reliable period range based on the discussions about Figures 4.14 to 4.17. The site amplification plots once again show that consideration of soil nonlinearity of large magnitude recordings results in a significant decrease in the soft site spectral amplitudes at short periods. This observation is consistent with the theoretically expected behavior (i.e. high amplitude ground-motion components lead to yielding in the softer sites) that cannot be captured by linear modeling. The linear and nonlinear site response models produce approximately same behavior for low magnitude and distant events. In the light of these observations, it can be stated that the site response simulations of this study exhibit the theoretically expected behavior of nonlinear site effects.

The final figure (Figure 4.23) presented in this chapter displays the behavior of mean spectral displacements of the simulated records in terms of magnitude, site class and faulting style. The increase in magnitude results in a shift of the spectral periods at the commencement of flat spectral plateau. This is consistent with the theoretical source spectrum concept (BSSC, 2003). Moreover, the commencement of flat plateau is sensitive to the site class; the corner period slightly shifts towards the larger spectral band as the site becomes softer. This is also consistent with the theoretical site response. The spectral quantities of shallow dipping events are slightly larger than strike-slip events that is also the observed trend of the empirical data. Thus the simulations of this study reflect the genuine features of real ground-motion records fairly well.

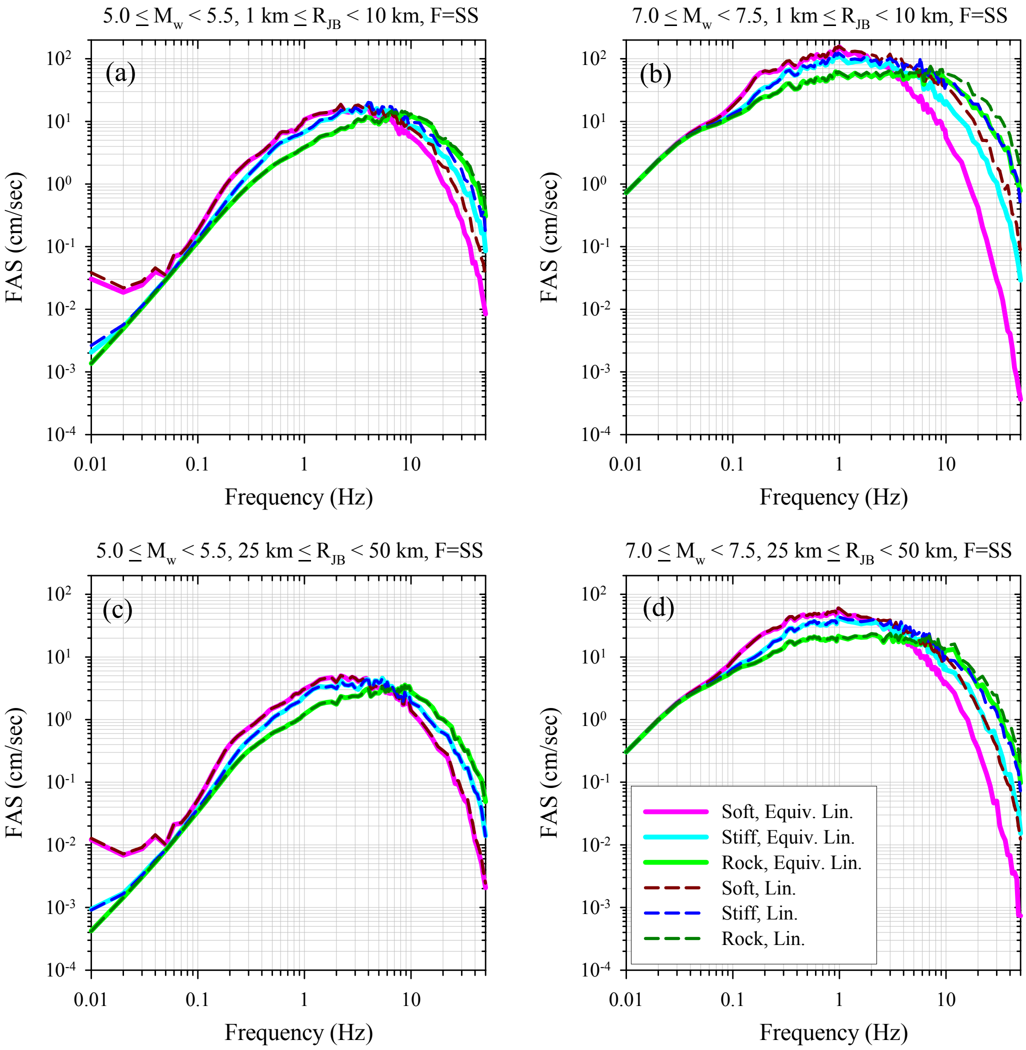

Figure 4.21 Comparison of mean FAS for simulations obtained from linear and nonlinear (equivalent linear) site response analyses (the abbreviations “Equiv. Lin.” and “Lin.” in the legend stand for “Equivalent Linear” and “Linear”, respectively).

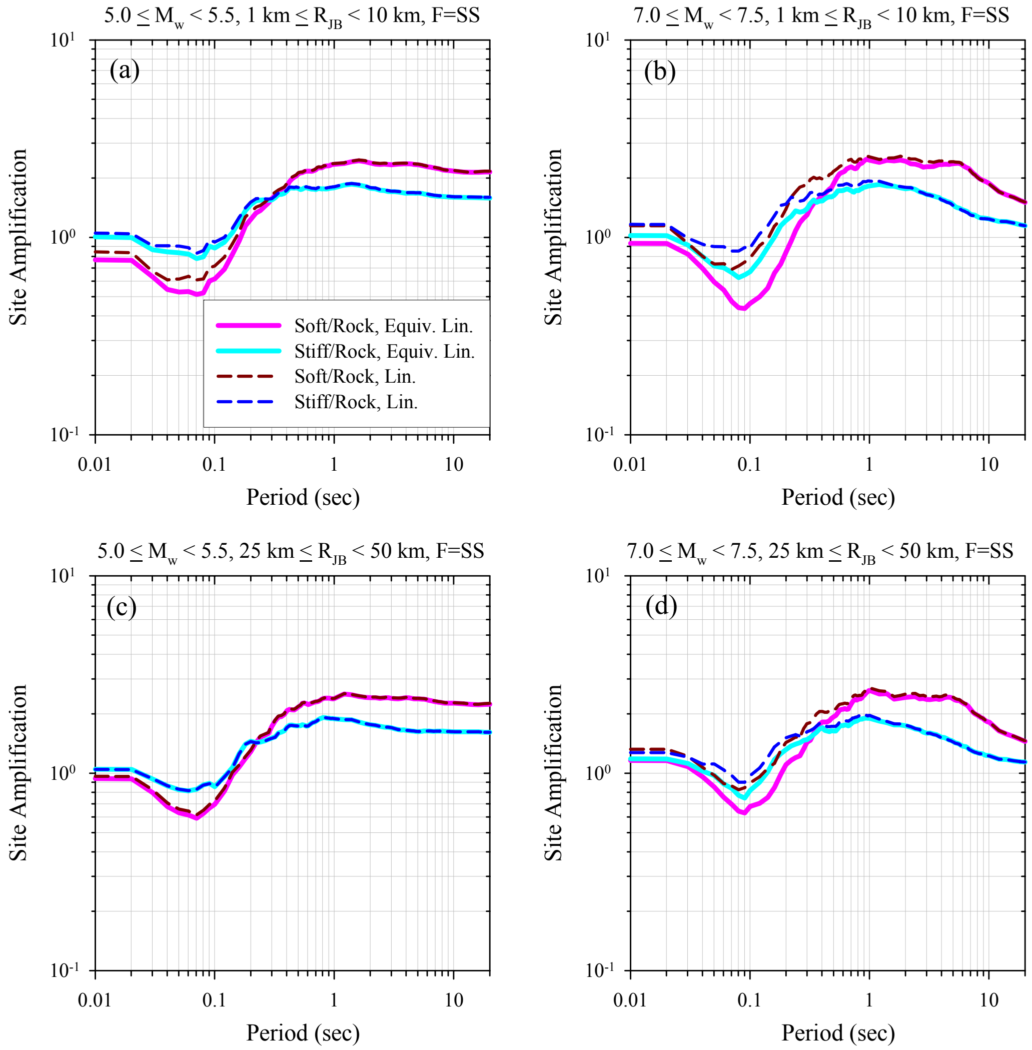

Figure 4.22 Comparison of mean site amplifications (i.e. soft and stiff site spectra normalized by the rock spectra) for simulations obtained from linear and nonlinear (equivalent linear) site response analyses (the abbreviations “Equiv. Lin.” and “Lin.” in the legend stand for “Equivalent Linear” and “Linear”, respectively).

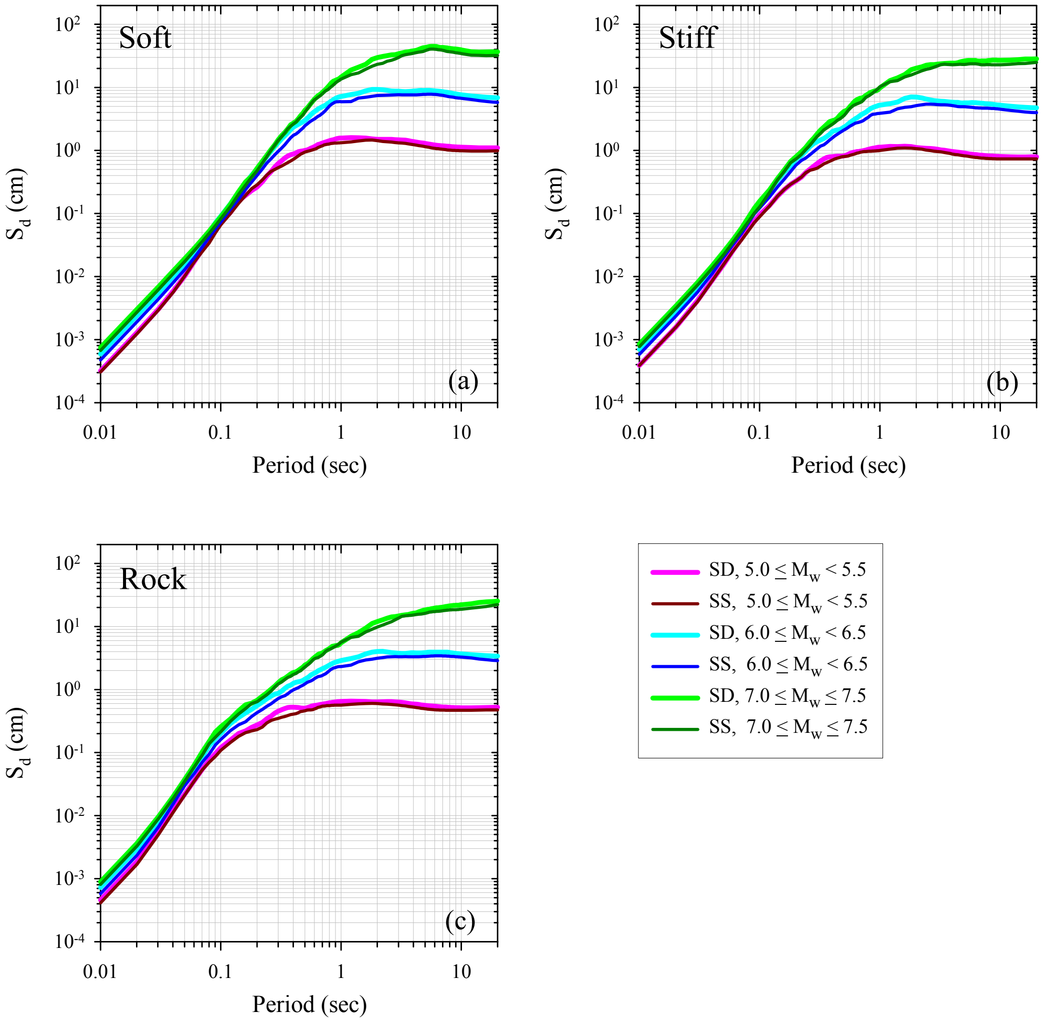

Figure 4.23 Comparison of 5% damped mean elastic displacement spectra (S_d, $\xi = 0.05$) of the simulations at (a) soft, (b) stiff and (c) rock sites for various magnitude bins. Both shallow dipping (SD) and strike-slip simulations (SS) are displayed in the figure. The distance range of the presented simulations presented is $1 \text{ km} \leq R_{JB} < 10 \text{ km}$.

CHAPTER 5

EVALUATION OF THE SIMULATED GROUND MOTIONS

5.1 General

This chapter presents the assessment of the simulated ground motions to determine the performance of the simulation procedure described in the previous chapters. The synthetics are first compared with another set of simulations generated by a non-stationary procedure proposed by Pousse et al. (2006). This way, the differences between the stationary and non-stationary stochastic simulation approaches are observed briefly. In the second part, the simulations are evaluated for several recently developed ground-motion prediction equations to assess its behavior with the estimations derived from actual recordings.

5.2 Comparison of the Simulated Ground Motions with Non-stationary Synthetics

As previously stated in Chapter 3, the stochastic method presented assumes that the frequency content of simulations is stationary in the time domain. This is not the case for actual ground-motion records because their frequency characteristics are time-dependent. Within this context, the generated ground motions are compared with the non-stationary simulations produced by the simulation technique proposed in Pousse et al. (2006)(5). The non-stationary synthetics are generated at rock sites

---

(5) The method is based on the approach presented by Sabetta and Pugliese (1996). Pousse et al. (2006) modified the model of Sabetta and Pugliese (1996) using ω-square model proposed by Frankel et al. (1996). In addition, they take into account the arrival time, energy, and broadening of the P- and S- pulses with distance, as well as the existence of scattered waves that produce the coda of the accelerograms. The method uses the peak ground acceleration, strong-motion duration, Arias

for various magnitude bins using the previously generated seismological parameters presented in Chapter 2. A total of 50 non-stationary time series is generated for each magnitude bin. The distance range is kept as 10 km $\leq R_{JB} < 25$ km in all bins.

Figure 5.1 compares the ground motions generated in this study with the non-stationary simulations. The comparisons are done in terms of mean spectral displacement (S_d) computed from each simulation bin. The figure also includes the mean S_d estimations obtained from the ground-motion prediction equations (GMPEs) proposed by Akkar and Bommer (2007b) and Boore and Atkinson (2008) to see the performance of these methodologies with respect to the empirically derived ground-motion models from actual recordings. The details about these GMPEs will be discussed in the following section. Figure 5.1 indicates that the spectral displacements of non-stationary simulations attain larger values than the S_d estimations of GMPEs and the synthetics generated in this study. It is also observed that the discrepancy between two simulation methods increases with increasing magnitude. The main source of this inconsistency can be attributed to the different source models used in the simulation procedures. In this study, the VHR simulations are generated using Atkinson and Silva (2000) source model. However, Pousse et al. (2006) employs the source model proposed by Frankel et al. (1996) that attains larger amplitudes compared to Atkinson and Silva (2000) model (Figure 5.2). Figure 5.1 suggests that, on average, stationary simulations of this study are in good agreement with the estimations of GMPEs. Consequently, the stationary frequency content of the simulated records does not mask the genuine ground-motion features. Considering this major observation, the simulations of this study are evaluated more thoroughly with several empirically developed predictive models that is described in the following sections.

---

intensity, and central frequency parameters for generating the non-stationary synthetics. Pousse et al. (2006) estimates these parameters from a set of empirical ground-motion prediction equations that are derived from the Japanese K-net database.

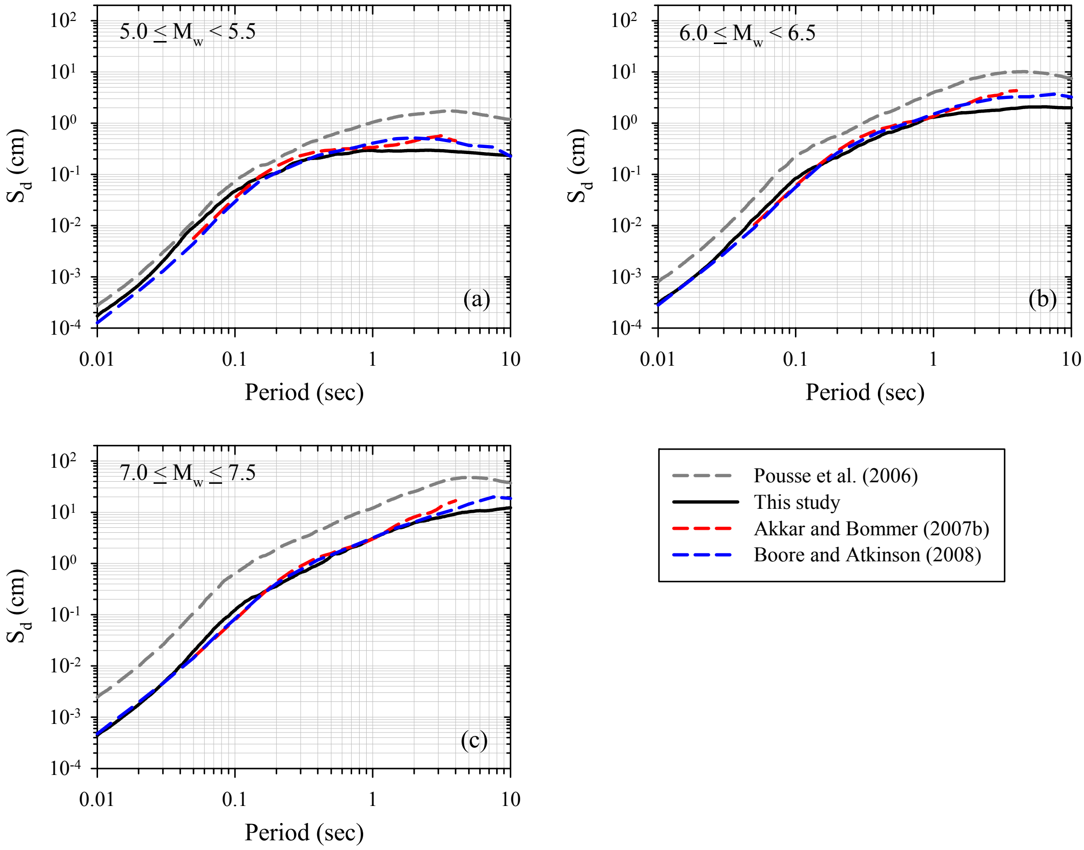

Figure 5.1 Comparison of stationary and non-stationary simulations in terms of mean spectral displacements of various magnitude ranges. The time series are simulated at rock sites (760 m/sec < $V_{S,30} \leq$ 1500 m/sec) for strike-slip (SS) events. The distance range is $10 \leq R_{JB} < 25$ km. The comparisons are done for periods up to 10.0 sec due to the period limits of the GMPEs. This period band is within the usable period range of the simulations discussed in Chapter 4.

5.3 Predictive Models Used for Evaluation

GMPEs proposed by Akkar and Bommer (2007a; 2007b), AB07a and AB07b, Abrahamson and Silva (2008), AS08, Boore and Atkinson (2008), BA08, Campbell and Bozorgnia (2008), CB08, and Chiou and Youngs (2008), CY08, are used for assessing the performance of the synthetics. Four of these empirical

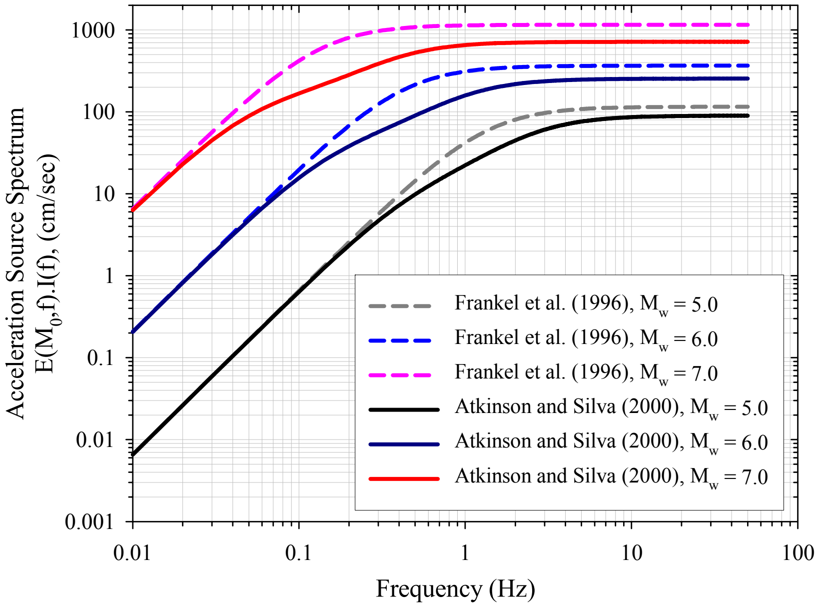

Figure 5.2 Comparison of source models proposed by Frankel et al. (1996) and Atkinson and Silva (2000) for various earthquake magnitudes. The acceleration source spectra are computed for $< R_{\Theta\phi} > = 0.50$.

models (AS08, BA08, CB08 and CY08) were developed within the context of “Next Generation of Ground-Motion Attenuation Models” (NGA) project (http://peer.berkeley.edu/products/nga_project.html). The developers of these models used the strong-motion database of Pacific Earthquake Engineering Research Center (PEER). The NGA models present empirical equations for peak ground acceleration (PGA), peak ground velocity (PGV) and 5% damped elastic pseudo-acceleration spectra (PSA) for periods up to 10 sec. They were derived for the rotation-independent average horizontal component (GMRotI50) that is independent of both sensor orientation and oscillator period (Watson-Lamprey and Boore, 2007).

The predictive models proposed by AB07a and AB07b were derived from the strong-motion database of Europe and Middle East that is compiled by Ambraseys et al. (2005). AB07a presents empirical prediction equations for PGV and AB07b proposes prediction equations for PGA and elastic displacement response spectra (S_d) for 2, 5, 10, 20 and 30% damping ratios up to 4 sec (S_d and PSA are directly related to each other through the natural frequency of the elastic oscillator, ω_n). Both equations were derived for geometric mean of horizontal components. AB07a also presents PGV estimations for the maximum horizontal component.

The GMPEs used in this chapter are applicable for the magnitude and distance ranges considered in this study (see Table 2.1). All empirical models, except BA08, also cover the mean S-wave velocity ($V_{S,30}$) ranges described here. The BA08 equation is applicable for sites with $V_{S,30} < 1300$ m/sec. The prediction equations of interest exhibit similarities and differences in the modeling of ground-motion parameters. Of these GMPEs the AB07a and AB07b equations are the simplest in terms of model parameters. Their functional form fundamentally considers the magnitude and distance. Dummy variables describe the site classes and different faulting styles in AB07a and AB07b. The site classes are based on $V_{S,30}$ intervals (180 m/sec $\leq V_{S,30} \leq$ 360 m/sec, 360 m/sec $< V_{S,30} \leq$ 760 m/sec and $V_{S,30} >$ 760 m/sec for soft, stiff and rock sites, respectively). The influence of soil nonlinearity is disregarded. Unlike the AB07a and AB07b, other predictive models express the site effects in terms of continuous functions that depend on the variations in $V_{S,30}$. Furthermore, the hanging wall, rupture depth and soil/sediment depth effects are accounted for by AS08, CB08 and CY08. All empirical models use moment magnitude, M_w, as the reference magnitude scale. There are two different primary distance definitions used in distance scaling. The functional forms of AB07a, AB07b and BA08 use R_{JB} whereas AS08, CB08 and CY08 are based on R_{rup}.

All NGA models account for the nonlinear site response effects using two different measures for the strength of the shaking. AS08, BA08, and CB08 use the median peak acceleration on a rock outcrop whereas CY08 considers the median spectral acceleration on a rock outcrop at the period of interest (Abrahamson et al., 2008). Moreover, AS08 and CB08 models constrain the nonlinear site response terms using the results of 1-D analytical site response model of Walling et al. (2008). The site amplification model of BA08 is based on the studies performed by Choi and Steward (2005). CY08 employs the nonlinear amplification model derived from the NGA data as part of the regression.

Besides the variations in mean S-wave velocity, the AS08, CB08 and CY08 equations account for the soil/sediment depth effect (basin effect) while modeling the site amplification. AS08 and CY08 consider depths to V_S = 1.0 km/sec (Z1.0) whereas CB08 uses depths to V_S = 2.5 km/sec (Z2.5) for this particular effect. In the AS08 model, the shallow soil/sediment depth scaling was constrained by using the analytical results of 1-D site amplification (Silva, 2005). The same model constrained the deep soil/sediment depth scaling from the analytical results of 3-D basin amplification (Day et al., 2006). CB08 also defined the basin term bearing on the 3-D simulations of Day et al. (2008) with additional empirical adjustments at short periods and shallow soil/sediment depths. The CY08 model defined the soil/sediment depth scaling using the NGA database.

AS08, CB08 and CY08 account for the rupture-depth effect in modeling of ground motions. In these predictive models, the rupture-depth effect is parameterized by the depth-to-top of the rupture (Z_{TOR}). The AS08 and CY08 models include rupture-depth dependence for both strike-slip and reverse earthquakes. However, the CB08 model includes the rupture-depth effect for reverse earthquakes only for depths greater than 1 km. The buried ruptures lead to stronger shaking than surface ruptures at the same distance.

All models present empirical set of equations for aleatory uncertainty. The AB07a, AB07b, AS08 and CY08 models present magnitude-dependent standard deviations whereas BA08 and CB08 estimate the standard deviations independent of magnitude. When the site effects are of concern, AS08, CB08 and CY08 additionally account for the influence of soil nonlinearity on the total uncertainty.

5.4 Assessment of Simulated Motions Using GMPEs

The median estimations of empirical models are computed using previously generated seismological parameters (Chapter 2). As stated in the previous section, the predictive models consider different source, distance and site parameters. The ground-motion estimations are computed for the particular distance metric specified in each model. The $V_{S,30}$ values obtained from randomly generated soil profiles (Chapter 4) are considered as the measured site parameters.

AS08, CB08 and CY08 models require the soil/sediment depth (Z1.0 or Z2.5) and depth-to-top of rupture (Z_{TOR}) parameters for the ground-motion estimations. The AS08 and CY08 models propose different relationships in terms of $V_{S,30}$ for the estimation of median Z1.0 values if the actual soil/sediment depth is unknown. In this study, AS08 and CY08 are evaluated by using the recommended relationships of the model proponents. The CB08 model uses Z2.5 as the soil/sediment depth parameter and the recommendation is to estimate Z2.5 from Z1.0 (Campbell and Bozorgnia, 2008). In this study, the Z2.5 values are estimated from the average Z1.0 predictions obtained through the relationships presented in AS08 and CY08. When Z_{TOR} is of concern, the median values obtained from the NGA database are considered: 6 km for $M_w = 5.0$, 3 km for $M_w = 6.0$, 1 km for $M_w = 7.0$, and 0 km for $M_w = 8.0$ (Abrahamson et al., 2008). The relationship between M_w and Z_{TOR} is assumed to be a quadratic polynomial that passes through the given median Z_{TOR} values (Figure 5.3).

As stated previously, the NGA models present empirical relationships for rotation-independent average horizontal component (GMRotI50) whereas AB07a and AB07b models predict ground motions for the geometric mean of horizontal components. In a recent study, Beyer and Bommer (2006) showed that the median estimate for "GMRotI50" is equivalent to the median estimate of the geometric mean. Beyer and Bommer (2006) also showed that the median ground motions estimated from random horizontal components (actual situation in the simulations of this study) are not different than the median estimations of "GMRotI50" and geometric mean. As a matter of fact, in the later studies by Campbell and Bozorgnia (2007) and Watson-Lamprey and Boore (2007), it was shown that the median geometric mean estimations are within a few percent of median "GMRotI50". Therefore, no modification is done in the estimated as well as simulated ground motions in terms of horizontal component definition.

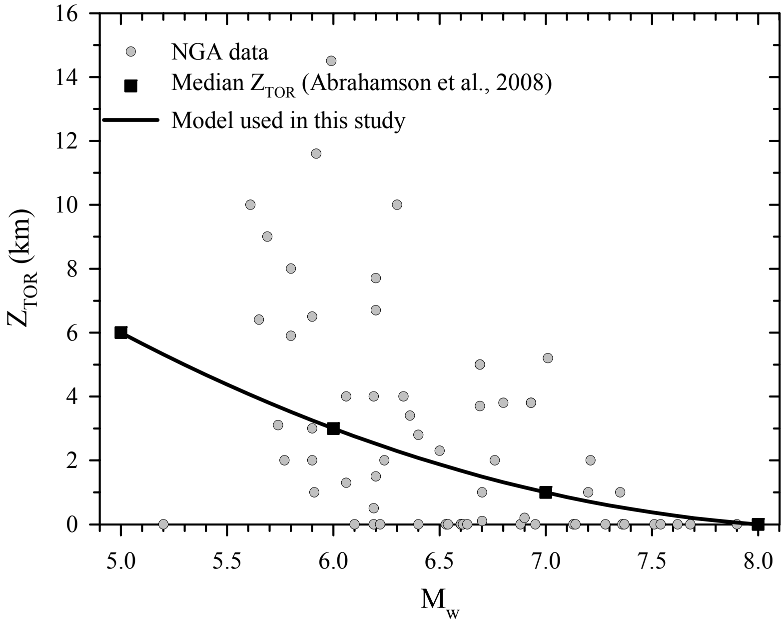

Figure 5.3 M_w-Z_{TOR} relationship (solid line) used for the computation of ground-motion estimations of predictive models

The median estimations of the GMPEs are computed for each simulated ground motion by considering the issues discussed above. Since the simulations of shallow dipping (SD) faults do not present normal/reverse classification, their evaluation with the GMPEs is done by randomly assigning normal or reverse faulting styles to the SD simulations with equal probabilities. It is worth to mention that no hanging wall effect is considered in this study.

5.4.1 Assessments in Terms of Mean Spectral Displacement

Figure 5.4 compares the simulations and GMPEs in terms of mean S_d for source-to-site distances between 1 km and 10 km. The comparisons are done in terms of SD (left column) and SS (right column) events at rock (760 m/sec < $V_{S,30} \leq 1500$ m/sec), stiff (360 m/sec < $V_{S,30} \leq 760$ m/sec) and soft (180 m/sec ≤ $V_{S,30} \leq 360$ m/sec) sites for small ($5.0 \leq M_w < 5.5$) and large ($7.0 \leq M_w \leq 7.5$) magnitude bins. It is observed that the simulations are fairly in good agreement with GMPEs for large magnitude events. However, for small magnitudes, the predictive models generally yield larger spectral displacements than the synthetics, particularly for $T \geq 1.0$ sec. Note also that the variations between the GMPEs are more pronounced for small magnitude events. When the influence of site class is of concern, it is observed that the synthetics and predictive models for stiff and rock sites yield similar spectral displacements. For soft sites, however, the simulations attain smaller spectral displacements than GMPEs. It is also depicted from Figure 5.4 that the similarity between the SD simulations and GMPEs is higher with respect to the SS simulations.

Figure 5.5 presents the similar comparisons for source-to-site distances between 10 km and 25 km. The interpretations made in the above paragraph are, in general, valid for this distance range. However, the discrepancy between the synthetics and GMPEs for this distance interval is smaller than those for source-to-site distances between 1 km and 10 km. This observation is valid for all magnitude ranges, faulting styles and site classes considered in this report.

The assessment of simulations with respect to GMPEs for source-to-site distances 25 km - 50 km and 50 km - 100 km are presented in Figures 5.6 and 5.7, respectively. The effects of magnitude and site class on the performance of the simulations are generally similar to those presented in Figures 5.4 and 5.5. When the influence of faulting style is of concern, for distances greater than 25 km, the discrepancy between synthetics and predictive models for SS simulations is slightly

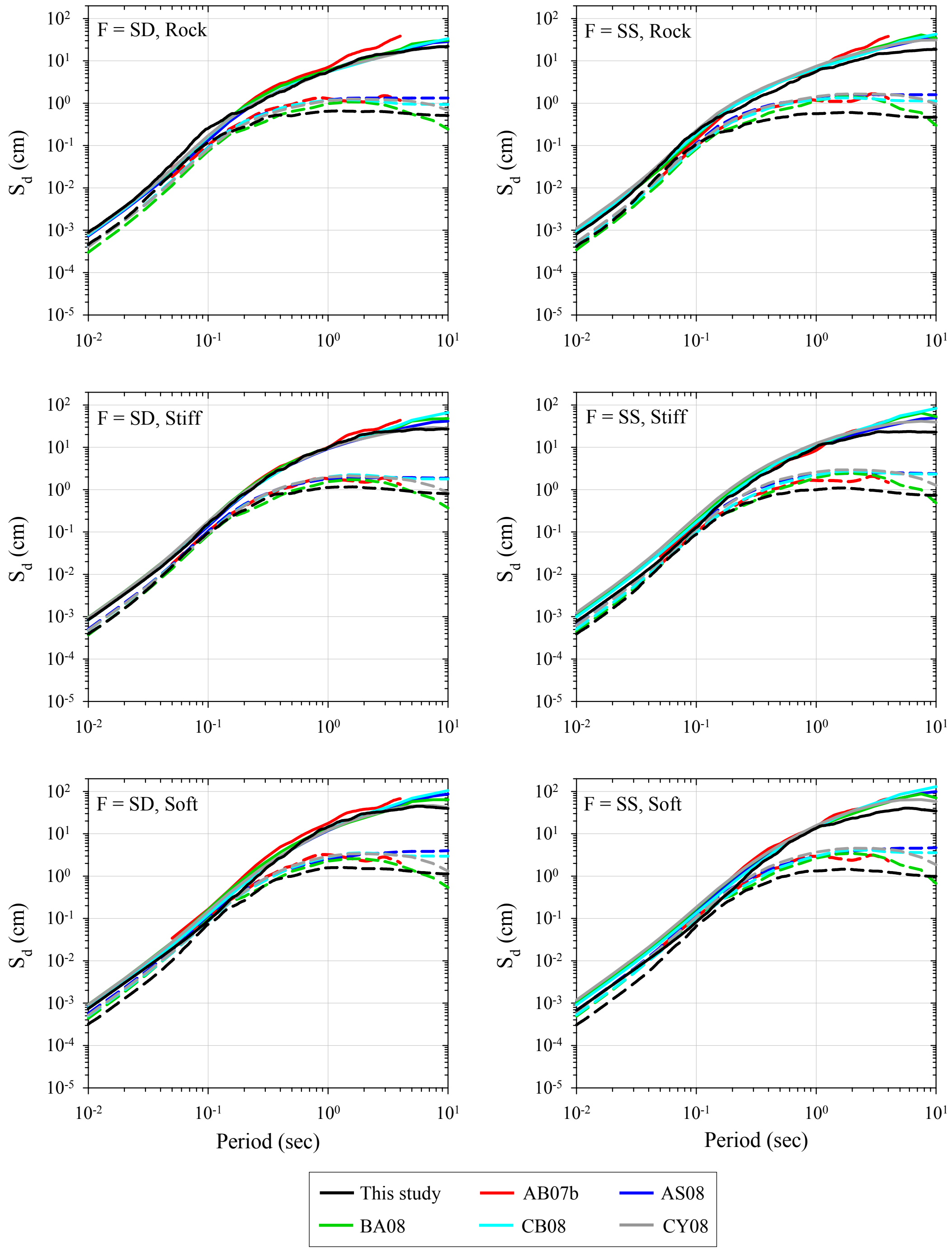

Figure 5.4 Comparison of simulations and GMPEs in terms of mean S_d ($\xi = 5\%$) for source-to-site distances between 1 km and 10 km. Dashed and solid lines represent the mean spectral displacements for $5.0 \leq M_w < 5.5$ and $7.0 \leq M_w \leq 7.5$, respectively.

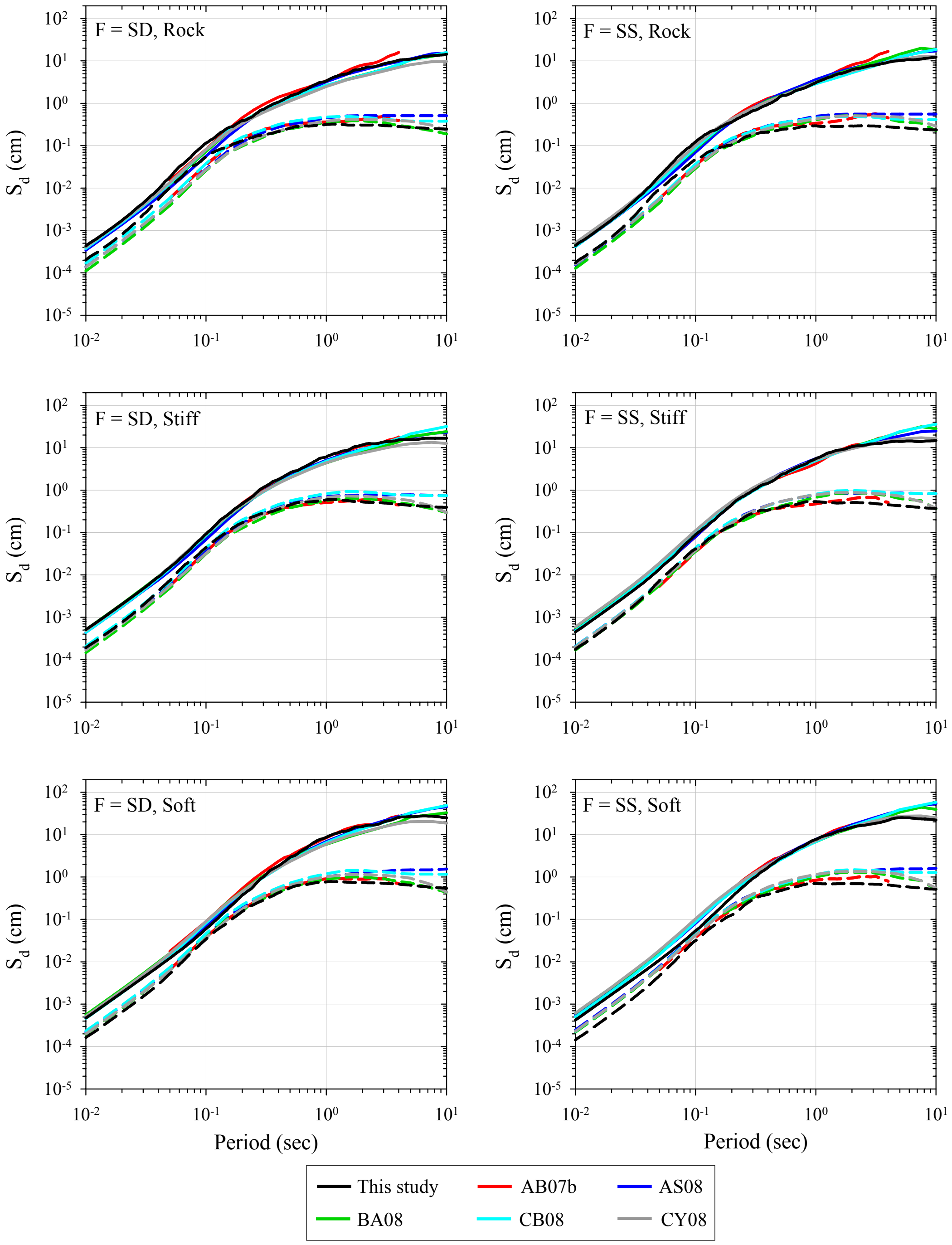

Figure 5.5 Comparison of simulations and GMPEs in terms of mean S_d ($\xi = 5\%$) for source-to-site distances between 10 km and 25 km. Dashed and solid lines represent the mean spectral displacements for $5.0 \leq M_w < 5.5$ and $7.0 \leq M_w \leq 7.5$, respectively.

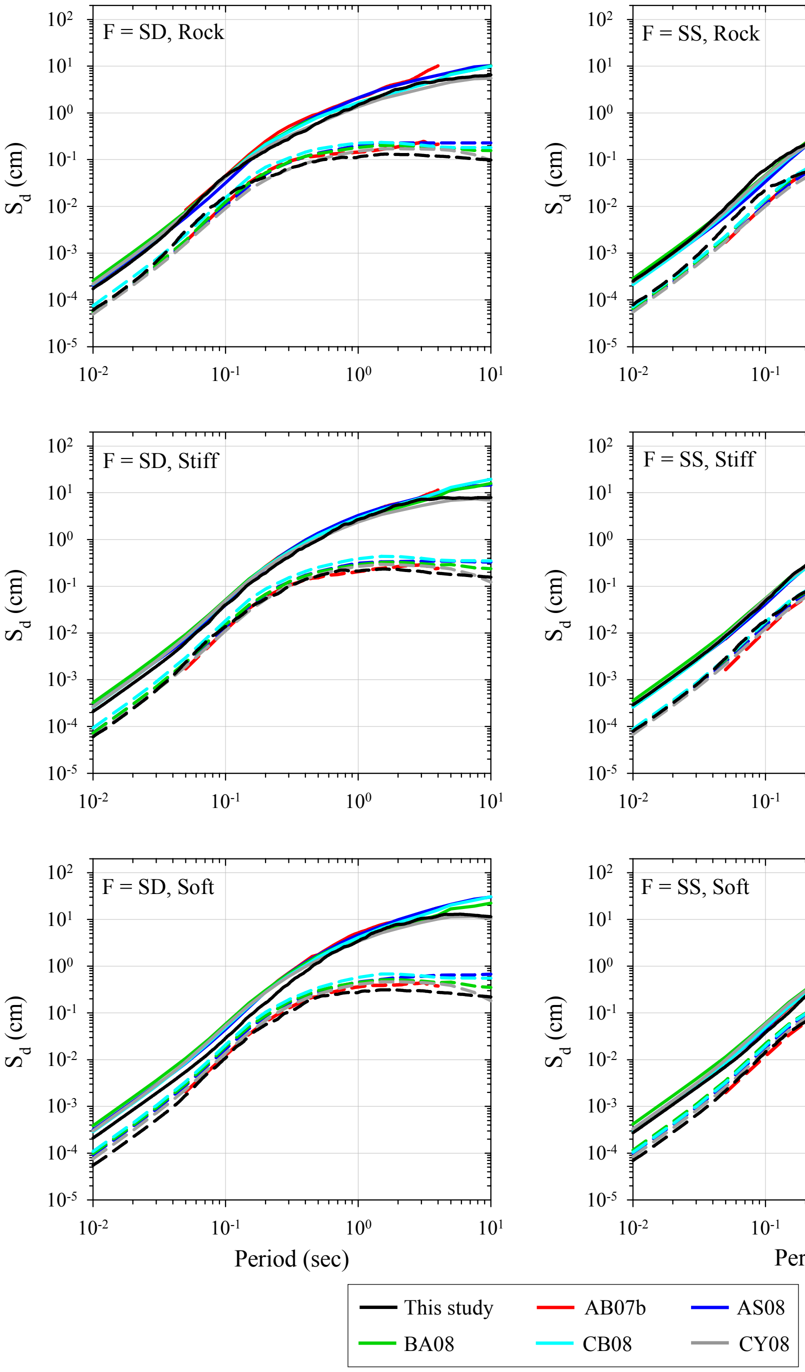

Figure 5.6 Comparison of simulations and GMPEs in terms of mean S_d ($\xi = 5\%$) for source-to-site distances between 25 km and 50 km. Dashed and solid lines represent the mean spectral displacements for $5.0 \leq M_w < 5.5$ and $7.0 \leq M_w \leq 7.5$, respectively.

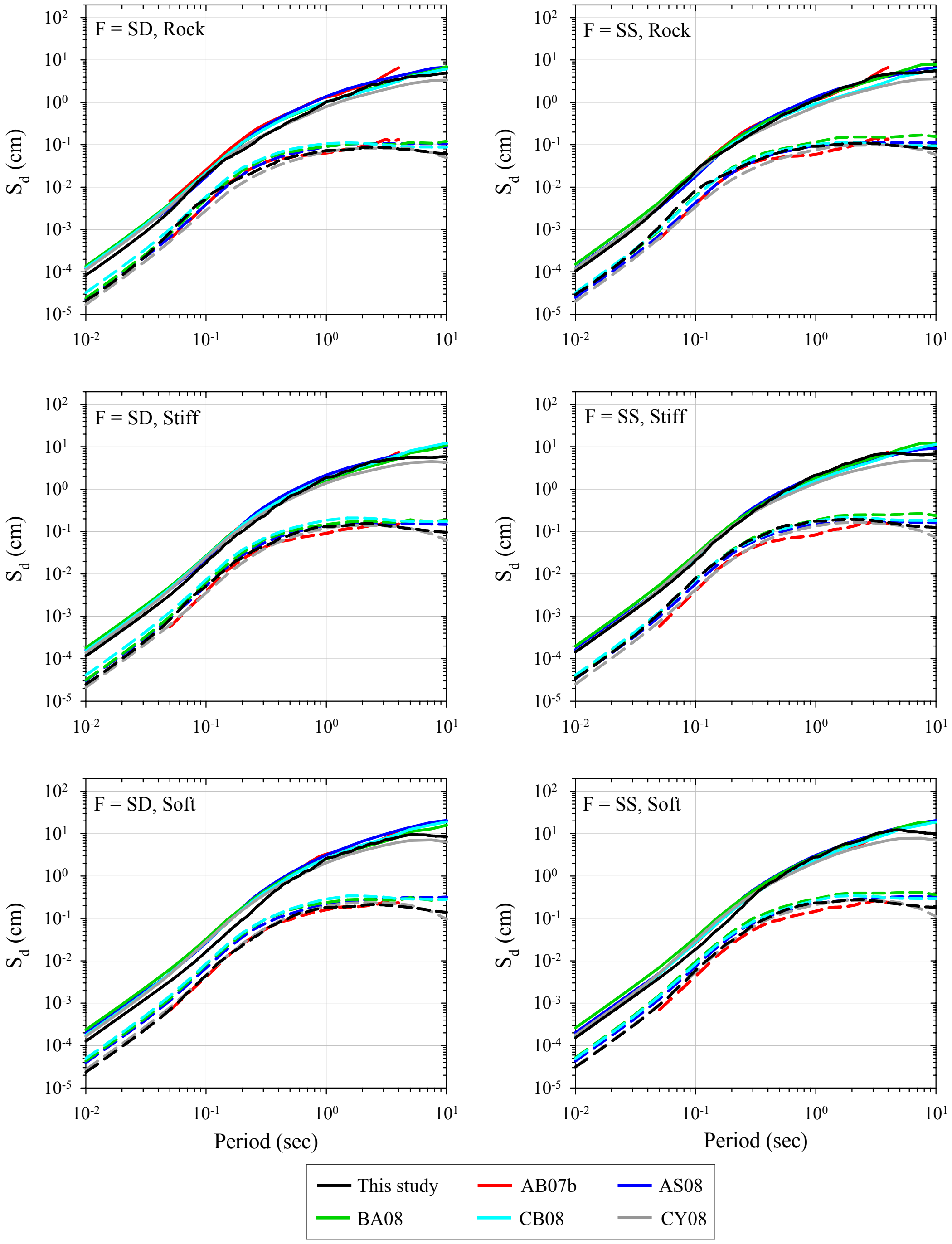

Figure 5.7 Comparison of simulations and GMPEs in terms of mean S_d ($\xi = 5\%$) for source-to-site distances between 50 km and 100 km. Dashed and solid lines represent the mean spectral displacements for $5.0 \leq M_w < 5.5$ and $7.0 \leq M_w \leq 7.5$, respectively.

smaller than those of SD simulations. This observation suggests that the performance of SD and SS simulations are distance-dependent.

Figures 5.4 to 5.7 indicate that the synthetics and predictive models show differences for small magnitude events. A closer look to these figures also reveals that the predictive models show considerable differences among each other for small magnitude events. One way of explaining the dispersive behavior in small magnitude events can be the magnitude distribution of ground-motion datasets. Abrahamson et al. (2008) stated that the NGA models present large amount of variation (up to a factor of 2) for small magnitude events due to the selection of sparse strong-motion data from small magnitude events. Bommer et al. (2007) also noted the importance of magnitude range in strong-motion datasets for the estimation of ground motions. Another reason for the discrepancy between the GMPEs and synthetics can be attributed to the modeling differences. The predictive models AS08, CB08 and CY08 account for the influence of rupture depth that is not taken into account for the synthetics in this study. The uncertainty in rupture depth is significant for small magnitude events (Figure 5.3) and its contribution can play a role in the observed differences between synthetics and GMPEs at small magnitudes.

Under the light of above observations, the simulations are further evaluated with respect to the GMPEs by making use of conventional residual analysis. The residual analysis are done for PGA, PGV and 5% damped S_d at T = 0.2, 1.0, 3.0 and 10.0 seconds. The PGA and PGV are the most frequently used peak ground-motion values whereas the spectral displacements at T = 0.2 sec and T = 1.0 sec can be used for constructing displacement compatible design spectrum (BSSC, 2003). S_d at T = 3.0 sec represents a typical medium period response quantity for the modern predictive models whereas S_d at T = 10.0 sec is the upper bound of most of the GMPEs presented in this study. The residuals are defined as the logarithmic difference between the simulations and estimations (i.e.

ln(sim/GMPE)). The details of the assessment of simulations are presented in the succeeding sub-sections.

5.4.2 Assessments in Terms of Magnitude Influence

Figures 5.8 to 5.19 present the M_w-dependent scatters of individual simulations for shallow dipping (SD) and strike-slip (SS) events at rock, stiff and soft sites. The distance range for the comparative plots is 10 km $\leq R_{JB} <$ 25 km. The residual plots for each GMPE are also presented in these figures in order to assess the compatibility of simulations with respect to each ground-motion model. Negative residuals indicate that the synthetics attain smaller values compared to the concerned predictive model. The median, 16% and 84% percentile estimations of GMPEs are superimposed in the simulation scatters together with the mean values of the synthetics that are computed at different magnitude intervals. This way, the general agreement between the simulations and the GMPEs can be visually inspected. The median and fractile estimations are computed for $R = 10$ km and $R = 25$ km where R denotes R_{JB} for AB07a, AB07b and BA08 and R_{rup} for AS08, CB08 and CY08. The scatter plots for SD events only present the median and fractile estimations for reverse faulting. The corresponding normal faulting estimations are not presented in order not to crowd the pictures. The bounds of normal faulting estimations would be within the reverse faulting limits, which implies that the general conclusions driven from these figures will not change. The linear trend lines presented in the residual scatters are used for describing the tendency of the simulations with respect to each GMPE. The residual plots also contain the p-values of the slopes of linear trend lines. A p-value smaller than 0.05 would suggest that the residual trend is significant with respect to the independent parameter, M_w. Although, the discussions in this sub-section are confined to Figures 5.8 to 5.19, they describe the most general observations for the entire synthetics computed in this study. Other relevant figures related to the discussions of this sub-section are presented in Appendix B.

Figures 5.8 and 5.9 present the magnitude-dependent comparisons in terms of PGA for SD and SS events, respectively. The plots show the individual simulation scatters and corresponding residuals for rock (top row), stiff (mid row) and soft (bottom row) sites using different GMPEs. The simulation scatters are homogenously distributed within the boundaries of the predictive models and the median values of the synthetics follow closely the median estimations of GMPEs. Thus, the simulations can grossly represent the seismological features captured by the empirically derived predictive models. The residual plots indicate that rock and stiff site simulations are slightly larger than the GMPE estimations for small magnitude events. For soft sites, however, the synthetics yield smaller values than the predictive models. These observations are valid for both faulting styles. With increasing M_w values, the discrepancy between the GMPEs and synthetics for SD events tend to decrease. However, regardless of the site class, the SS simulations attain smaller PGA values than the estimations of GMPEs for large magnitudes.

Figures 5.10 and 5.11 display the similar comparisons for PGV for SD and SS events, respectively. The simulations and ground motion models are fairly in good agreement for the entire magnitude band for SD events at rock and stiff sites. However, when the SS simulations are of concern, the rock and stiff site synthetics attain smaller values than GMPEs. Regardless of faulting style, the soft site simulations tend to attain smaller values with respect to the predictive models as presented by the comparisons with AB07a. For NGA models, however, the discrepancy between simulations and empirical models for soft sites decreases as the magnitude increases (Figures B.9 and B.12).

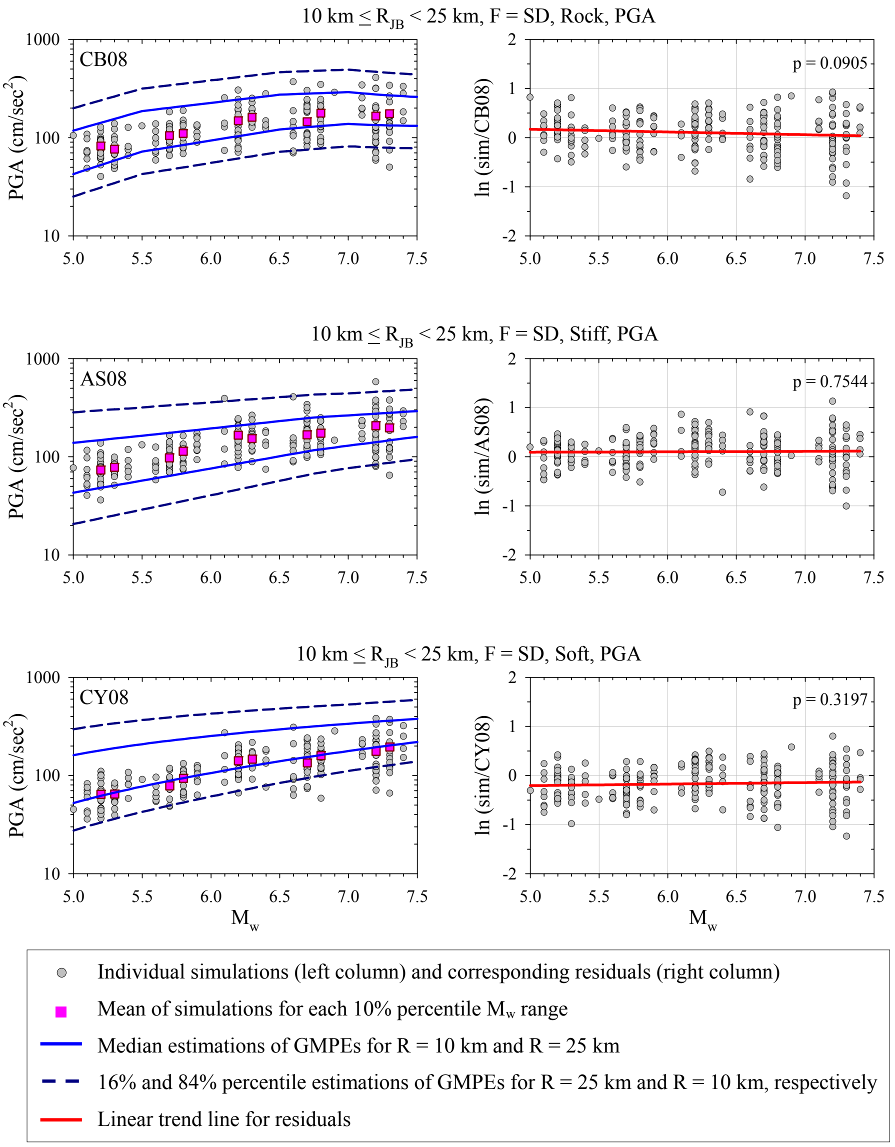

Figure 5.8 Magnitude-dependent comparisons of simulations and GMPEs in terms of PGA for shallow dipping (SD) faults

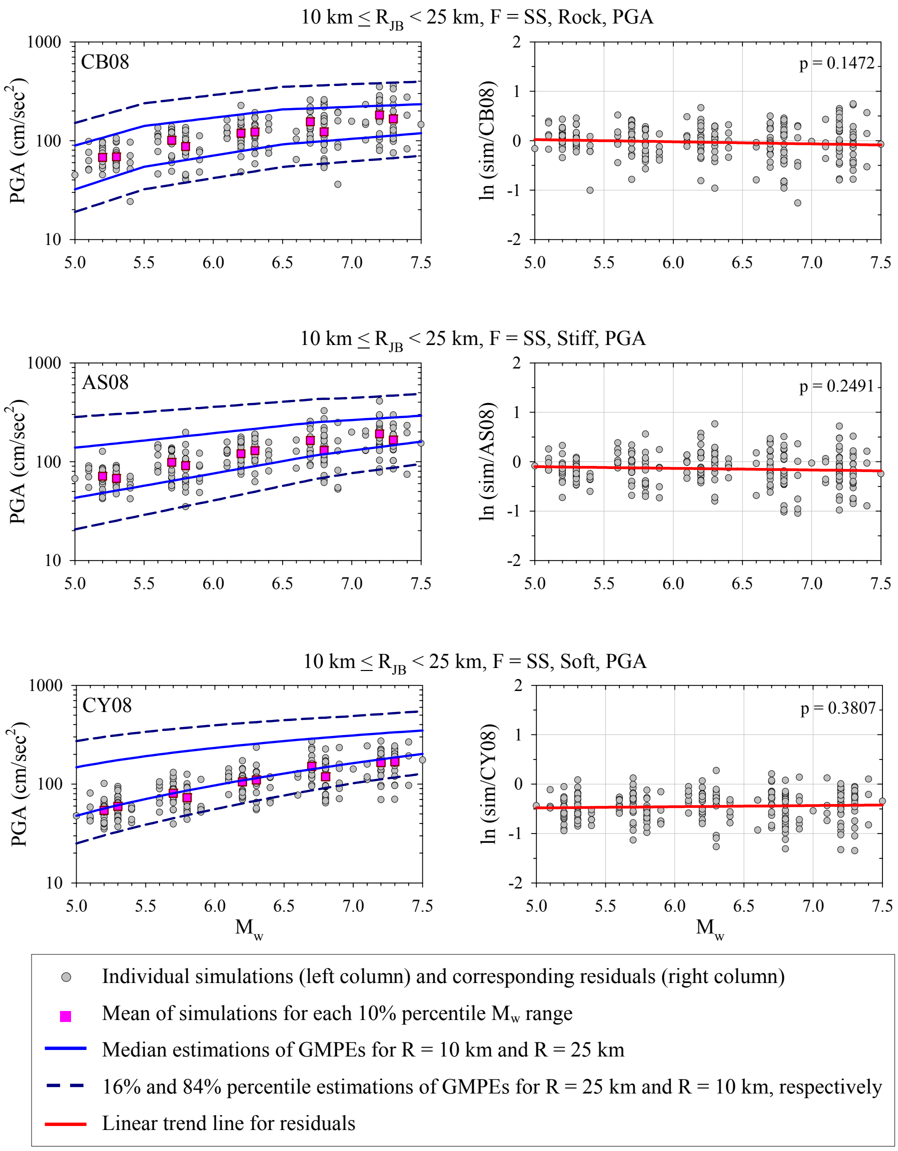

Figure 5.9 Magnitude-dependent comparisons of simulations and GMPEs in terms of PGA for strike-slip (SS) faults

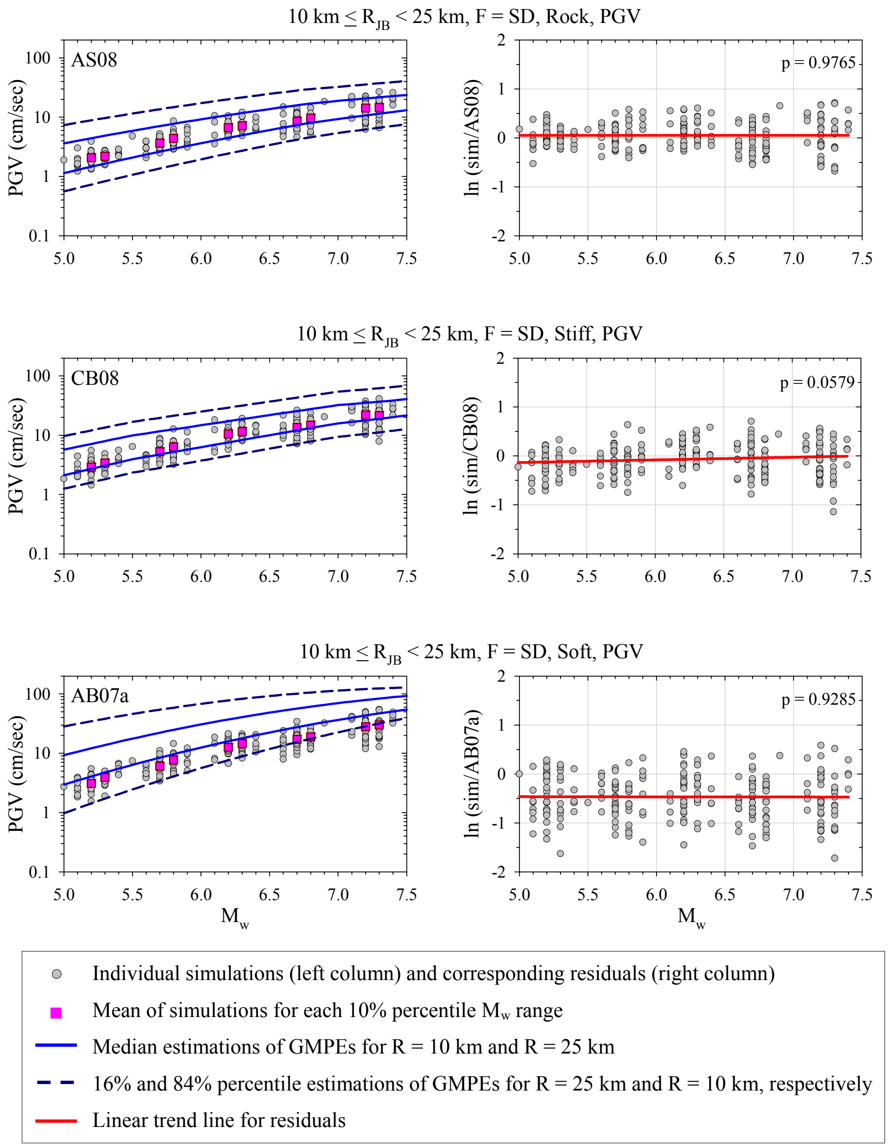

Figure 5.10 Magnitude-dependent comparisons of simulations and GMPEs in terms of PGV for shallow dipping (SD) faults

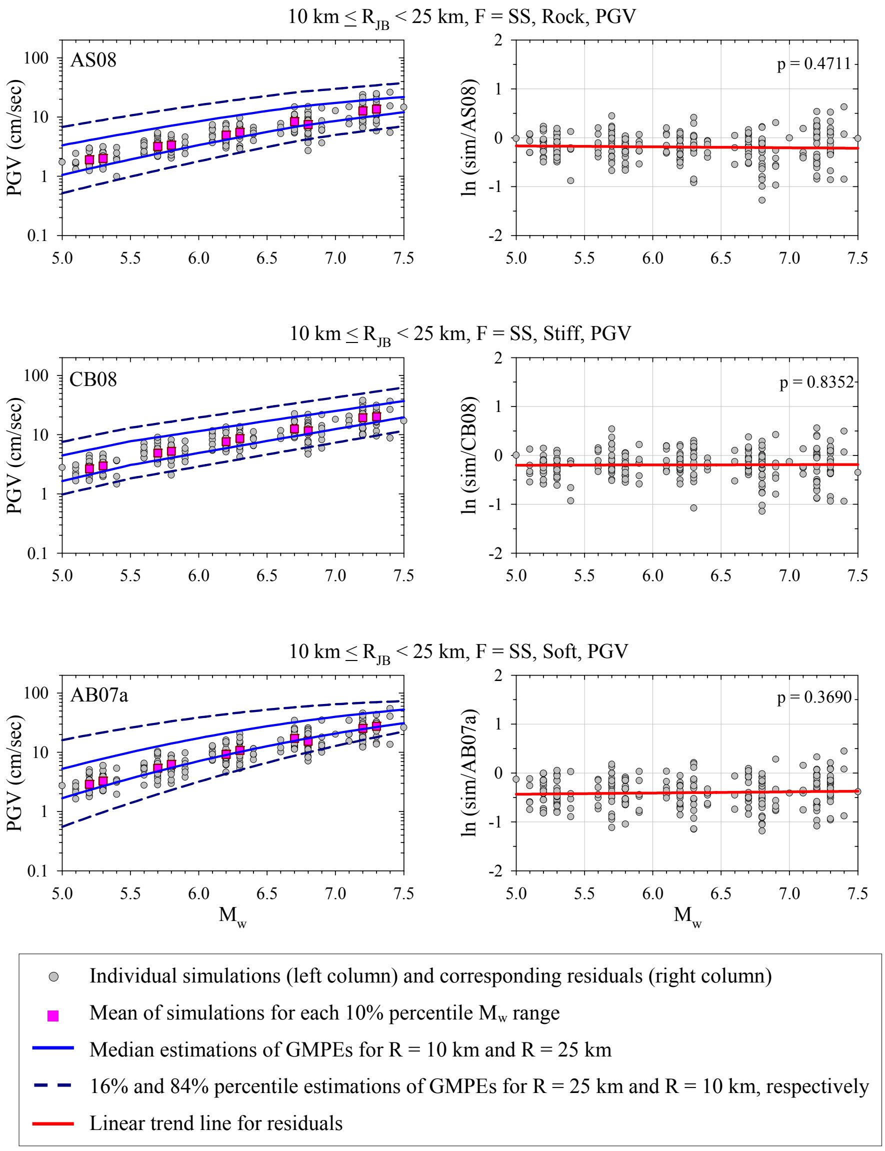

Figure 5.11 Magnitude-dependent comparisons of simulations and GMPEs in terms of PGV for strike-slip (SS) faults

Figures 5.12 to 5.15 describe the magnitude-dependent behavior of simulations for spectral displacements at T = 0.2 sec and T = 1.0 sec for SD and SS events. For both spectral periods, the small magnitude estimations by the predictive models are larger than the simulations of soft sites, regardless of the faulting style. For the short-period S_d, this trend is valid for large magnitudes as well (Figures 5.12 and 5.13). However, the discrepancy between the simulated soft site S_d at T = 1.0 sec

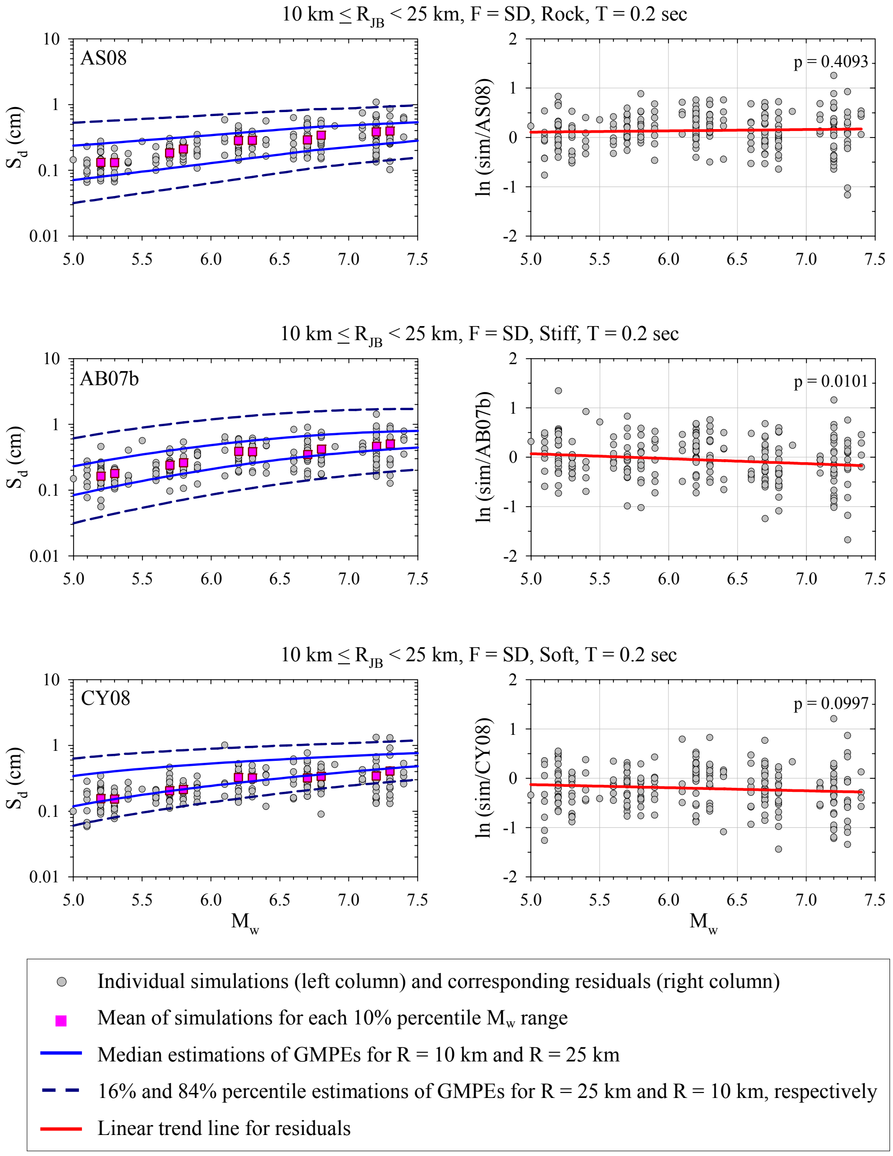

Figure 5.12 Magnitude-dependent comparisons of simulations and GMPEs in terms of S_d (ξ = 5%) at T = 0.2 sec for shallow dipping (SD) faults

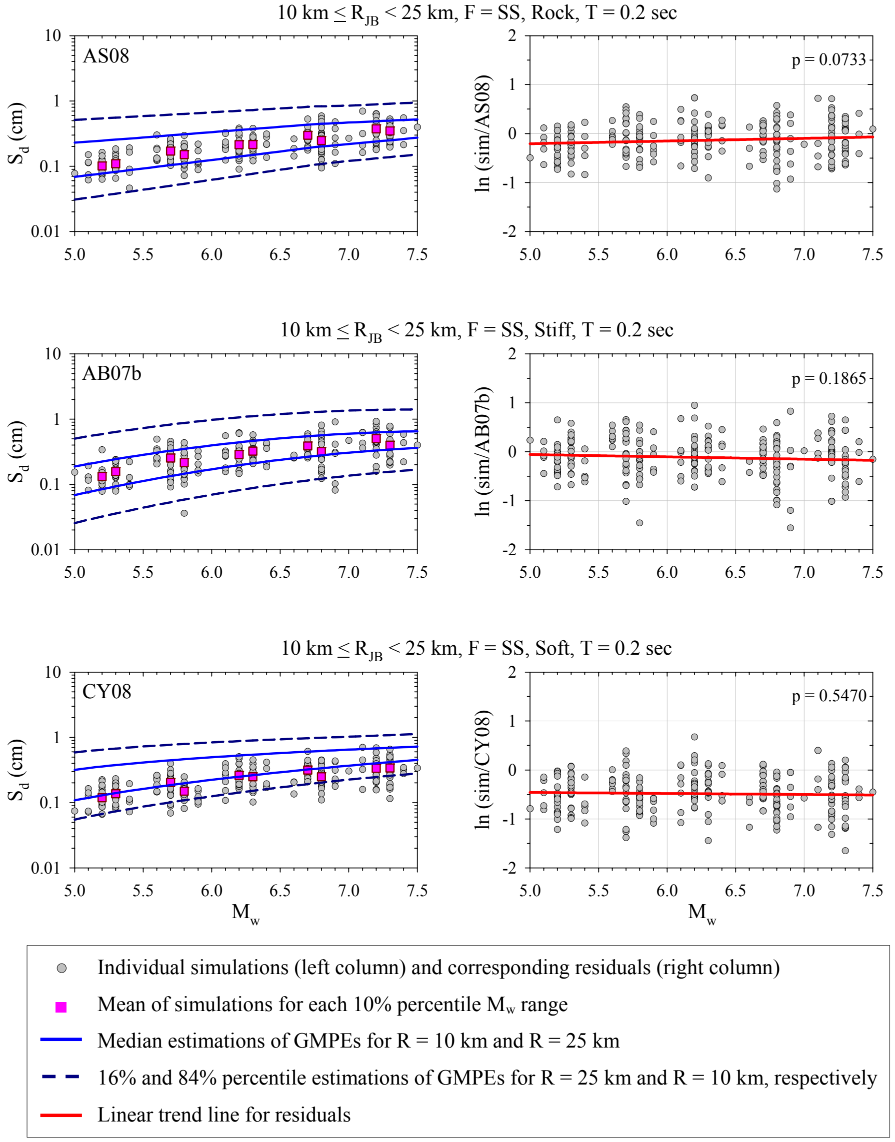

Figure 5.13 Magnitude-dependent comparisons of simulations and GMPEs in terms of S_d ($\xi = 5\%$) at T = 0.2 sec for strike-slip (SS) faults

and corresponding estimations of GMPEs decreases with increasing magnitude (Figures 5.14 and 5.15). Note that regardless of the site class, the SD simulations start yielding larger values with respect to NGA models for this particular case (Figures B.19 to B.21). The short-period spectral displacements of the simulations at rock and stiff sites are fairly in good agreement with the predictive models, for both faulting styles. At T = 1.0 sec, the residual scatters of the rock and stiff site simulations show similar trends with the soft site simulations. It is also worth mentioning that the discrepancy between the synthetics and GMPEs is more apparent for SS events.

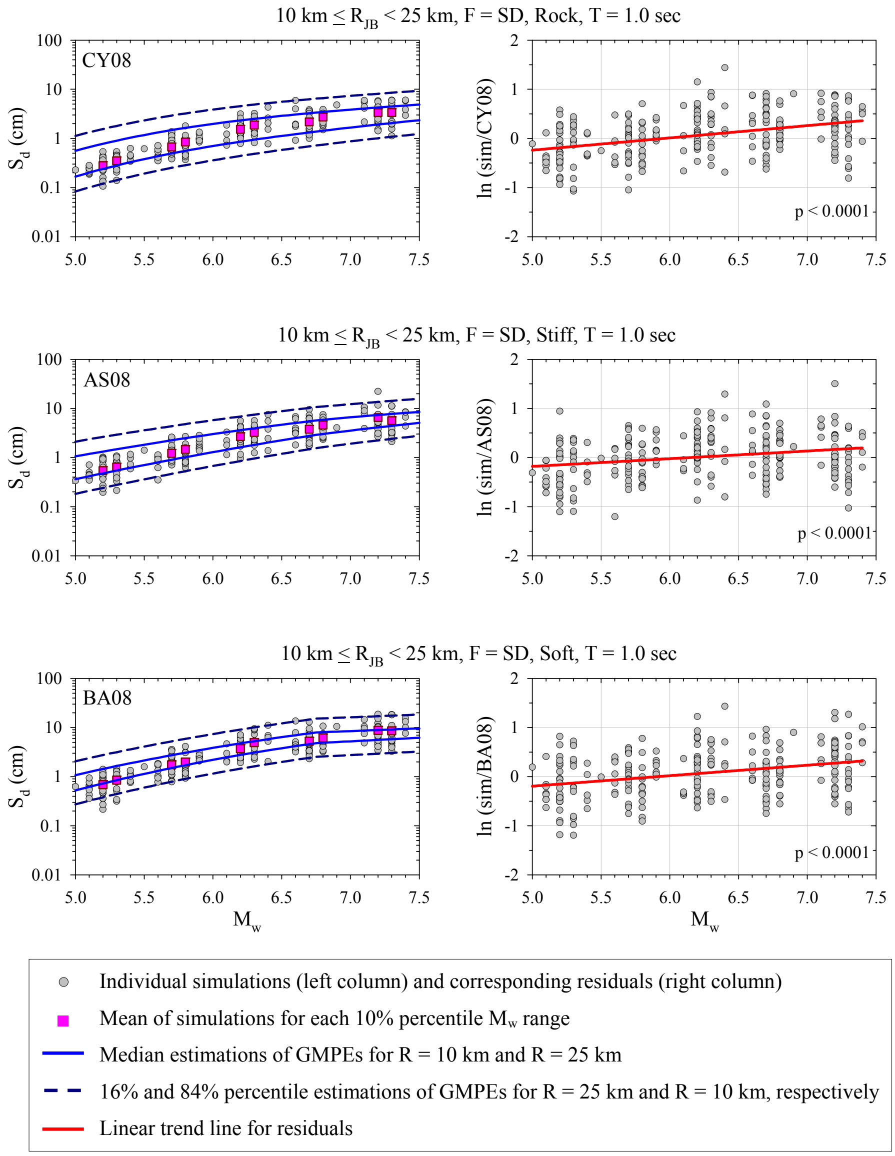

Figure 5.14 Magnitude-dependent comparisons of simulations and GMPEs in terms of S_d ($\xi = 5\%$) at T = 1.0 sec for shallow dipping (SD) faults

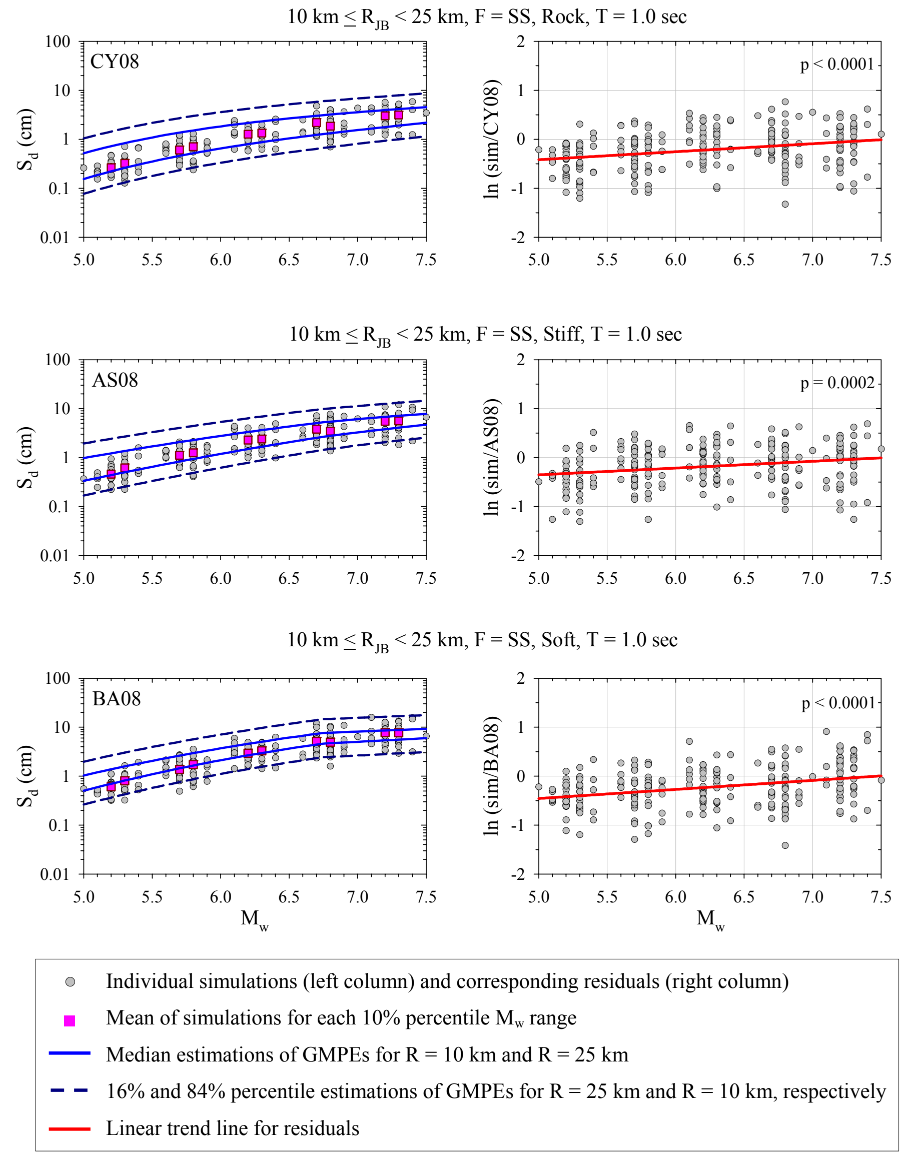

Figure 5.15 Magnitude-dependent comparisons of simulations and GMPEs in terms of S_d ($\xi = 5\%$) at T = 1.0 sec for strike-slip (SS) faults

Regardless of the site class and faulting style, the spectral displacements of simulations at T = 3.0 sec yield smaller values than the corresponding estimations of the predictive models (Figures 5.16 and 5.17). This discrepancy seems to decrease with increasing M_w. It vanishes for large magnitude SD simulations.

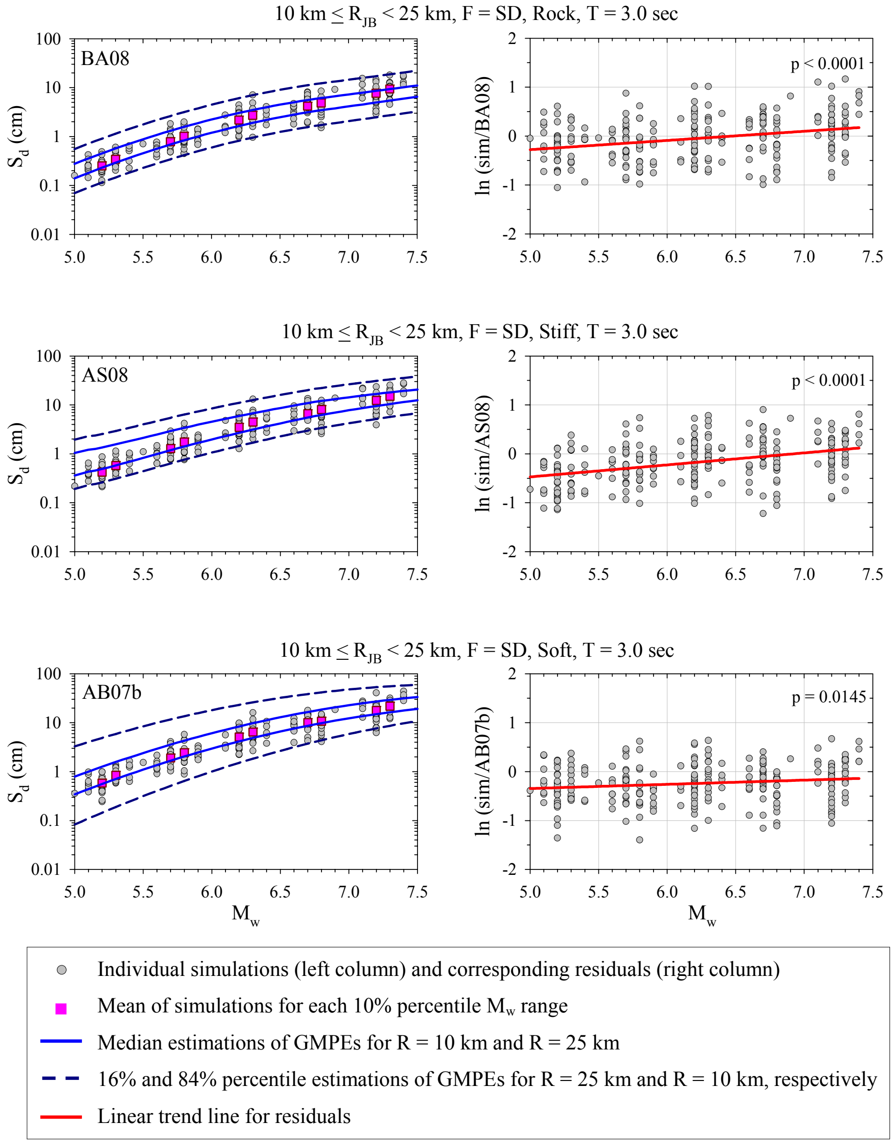

Figure 5.16 Magnitude-dependent comparisons of simulations and GMPEs in terms of S_d (ξ = 5%) at T = 3.0 sec for shallow dipping (SD) faults

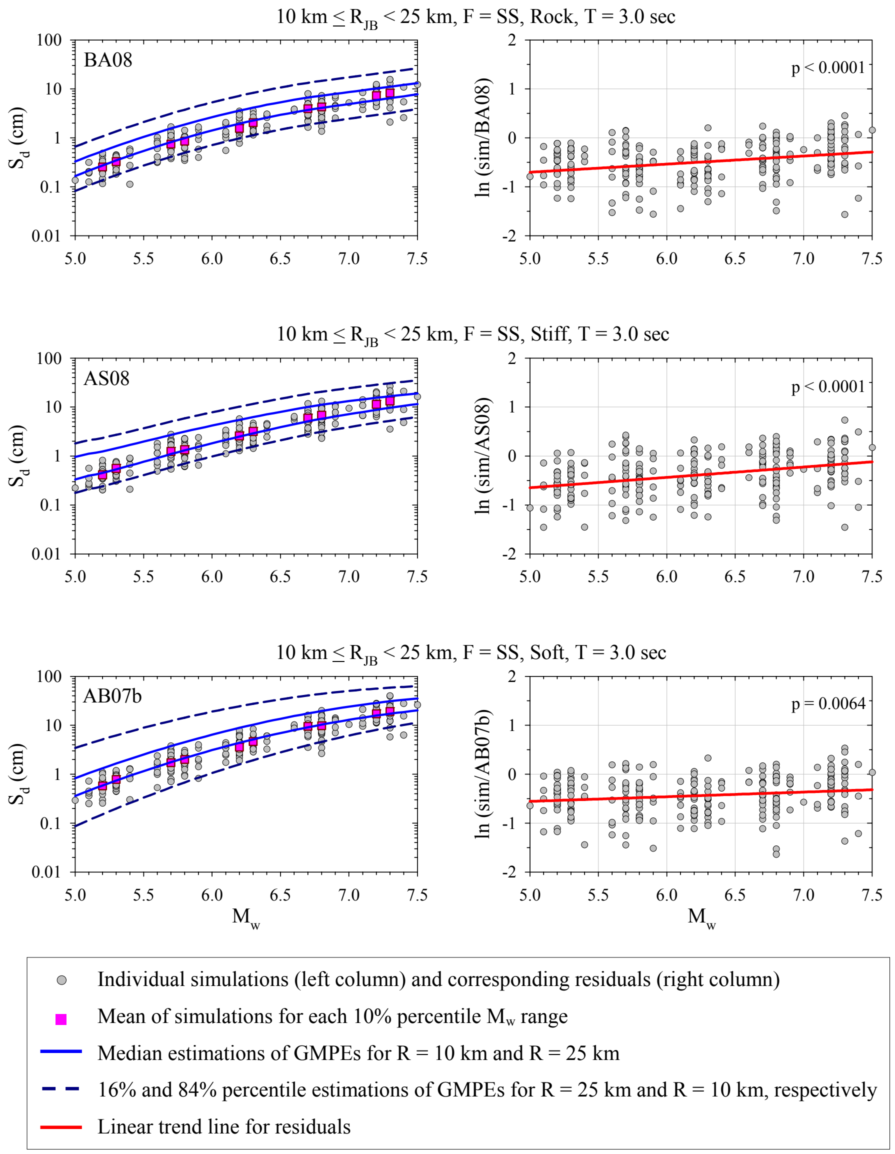

Figure 5.17 Magnitude-dependent comparisons of simulations and GMPEs in terms of S_d ($\xi = 5\%$) at T = 3.0 sec for strike-slip (SS) faults

The last two figures of this sub-section present magnitude-dependent comparative plots for the spectral displacements at T = 10.0 sec. Unlike the other spectral quantities and peak ground motion values, there are no consistent trends between the simulations and predictive model estimations for this particular spectral displacement value. Depending on the predictive model, the GMPEs tend to attain

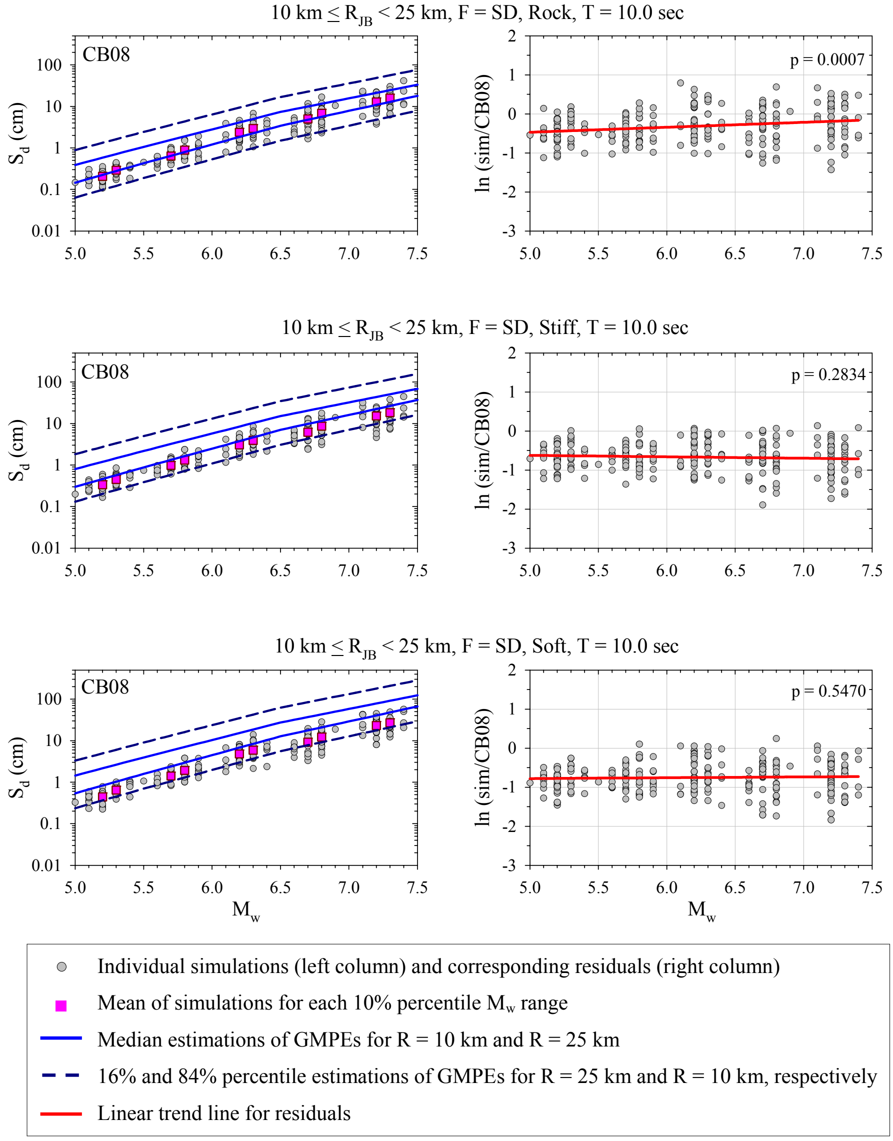

Figure 5.18 Magnitude-dependent comparisons of simulations and CB08 estimations in terms of S_d ($\xi = 5\%$) at T = 10.0 sec for shallow dipping (SD) faults

larger or smaller results than those of simulations as presented in Figures 5.18 and 5.19. Although it is not shown here, this inconsistency for different GMPEs is also valid for SS events (Figure B.34 to B.36).

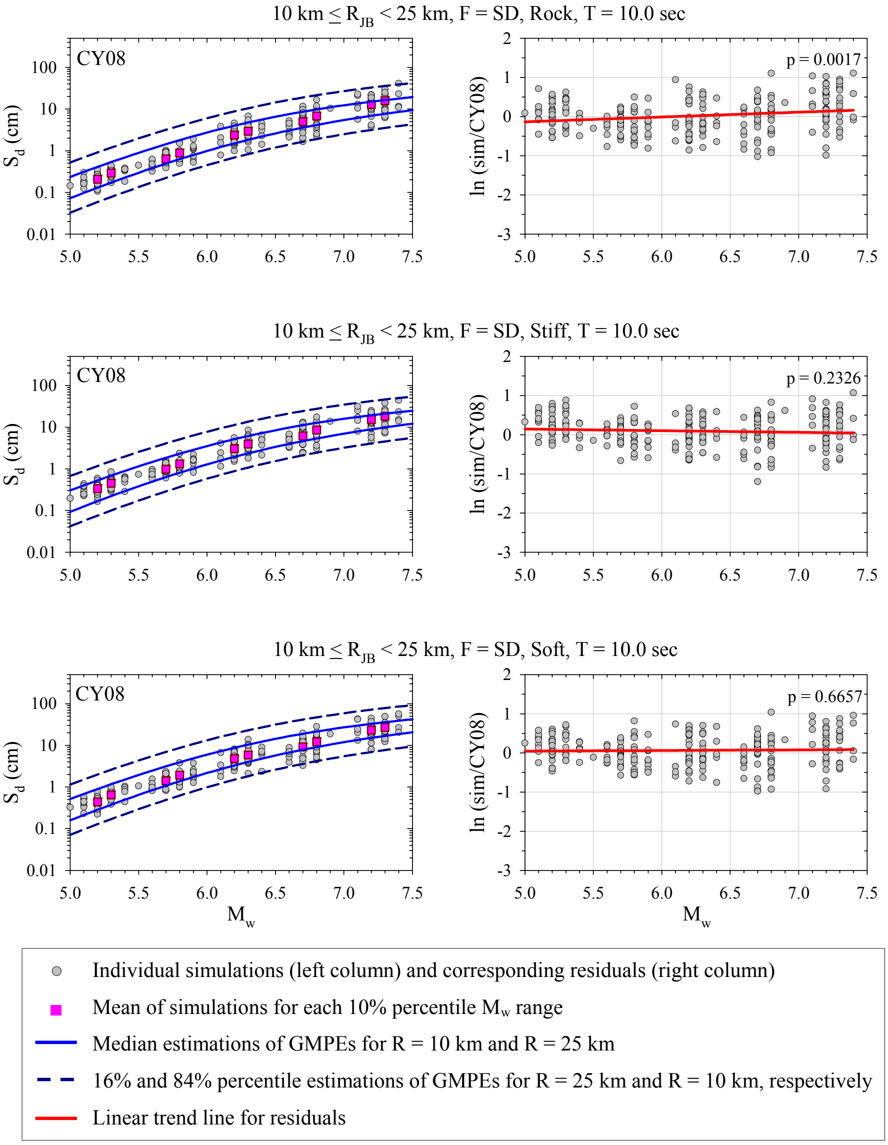

Figure 5.19 Magnitude-dependent comparisons of simulations and CY08 estimations in terms of S_d ($\xi = 5\%$) at T = 10.0 sec for shallow dipping (SD) faults

5.4.3 Assessments in Terms of Distance Influence

Similar to the plots presented in the previous sub-section, Figures 5.20 to 5.28 display the representative distance-dependent scatters of individual simulations for shallow dipping (SD) and strike-slip (SS) events at rock, stiff and soft sites and corresponding residuals for each predictive model. The magnitude range of these plots is $6.0 \leq M_w < 6.5$. For each predictive model, the corresponding reference distance metric is used (i.e. R refers to R_{JB} for AB07a, AB07b and BA08 predictive models and R_{rup} for AS08, CB08 and CY08 equations). Figures 5.20 to 5.28 portray the general remarks about the assessment of synthetics in terms of distance influence. The rest of the comparative plots between the simulations and predictive models that complete the discussions in this sub-section are presented in Appendix C.

Figures 5.20 and 5.21 display the distance-dependent comparisons in terms of PGA for SD and SS simulations, respectively. When the SD simulations of rock sites are of concern, the simulated PGA values attain large values with respect to the GMPE estimations at close-to-intermediate distances. This trend is reversed at larger distances. For stiff sites, the simulations and predictive models yield similar PGAs whereas the PGA of synthetics generated for soft sites are lower than the corresponding GMPE estimations. The increase in distance generally results in more conservative GMPE estimations for soft sites (Figure C-3). Figure 5.21 indicates that SS simulations at rock and stiff sites are fairly in good agreement with the predictive models in terms of PGA at close-to-intermediate distances. However, the soft site SS simulations result in smaller PGA values than GMPEs. The SS simulations attain larger PGAs when compared to GMPEs at far distances, regardless of the site class.

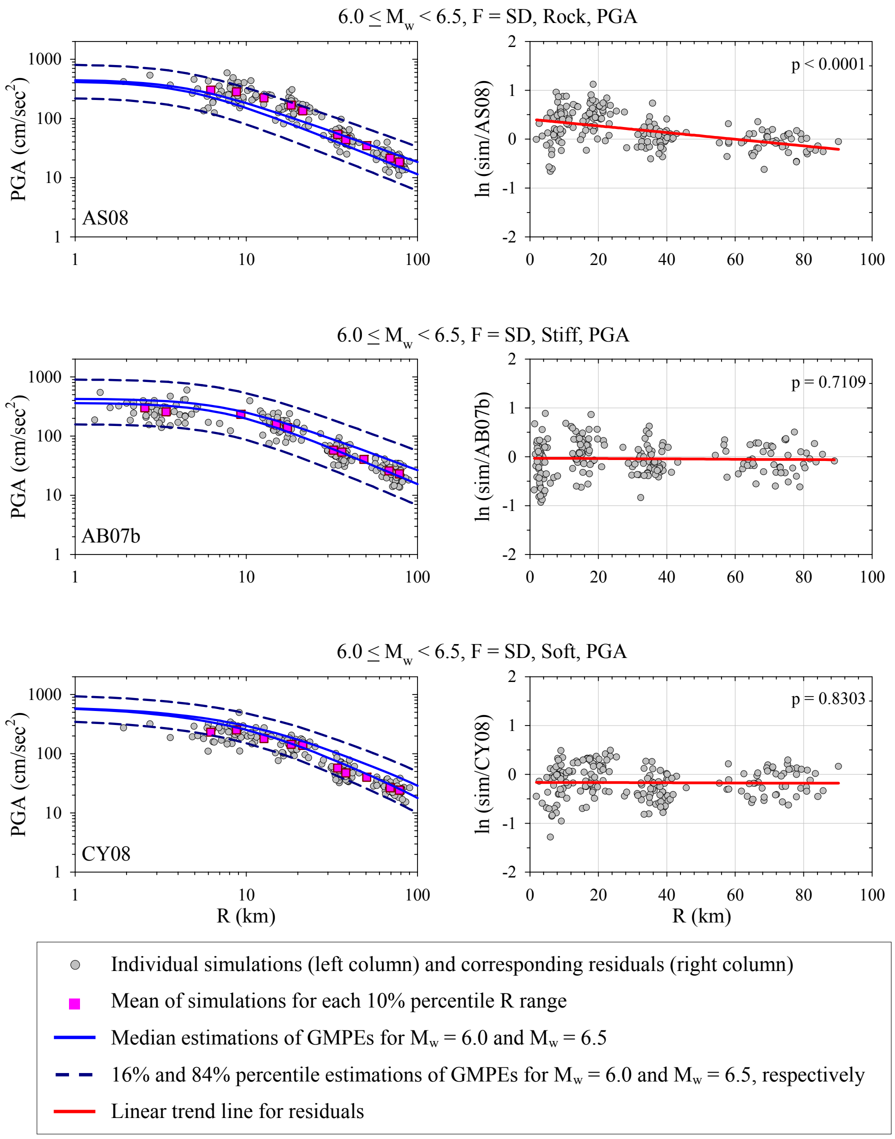

Figure 5.20 Distance-dependent comparisons of simulations and GMPEs in terms of PGA for shallow dipping (SD) faults

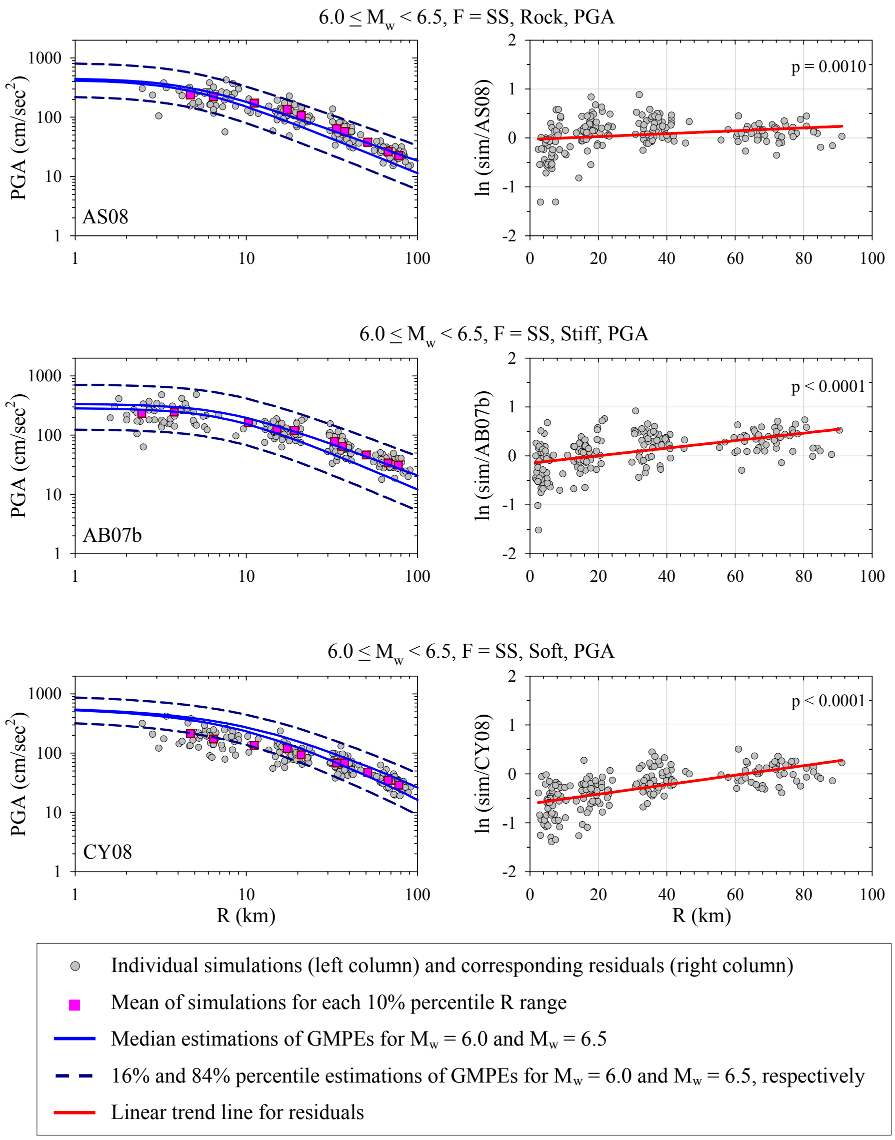

Figure 5.21 Distance-dependent comparisons of simulations and GMPEs in terms of PGA for strike-slip (SS) faults

Similar comparisons between the simulations and GMPEs in terms of PGV for SD and SS cases are shown in Figures 5.22 and 5.23, respectively. The comments made on PGA variations for the stiff and soft site SD simulations also hold for the PGV based evaluations (Figure 5.22). For rock sites, the predictive models and simulations are in good agreement at close distances. However, the increase in distance yields in conservative GMPE estimations with respect to simulated

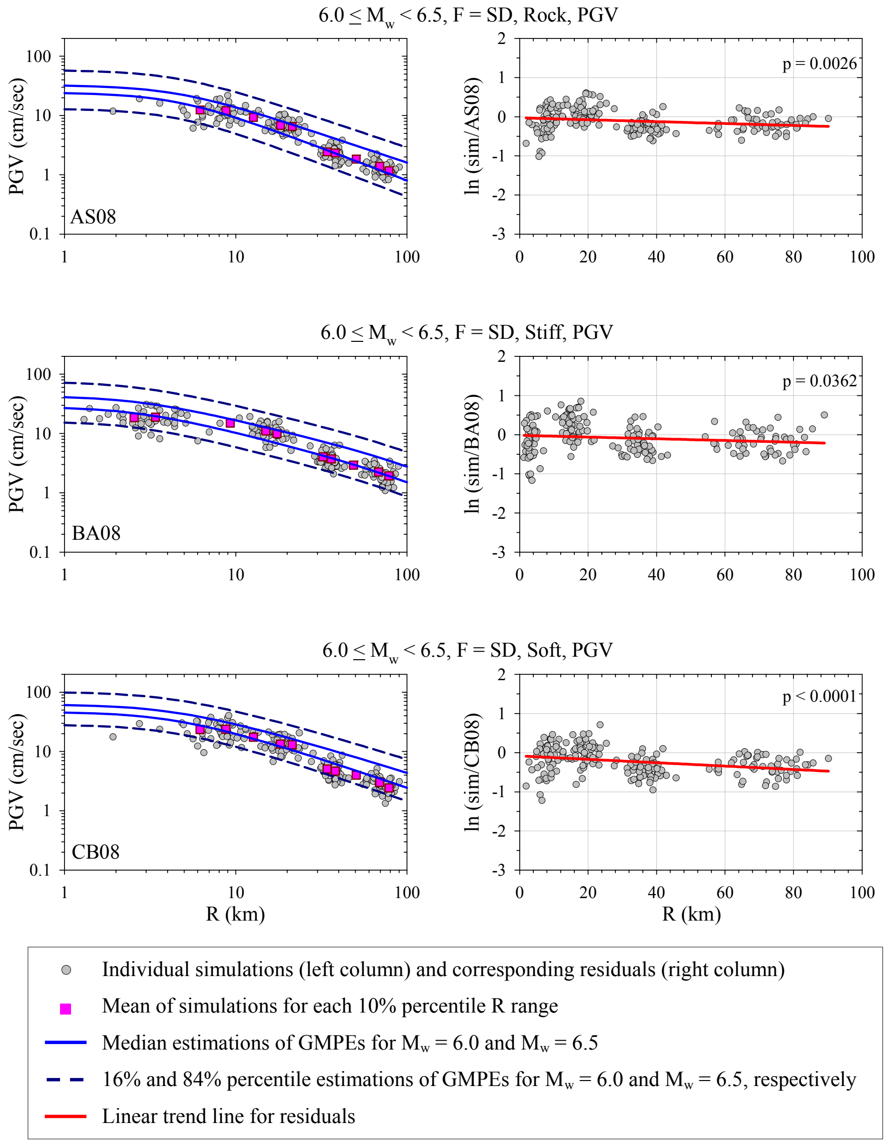

Figure 5.22 Distance-dependent comparisons of simulations and GMPEs in terms of PGV for shallow dipping (SD) faults

motions. When the SS simulations are of concern, regardless of the site class, the synthetics yield smaller PGVs than the predictive model estimations at close distances. At far distances this trend reverses and the SS simulations attain larger values than the GMPEs.

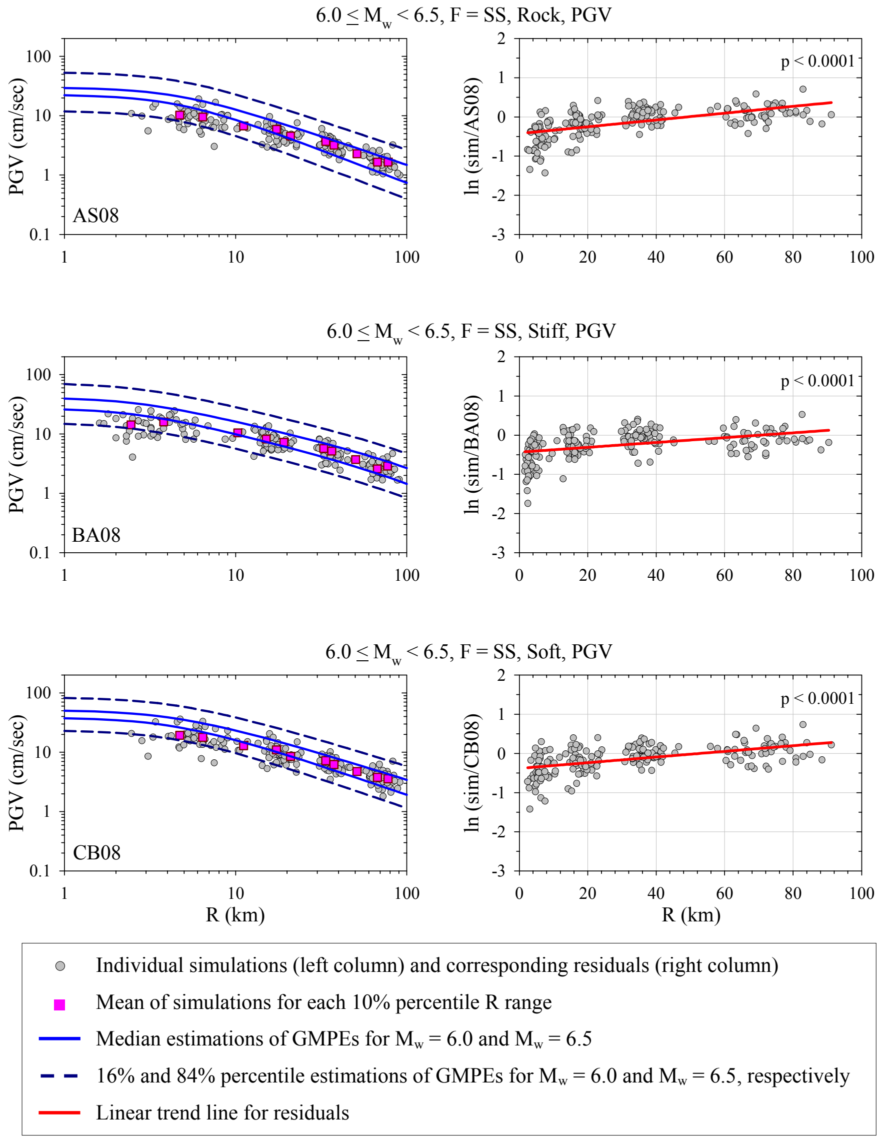

Figure 5.23 Distance-dependent comparisons of simulations and GMPEs in terms of PGV for strike-slip (SS) faults

The comparative plots shown in Figure 5.24 indicate that rock and stiff site spectral displacements of SD synthetics at T = 0.2 sec and the corresponding GMPE estimations, on average, attain similar values or the differences are rather negligible. For relatively softer site recordings, the S_d estimations at T = 0.2 sec attain larger values with respect to the spectral displacements of simulations. Similar to the discussions made for PGA and PGV, the increase in distance

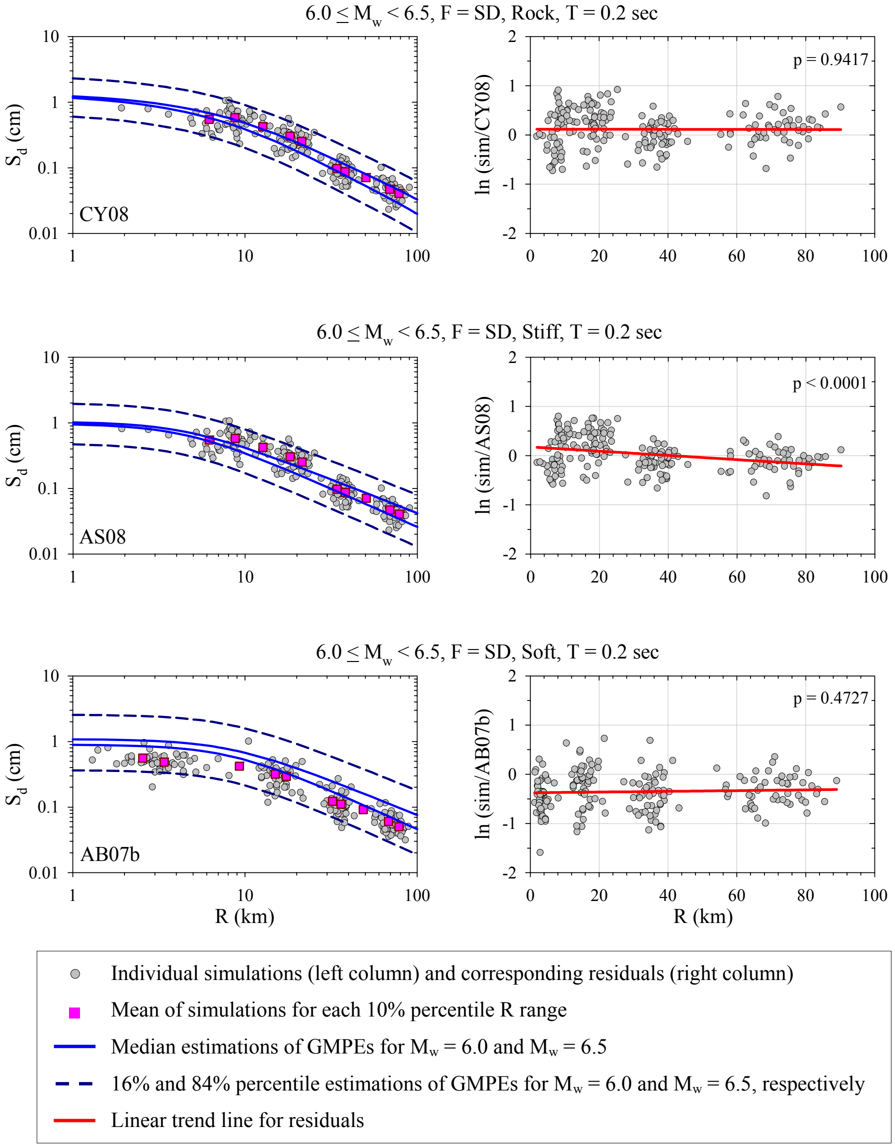

Figure 5.24 Distance-dependent comparisons of simulations and GMPEs in terms of S_d (ξ = 5%) at T = 0.2 sec for shallow dipping (SD) faults

generally results in more conservative GMPE estimations for this case as well. It is observed that the performance of the simulations shows significant variations at far distances depending on the predictive model (Figures C.13 and C.14). When the SS simulations are of concern (Figure 5.25), the residual scatters of the spectral displacements at T = 0.2 sec show significant distance dependence. At close

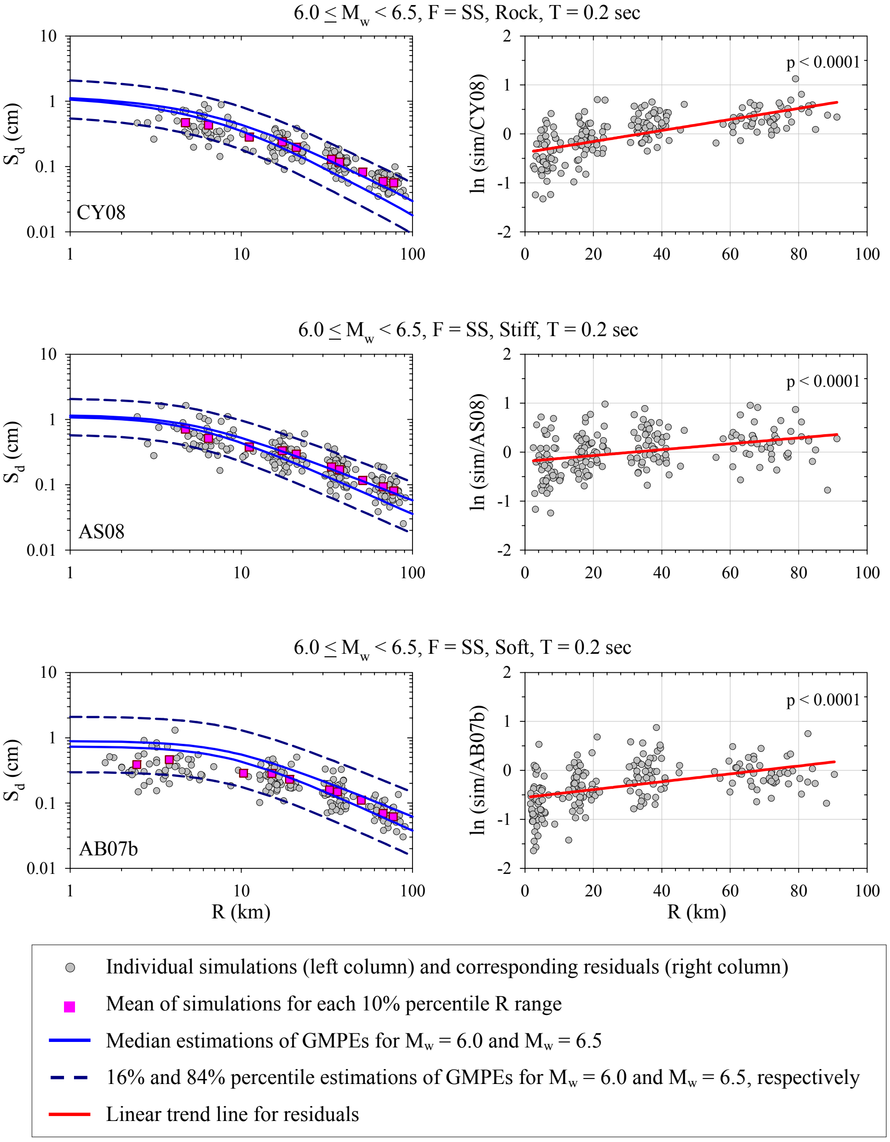

Figure 5.25 Distance-dependent comparisons of simulations and GMPEs in terms of S_d ($\xi = 5\%$) at T = 0.2 sec for strike-slip (SS) faults

distances, the SS simulations yield smaller values than the predictive models and at far distances, the synthetics attain conservative values with respect to the GMPEs. This observation is valid for all site classes.

Figures 5.26 and 5.27 describe the distance-dependent comparisons of SD simulations for spectral displacements at T = 1.0 sec and T = 3.0 sec, respectively. Regardless of the site class, the spectral displacements of T = 1.0 sec obtained from the SD synthetics and predictive models are similar to each other at close distances. This situation changes for the spectral displacements at T = 3.0 sec. The estimations from GMPEs take larger values with respect to the corresponding spectral displacements of ground-motion simulations. With the increasing distance, the GMPE estimations tend to be larger than the ground-motion simulations for the S_d at T = 1.0 sec case (see Figures C.19 to C.21). For the medium-period response quantity (i.e. S_d at T = 3.0 sec), the increase in distance results in decreasing discrepancy between the predictive model estimations and ground-motion simulations.

When the close distance SS simulations are considered, regardless of the site class, the estimations of the predictive models are more conservative than those of the simulations for spectral ordinates at T = 1.0 sec (Figures C.22 to C.24) and T = 3.0 sec (Figures C.28 to C.30). The spectral quantities of synthetics tend to attain closer values (or in some cases larger values) to those of GMPE estimations with the increased distance (i.e. for distances mostly larger than 50 km).

The last comparative plots between the simulations and GMPE estimations for SD events are presented in Figure 5.28 for spectral displacements at T = 10.0 sec. The residual scatters suggest that at close distances, the S_d estimations from the predictive models are larger than the spectral displacements computed from the simulated ground motions. This observation does not depend on the variations in site classes. Depending on the predictive model, the increase in distance either results in conservative GMPE estimations with respect to synthetics or decreases the discrepancy between the GMPE estimations and simulations. These interpretations are also valid for SS simulations as presented in Figures C.34 to C.36.

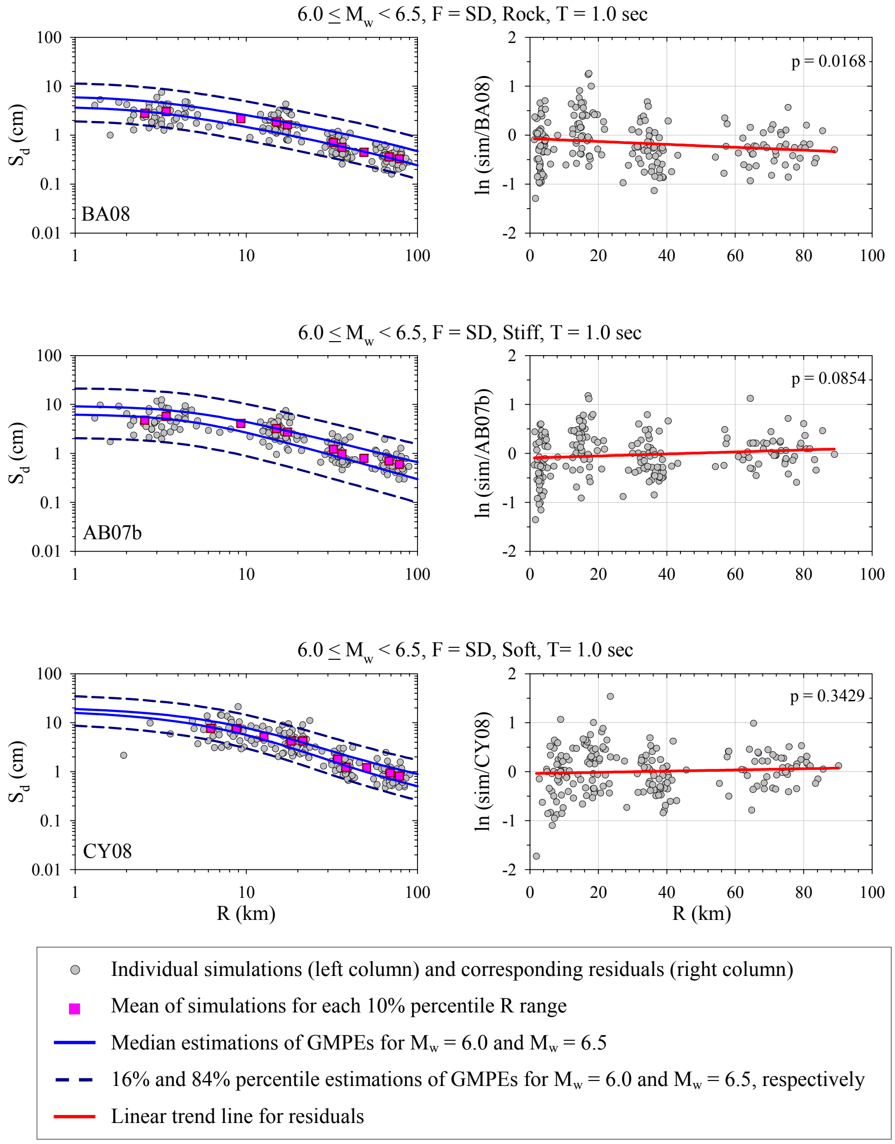

Figure 5.26 Distance-dependent comparisons of simulations and GMPEs in terms of S_d ($\xi = 5\%$) at T = 1.0 sec for shallow dipping (SD) faults

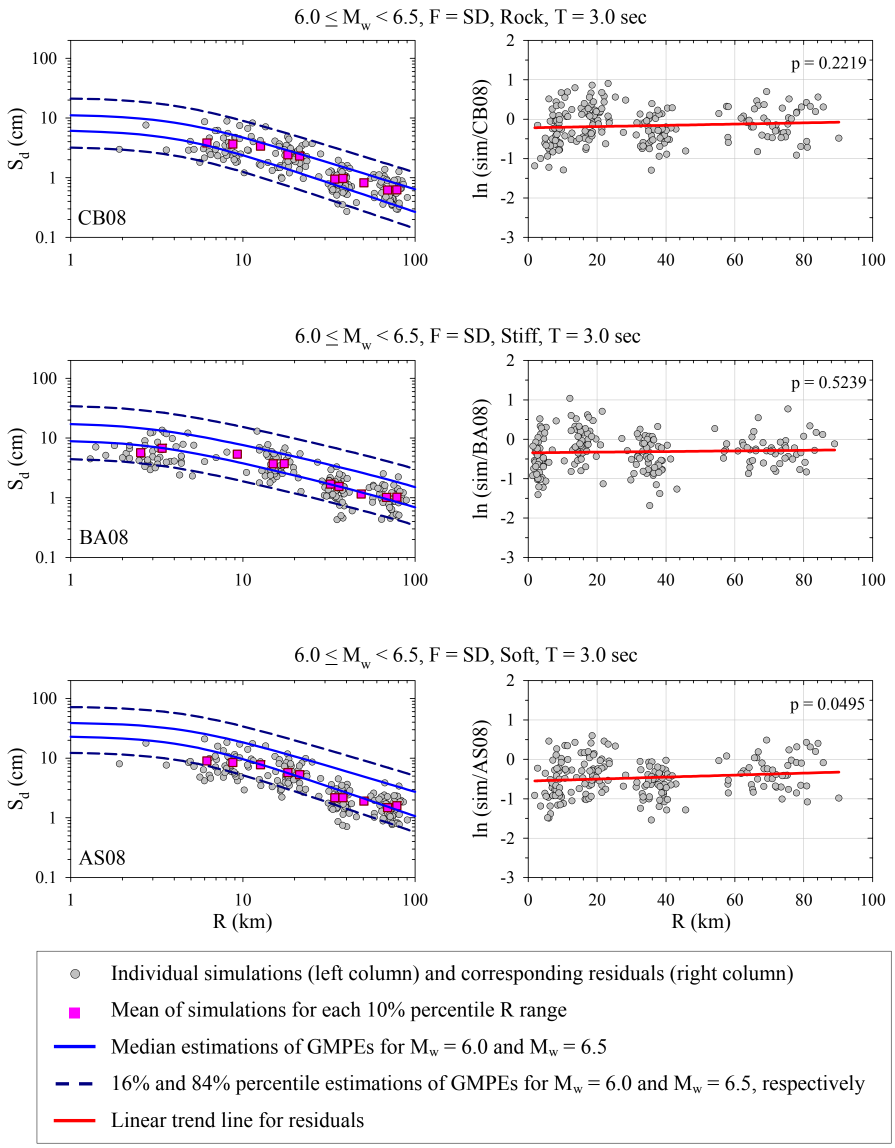

Figure 5.27 Distance-dependent comparisons of simulations and GMPEs in terms of S_d ($\xi = 5\%$) at T = 3.0 sec for shallow dipping (SD) faults

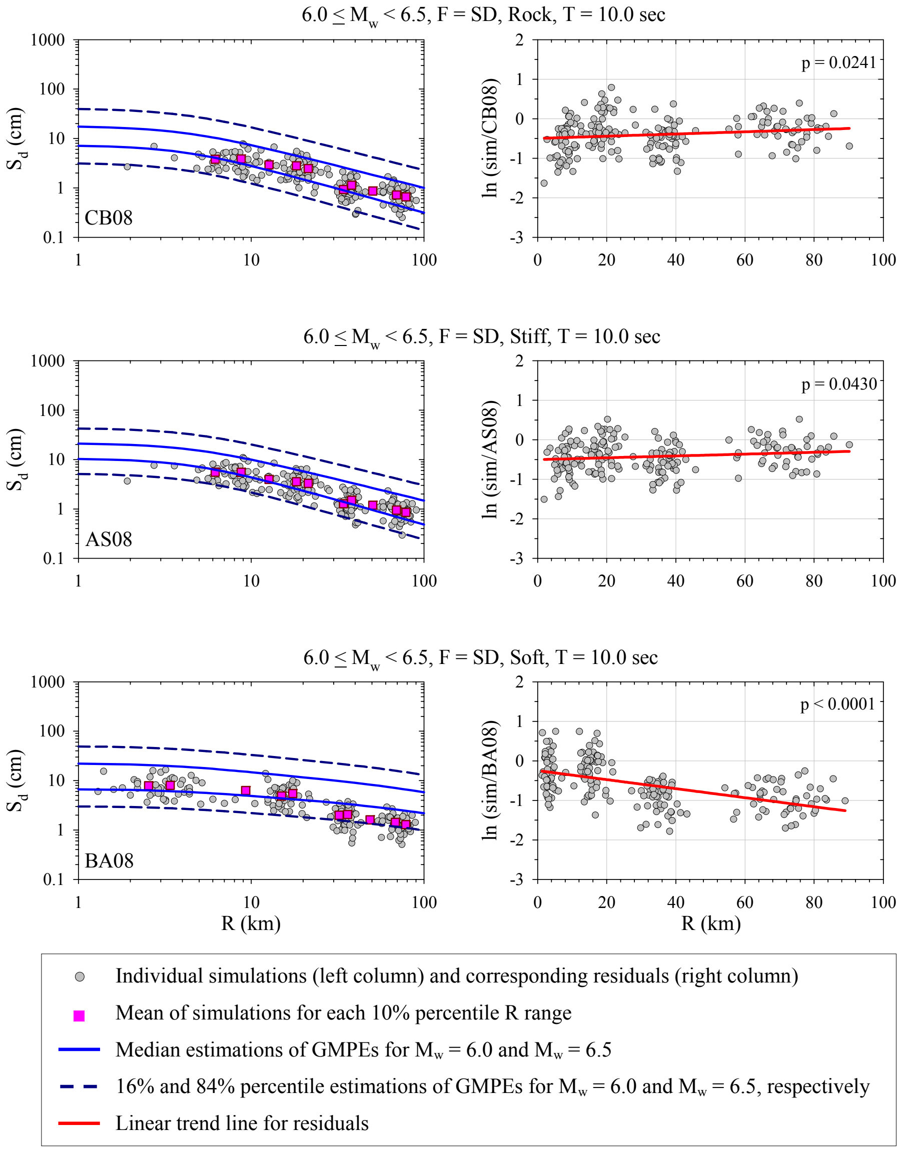

Figure 5.28 Distance-dependent comparisons of simulations and GMPEs in terms of S_d ($\xi = 5\%$) at T = 10.0 sec for shallow dipping (SD) faults

5.5 Summary of the Observations

Tables 5.1 and 5.2 summarize the general evaluations made on the performance of synthetics with respect to the predictive models considered in this study. Table 5.1 briefs the magnitude-dependent performance of synthetics whose details are presented in section 5.42. In a similar manner, Table 5.2 summarizes the distance-dependent evaluations that are discussed broadly in section 5.4.3.

Tables 5.1 and 5.2 indicate that the SD simulations at stiff and rock sites are generally in good agreement with the GMPEs. However, SS simulations at rock and stiff sites generally attain smaller values with respect to GMPE estimations for small magnitude events and close distances. For SS faulting style, the increase in magnitude results in a decrease in the discrepancy between simulations and GMPE. The increase in distance yields larger amplitude simulations than the predictive models.

In case of soft site simulations, the synthetics attain smaller values than GMPEs for small magnitude events and close distances. This observation holds for both faulting styles. For large magnitudes, soft site simulations yield similar or relatively smaller values than the predictive models for SD and SS events (Table 5.1). The increase in distance yields the soft site simulations to attain larger values than the predictive models for SS faulting (Table 5.2). The observed discrepancy between simulations and GMPEs at close distances could be due to the limitations of the point-source approximation at this distance range.

Table 5.1 Summary of magnitude-dependent evaluation of the simulated ground-motions with respect to the predictive models

Site	Shallow Dipping Fault		Strike-Slip Fault	
Class	Small Magnitude	Large Magnitude	Small Magnitude	Large Magnitude
Soft	Smaller(6)	Fairly Good(6)	Smaller(6)	Smaller(6,7)
Stiff	Fairly Good(6)	Fairly Good(6)	Smaller(6)	Smaller(6,7)
Rock	Fairly Good(6)	Fairly Good(6)	Smaller(6)	Smaller(6,7)

---

(6) "Smaller" term denotes the synthetics attain smaller values than the GMPE estimations. The term "Fairly Good" indicates that the synthetics and GMPEs agree with each other whereas "Larger" describes larger values of synthetics with respect to GMPE estimations.

(7) Discrepancy between simulations and GMPEs decreases with increasing magnitude.

Table 5.2 Summary of distance-dependent evaluation of the simulated ground-motions with respect to the predictive models

Site	Shallow Dipping Fault		Strike-Slip Fault	
Class	Close Distance	Far Distance	Close Distance	Far Distance
Soft	Smaller	Smaller	Smaller	Larger
Stiff	Fairly Good	Fairly Good	Smaller	Larger
Rock	Fairly Good	Fairly Good	Smaller	Larger

To quantify the performance of simulations with respect to GMPEs, the mean S_d obtained from synthetics are compared with ±20% range of the envelope of predictive models (Figures 5.29 to 5.32). The comparisons are made in terms of SD (left column) and SS (right column) events at rock (top row), stiff (middle row) and soft sites (bottom row) for small ($5.0 \leq M_w < 5.5$) and large ($7.0 \leq M_w \leq 7.5$) magnitude bins. The comparative plots suggest that the simulations are, in general, within ±20% range of GMPE estimations.

5.6 Studies on Improvement of Simulations

As discussed in sections 5.4.1 and 5.4.2, the discrepancy between the simulations and predictive models can be attributed to many parameters including the modeling differences between the GMPEs and synthetics as well as the magnitude distributions of the datasets used during the derivation of GMPEs. The distance-dependent differences between the GMPEs and synthetics that are presented in section 5.4.3 guided this study to use another distance metric for the simulation of soft site motions.

Recall that Scherbaum et al. (2006) performed simulations for generic stiff to rock sites ($V_{S,30}$ = 620 m/sec) and evaluated their results with various GMPEs for a number of distance metrics. They showed that the use of hypocentral distance (R_{hyp}) for the simulation of ground motions provides the lowest-misfit stochastic

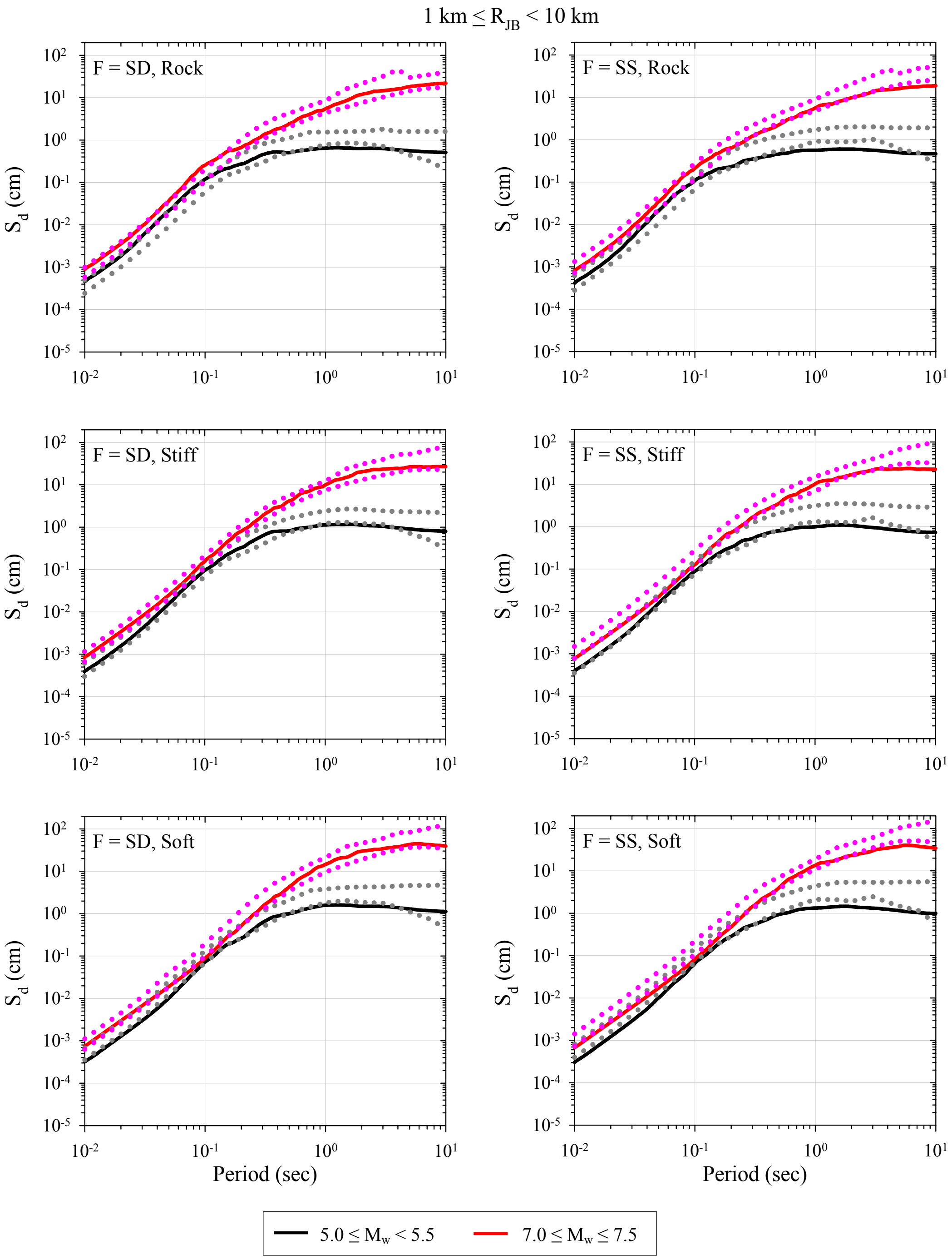

Figure 5.29 Comparison of simulations (solid lines) with ±20% range of the envelope of GMPE estimations (dotted lines) in terms of mean S_d ($\xi = 5\%$). The distance range is 1 km ≤ R_{JB} < 10 km.

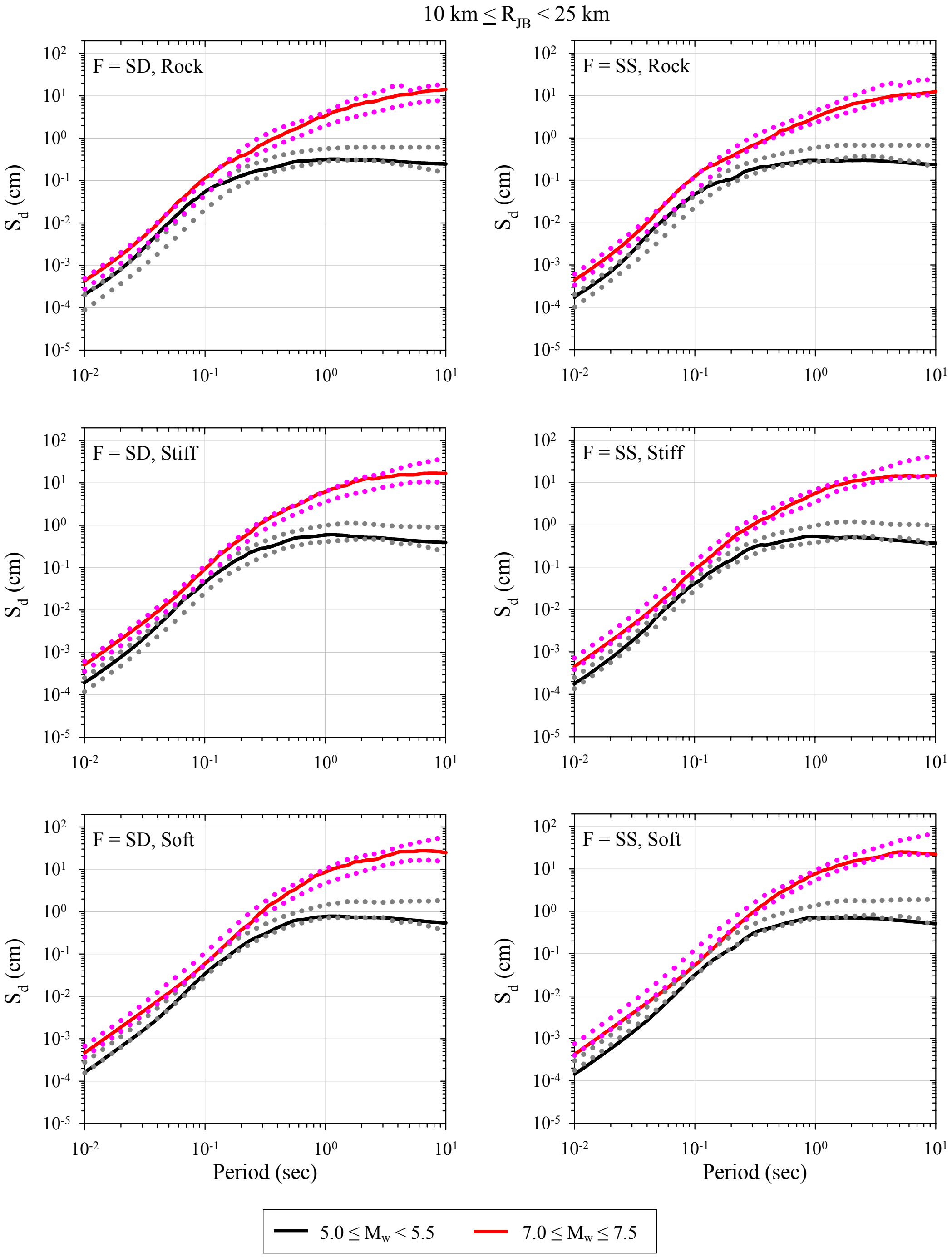

Figure 5.30 Comparison of simulations (solid lines) with ±20% range of the envelope of GMPE estimations (dotted lines) in terms of mean S_d ($\xi = 5\%$). The distance range is 10 km ≤ R_{JB} < 25 km.

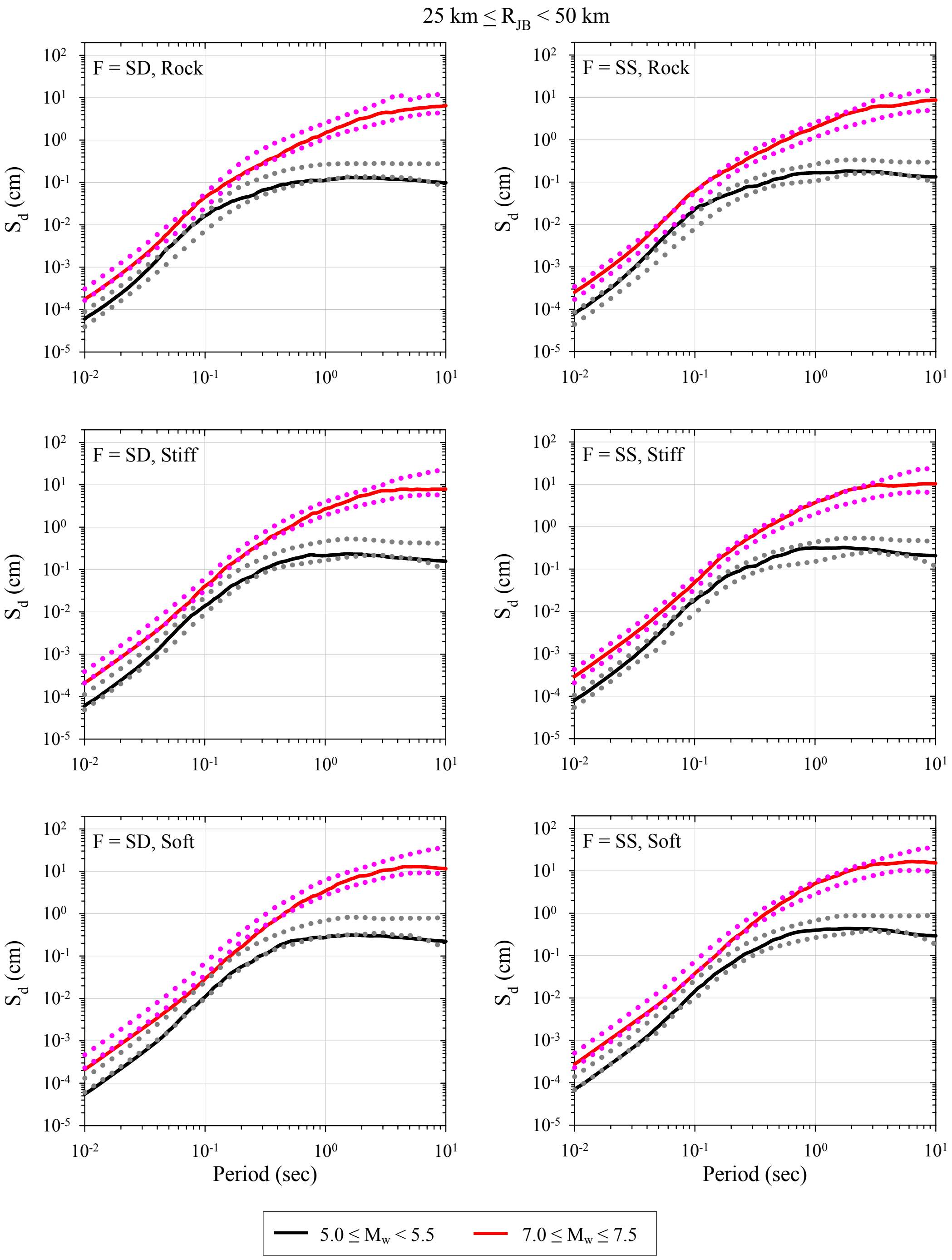

Figure 5.31 Comparison of simulations (solid lines) with ±20% range of the envelope of GMPE estimations (dotted lines) in terms of mean S_d ($\xi = 5\%$). The distance range is 25 km ≤ R_{JB} < 50 km.

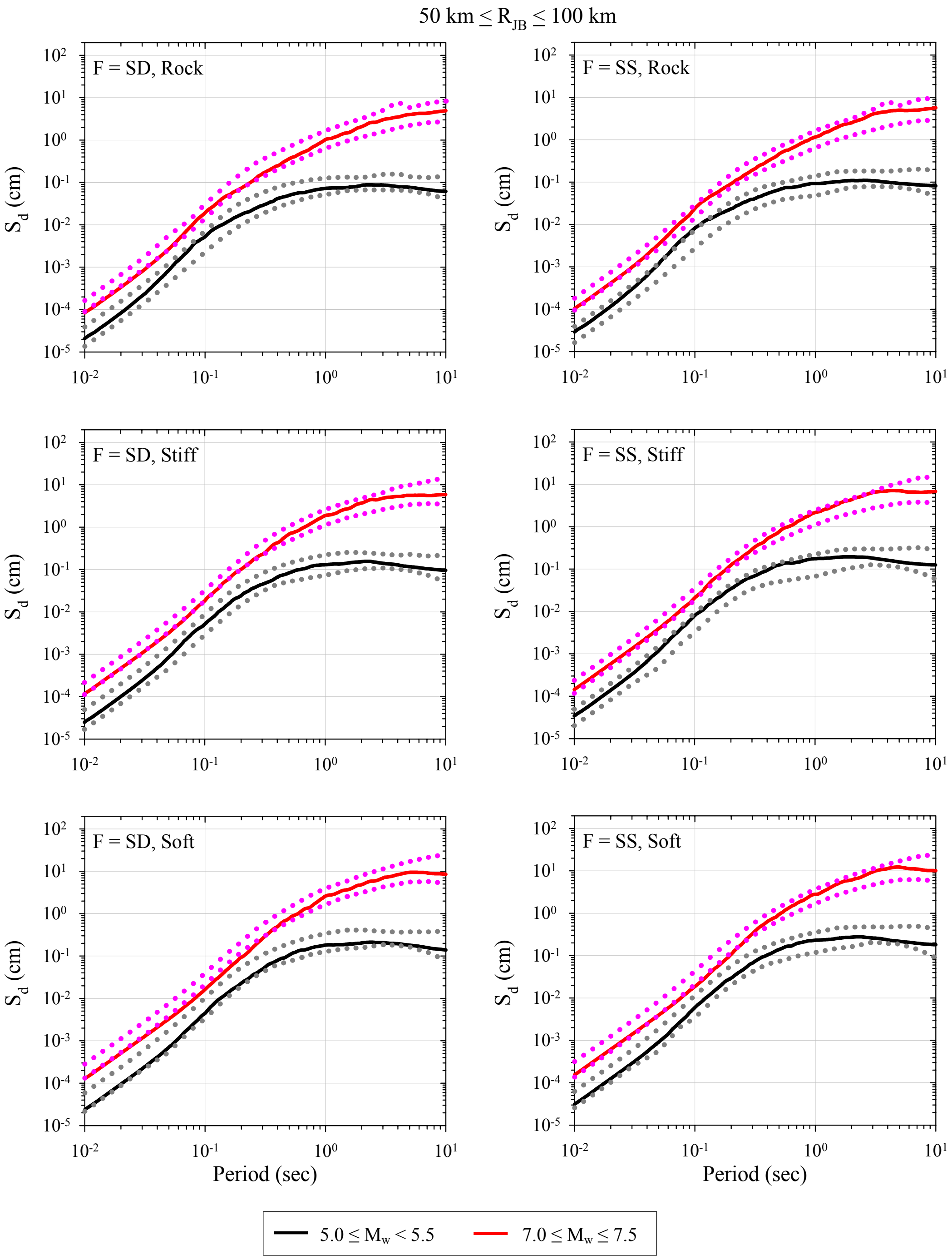

Figure 5.32 Comparison of simulations (solid lines) with ±20% range of the envelope of GMPE estimations (dotted lines) in terms of mean S_d ($\xi = 5\%$). The distance range is 50 km ≤ R_{JB} < 100 km.

models for most of the empirical attenuation equations. However, the influence of faulting style and site class on the quality of fit was not taken into account by Scherbaum et al. (2006).

In this study, R_{hyp} is used as the reference distance metric for the simulation of VHR motions based on the recommendations made by Scherbaum et al. (2006). As indicated by Scherbaum et al. (2006), the rock and stiff site simulations for SD events match fairly well with the GMPEs. On the other hand, for the certain cases dictated above, the synthetics attain smaller ground motions than the predictive models considered in this study.

Using these observations, the VHR simulations are repeated by using R_{rup} as the reference distance metric to investigate the possible improvements of the performance of the simulations. Figures 5.33 to 5.35 compare the distance-dependent residuals obtained from the synthetics that are generated by using R_{hyp} (left column) and R_{rup} (right column). The figures present the residual scatters for SD and SS simulations at soft sites. Similar to the evaluations in the section 5.4.3, the magnitude range for the comparative plots is taken as $6.0 \leq M_w < 6.5$. Although, the discussions in this sub-section are confined to Figures 5.33 to 5.35, they describe the most general observations. Other relevant figures related to the discussions of this sub-section are presented in Appendix D.

Figures 5.33 to 5.35 indicate that the use of R_{rup} in the simulation of ground motions considerably improves the residuals, at close-to-intermediate distances for both SS and SD simulations at soft sites. However, the residuals for far distance simulations do not show improvement because both distance metrics attain nearly the same values at far distances. The improvements presented in the simulations will be reduced at small magnitude events since R_{hyp} and R_{rup} are almost equal to each other for these cases.

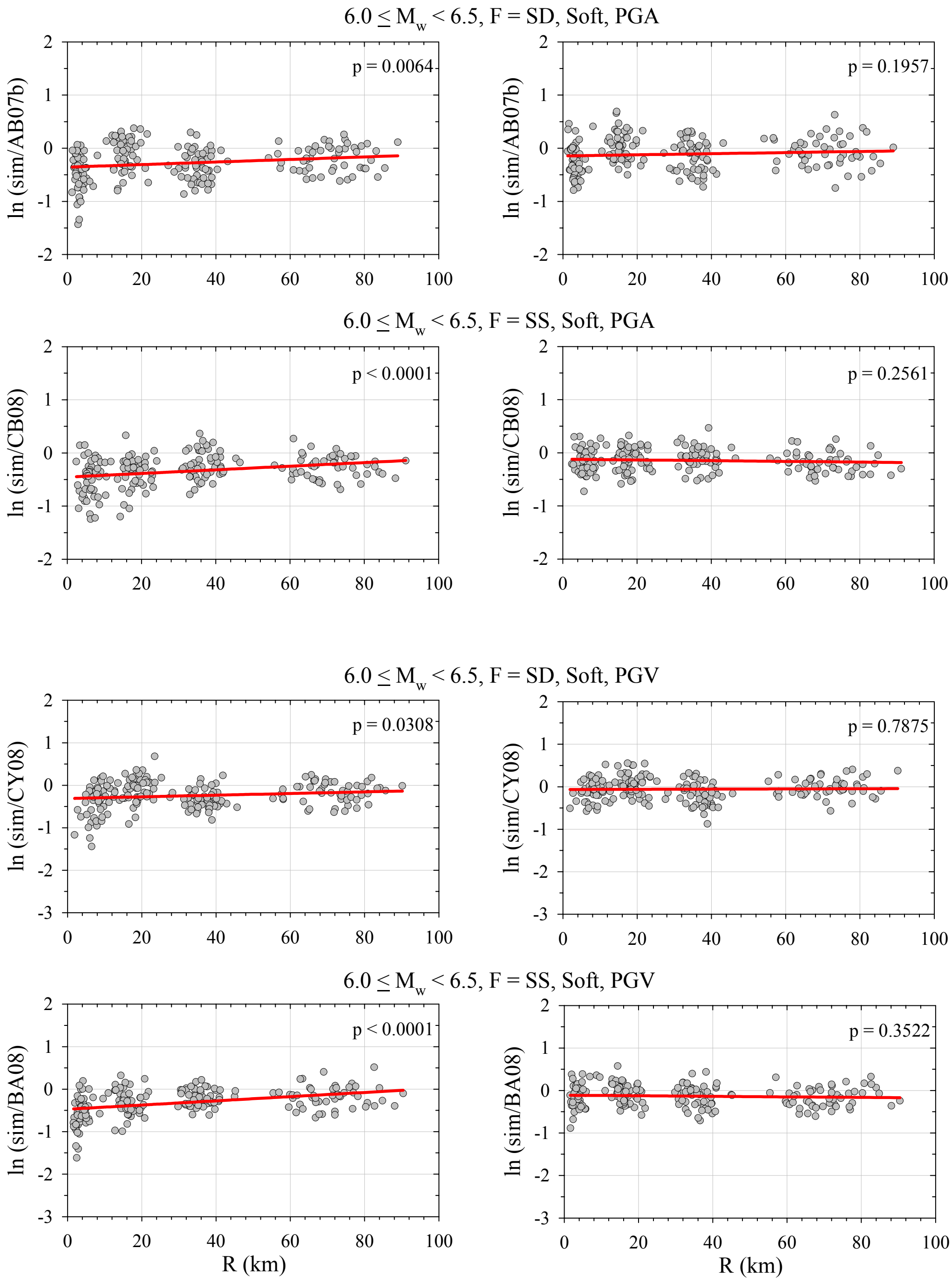

Figure 5.33 Distance-dependent comparisons of PGA and PGV residuals obtained from synthetic ground motions generated by using R_{hyp} (left column) and R_{rup} (right column)

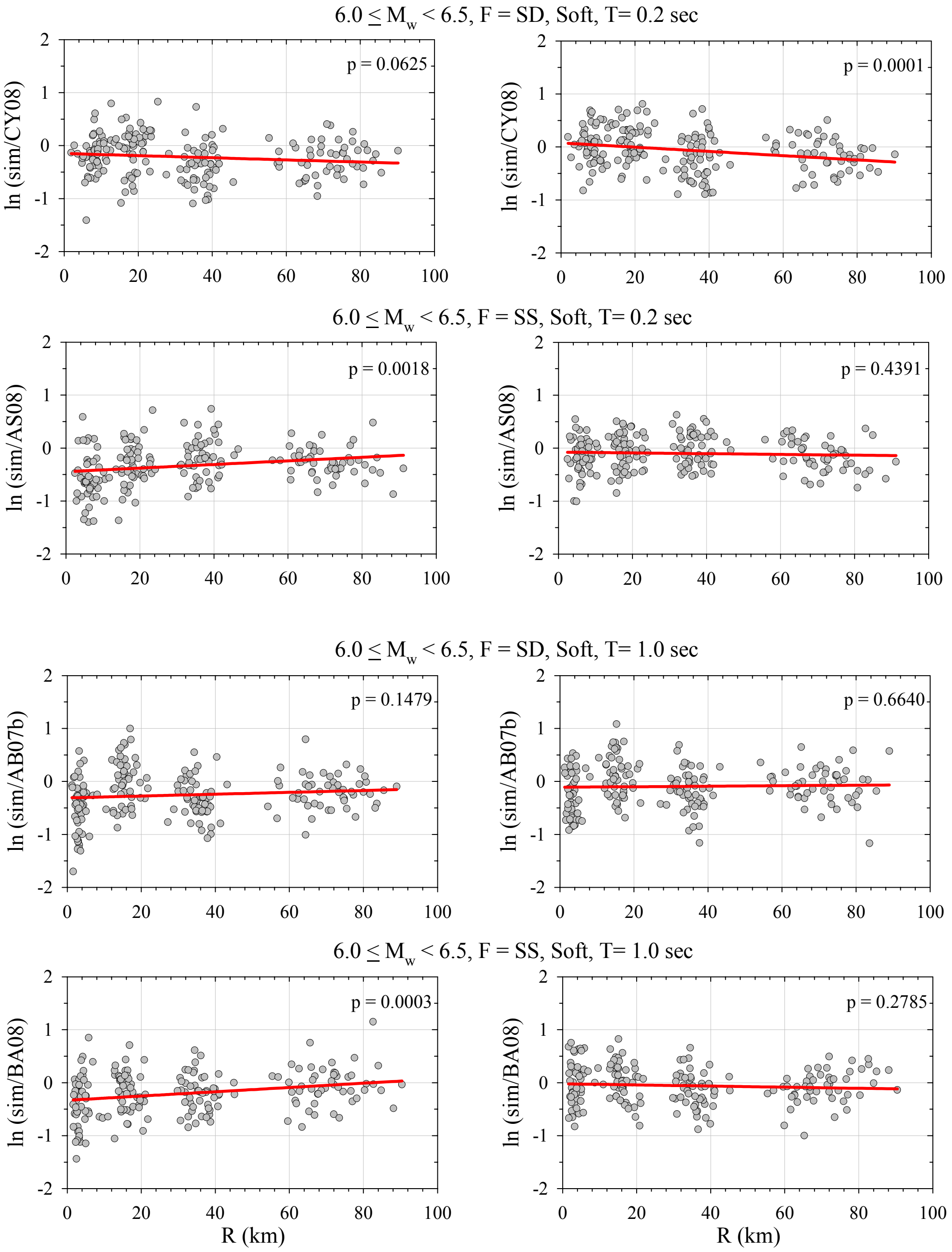

Figure 5.34 Distance-dependent comparisons of residuals for S_d ($\xi = 5\%$) at T = 0.2 sec and T = 1.0 sec obtained from synthetic ground motions generated by using R_{hyp} (left column) and R_{rup} (right column)

$6.0 \le M_w < 6.5$, F = SD, Soft, T= 3.0 sec

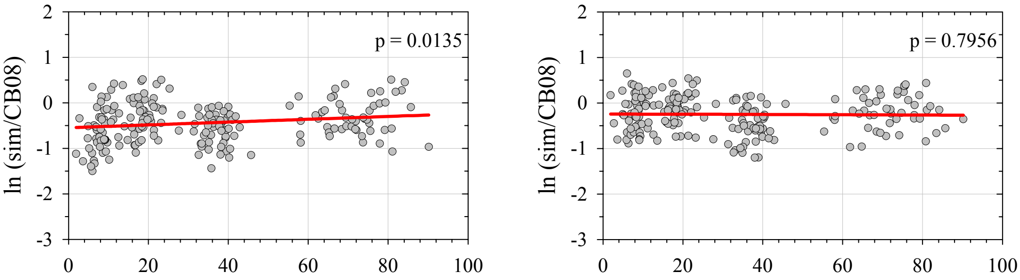

$6.0 \le M_w < 6.5$, F = SS, Soft, T= 3.0 sec

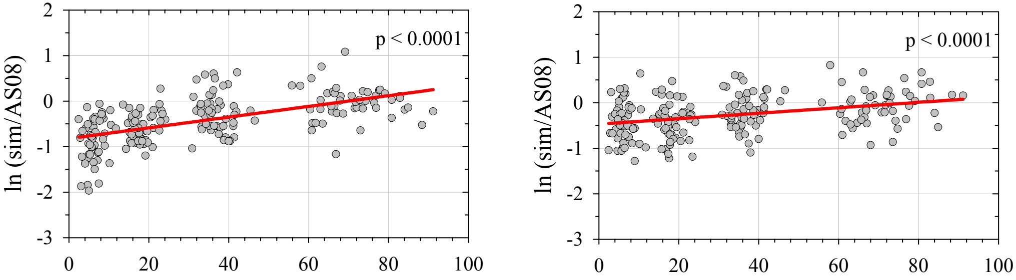

$6.0 \le M_w < 6.5$, F = SD, Soft, T= 10.0 sec

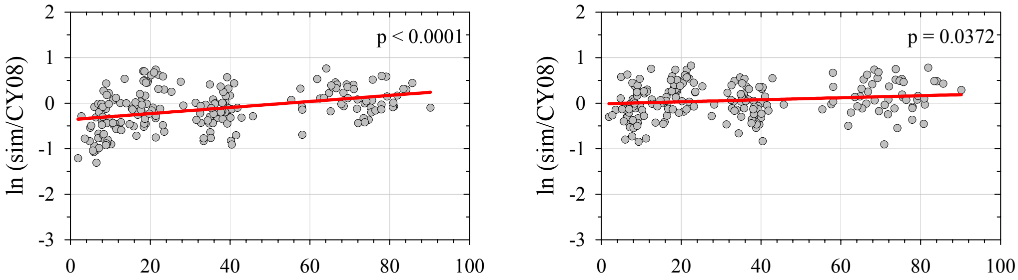

$6.0 \le M_w < 6.5$, F = SS, Soft, T= 10.0 sec

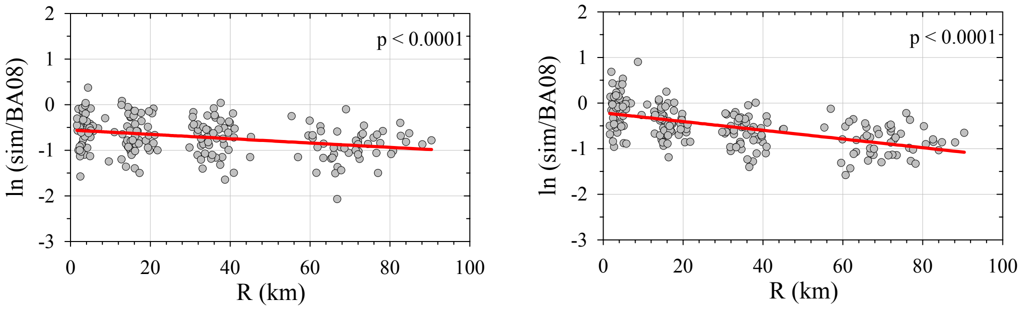

Figure 5.35 Distance-dependent comparisons of residuals for S_d ($\xi = 5\%$) at T = 3.0 sec and T = 10.0 sec obtained from synthetic ground motions generated by using R_{hyp} (left column) and R_{rup} (right column)

CHAPTER 6

SUMMARY AND CONCLUSIONS

6.1 Summary

In this study, the limitations of stochastic point-source stationary ground motion simulations are investigated in terms of magnitude, distance, faulting style and site class influences. Within this context, synthetic acceleration time series are generated for various magnitude ($5.0 \leq M_w \leq 7.5$), distance (1 km $\leq R_{JB} \leq 100$ km), faulting style (shallow dipping and strike-slip) and site class (soft, stiff and rock) bins. The ground motions are simulated from randomly generated seismological parameters (i.e. magnitude and distance values) using the Monte Carlo simulation technique.

The simulation process is divided into two main stages. Firstly, accelerograms at outcropping very hard rock (VHR) sites are simulated based on the stochastic method proposed by Boore (1983, 2003). The randomly generated magnitude and distance values described above are used for VHR simulations. A total of 2000 ground motions are generated at outcropping VHR sites for magnitude $5.0 \leq M_w \leq 7.5$ and distance 1 km $\leq R_{JB} \leq 100$ km ranges, for shallow dipping and strike-slip events. The double-corner point-source spectrum proposed by Atkinson and Silva (2000) is used for these synthetics that is attenuated by the empirical travel-path attenuation functions derived by Raoof et al. (1999) and amplified by the site amplification factors for VHR sites presented by Boore and Joyner (1997).

In the second stage of simulation process, the stochastically simulated outcropping VHR motions are modified by performing site response analyses to generate the free-field motions at soft, stiff and rock sites. The site response analyses are carried out via ProShake v1.12 software (2007) that makes use of 1-D equivalent linear analysis method. Soil profiles are randomly generated based on the statistical evaluation of the datasets compiled from the USGS, Turkish NSMP and NGA databases. Within this context, the depth-dependent probabilistic S-wave slowness models for soft, stiff and rock sites are derived using the statistics obtained from the complied actual soil profiles. A total of 6000 (= 2000 x 3) free-field surface motions are generated at soft, stiff and rock sites.

The final synthetic ground motions are compared with another set of simulations generated by a non-stationary procedure proposed by Pousse et al. (2006) to identify the differences between the stationary (this study) and non-stationary stochastic simulation approaches. To determine the performance of the simulation procedure, the synthetics are assessed for several recently developed GMPEs: Akkar and Bommer (2007a; 2007b), AB07a and AB07b, Abrahamson and Silva (2008), AS08, Boore and Atkinson (2008), BA08, Campbell and Bozorgnia (2008), CB08, and Chiou and Youngs (2008), CY08. The performance of the simulations are assessed with respect to the GMPEs in terms of magnitude, distance, faulting style and site class influence for PGA, PGV and 5% damped spectral displacements.

6.2 Conclusions

The main conclusions drawn from the study are listed below:

(i) The comparisons of randomly generated distance values for R_{JB}, R_{hyp} and R_{rup} indicate that the distance metric conversion procedure proposed by Scherbaum et al. (2004) yields physically rational variations.

(ii) The evaluation of the proposed depth-dependent slowness models suggests that estimations computed from the proposed models are fairly unbaised and they are able to capture the variation of actual S-wave slowness.

(iii) The preliminary analyses on the dynamic modulus reduction and damping ratio curves proposed by Ishibashi and Zhang (1993) show that for relatively small cyclic shear strains, they result in unrealistic values (i.e. $G/G_{max} > 1.0$ and $\xi < 0$) at high confining pressures. Thus, for such cases, the proposed curves need to be modified as demonstrated in Chapter 4.

(iv) The evaluation of final simulations in terms of ground displacements indicates that small to moderate magnitude synthetics at soft and stiff sites show unphysical linear trends. The Fourier amplitude spectra (FAS) comparisons show that for small magnitude events, the soft site simulations are contaminated by long-period noise at frequencies lower than 0.05 Hz. It is observed that the small magnitude, stiff site simulations also exhibit some amount of long-period noise but this deviation is negligible when compared to the soft site simulations. The long-period noise seems to be introduced during the site response analyses because the input VHR motions do not present such unphysical variations. The level of noise contamination decreases with increasing magnitude for both soft and stiff sites. When the rock site simulations are of concern, it is observed that they are not influenced by the long-period noise. It can be stated that the long-period noise that is probably introduced during the site response analysis may limit the use of soft and stiff site simulations for spectral periods beyond ~20 sec.

(v) The comparisons of synthetics with a set of non-stationary simulations generated the procedure proposed by Pousse et al. (2006) demonstrate that S_d of non-stationary simulations attain larger values than the S_d estimations of GMPEs (AB07b and BA08) and the synthetics generated in this study. The main source of this inconsistency is attributed to the different source models used in the simulation procedures. The stationary simulations (this study) are found to be, on average, in good agreement with the estimations of GMPEs. Based on this observation it is concluded that the stationary frequency content of the simulated records does not mask the genuine ground-motion features.

(vi) The assessment of synthetics with respect to GMPEs demonstrates that SD simulations at rock and stiff sites, on average, attain similar values to the estimations of GMPEs, regardless of the magnitude and distance. However, SD simulations at soft sites yield smaller values than the predictive models for small magnitudes, for the entire distance range considered. For this particular group of simulations, the discrepancy between the synthetics and GMPEs decreases with increasing magnitude.

(vii) Strike-slip simulations attain values smaller than GMPEs for small magnitude events and close distances. The increase in magnitude results in a decrease in the discrepancy between synthetics and predictive models. Strike-slip simulations yield larger amplitudes than GMPEs at far distances. These observations hold for all site classes.

(viii) It is observed that the estimations obtained from GMPEs show variations among each other and this is more pronounced for small magnitudes and far distances.

(ix) The comparisons of the simulated ground motions with the GMPEs in terms of mean S_d demonstrates that the synthetics are, in general, within ±20% range of GMPEs.

(x) It is observed that the performance of simulations is sensitive to the reference distance metric used. When compared with the GMPE estimations, the use of R_{rup} as the reference distance metric for VHR simulations considerably improves the performance of soft site simulations at close-to-intermediate distances.

6.3 Future Studies

In this study, the performance of the stochastic point-source simulations are investigated in terms of various magnitude, distance, faulting style and site class bins to determine how well the stochastically simulated ground motions represent the actual ground-motion records. Based on the outcomes of this study some future studies are discussed below:

(i) The equivalent point-source models shall be investigated further to derive more sophisticated models that account for the effect of fault rupture depth and yield better simulations for small magnitude events.

(ii) Ground motion scaling models that can be used for the modification actual recordings to obtain ground motions for certain conditions shall be derived by using simulated ground motions.

(iii) The limitations of the simulated ground motions in terms of linear single-degree of freedom (SDOF) response are described in this study. The performance of the simulations can be examined for nonlinear SDOF and multi-degree of freedom (MDOF) response for the use of simulations in time history analyses of structures.

REFERENCES

Abrahamson, N. and Silva, W., (2008). Summary of the Abrahamson & Silva NGA Ground-Motion Relations, *Earthquake Spectra*, Vol. 24, 67-97.

Abrahamson, N., Atkinson, G. M., Boore, D. M., Bozorgnia, Y., Campbell, K. W., Chiou, B. S.-J., Idriss, I. M., Silva, W., and Youngs, R. R., (2008). Comparisons of the NGA ground-motion relations, *Earthquake Spectra*, Vol. 24, 45-66.

Akcelik, V., Bielak, J., Biros, G., Epanomeritakis, I., Fernandez, A., Ghattas, O., Kim, E. J., Lopez, J., O'Hallaron, D., Tu, T., and Urbanic, J., (2003), High-resolution forward and inverse earthquake modeling on terascale computers, *Proceedings of ACM/IEEE SC2003*.

Akkar, S. and Bommer, J. J., (2007a). Empirical prediction equations for peak ground velocity derived from strong-motion records from Europe and the Middle East, *Bulletin of Seismological Society of America*, Vol. 97, 511-530.

Akkar, S. and Bommer, J. J., (2007b). Prediction of elastic displacement response spectra in Europe and the Middle East, *Earthquake Engineering and Structural Dynamics*, Vol. 36, 1275-1301.

Ambraseys, N. N., Douglas, J., Sarma, S. K., and Smit, P. M., (2005). Equations for the estimation of strong ground motions from shallow crustal earthquakes using data from Europe and the Middle East: horizontal peak ground acceleration and spectral acceleration, *Bulletin of Earthquake Engineering*, Vol. 3, 1–53.

Anderson, J. and Hough, S., (1984). A model for the shape of the Fourier amplitude spectrum of acceleration at high frequencies, *Bulletin of Seismological Society of America*, Vol. 74, 1969-1993.

Ang, A. H-S. and Tang, W. H., (1984). *Probability Concept in Engineering Planning and Design, Volume II: Decision, Risk and Reliability*, John Wiley & Sons, New York.

Atkinson, G. M., (1996). The high-frequency shape of the source spectrum for earthquakes in eastern and western Canada, *Bulletin of Seismological Society of America*, Vol. 86, 106-112.

Atkinson, G. M. and Mereu, R. F., (1992). The shape of ground motion attenuation curves in southeastern Canada, *Bulletin of the Seismological Society of America*, Vol. 82, 2014-2031.

Atkinson, G. and Somerville, P., (1994). Calibration of time history simulation methods, *Bulletin of Seismological Society of America*, Vol. 84, 400-414.

Atkinson, G. M. and Boore, D. M., (1995). Ground-motion relations for eastern North America, *Bulletin of Seismological Society of America*, Vol. 85, 17-30.

Atkinson, G. M. and Silva, W., (1997). An empirical study of earthquake source spectra for California earthquakes, *Bulletin of Seismological Society of America*, Vol. 87, 97-113.

Atkinson, G. M., and Silva, W., (2000). Stochastic modeling of California ground motions, *Bulletin of Seismological Society of America*, Vol. 90, 255-274.

Atkinson, G. M. and Boore, D. M., (2006). Earthquake ground-motion prediction equations for eastern North America, *Bulletin of Seismological Society of America*, Vol. 96, 2181-2205.

Berardi, R., Jimenez, M., Zonno, G., and Garcia-Fernandez, M., (1999). Calibration of stochastic ground motion simulations for the 1997 Umbria-Marche, Central Italy, earthquake sequence, *Proceedings of the 9th International Conference on Soil Dynamics and Earthquake Engineering*, Bergen, Norway.

Beresnev, I. A. and Atkinson, G. M. (1997). Modeling finite-fault radiation from the ω^n spectrum, *Bulletin of Seismological Society of America*, Vol. 87, 67-84.

Beresnev, I. A. and Atkinson, G. M. (1998). Stochastic finite-fault modeling of ground motions from the 1994 Northridge, California Earthquake. I. Validation on rock sites, *Bulletin of Seismological Society of America*, Vol. 88, 1392-1401.

Beyer, K. and Bommer, J. J., (2006). Relationships between median values and between aleatory variabilities for different definitions of the horizontal component of motion, *Bulletin of Seismological Society of America*, Vol. 96, 1512–1522.

Boatwright, J. and Choy, G. L., (1992). Acceleration source spectra anticipated for large earthquakes in northeastern North America, *Bulletin of Seismological Society of America*, Vol. 82, 660–682.

Bolt, B. A., (1995). Intraplate seismicity and zonation, *Proceedings of the 5th Pacific Conference on Earthquake Engineering*, Melbourne, Australia, Vol. 1, 1-11.

Bommer, J. J. and Acevedo, A. B., (2004). The use of real earthquake accelerograms as input to dynamic analysis, *Journal of Earthquake Engineering*, Vol. 8, 43-91.

Bommer, J. J., Stafford, P. J., Alarcon, J. E., and Akkar, S., (2007). The influence of magnitude range on empirical ground-motion prediction, *Bulletin of Seismological Society of America*, Vol. 97, 2152-2170.

Boore, D. M., (1983). Stochastic simulation of high-frequency ground motions based on seismological models of the radiated spectra, *Bulletin of Seismological Society of America*, Vol. 73, 1865-1894.

Boore, D. M., (1986). Short-period P- and S-wave radiation from large earthquakes: implications for spectral scaling relations, *Bulletin of Seismological Society of America*, Vol. 76, 43-64.

Boore, D. M., (2003). Simulation of ground motion using the stochastic method, *Pure and Applied Geophysics*, Vol. 160, 635-376.

Boore, D. M., (2005). *SMSIM – Fortran programs for simulating ground motions from earthquakes: Version 2.3 – A Revision of OFR 96-80-A*, http://quake.wr.usgs.gov/~boore/software_online.htm, last visited on May 2007.

Boore, D. M., (2007). *Some thoughts on relating density to velocity, unpublished online notes*, http://quake.wr.usgs.gov/~boore/daves_notes.php, last visited on May 2007.

Boore, D. M. and Boatwright, J., (1984). Average body-wave radiation coefficients, *Bulletin of Seismological Society of America*, Vol. 74, 1615-1621.

Boore, D. M. and Joyner, W. B., (1991). Estimation of ground motion at deep-soil sites in eastern North America, *Bulletin of Seismological Society of America*, Vol. 81, 2167-2185.

Boore, D. M., Joyner, W. B., and Wennerberg, L., (1992). Fitting the stochastic ω^{-2} source model to observed response spectra in western North America: trade-offs between $\Delta\sigma$ and κ, *Bulletin of Seismological Society of America*, Vol. 82, 1956-1963.

Boore, D. M. and Joyner, W. B., (1997). Site amplifications for generic rock sites, *Bulletin of Seismological Society of America*, Vol. 87, 327-341.

Boore, D. M. and Bommer, J. J., (2005). Processing of strong-motion accelerograms: Needs, options and consequences, *Soil Dynamics and Earthquake Engineering*, Vol. 25, 93-115.

Boore, D. M. and Thompson, E. M., (2007). On using surface-source downhole-receiver logging to determine seismic slownesses, *Soil Dynamics and Earthquake Engineering*, Vol. 27, 971-985.

Boore, D. M. and Asten, M. W., (2008). Comparisons of shear-wave slowness in the Santa Clara Valley, California, using blind interpretations of data from invasive and voninvasive methods, *Bulletin of the Seismological Society of America*, Vol. 98: 1983-2003.

Boore, D. M. and Atkinson, G. M., (2008). Ground-motion prediction equations for the average horizontal component of PGA, PGV, and 5%-damped PSA at spectral periods between 0.01 s and 10.0 s, *Earthquake Spectra*, Vol. 24, 99-138.

Brocher, T. M., (2005). Empirical relations between elastic wavespeeds and density in the Earth’s crust, *Bulletin of Seismological Society of America*, Vol. 95, 2081-2092.

Brune, J. N., (1970). Tectonic stress and the spectra of seismic shear waves from earthquakes, *Journal of Geophysical Research*, Vol. 75, 4997-5009.

BSSC (Building Seismic Safety Council), (2003). *The 2003 NEHRP recommended provisions for new buildings and other structures. Part 1: Provisions (FEMA 450)*, Federal Emergency Management Agency, Washington, DC.

Campbell, K. W. (2003). Prediction of strong ground motion using the hybrid empirical method and its use in the development of ground-motion (attenuation) relations in Eastern North America, *Bulletin of Seismological Society of America*, Vol. 93, 1012-1033.

Campbell, K. W. (2004). Erratum to Prediction of strong ground motion using the hybrid empirical method and its use in the development of ground-motion (attenuation) relations in Eastern North America, *Bulletin of Seismological Society of America*, Vol. 94, 2418.

Campbell, K. W. and Bozorgnia, Y., (2007). Campbell-Bozorgnia NGA ground motion relations for the geometric mean horizontal component of peak and spectral ground motion parameters, *PEER Report No. 2007/02*, Pacific Earthquake Engineering Research Center, University of California, Berkeley.

Campbell, K. W. and Bozorgnia, Y., (2008). NGA ground motion model for the geometric mean horizontal component of PGA, PGV, PGD and 5% damped linear elastic response spectra for periods ranging from 0.01 to 10 s, *Earthquake Spectra*, Vol. 24, 139-171.

Chiou, B. S.-J. and Youngs, R. R., (2008). An NGA model for the average horizontal component of peak ground motion and response spectra, *Earthquake Spectra*, Vol. 24, 173-215.

Choi, Y. and Stewart, J. P., (2005). Nonlinear site amplification as function of 30 m shear wave velocity, *Earthquake Spectra*, Vol. 21, 1-30.

Day, S. M., Graves, R., Bielak, J., Dreger, D., Larsen, S., Olsen, K. B., Pitarka, A., and Ramirez-Guzman, L., (2008). Model for basin effects on long-period response spectra in Southern California, *Earthquake Spectra*, Vol. 24, 257-277.

Erdoğan, Ö., (2008). *Main seismological features of recently compiled Turkish strong motion database*, M. Sc. Thesis, Civil Engineering Department, Middle East Technical University, Ankara.

Frankel, A., Mueller, C., Barnhard, T., Perkins, D., Leyendecker, E., Dickman,N., Hanson, S., and Hopper, M., (1996). National Seismic Hazard Maps: Documentation June 1996. *U.S. Geological Survey Open File Report*, 96-152.

Gardner, G. H., Gardner, F. L. W., and Gregory, A. R., (1974). Formation velocity and density-the diagnostic basics for stratigraphic traps, *Geophysics*, Vol. 39, 770-780.

Gasparini, D. A. and Vanmarcke, E. H., (1979). Simulated earthquake motions compatible with prescribed response spectra, *Evaluation of Seismic Safety of Buildings Report No. 2*, Department of Civil Engineering, MIT, Cambridge, Massachusetts.

Graves, R., (1996), Simulating seismic wave propagation in 3D elastic media using staggered grid finite differences, *Bulletin of Seismological Society of America*, Vol. 86, 1091-1106.

Hanks, T. C., (1979). b values and $\omega^{-\gamma}$ seismic source models: implications for tectonic stress variations along active crustal fault zones and the estimation of high-frequency strong ground motion, *Journal of Geophysical Research*, Vol. 84, 2235-2242.

Hanks, T. C., (1982). f_{max}, *Bulletin of Seismological Society of America*, Vol. 72, 1867-1879.

Hanks, T. C. and Kanamori, H., (1979). A Moment Magnitude Scale, *Journal of Geophysical Research*, Vol. 84, 2348-2350.

Hanks, T. C. and McGuire, R. K., (1981). The character of high-frequency strong ground motion, *Bulletin of Seismological Society of America*, Vol. 71, 2071-2095.

Hartzell, S., Harmsen, S., Frankel, A., and Larsen, S., (1999), Calculation of broadband time histories of ground motion: comparison of methods and validation using strong-ground motion from the 1994 Northridge Earthquake, *Bulletin of Seismological Society of America*, Vol. 89, 1484-1504.

Irikura, K., (1986). Prediction of strong acceleration motions using empirical Green's function, *Proceedings of the 7th Japan Earthquake Engineering Symposium*, Japan, 151-156.

Irikura, K. and Kamae, K., (1994). Simulation of strong ground motion based on fractal composite faulting model and empirical Green's function, *Proceedings of the 9th Japan Earthquake Engineering Symposium*, Tokyo, Japan, Vol. 3, E019-024.

Ishibashi, I. and Zhang, X., (1993). Unified dynamic shear moduli and damping ratios of sand and clay, *Soils and Foundations*, Vol. 33, 182-191.

Joyner, W. B. and Boore, D. M., (1981). Peak horizontal acceleration and velocity from strong motion records including records from the 1979 Imperial Valley, California, earthquake, *Bulletin of Seismological Society of America*, Vol. 71, 2011-2038.

Kaul, M. K., (1978). Spectrum-consistent time-history generation, *ASCE Journal of the Engineering Mechanics Division*, Vol. 104, 781-788.

Kramer, S. L., (1996). *Geotechnical Earthquake Engineering*, Prentice Hall Inc., Upper Saddle River, New Jersey.

Lam, N., Wilson, J., and Hutchinson, G., (2000). Generation of synthetic earthquake accelerograms using seismological modeling: a review, *Journal of Earthquake Engineering*, Vol. 4, 321-354.

Margaris, B. N. and Boore, D. M., (1998). Determination of $\Delta\sigma$ and κ_0 from response spectra of large earthquakes in Greece, *Bulletin of Seismological Society of America*, Vol. 88, 170-182.

McGuire, R. K. and Hanks, T. C., (1980). RMS accelerations and spectral amplitudes of strong ground motion during the San Fernando, California, Earthquake, *Bulletin of Seismological Society of America*, Vol. 70, 1907-1919.

Naeim, F. and Lew, M., (1995). On the use of design spectrum compatible time histories, *Earthquake Spectra*, Vol. 11, 111-127.

Papageorgiou, A. and Aki, K., (1983). A specific barrier model for the quantitative description of inhomogeneous faulting and the prediction of strong ground motion. Part I: description of the model, *Bulletin of Seismological Society of America*, Vol. 73, 693-722.

Pitarka, A., (1998), 3D elastic finite difference modeling of seismic wave propagation using staggered grid with non-uniform spacing. *Bulletin of Seismological Society of America*, Vol. 88, 54-68.

Pousse, G., Bonilla, L. F., Cotton, F., and Margerin, L., (2006). Nonstationary Stochastic simulation of strong ground motion time histories including natural variability: application to the K-Net Japanese database, *Bulletin of Seismological Society of America*, Vol. 96, 2103-2117.

ProShake v1.12 (2007) *EduPro Civil Systems, Inc.*, Redmond, Washington.

Raoof, M., Herrmann, R. B., and Malagnini, L., (1999). Attenuation and excitation of three-component ground motion in southern California, *Bulletin of Seismological Society of America*, Vol. 89, 888-902.

Romero, S. and Rix, G. J., (2001). Ground motion amplification in Mississippi embayment deposits, *Report No. GIT-CEE/GEO-01-1*, National Science Foundation Mid America Earthquake Center, Georgia Institute of Technology, Atlanta, Georgia.

Rovelli, A., Cocco, M., Console, R., Alessandrini, B., and Mazza, S., (1991). Ground motion waveforms and source spectral scaling from close-distance accelerograms in a compressional regime area (Friuli, northeastern Italy), *Bulletin of Seismological Society of America*, Vol. 81, 57-80.

Rovelli, A., Caserta, A., Malignini, L., and Marra, F., (1994). Assessment of potential strong motions in the city of Rome, *Annali di Geofisica*, Vol. 37, 1745-1769.

Sabetta, F. and Pugliese, A., (1996). Estimation of response spectra and simulation of nonstationary earthquake ground motions, *Bulletin of Seismological Society of America*, Vol. 86, 337-352.

Sandıkkaya, M. A., (2008). *Site classification of Turkish national strong-motion recording sites*, M. Sc. Thesis, Civil Engineering Department, Middle East Technical University, Ankara.

Scherbaum, F., Schmedes, J., and Cotton, F., (2004). On the conversion of source-to-site distance for extended earthquake source models, *Bulletin of Seismological Society of America*, Vol. 94, 1053-1069.

Scherbaum, F., Cotton, F., and Staedtke, H., (2006). The estimation of minimum-misfit stochastic models from empirical ground-motion prediction equations, *Bulletin of Seismological Society of America*, Vol. 96, 427-445.

Schnabel, P. B., Lysmer, J., and Seed, H. B., (1972). SHAKE: A computer program for earthquake response analysis of horizontally layered sites, *Report No. EERC 72-12*, Earthquake Engineering Research Center, University of California, Berkeley, California.

Silva, W. J., (2005). Site response simulations for the NGA project, *Report prepared for the Pacific Earthquake Engineering Research Center*.

Silva, W. J., and Lee, K., (1987). WES RASCAL code for synthesizing earthquake ground motions, *State-of-the-Art for Assessing Earthquake Hazards in the United States, Report 24, Miscellaneous Paper S-73-1*. U.S. Army Corps of Engineers, Vicksburg, Mississippi.

Silva, W. J. and Darragh, R. B., (1995). Engineering Characterization of Strong Ground Motion Recorded at Rock Sites, *Report No. TR-102262*, *Electric Power Research Institute*, Palo Alto, California.

Silva, W. J., Abrahamson, N., Toro, G., and Costantino, C., (1997). Description and validation of the stochastic ground motion model, *Submitted to Brookhaven National Laboratory, Associated Universities*, Inc. Upton, New York.

Sokolov, V., (1997). Empirical models for estimating Fourier-amplitude spectra of ground acceleration in the Northern Caucasus (Racha Seismogenic Zone), *Bulletin of Seismological Society of America*, Vol. 87, 1401-1412.

Sokolov, V., Bonjer, K. P., Wenzel, F., Grecu, B., and Radulian, M., (2008). Ground-motion prediction equations for the intermediate depth Vrancea (Romania) earthquakes, *Bulletin of Earthquake Engineering*, Vol. 6, 367-388.

Toro, G., Abrahamson, N., and Schneider, J., (1997). Model of strong ground motion in eastern and central North America: best estimates and uncertainties, *Seismological Research Letters*, Vol. 68, 41–57.

Vanmarcke, E. H., (1977). *Seismic Risk and Engineering Decisions*, Elsevier Publishing Co., Amsterdam and New York.

Vanmarcke, E. H., (1979). Representation of earthquake ground motion: scaled accelerograms and equivalent response spectra, *State-of-the-Art for Assessing Earthquake Hazards in the United States, Report 14, Miscellaneous Paper S-73-1*, US Army Corps of Engineers, Vicksburg, Mississippi.

Walling, M., Silva, W., and Abrahamson, N., (2008). Nonlinear site amplification factors for constraining the NGA models, *Earthquake Spectra*, Vol. 24, 243-255.

Watson-Lamprey, J. A. and Boore, D. M., (2007). Beyond Sa_{GMRotI}: Conversion to Sa_{Arb}, Sa_{SN}, and Sa_{MaxRot}, *Bulletin of Seismological Society of America*, Vol. 97, 1511–1524.

Wells, D. and Coppersmith, K., (1994). New empirical relationships among magnitude, rupture length, rupture width, rupture area, and surface displacement, *Bulletin of Seismological Society of America*, Vol. 84, 974–1002.

Yılmaz, Ö., Savaşkan, E., Bakır, B. S., Yılmaz, M. T., Eser, M., Akkar, S., Tüzel, B., İravul, Y., Özmen, Ö., Denizlioğlu, Z., Alkan, A., and Gürbüz, M., (2008). Shallow seismic and geotechnical site surveys at the Turkish national grid for strong-motion seismograph stations, *Proceedings of 14th World Conference on Earthquake Engineering*, Beijing, China, Paper No. 03-03-0013.

APPENDIX A

VERIFICATION OF PROBABILITY DISTRIBUTION ASSUMPTIONS MADE FOR VARIOUS SITE PARAMETERS

The probability plots are inspected visually to justify the probability distribution assumptions made for depth-to-bedrock, S-wave slowness and layer thickness. In all plots, the actual data are displayed by red dots and the reference probability lines are shown by blue lines.

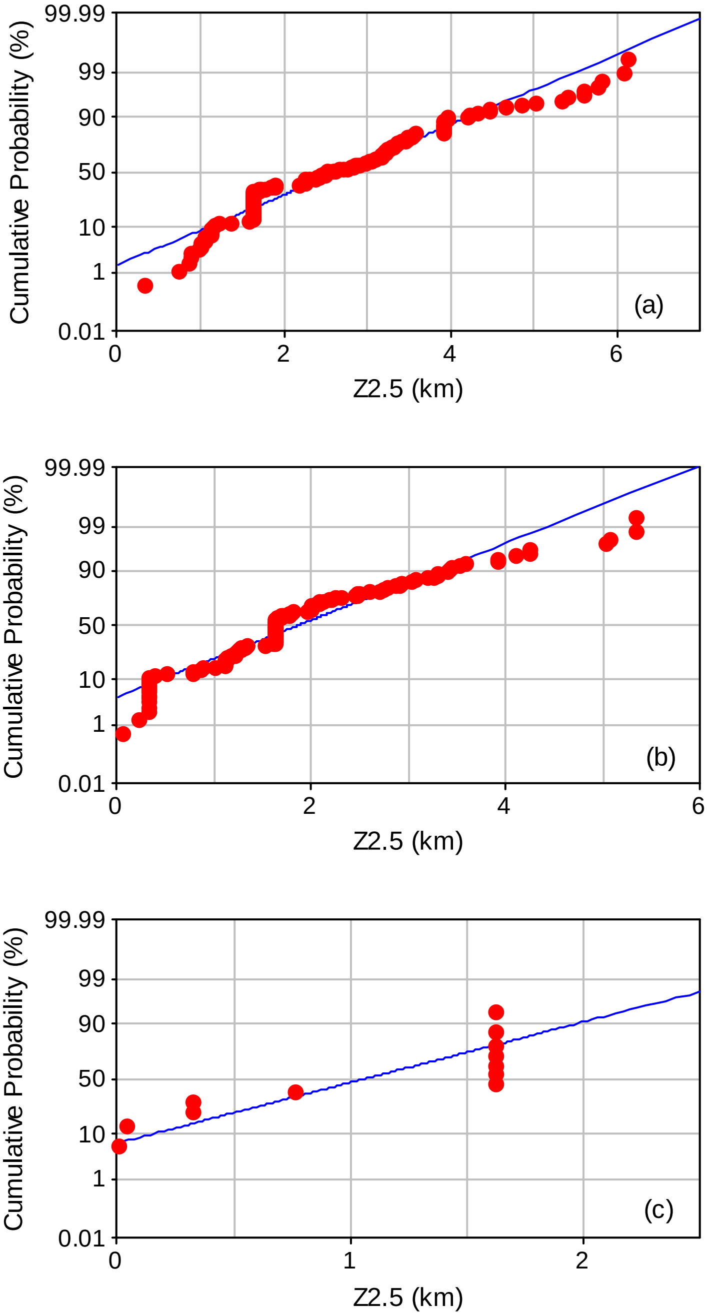

Figure A.1 Normal probability plots of depths to V_S = 2.5 km/sec (Z2.5) for (a) soft, (b) stiff and (c) rock sites

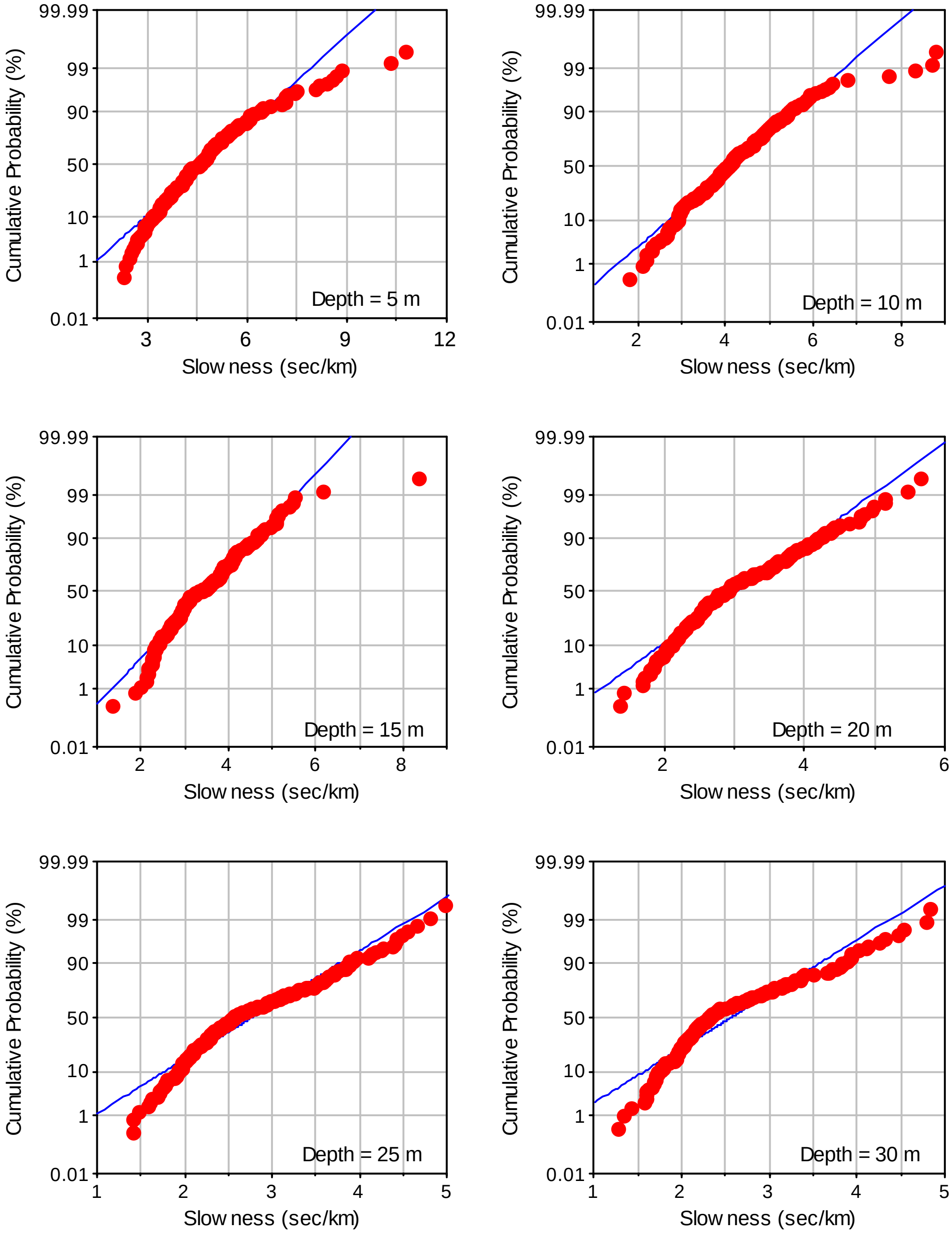

Figure A.2 Normal probability plots of the actual slowness data at various depths for soft sites

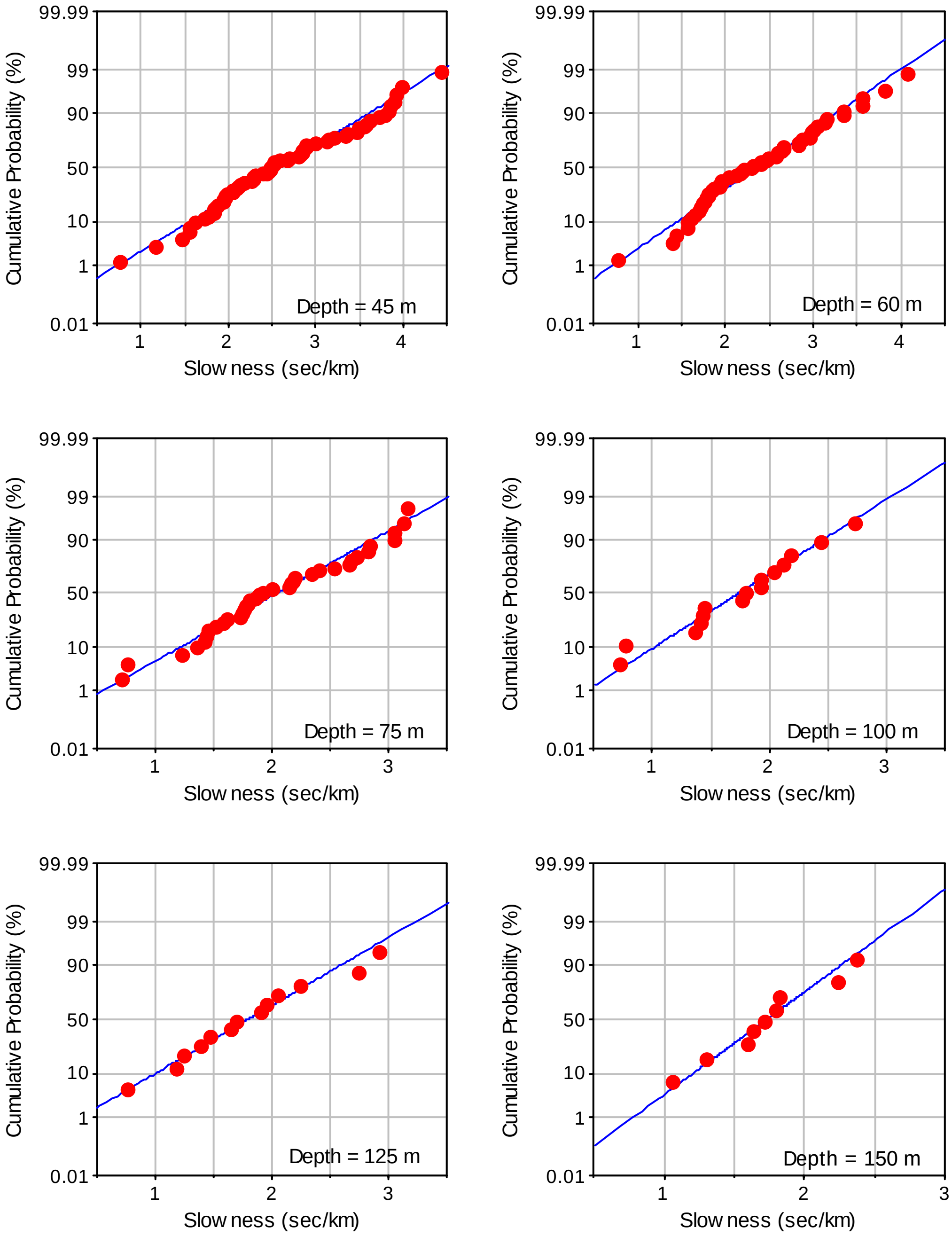

Figure A.2 (continued)

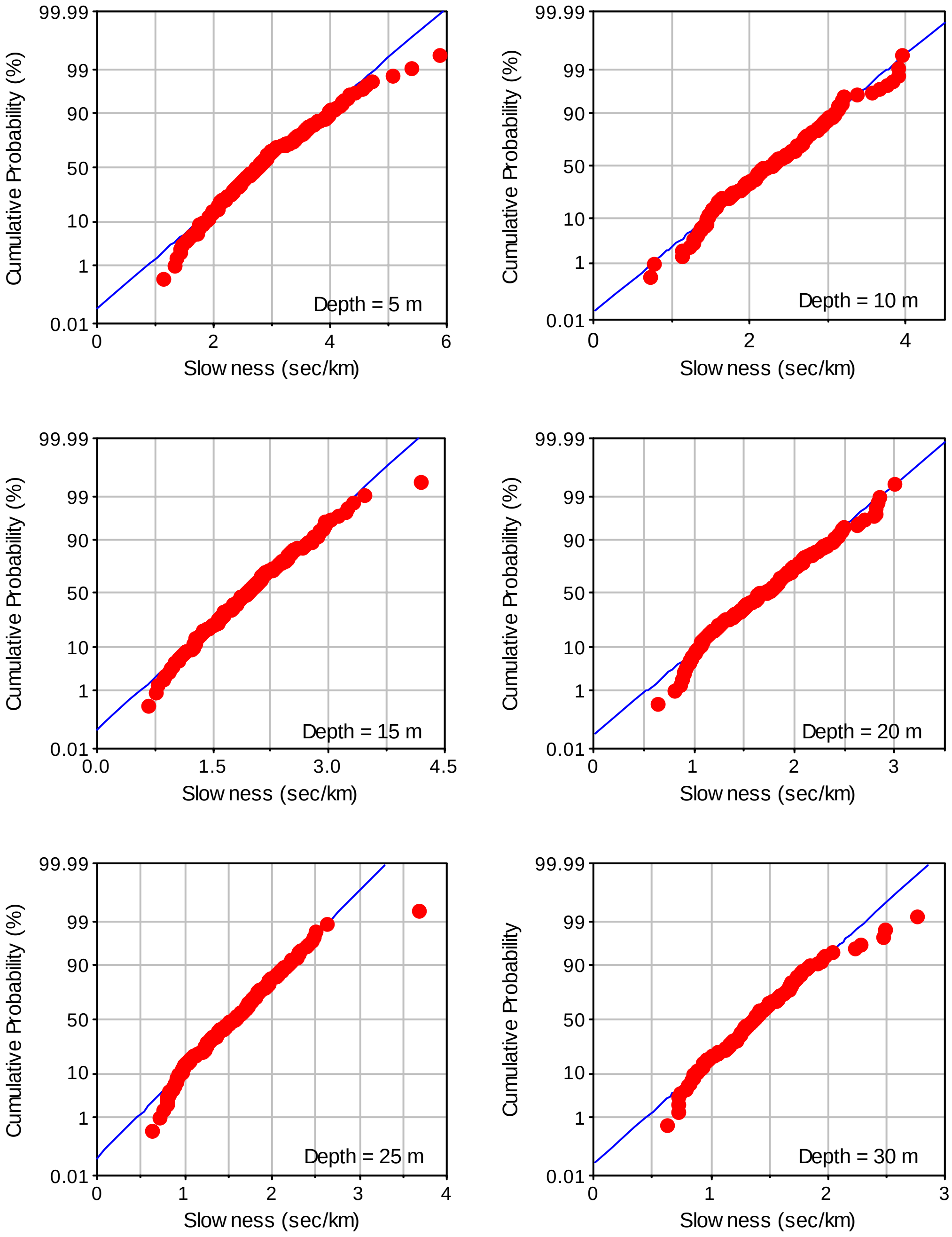

Figure A.3 Normal probability plots of the actual slowness data at various depths for stiff sites

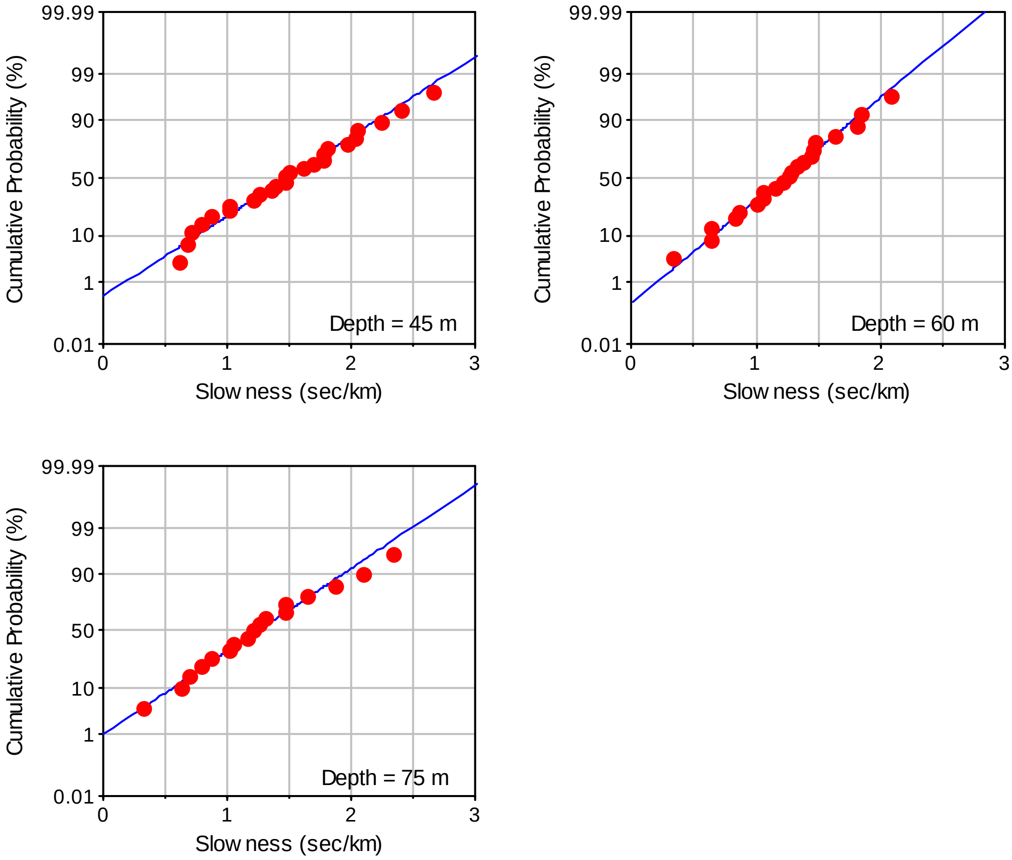

Figure A.3 (continued)

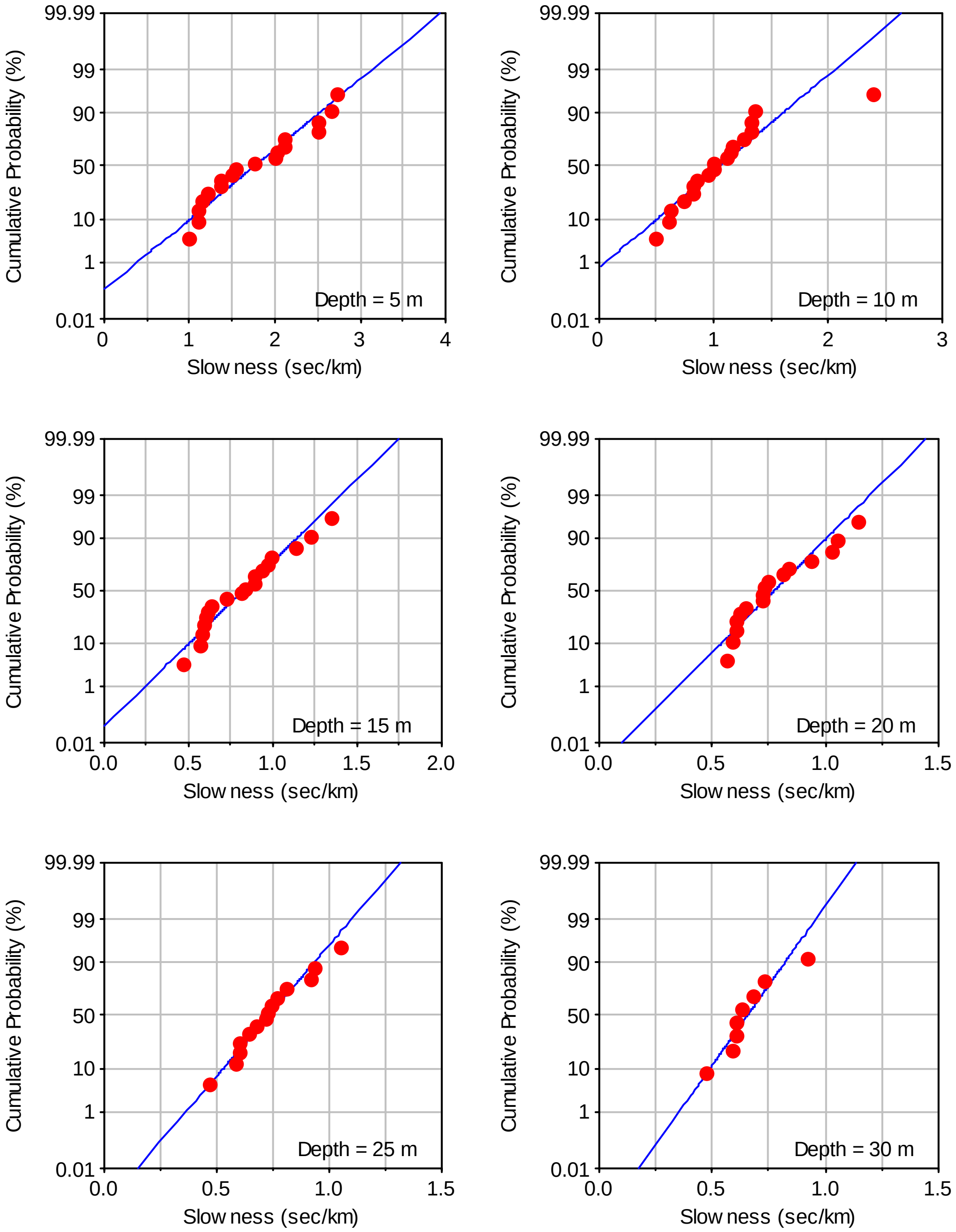

Figure A.4 Normal probability plots of the actual slowness data at various depths for rock sites

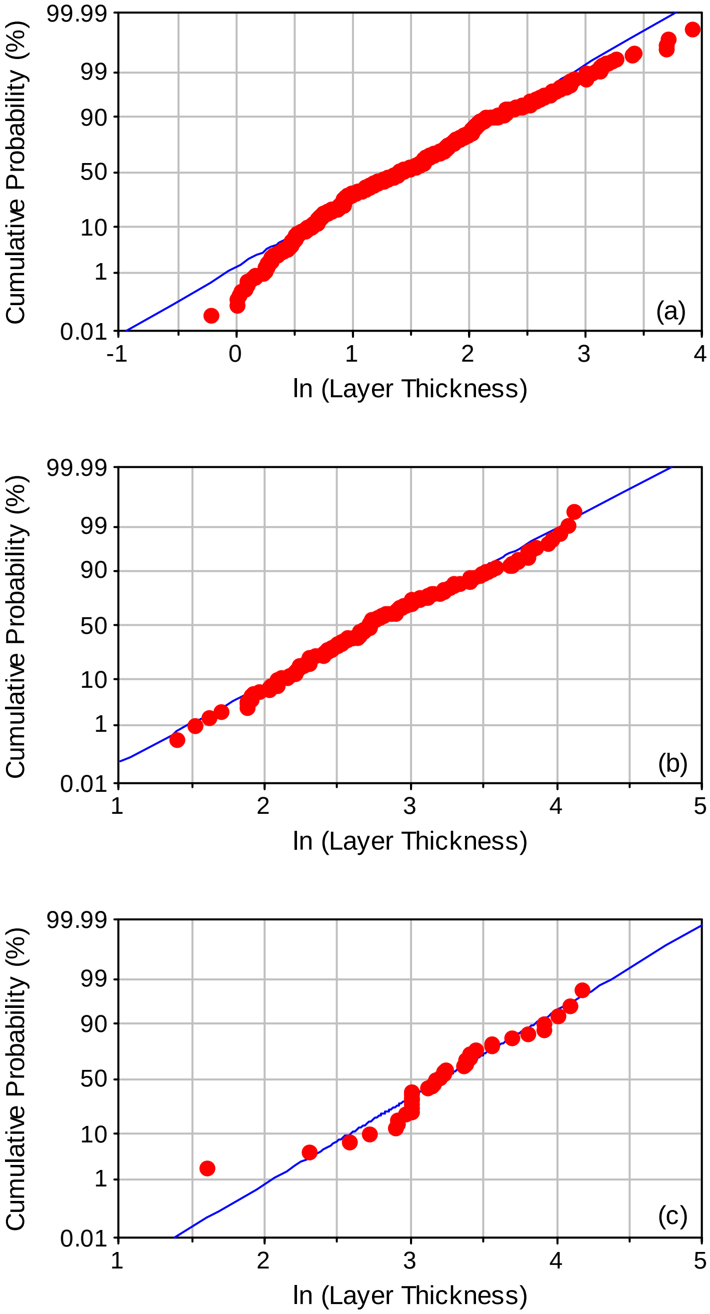

Figure A.5 Normal probability plots of the natural logarithm of the layer thickness' for (a) 0 - 30 m, (b) 30 m - 75 m and (c) 75 m - 150 m depth intervals

APPENDIX B

MAGNITUDE-DEPENDENT ASSESSMENT OF SIMULATIONS

M_w-dependent scatter plots for individual simulations and corresponding residuals for shallow dipping (SD) and strike-slip (SS) events at rock (760 m/sec < $V_{S,30} \leq$ 1500 m/sec), stiff (360 m/sec < $V_{S,30} \leq$ 760 m/sec) and soft (180 m/sec $\leq V_{S,30} \leq$ 360 m/sec) sites are presented. The distance range for the comparative plots is 10 km $\leq R_{JB} <$ 25 km. The median, 16% and 84% percentile estimations of GMPEs are also superimposed in the simulation scatters together with the mean values of the synthetics that are computed at different magnitude intervals. The median and fractile estimations are computed for R = 10 km and R = 25 km where R denotes R_{JB} for AB07a, AB07b and BA08 and R_{rup} for AS08, CB08 and CY08.

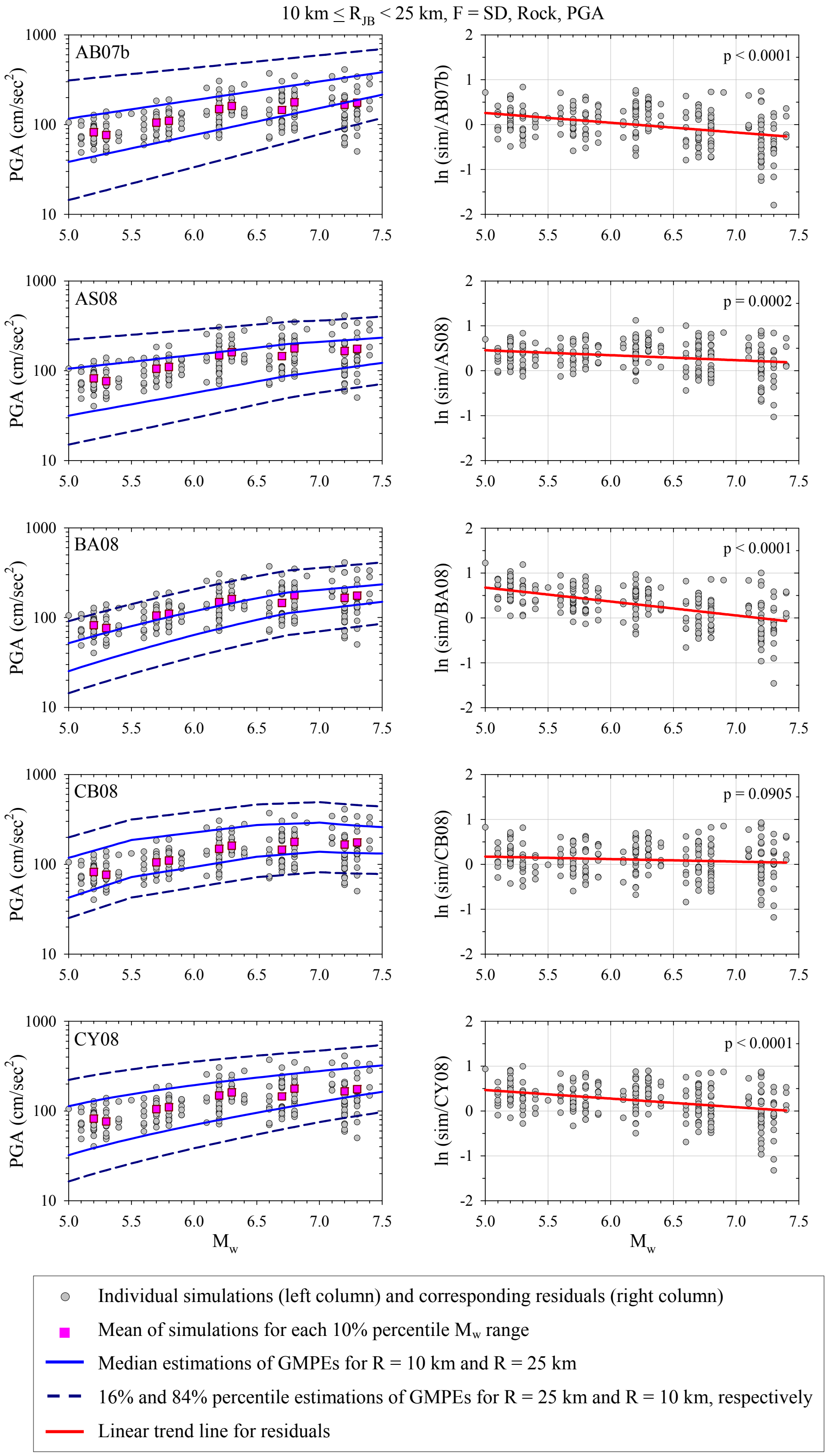

Figure B.1 Magnitude-dependent comparison of rock site simulations and GMPEs in terms of PGA for shallow dipping (SD) faults

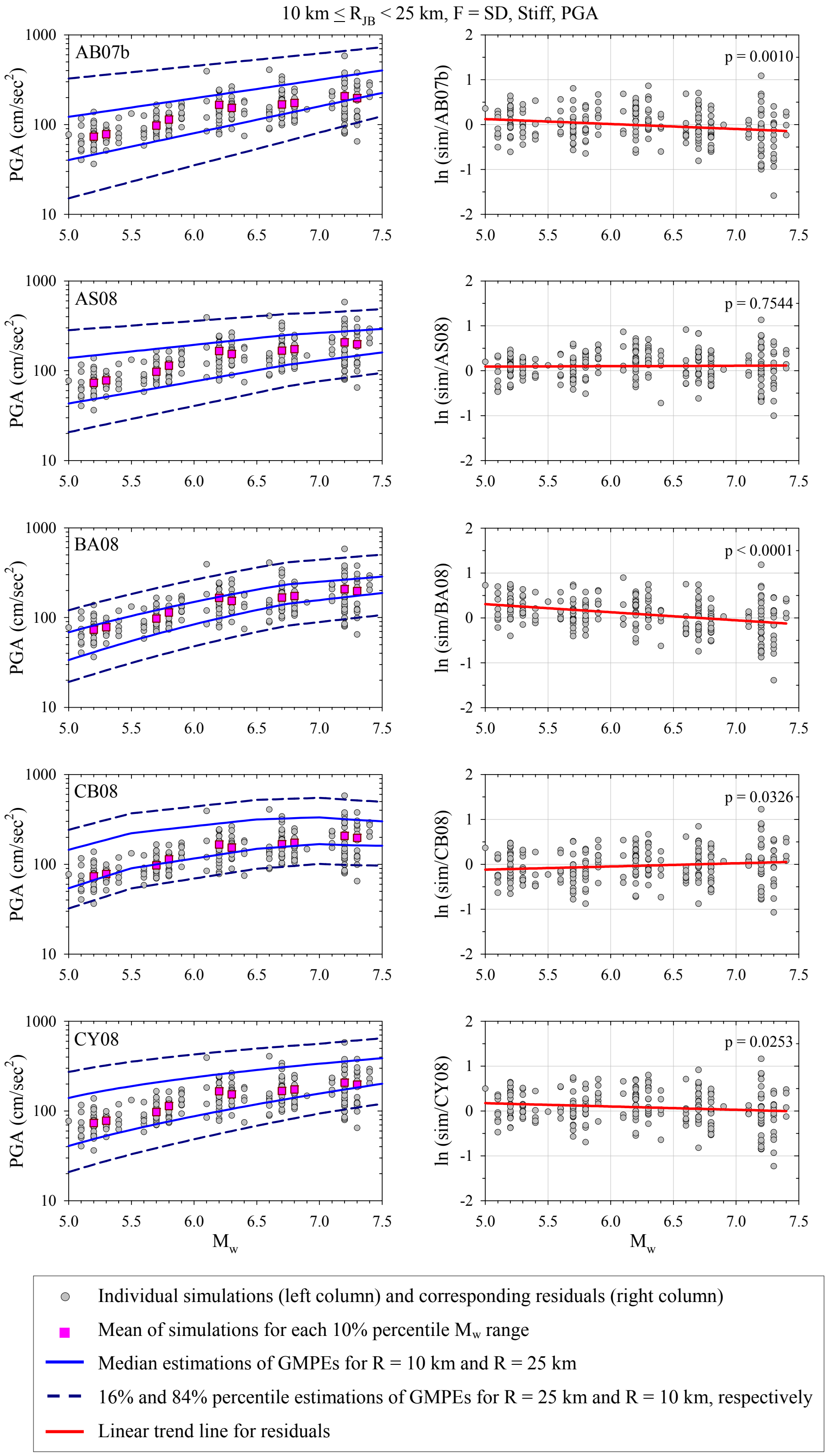

Figure B.2 Magnitude-dependent comparison of stiff site simulations and GMPEs in terms of PGA for shallow dipping (SD) faults

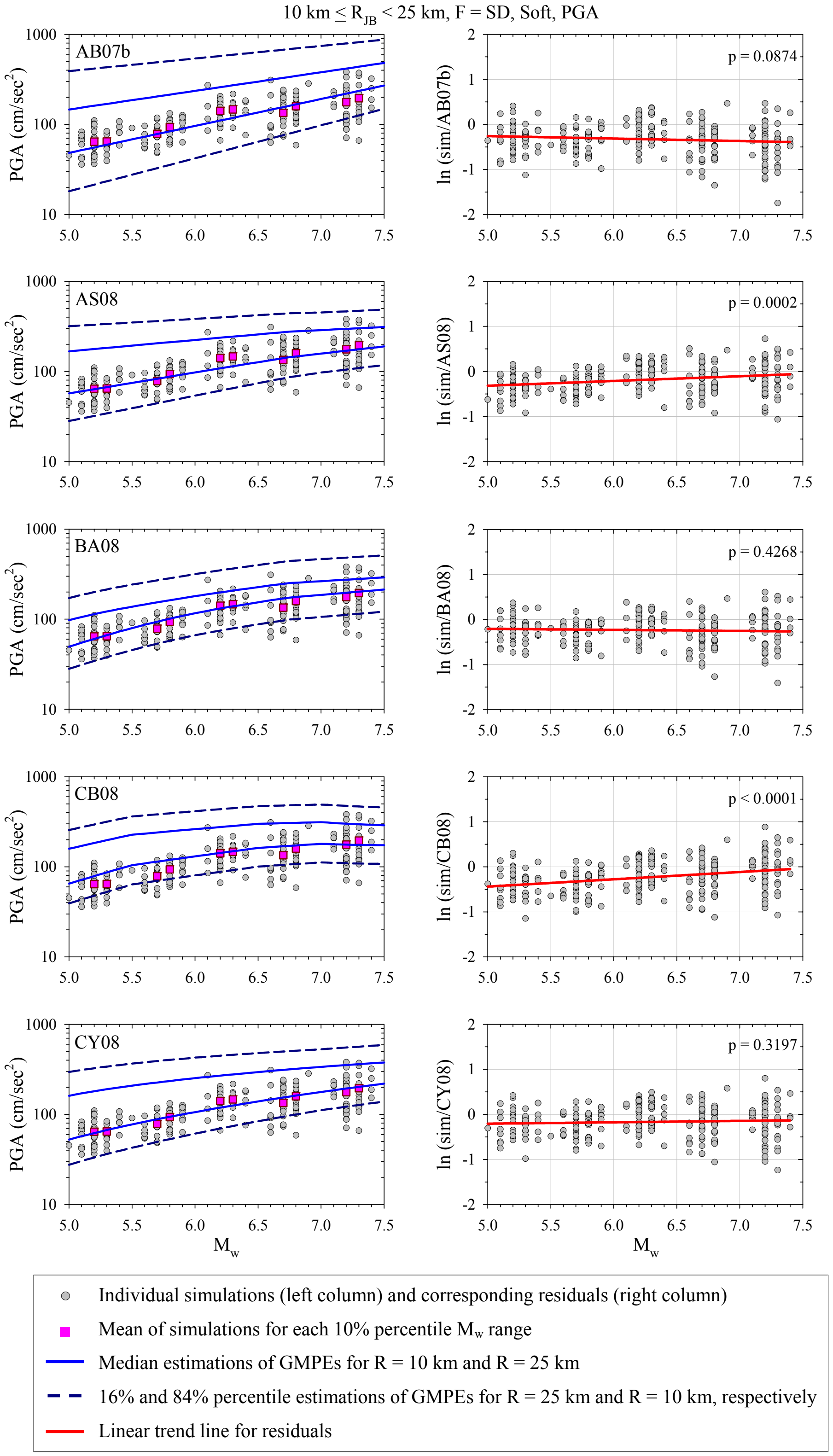

Figure B.3 Magnitude-dependent comparison of soft site simulations and GMPEs in terms of PGA for shallow dipping (SD) faults

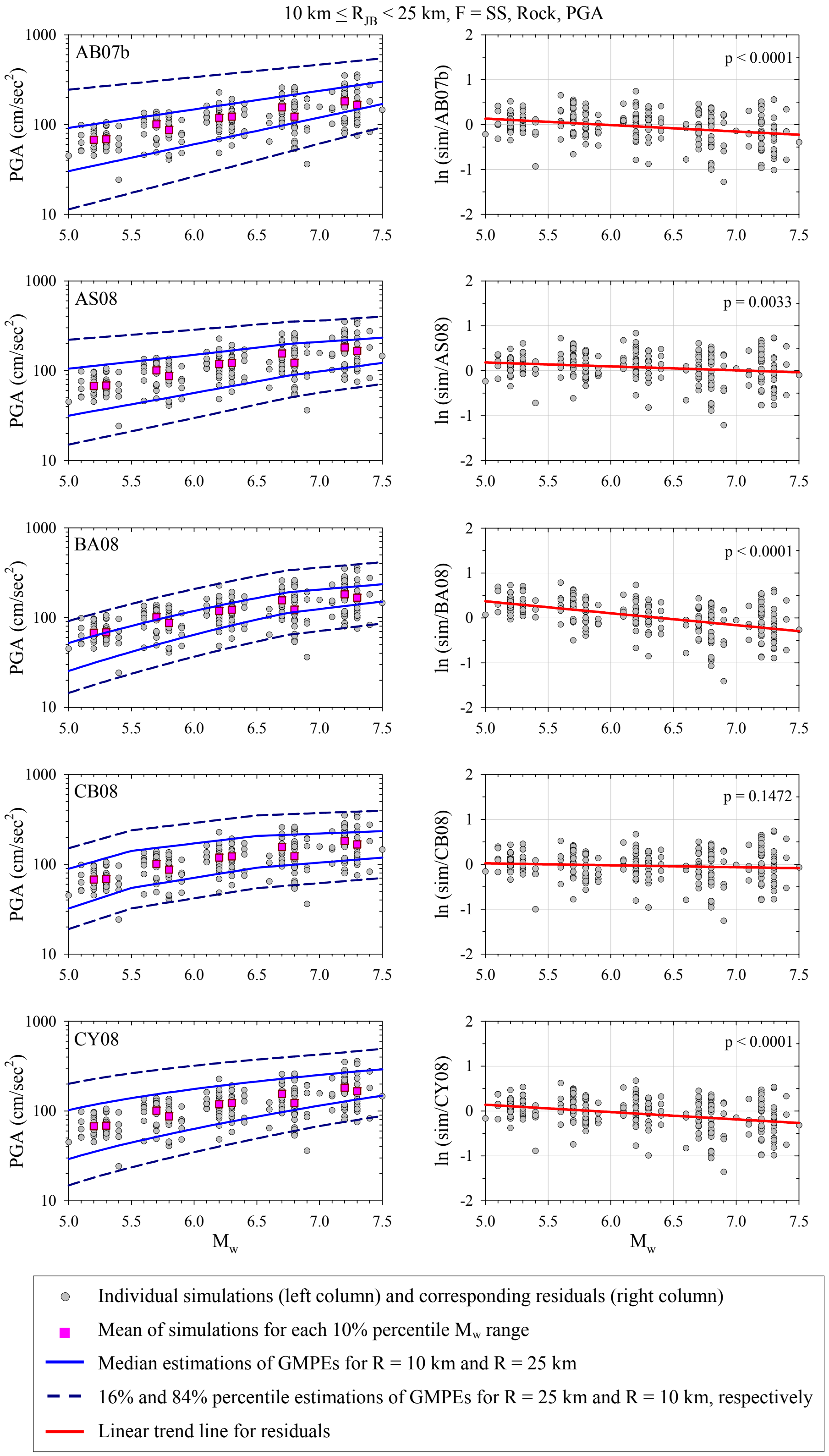

Figure B.4 Magnitude-dependent comparison of rock site simulations and GMPEs in terms of PGA for strike-slip (SS) faults

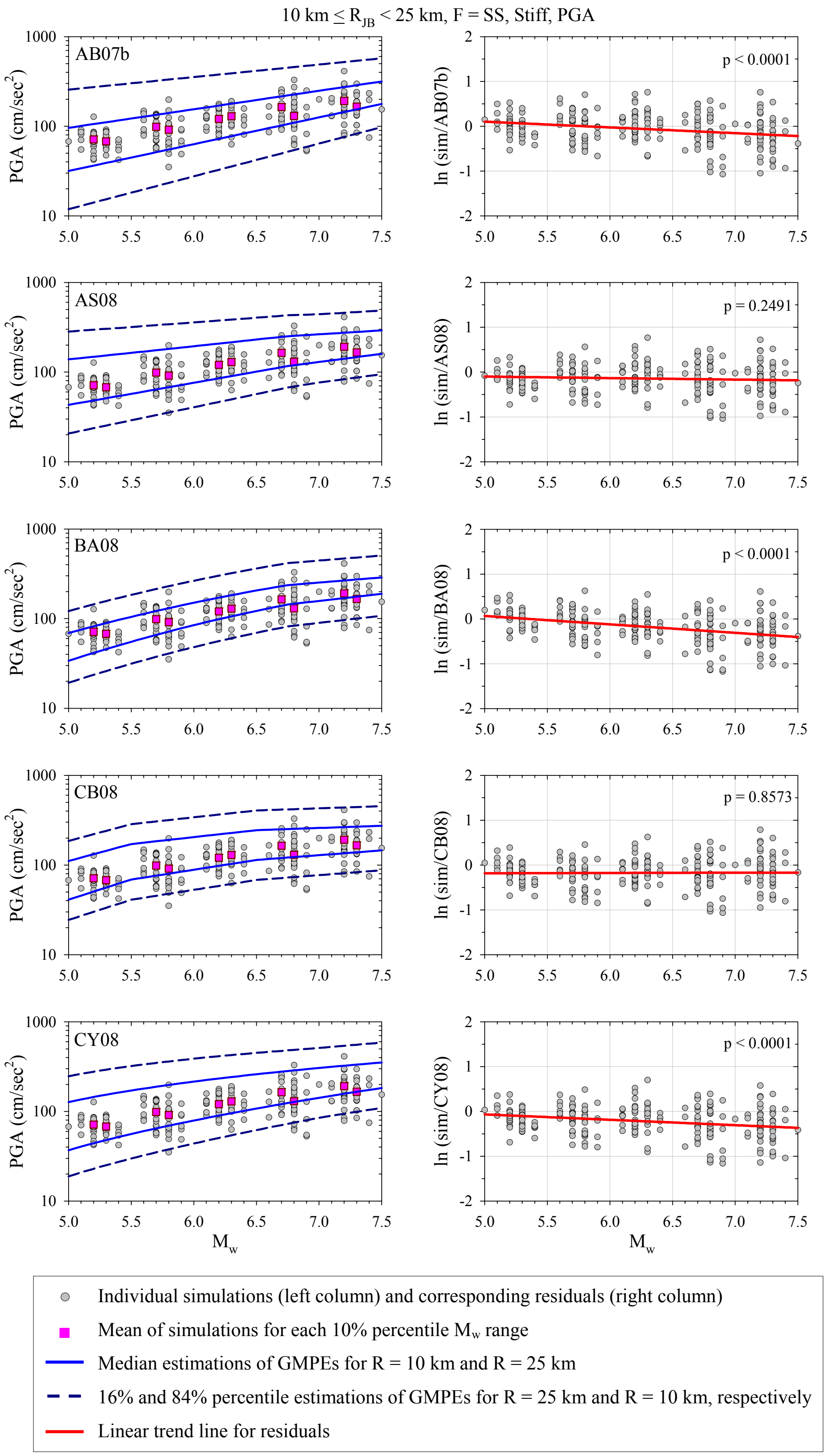

Figure B.5 Magnitude-dependent comparison of stiff site simulations and GMPEs in terms of PGA for strike-slip (SS) faults

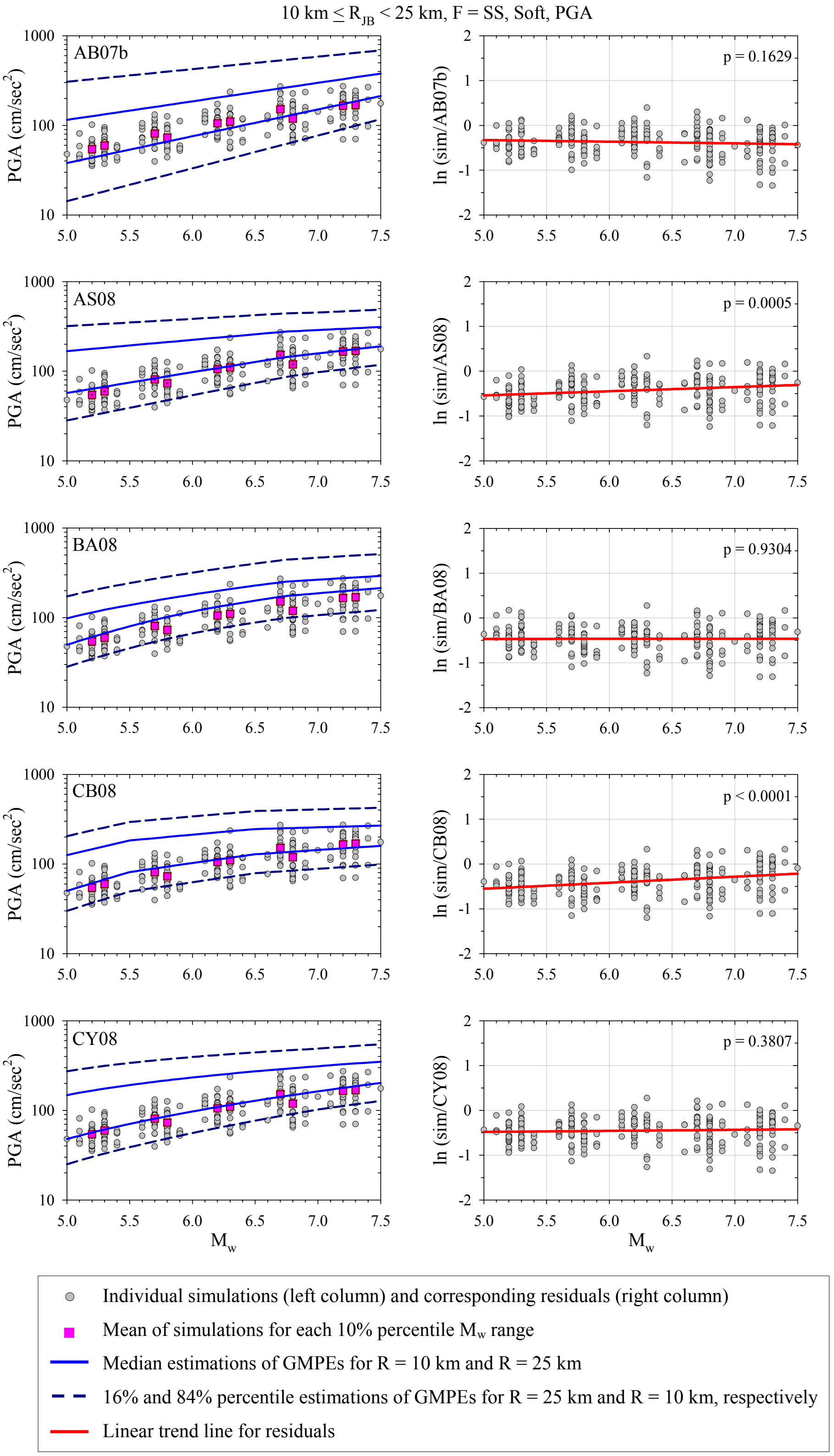

Figure B.6 Magnitude-dependent comparison of soft site simulations and GMPEs in terms of PGA for strike-slip (SS) faults

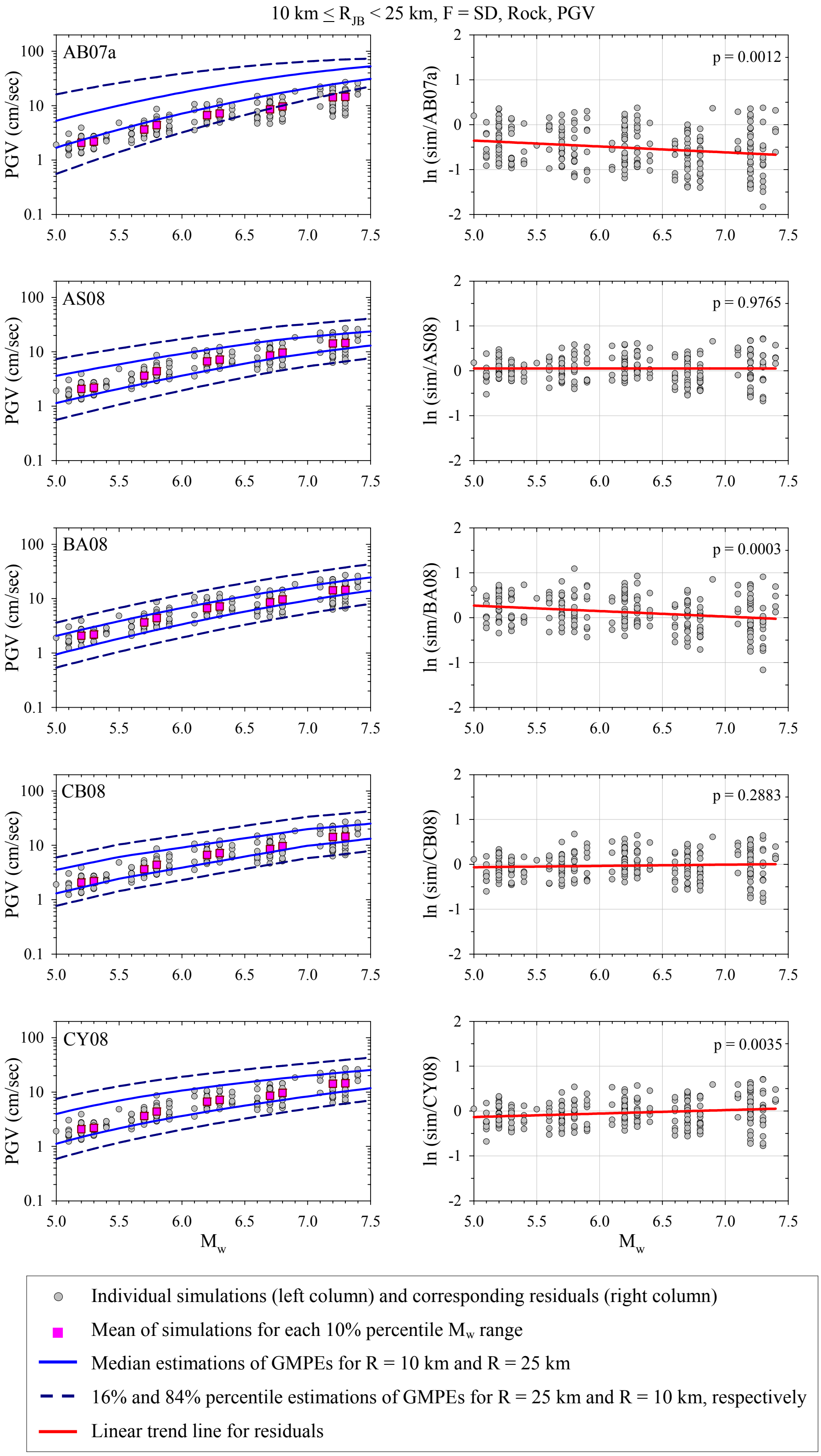

Figure B.7 Magnitude-dependent comparison of rock site simulations and GMPEs in terms of PGV for shallow dipping (SD) faults

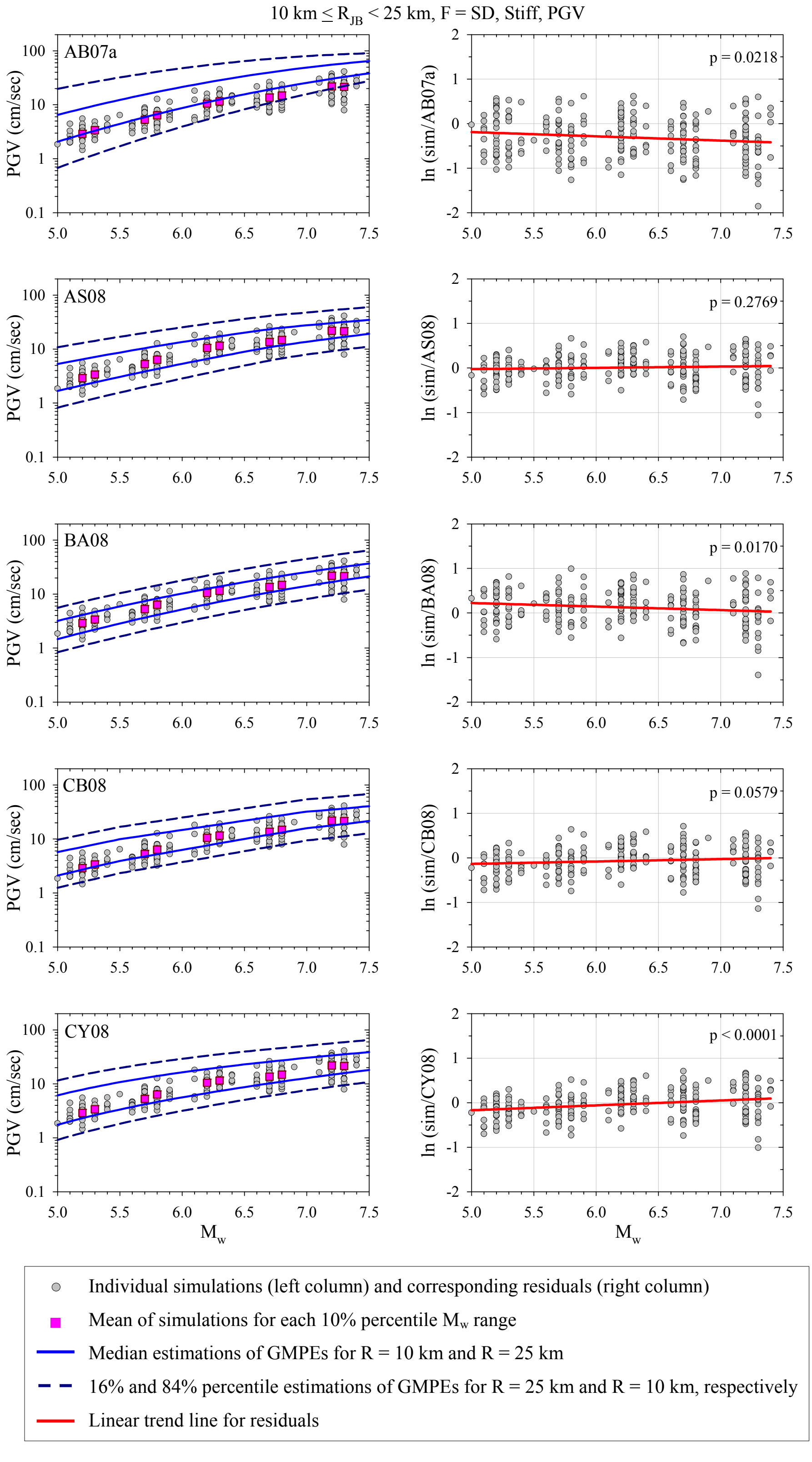

Figure B.8 Magnitude-dependent comparison of stiff site simulations and GMPEs in terms of PGV for shallow dipping (SD) faults

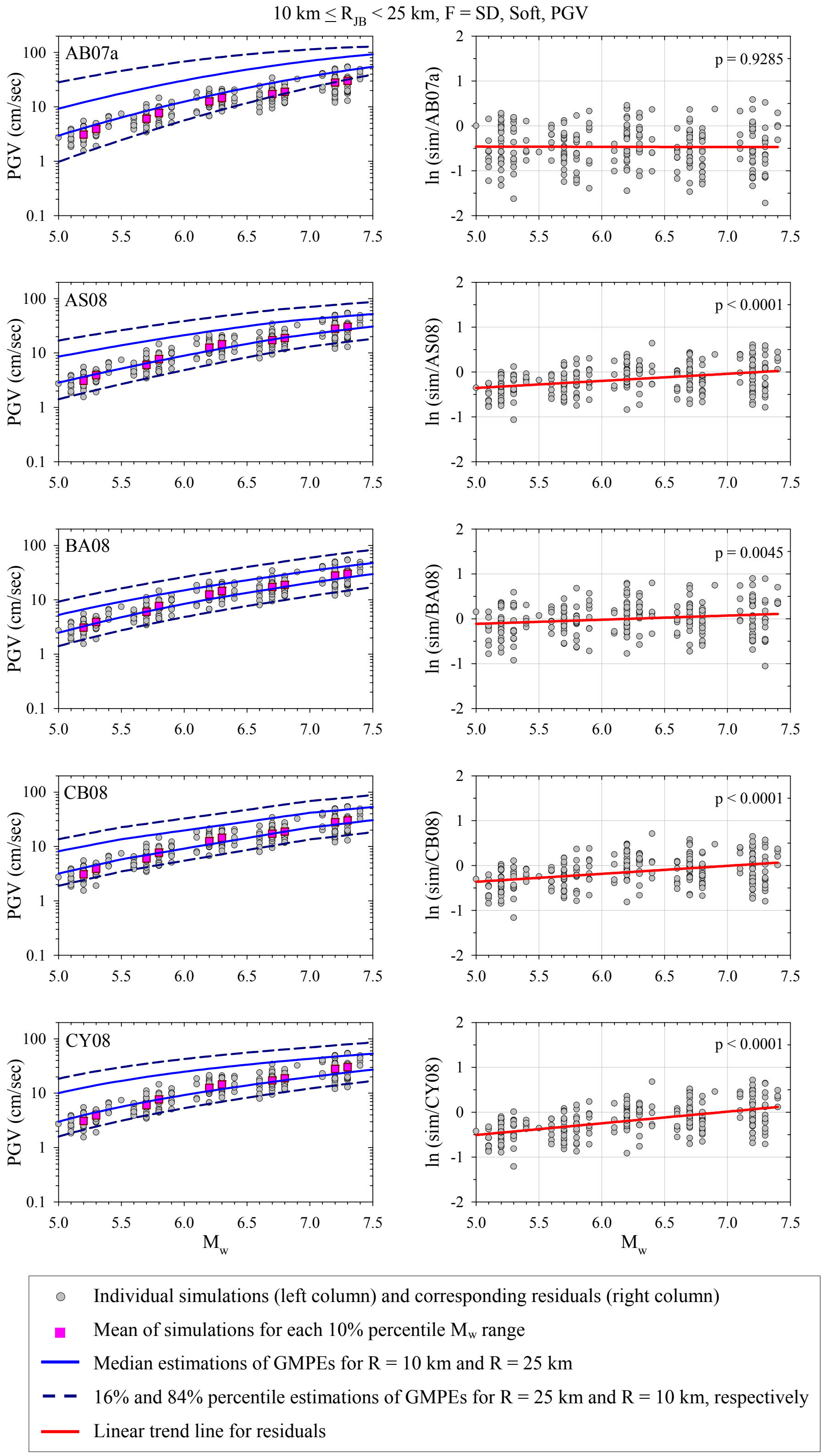

Figure B.9 Magnitude-dependent comparison of soft site simulations and GMPEs in terms of PGV for shallow dipping (SD) faults

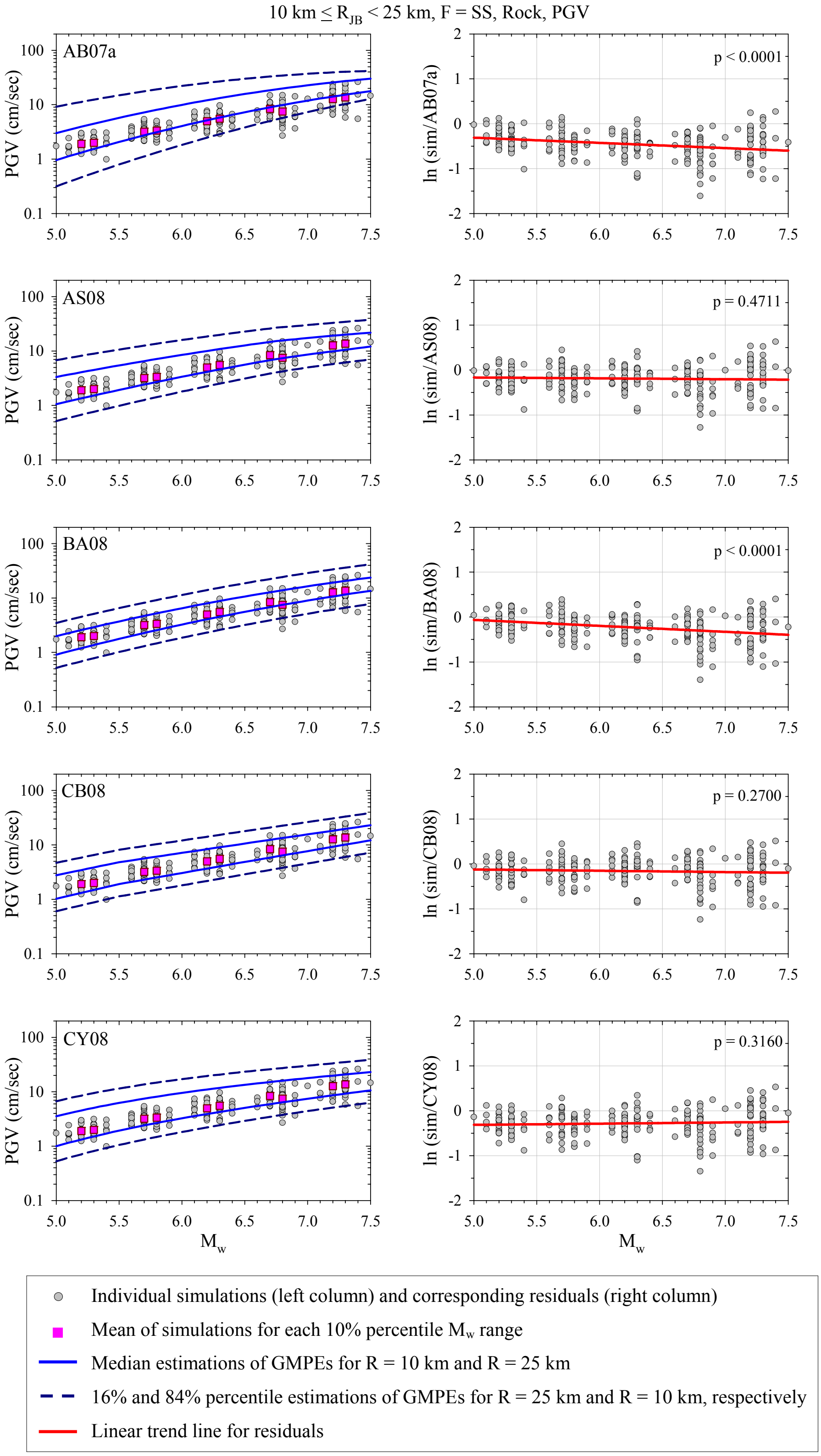

Figure B.10 Magnitude-dependent comparison of rock site simulations and GMPEs in terms of PGV for strike-slip (SS) faults

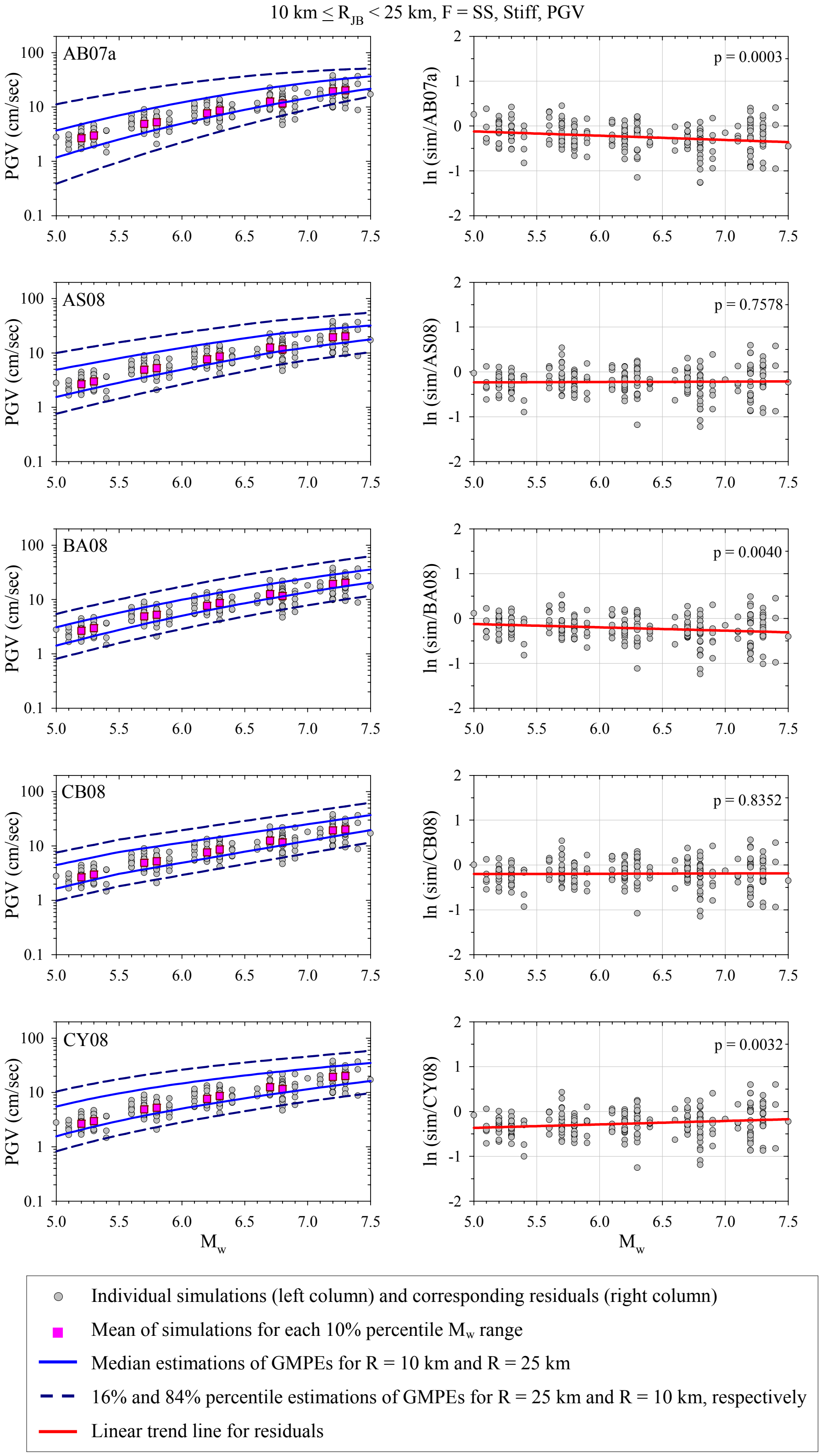

Figure B.11 Magnitude-dependent comparison of stiff site simulations and GMPEs in terms of PGV for strike-slip (SS) faults

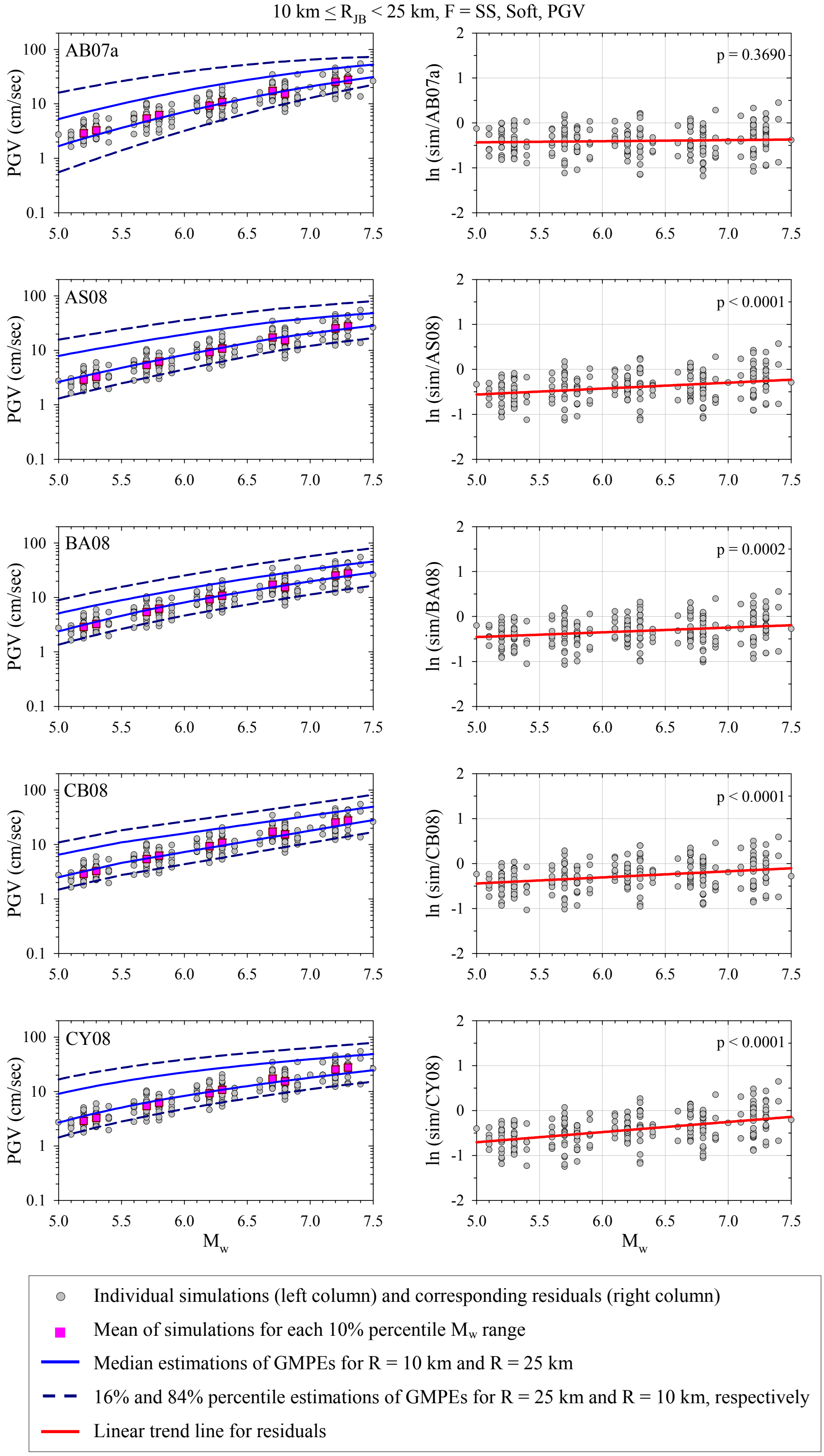

Figure B.12 Magnitude-dependent comparison of soft site simulations and GMPEs in terms of PGV for strike-slip (SS) faults

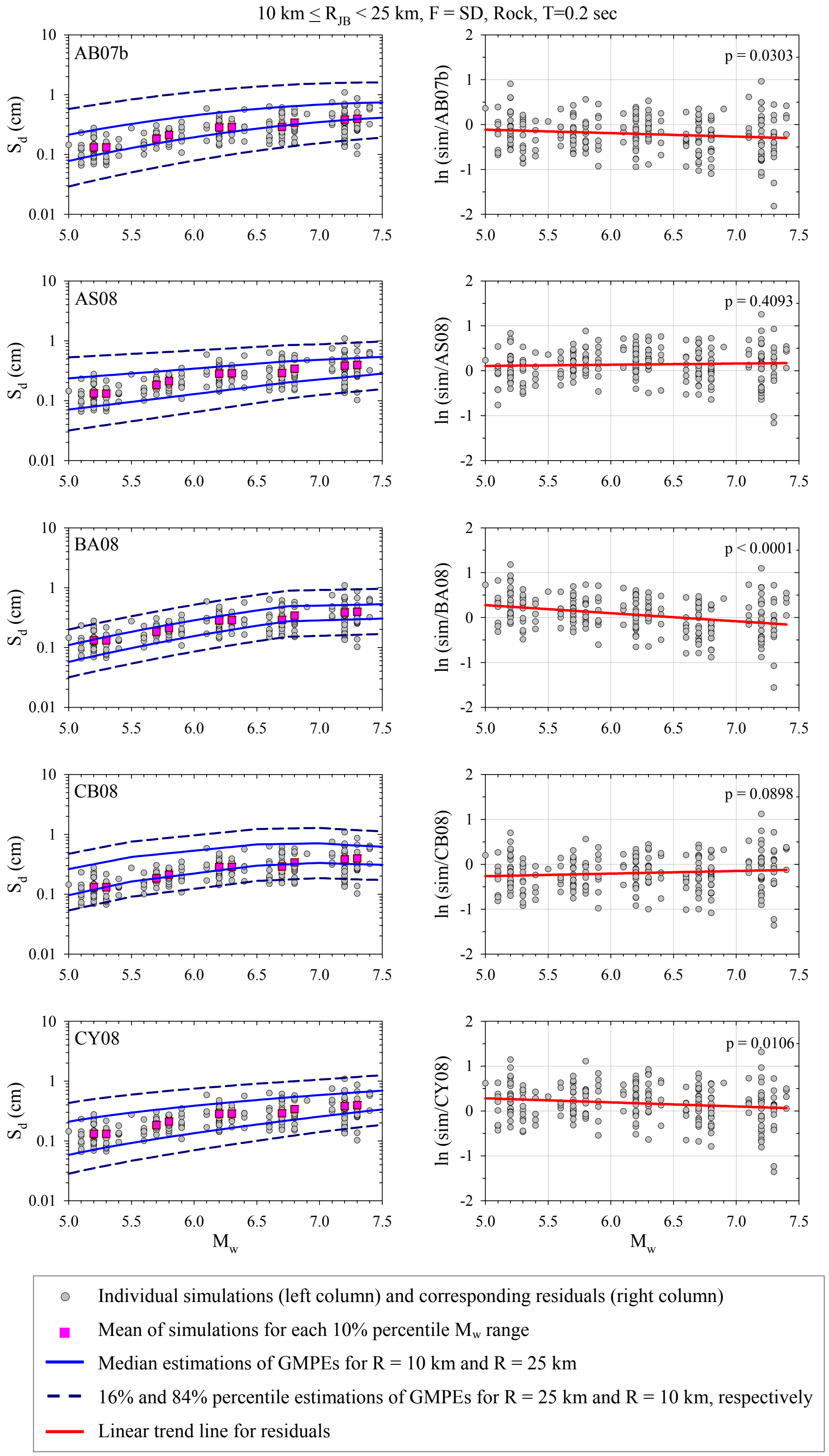

Figure B.13 Magnitude-dependent comparison of rock site simulations and GMPEs in terms of S_d ($\xi = 5\%$) at T = 0.2 sec for shallow dipping (SD) faults

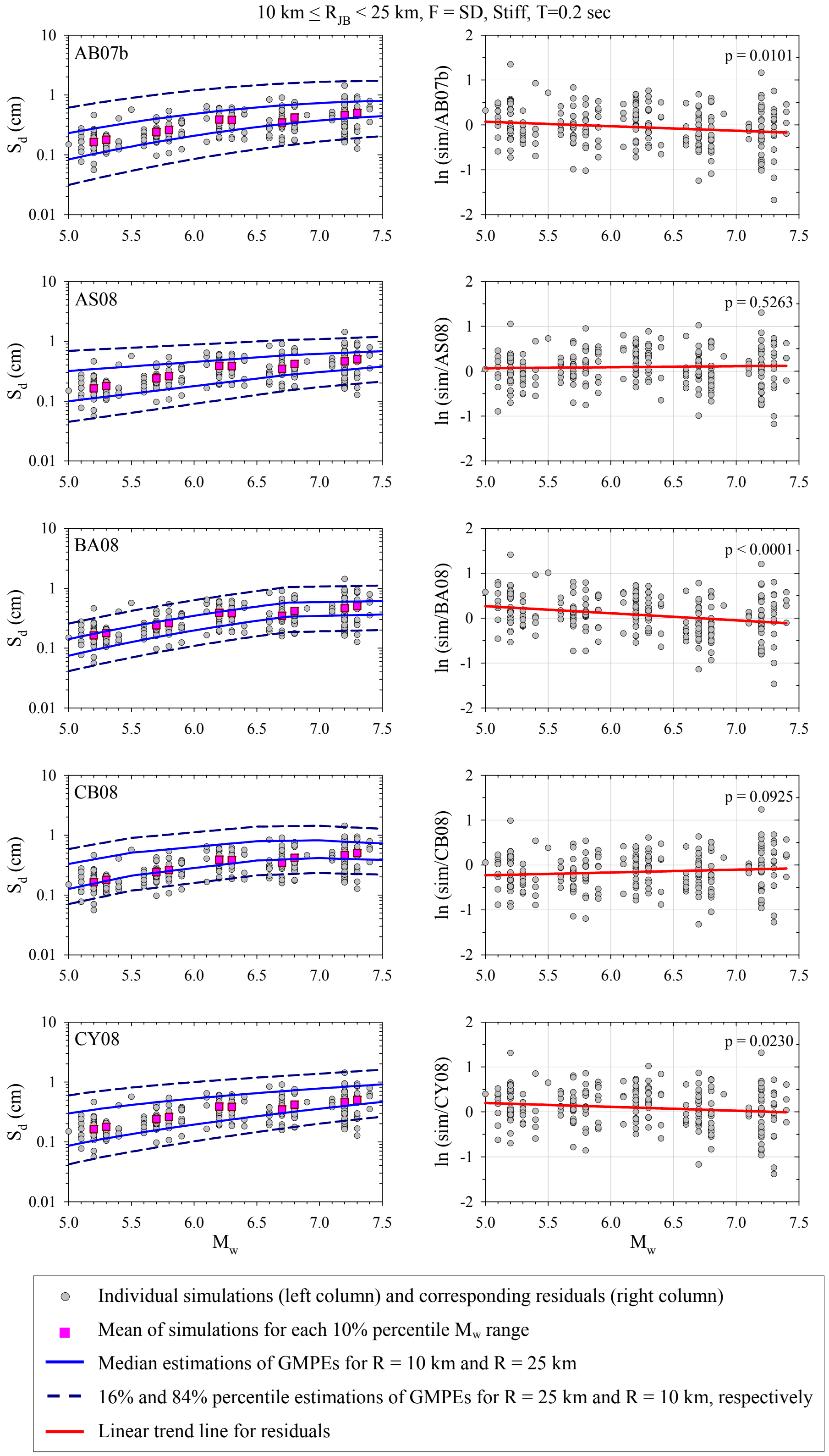

Figure B.14 Magnitude-dependent comparison of stiff site simulations and GMPEs in terms of S_d ($\xi = 5\%$) at T = 0.2 sec for shallow dipping (SD) faults

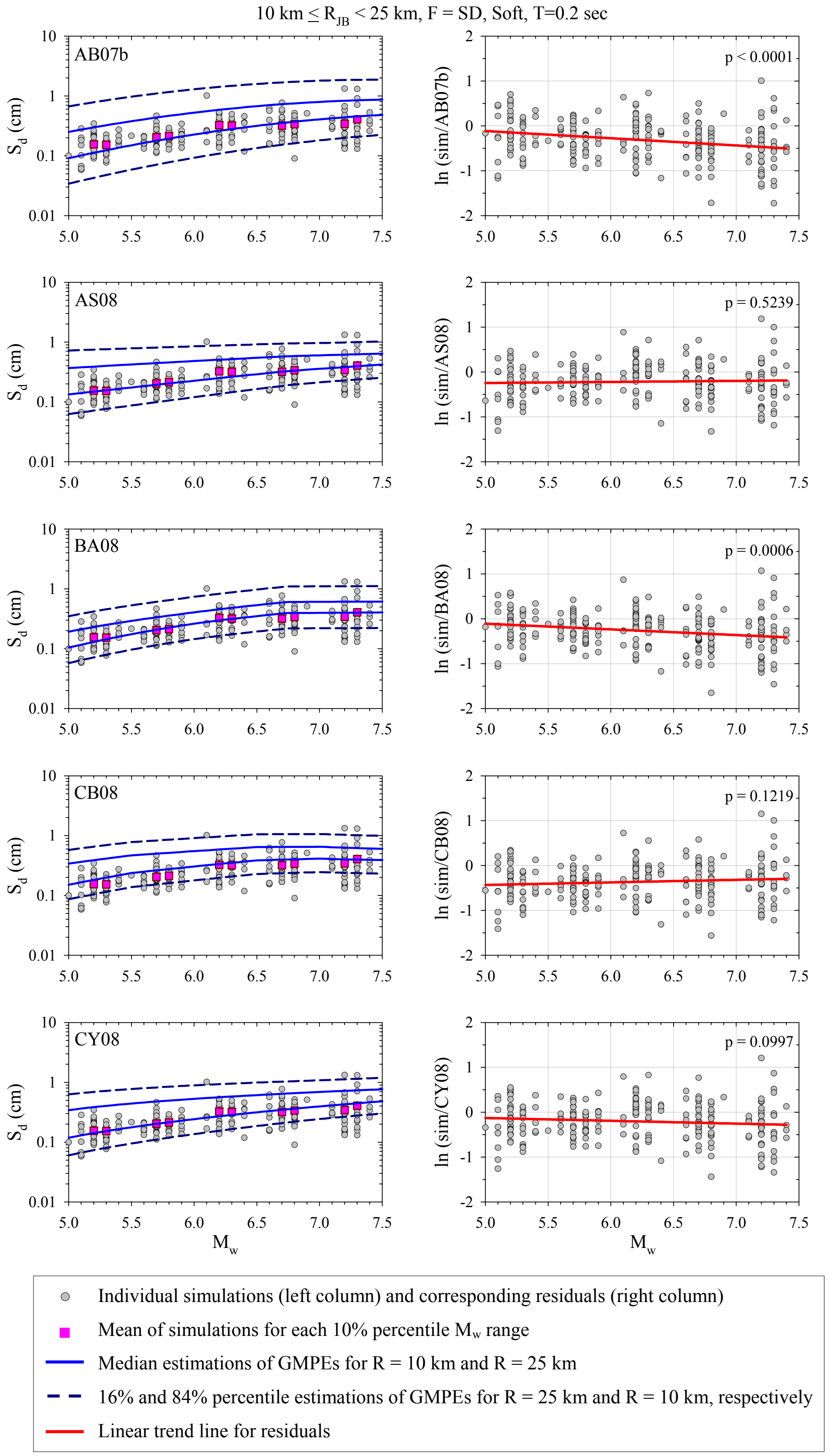

Figure B.15 Magnitude-dependent comparison of soft site simulations and GMPEs in terms of S_d ($\xi = 5\%$) at T = 0.2 sec for shallow dipping (SD) faults

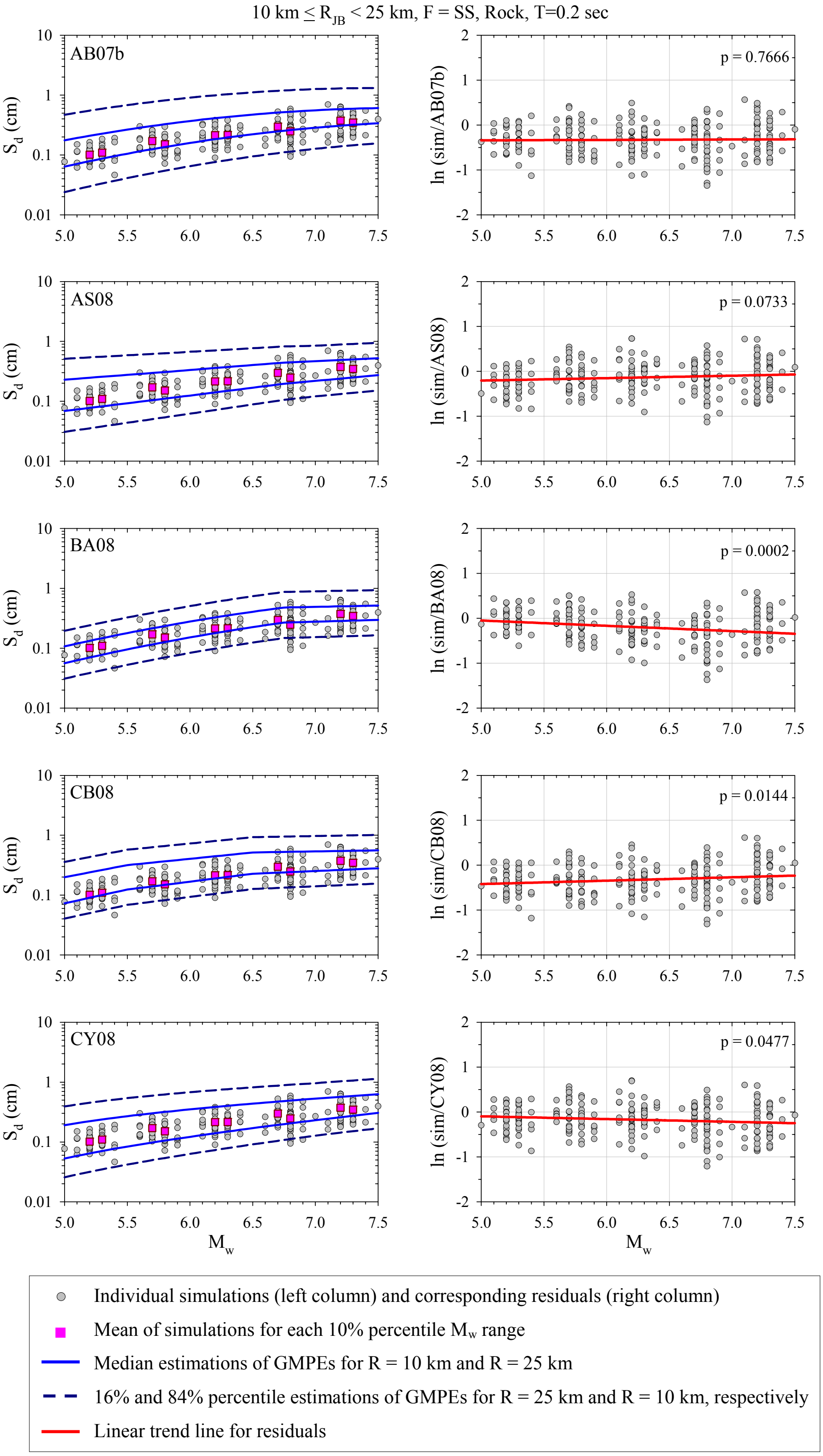

Figure B.16 Magnitude-dependent comparison of rock site simulations and GMPEs in terms of S_d ($\xi = 5\%$) at T = 0.2 sec for strike-slip (SS) faults

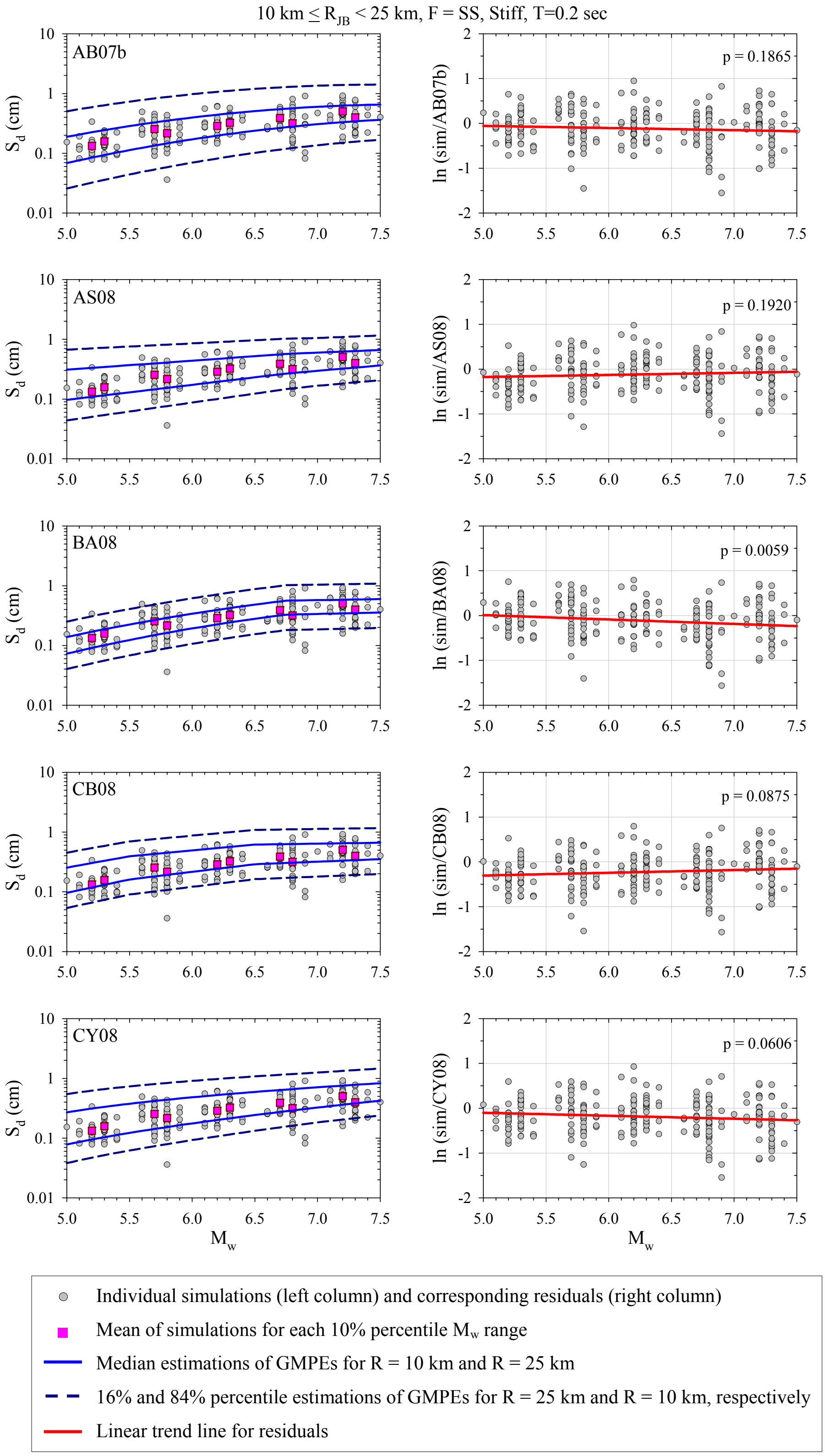

Figure B.17 Magnitude-dependent comparison of stiff site simulations and GMPEs in terms of S_d ($\xi = 5\%$) at T = 0.2 sec for strike-slip (SS) faults

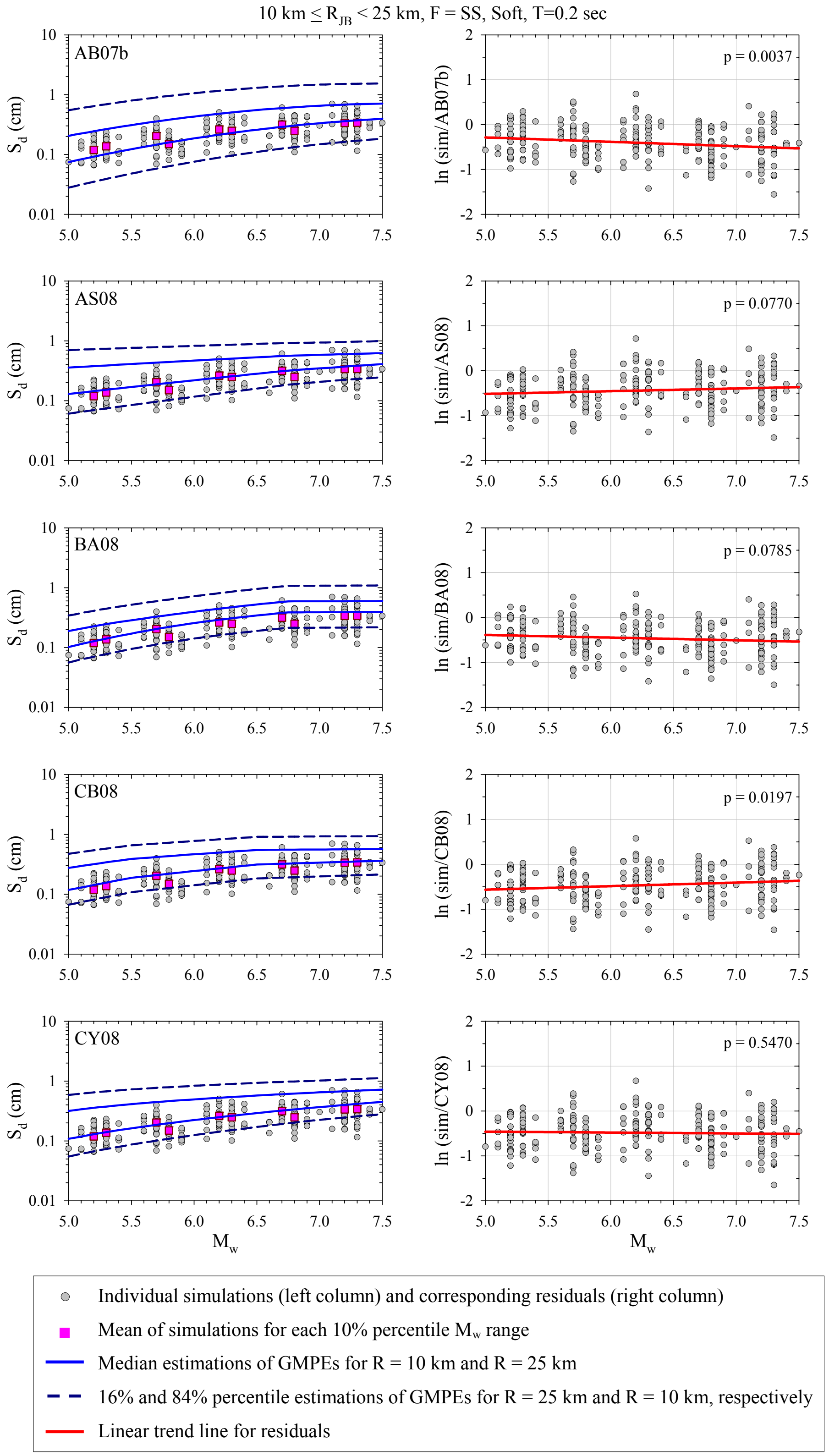

Figure B.18 Magnitude-dependent comparison of soft site simulations and GMPEs in terms of S_d ($\xi = 5\%$) at T = 0.2 sec for strike-slip (SS) faults

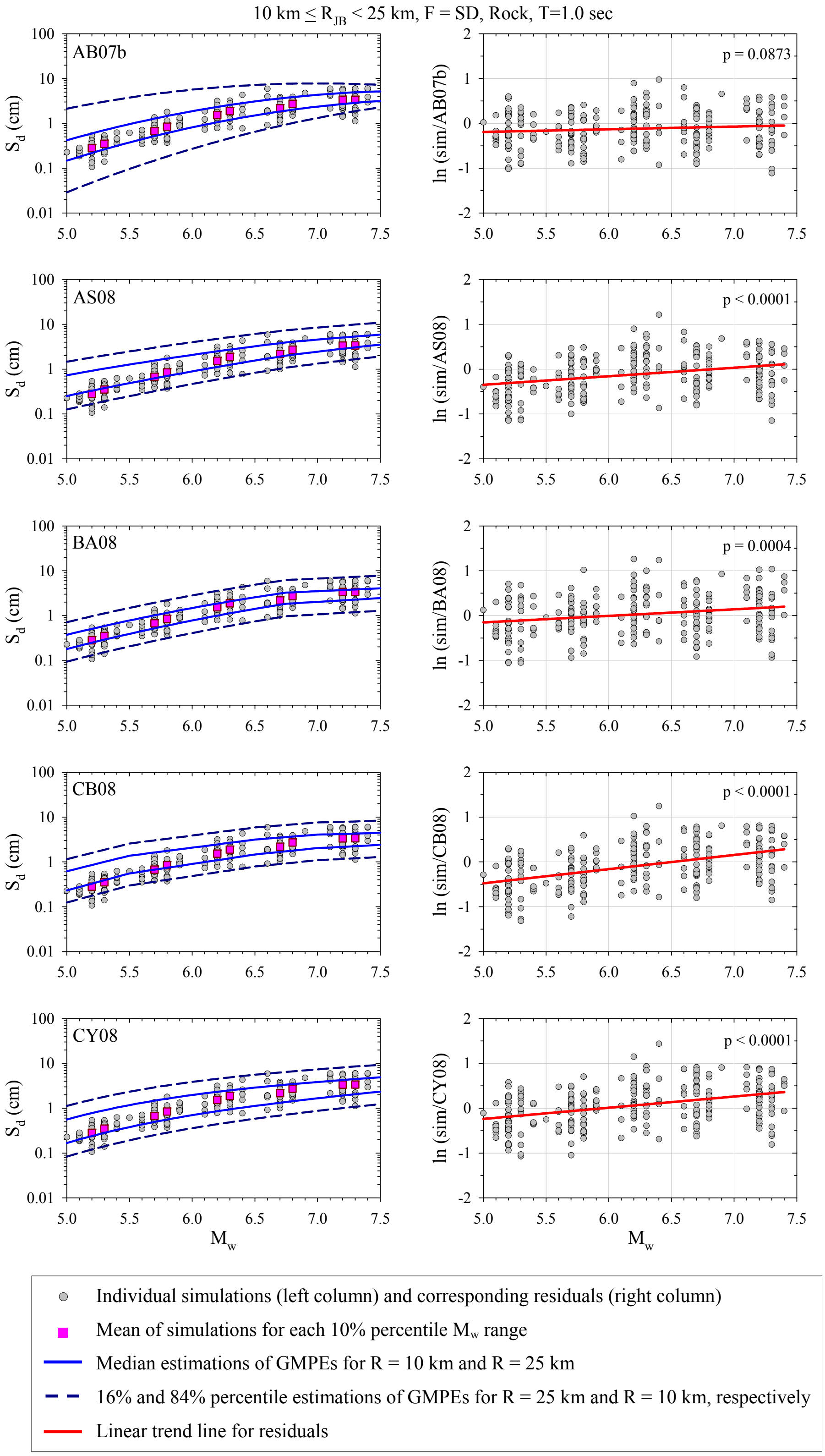

Figure B.19 Magnitude-dependent comparison of rock site simulations and GMPEs in terms of S_d ($\xi = 5\%$) at T = 1.0 sec for shallow dipping (SD) faults

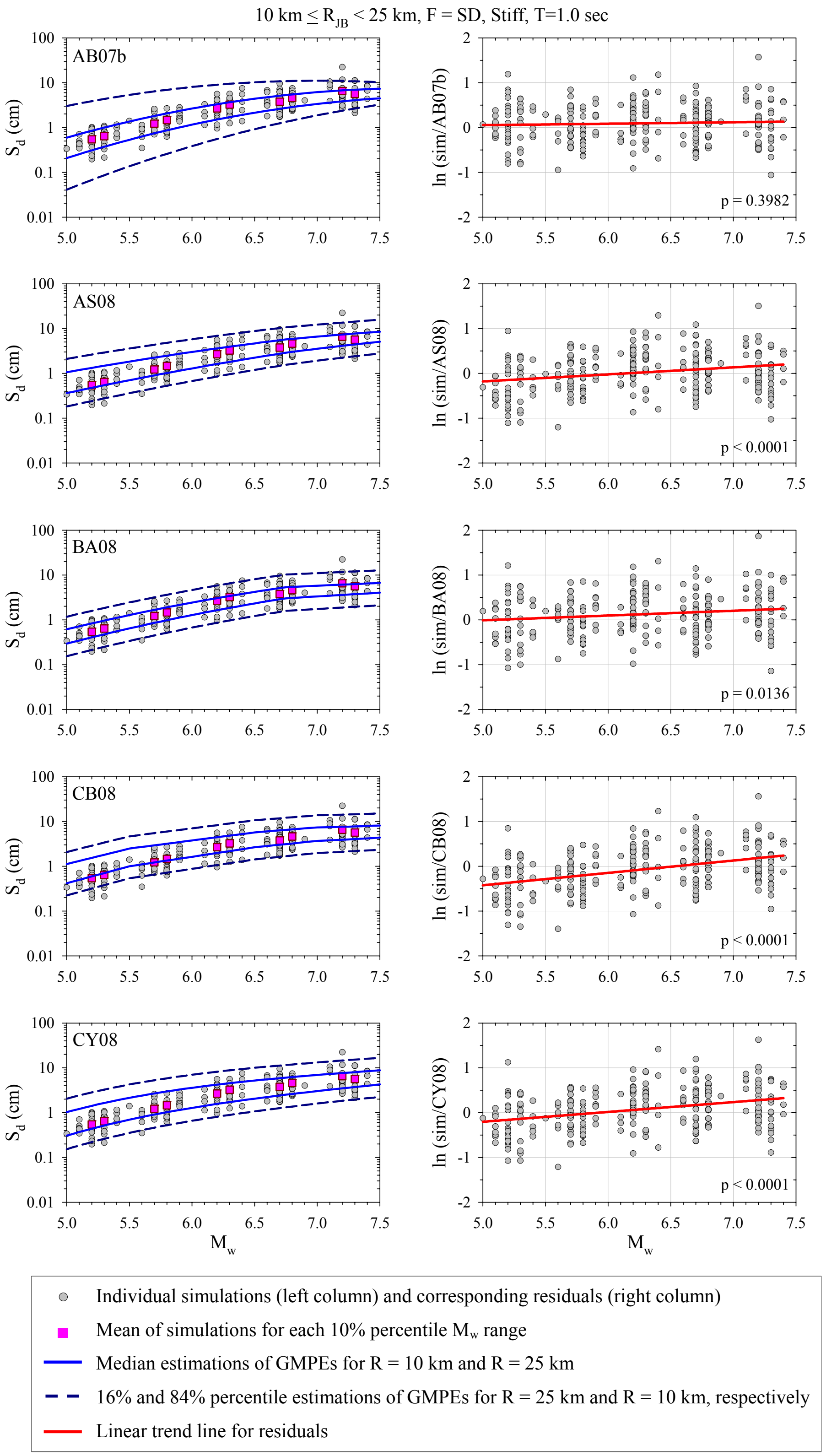

Figure B.20 Magnitude-dependent comparison of stiff site simulations and GMPEs in terms of S_d ($\xi = 5\%$) at T = 1.0 sec for shallow dipping (SD) faults

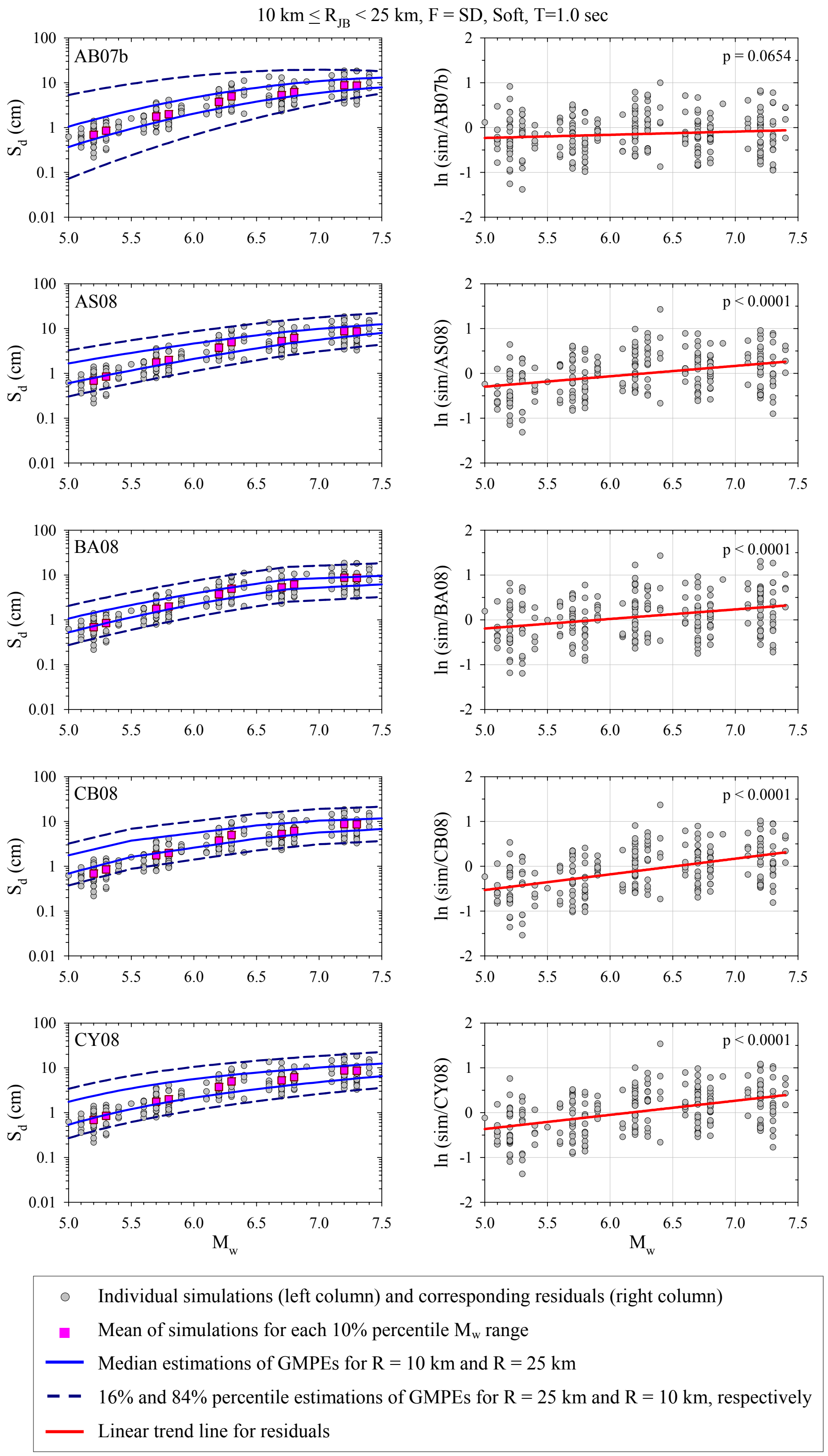

Figure B.21 Magnitude-dependent comparison of soft site simulations and GMPEs in terms of S_d ($\xi = 5\%$) at T = 1.0 sec for shallow dipping (SD) faults

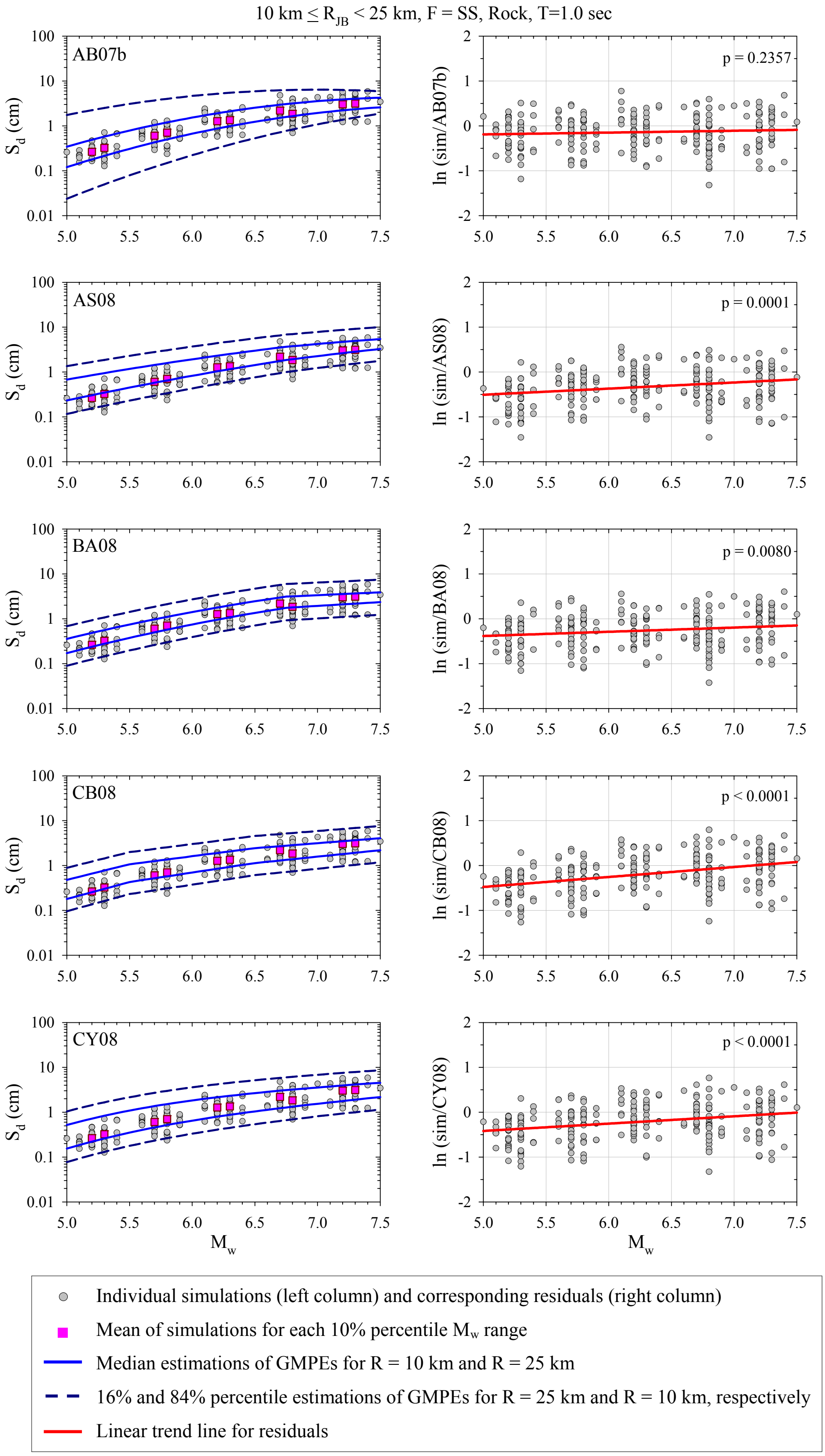

Figure B.22 Magnitude-dependent comparison of rock site simulations and GMPEs in terms of S_d ($\xi = 5\%$) at T = 1.0 sec for strike-slip (SS) faults

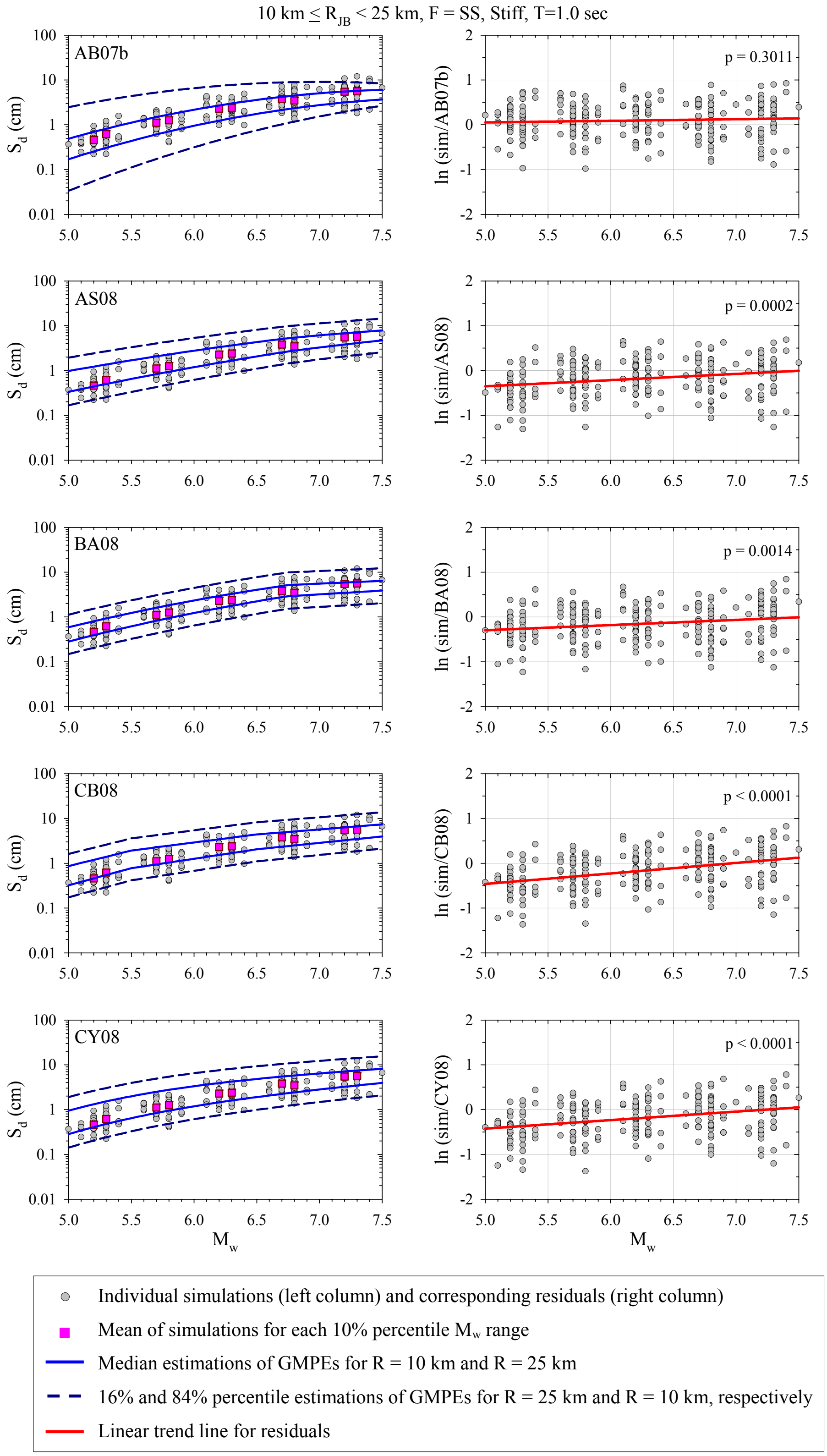

Figure B.23 Magnitude-dependent comparison of stiff site simulations and GMPEs in terms of S_d ($\xi = 5\%$) at T = 1.0 sec for strike-slip (SS) faults

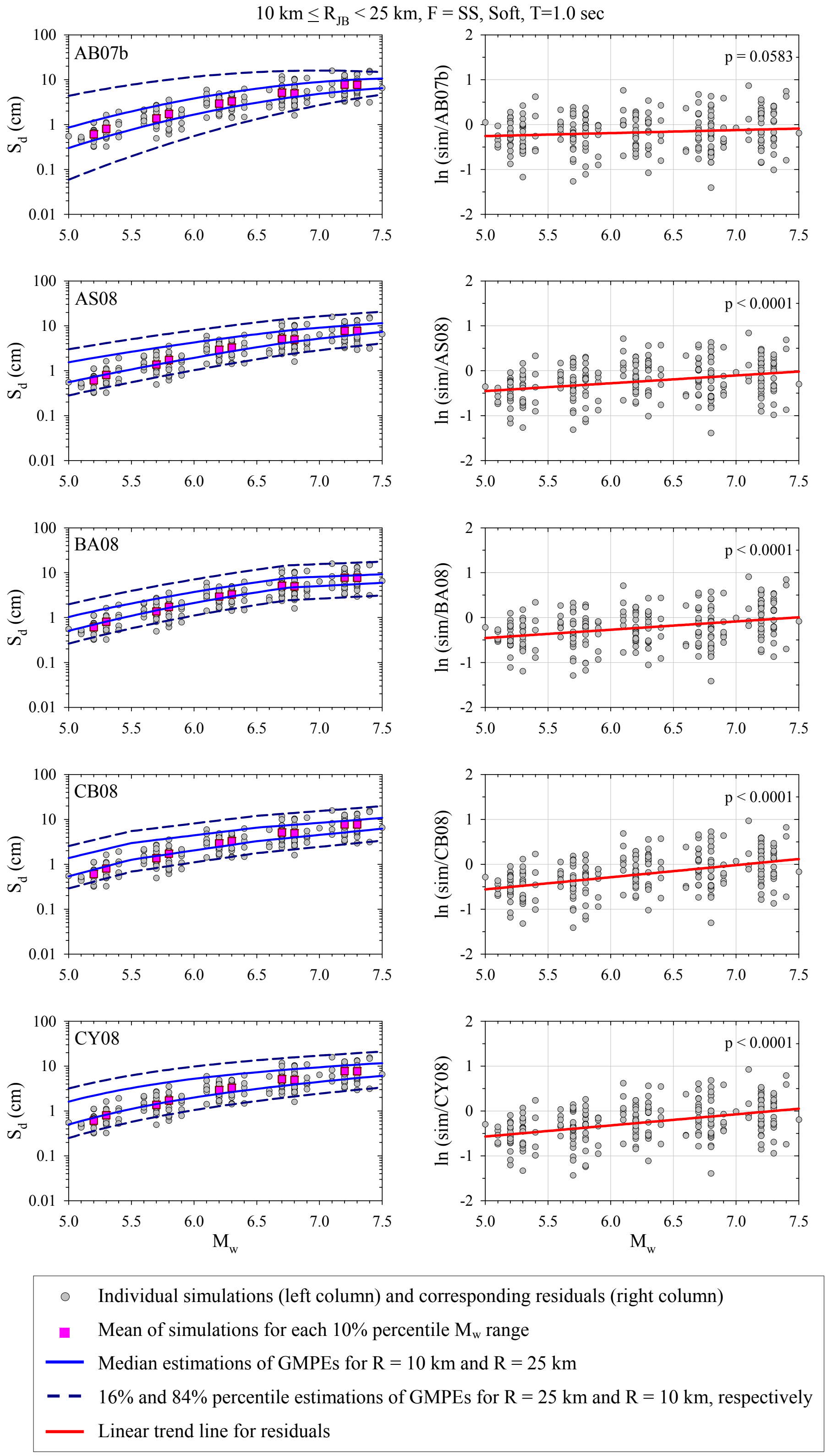

Figure B.24 Magnitude-dependent comparison of soft site simulations and GMPEs in terms of S_d ($\xi = 5\%$) at T = 1.0 sec for strike-slip (SS) faults

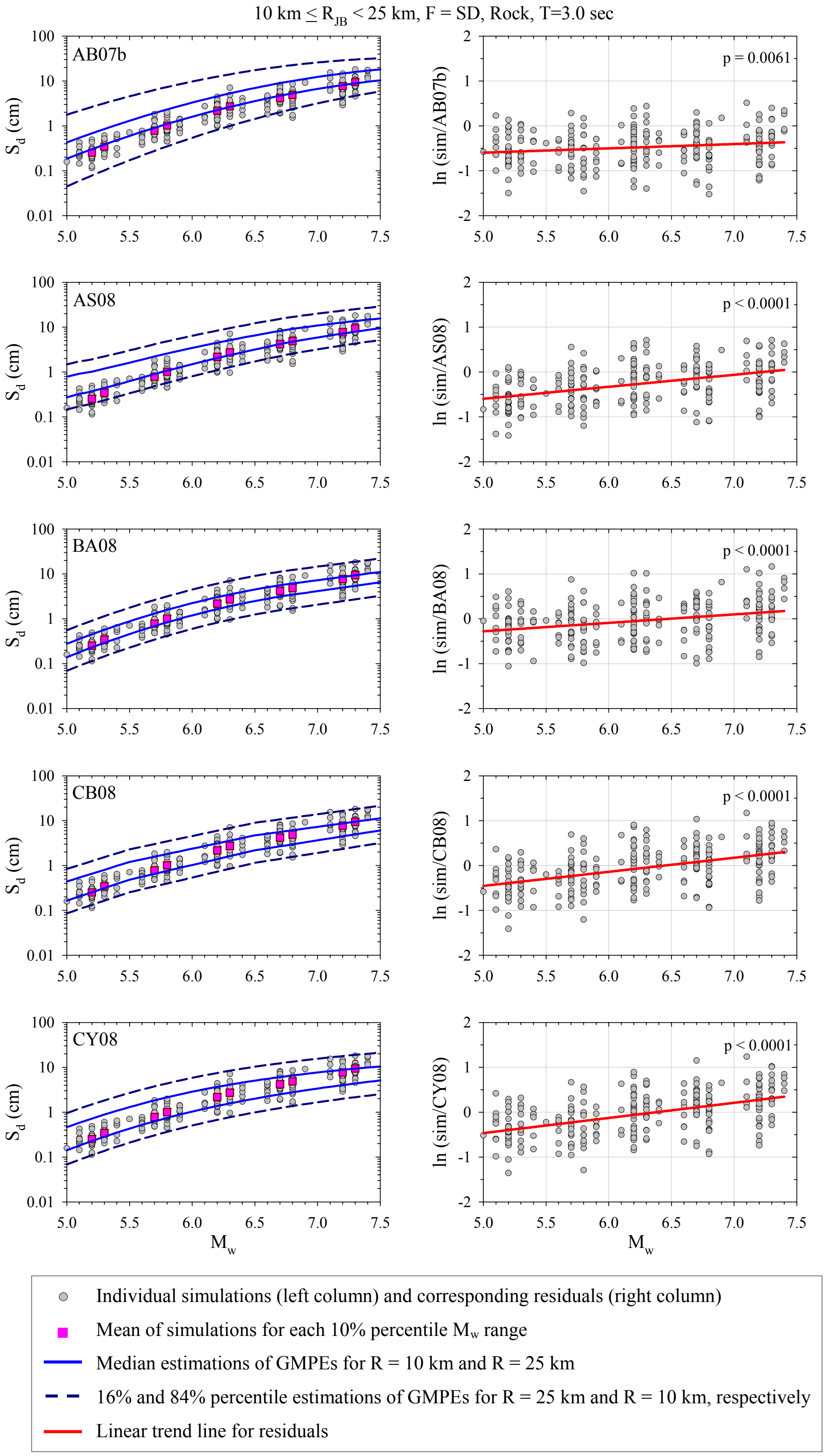

Figure B.25 Magnitude-dependent comparison of rock site simulations and GMPEs in terms of S_d ($\xi = 5\%$) at T = 3.0 sec for shallow dipping (SD) faults

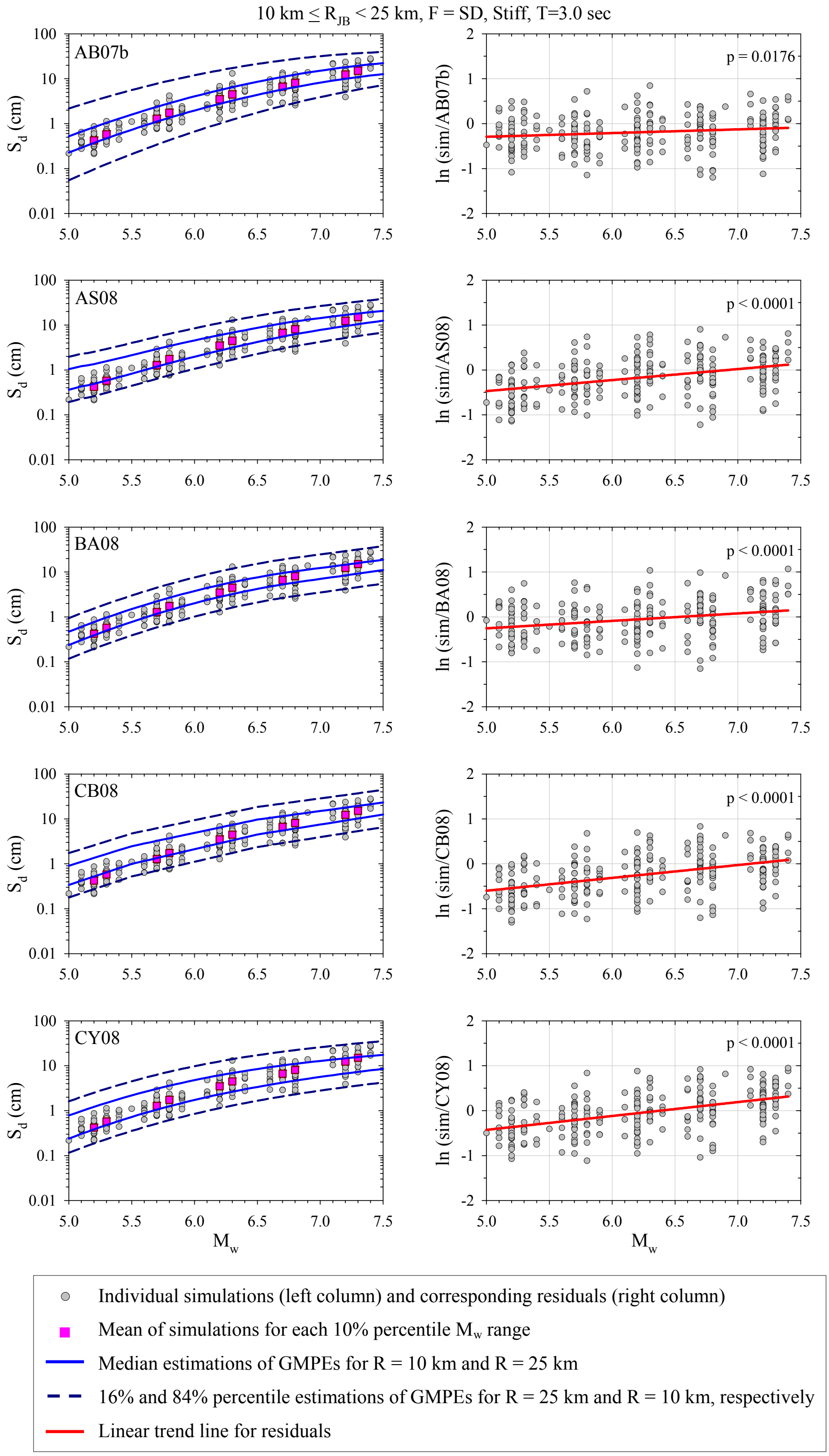

Figure B.26 Magnitude-dependent comparison of stiff site simulations and GMPEs in terms of S_d ($\xi = 5\%$) at T = 3.0 sec for shallow dipping (SD) faults

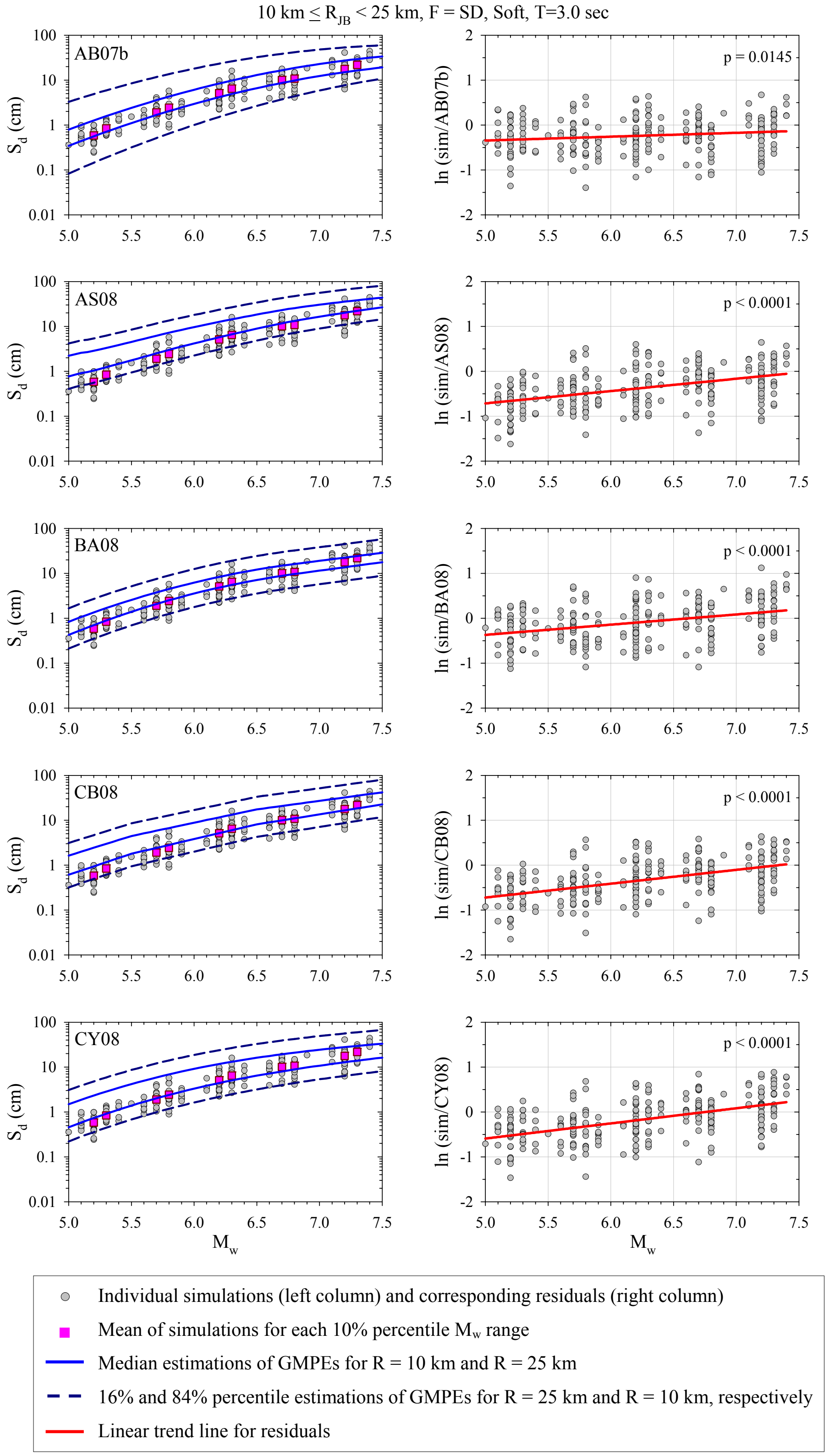

Figure B.27 Magnitude-dependent comparison of soft site simulations and GMPEs in terms of S_d ($\xi = 5\%$) at T = 3.0 sec for shallow dipping (SD) faults

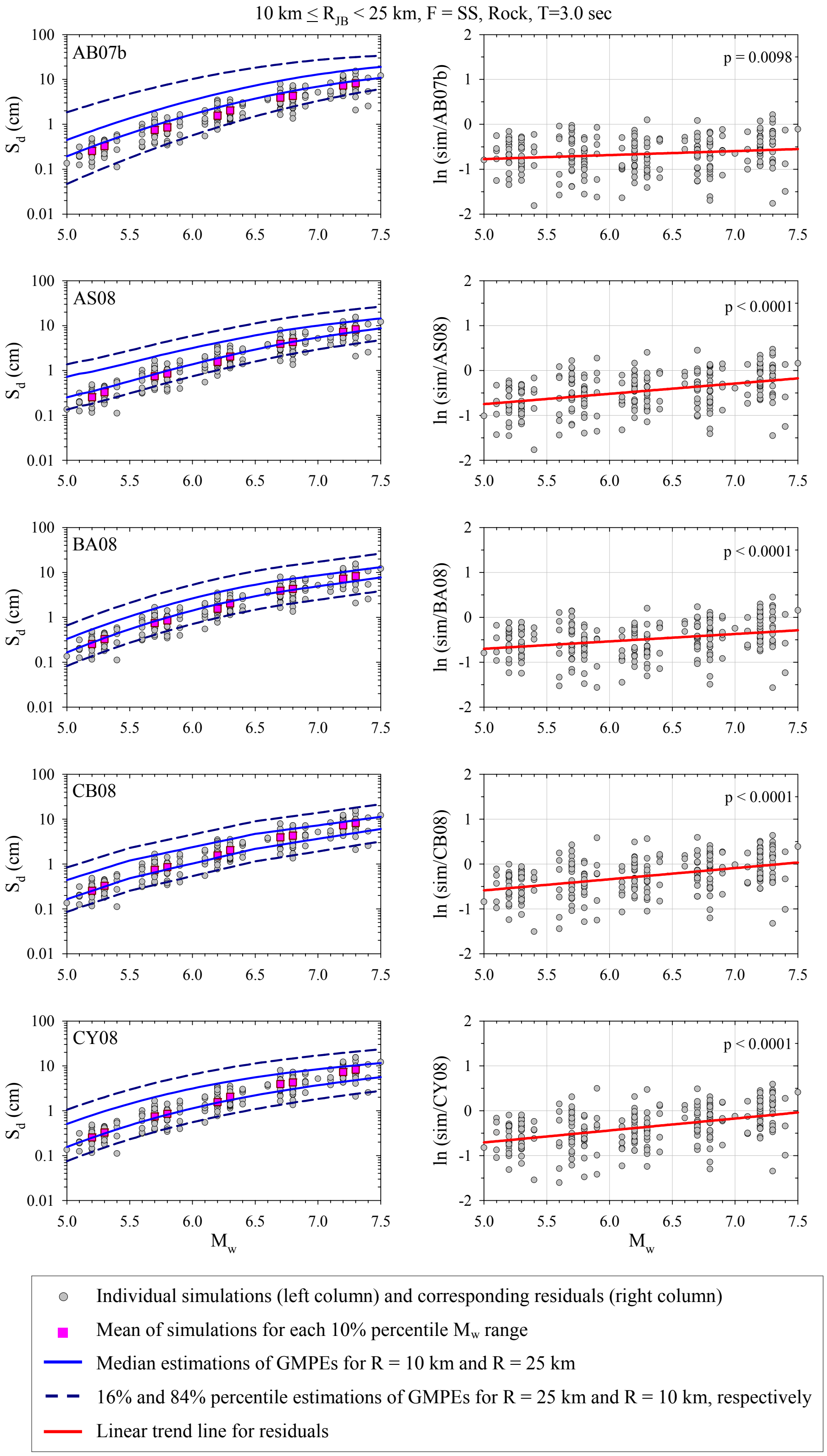

Figure B.28 Magnitude-dependent comparison of rock site simulations and GMPEs in terms of S_d ($\xi = 5\%$) at T = 3.0 sec for strike-slip (SS) faults

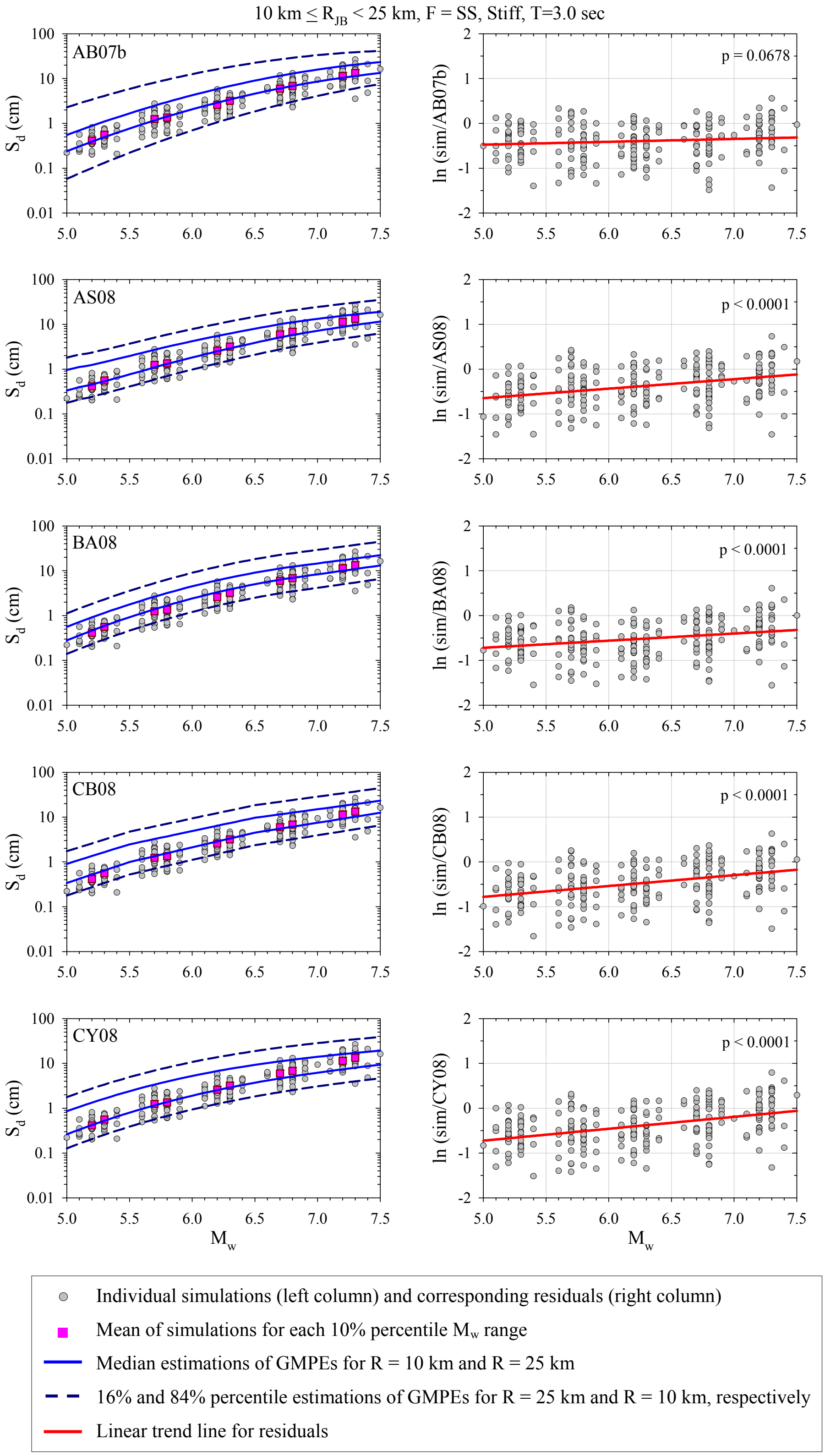

Figure B.29 Magnitude-dependent comparison of stiff site simulations and GMPEs in terms of S_d ($\xi = 5\%$) at T = 3.0 sec for strike-slip (SS) faults

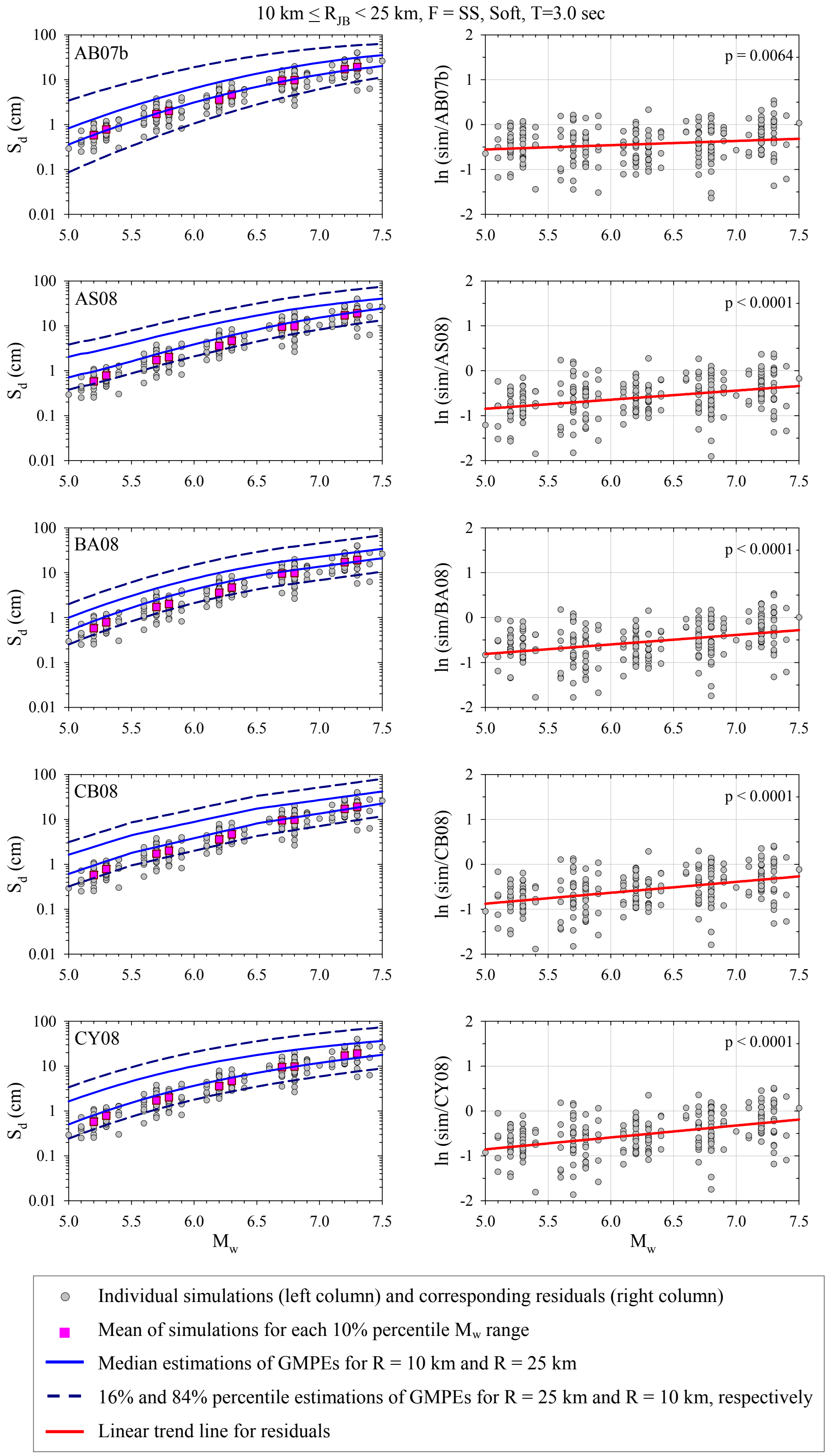

Figure B.30 Magnitude-dependent comparison of soft site simulations and GMPEs in terms of S_d ($\xi = 5\%$) at T = 3.0 sec for strike-slip (SS) faults

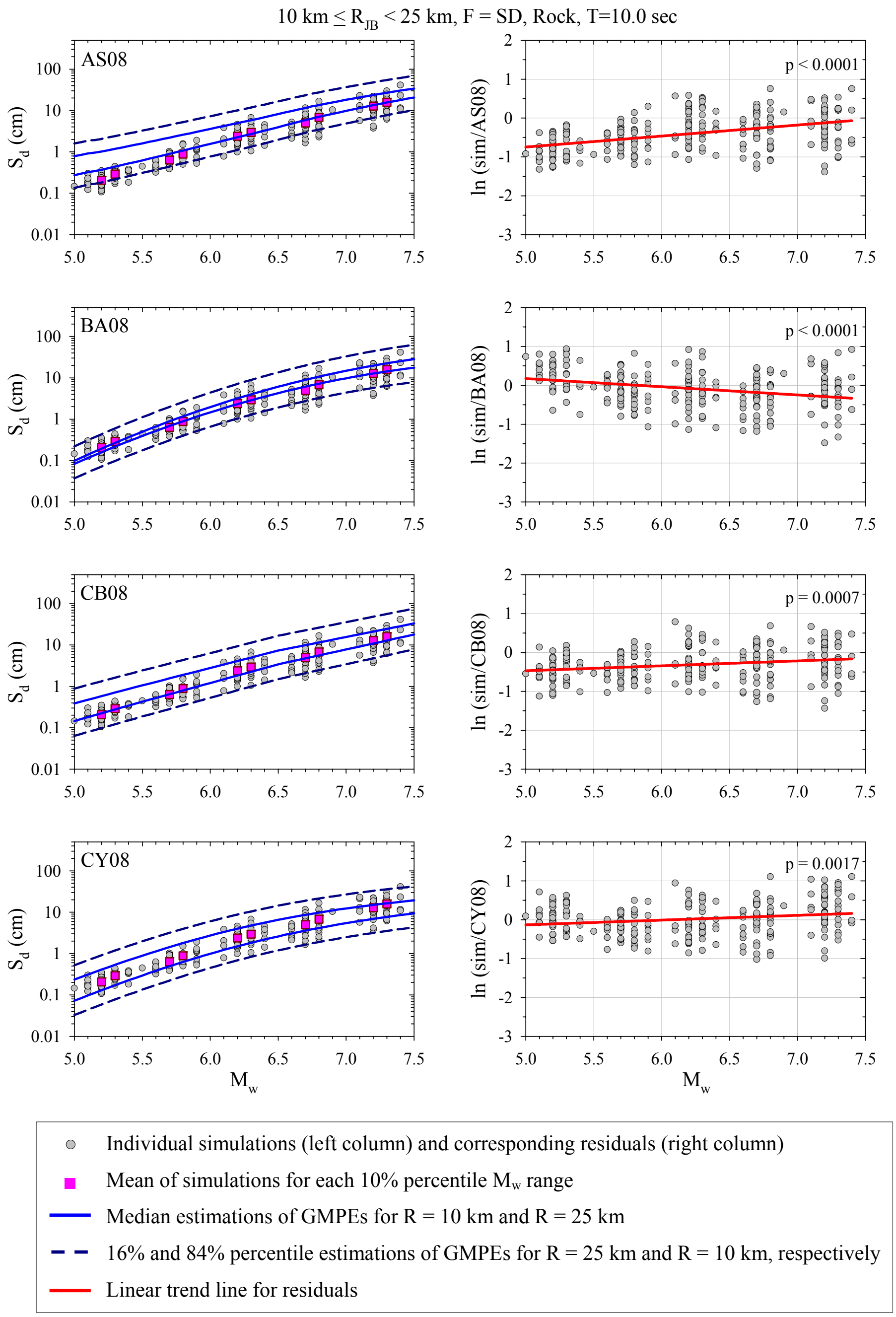

Figure B.31 Magnitude-dependent comparison of rock site simulations and GMPEs in terms of S_d ($\xi = 5\%$) at T = 10.0 sec for shallow dipping (SD) faults

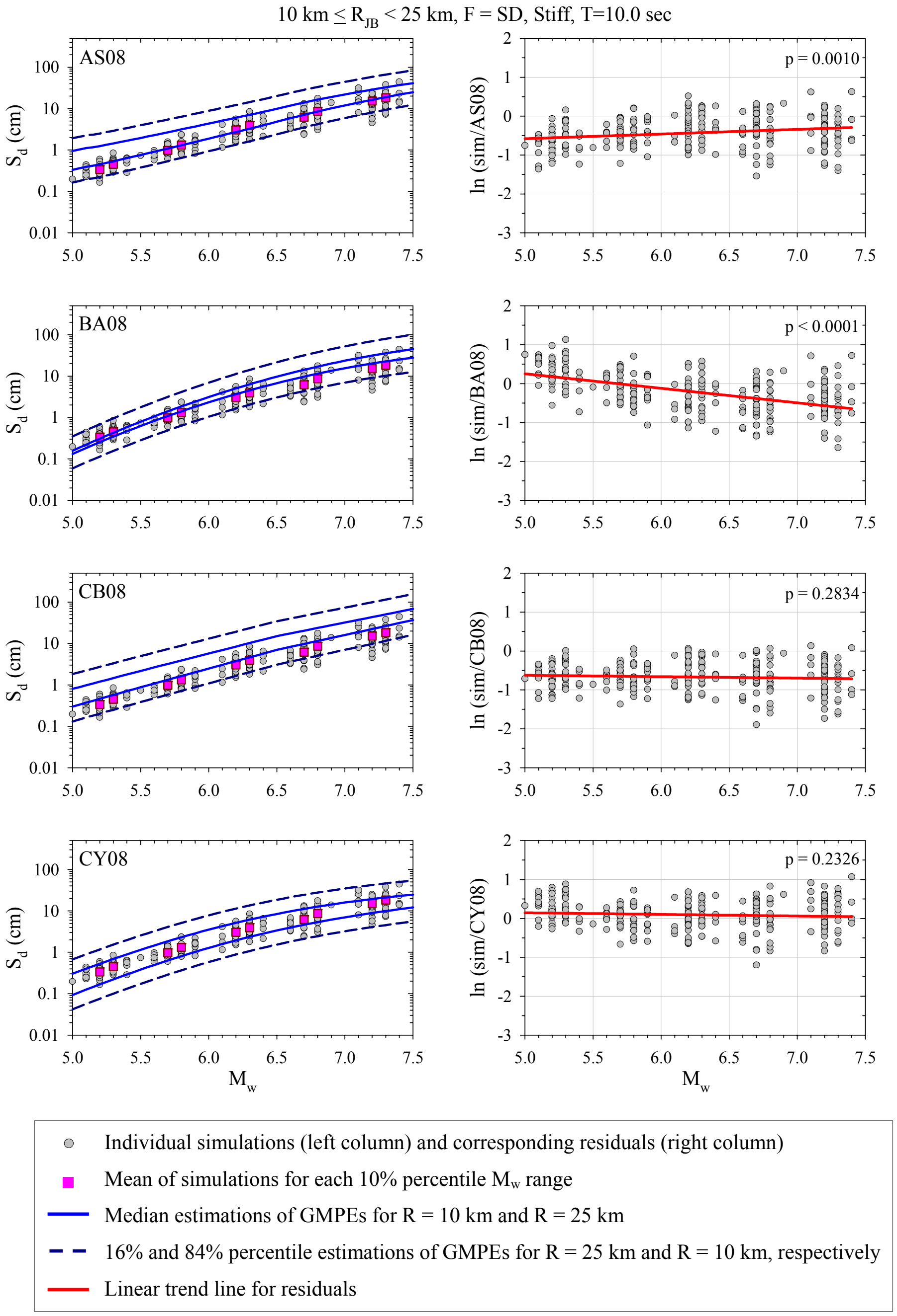

Figure B.32 Magnitude-dependent comparison of stiff site simulations and GMPEs in terms of S_d ($\xi = 5\%$) at T = 10.0 sec for shallow dipping (SD) faults

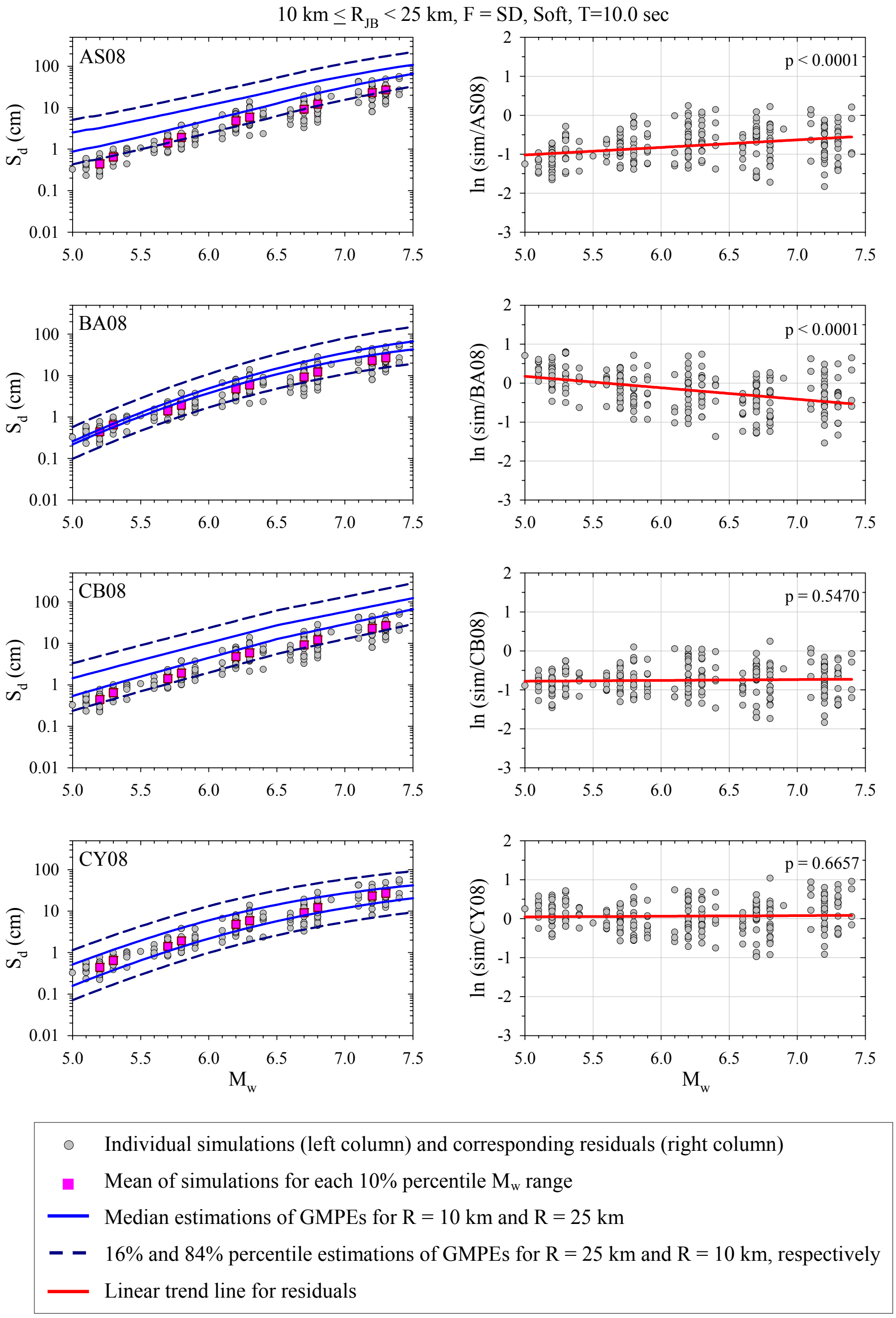

Figure B.33 Magnitude-dependent comparison of soft site simulations and GMPEs in terms of S_d ($\xi = 5\%$) at T = 10.0 sec for shallow dipping (SD) faults

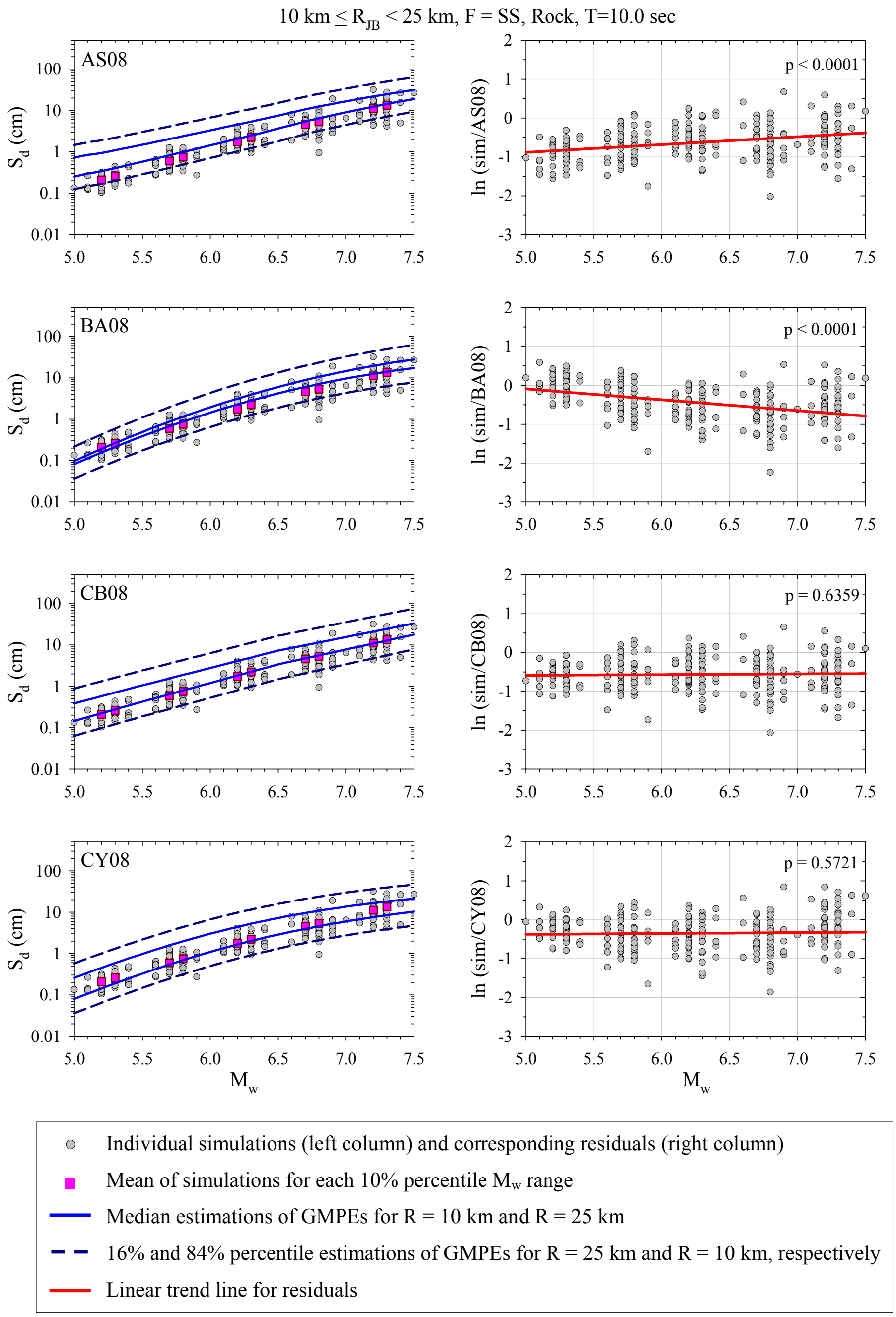

Figure B.34 Magnitude-dependent comparison of rock site simulations and GMPEs in terms of S_d (ξ = 5%) at T = 10.0 sec for strike-slip (SS) faults

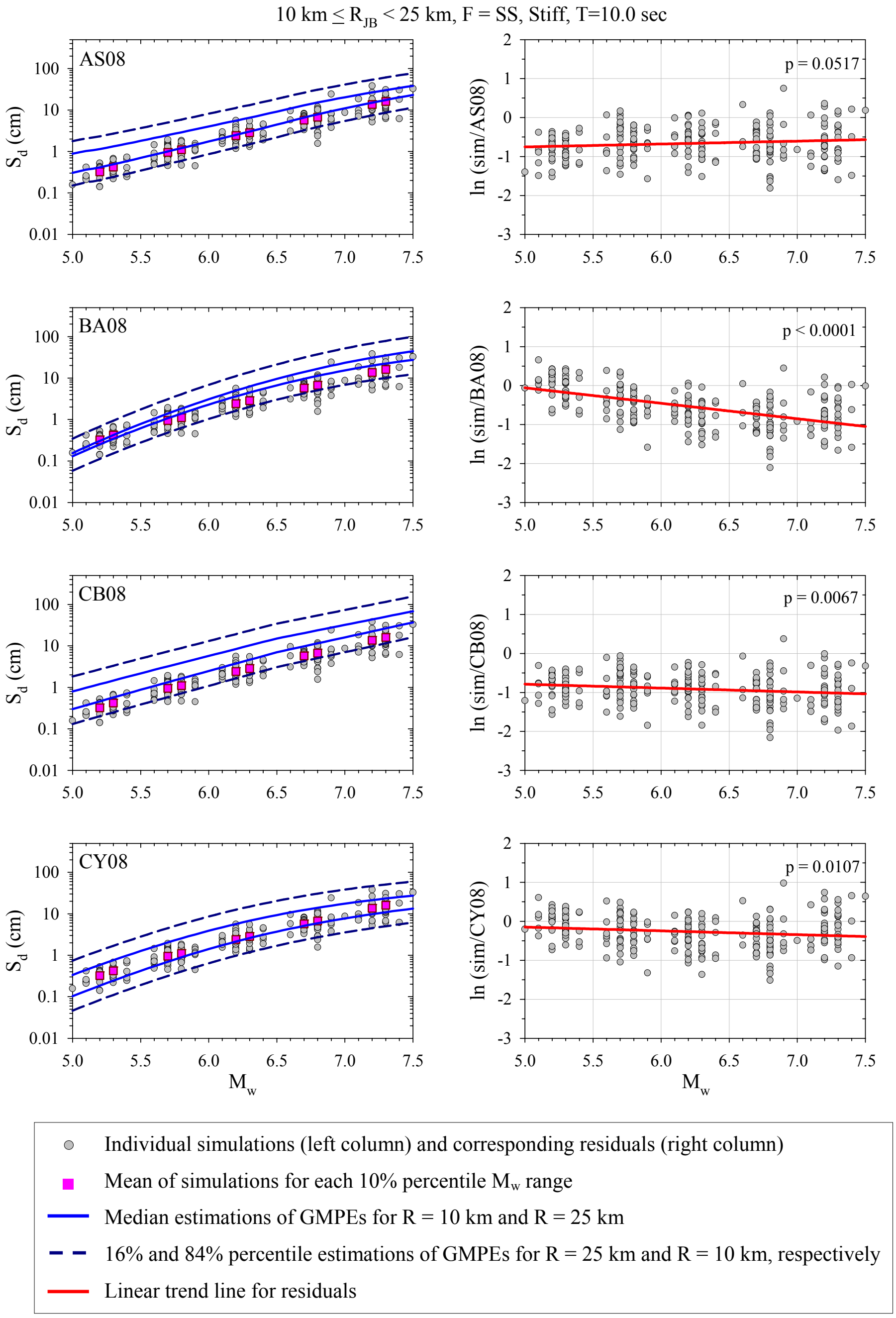

Figure B.35 Magnitude-dependent comparison of stiff site simulations and GMPEs in terms of S_d ($\xi = 5\%$) at T = 10.0 sec for strike-slip (SS) faults

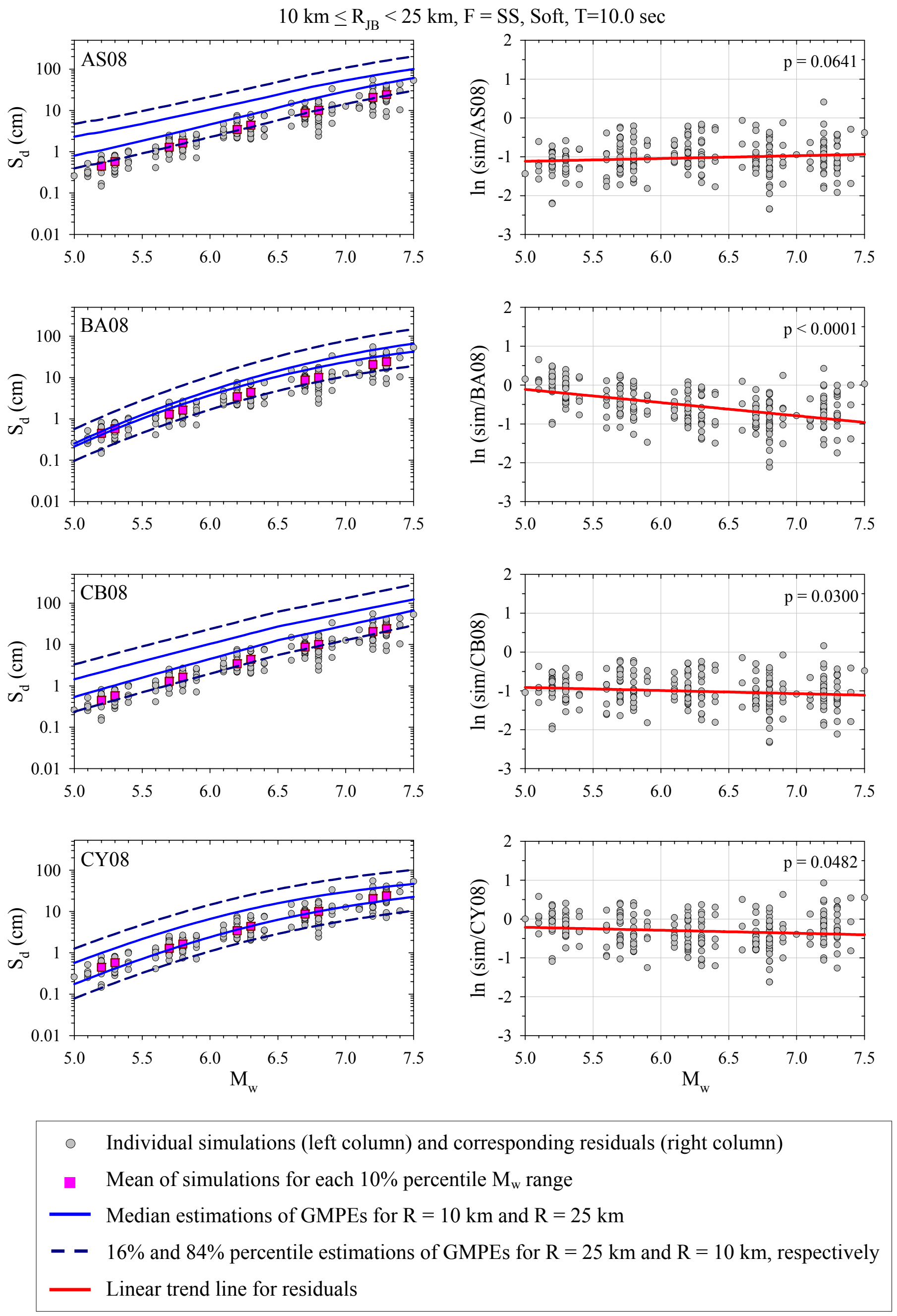

Figure B.36 Magnitude-dependent comparison of soft site simulations and GMPEs in terms of S_d ($\xi = 5\%$) at T = 10.0 sec for strike-slip (SS) faults

APPENDIX C

DISTANCE-DEPENDENT ASSESSMENT OF SIMULATIONS

The distance-dependent scatter plots for individual simulations and corresponding residuals for shallow dipping (SD) and strike-slip (SS) events at rock (760 m/sec < $V_{S,30} \leq$ 1500 m/sec), stiff (360 m/sec < $V_{S,30} \leq$ 760 m/sec) and soft (180 m/sec $\leq V_{S,30} \leq$ 360 m/sec) sites are presented. The magnitude range for the comparative plots is $6.0 \leq M_w < 6.5$.

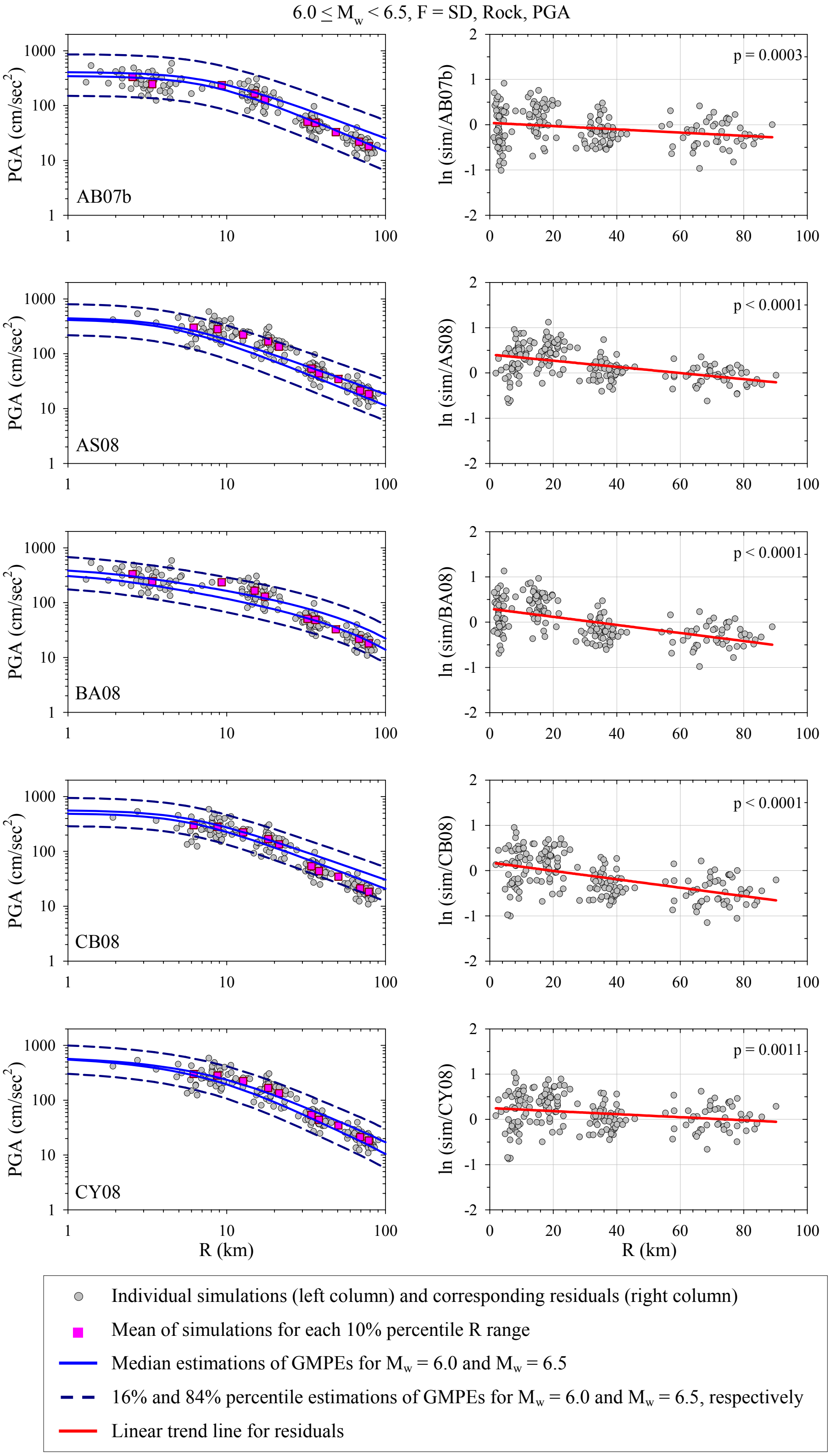

Figure C.1 Distance-dependent comparisons of rock site simulations and GMPEs in terms of PGA for shallow dipping (SD) faults

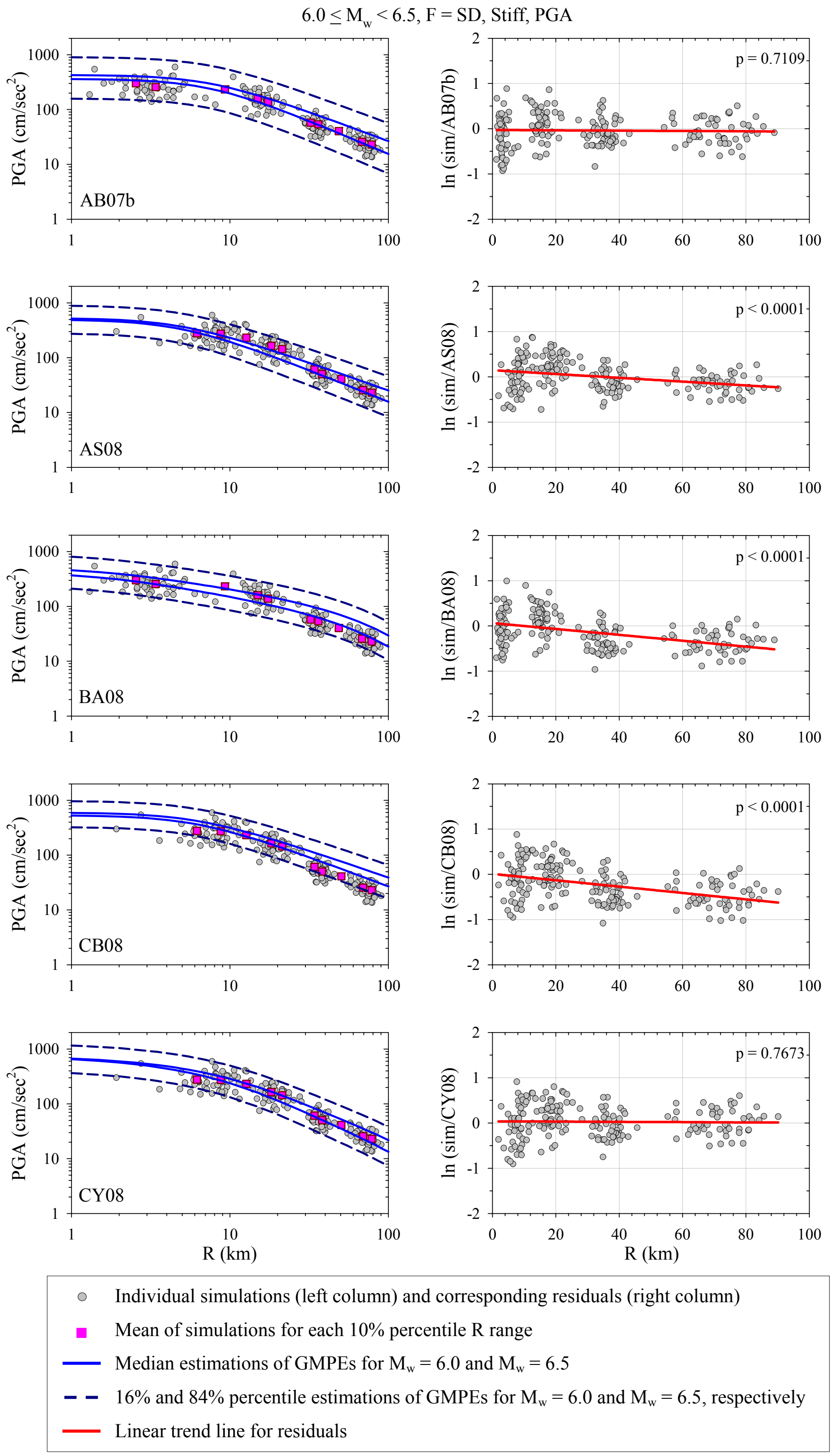

6.0 ≤ M_w < 6.5, F = SD, Stiff, PGA

Figure C.2 Distance-dependent comparisons of stiff site simulations and GMPEs in terms of PGA for shallow dipping (SD) faults

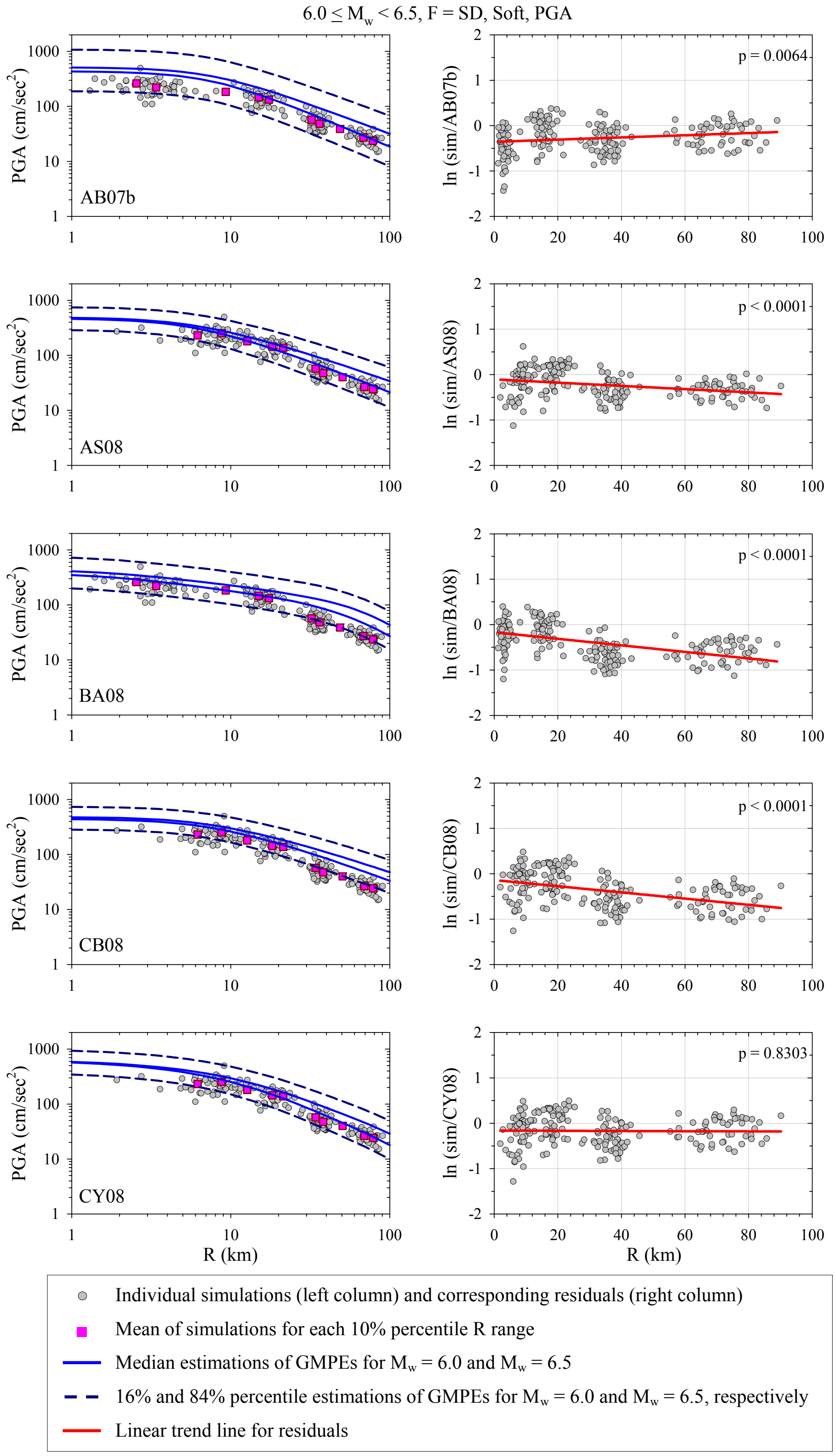

Figure C.3 Distance-dependent comparisons of soft site simulations and GMPEs in terms of PGA for shallow dipping (SD) faults

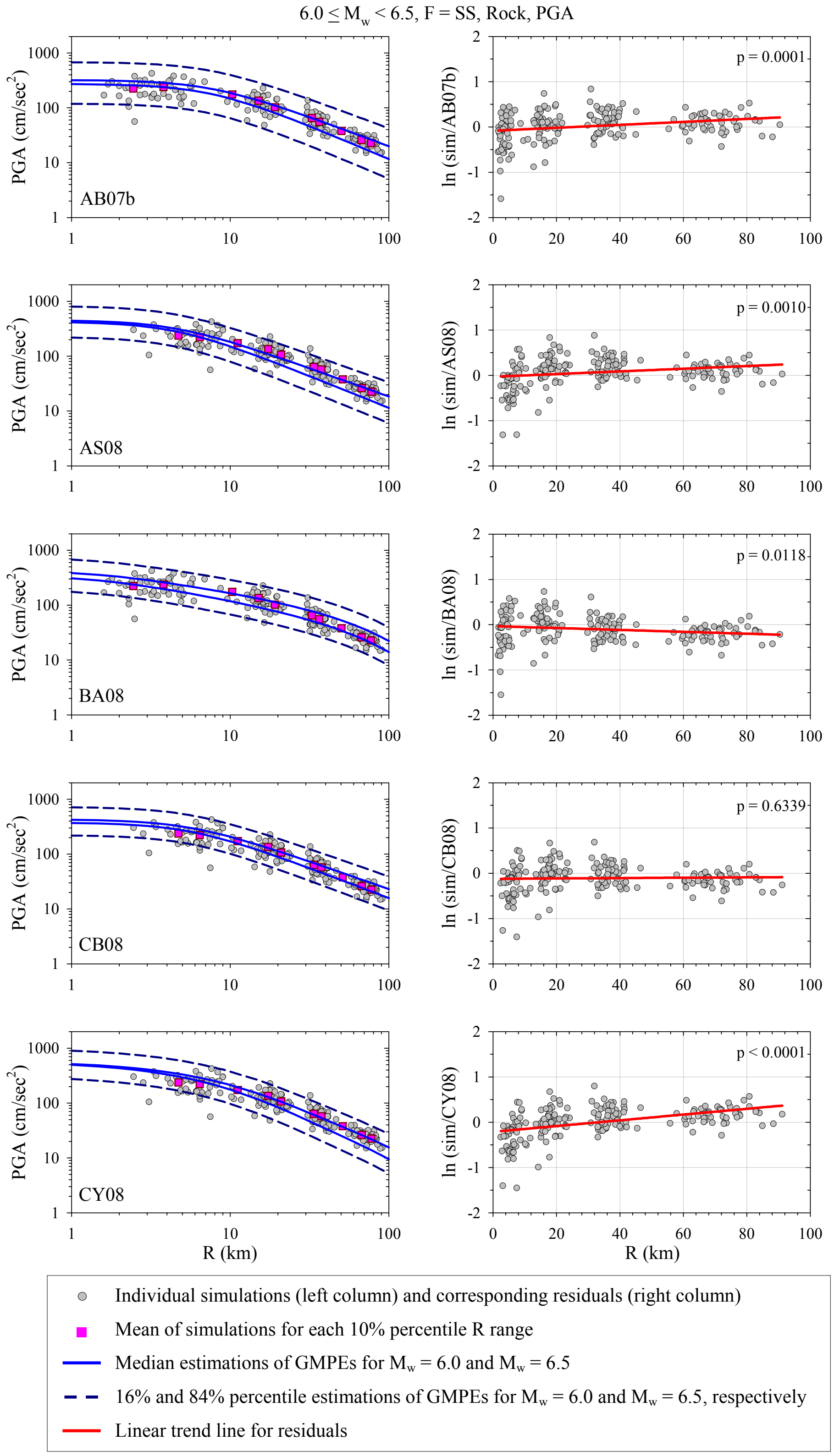

Figure C.4 Distance-dependent comparisons of rock site simulations and GMPEs in terms of PGA for strike-slip (SS) faults

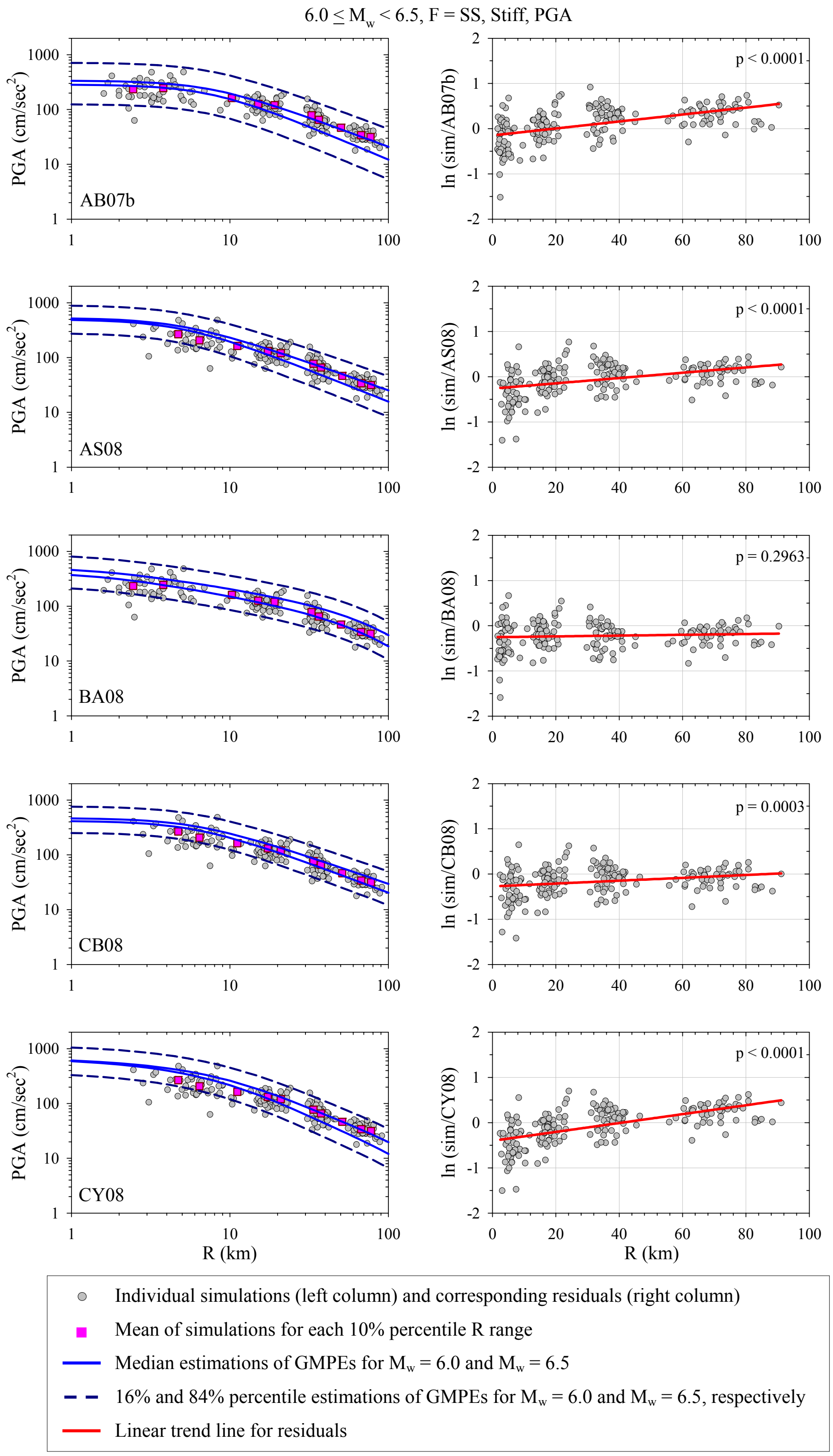

Figure C.5 Distance-dependent comparisons of stiff site simulations and GMPEs in terms of PGA for strike-slip (SS) faults

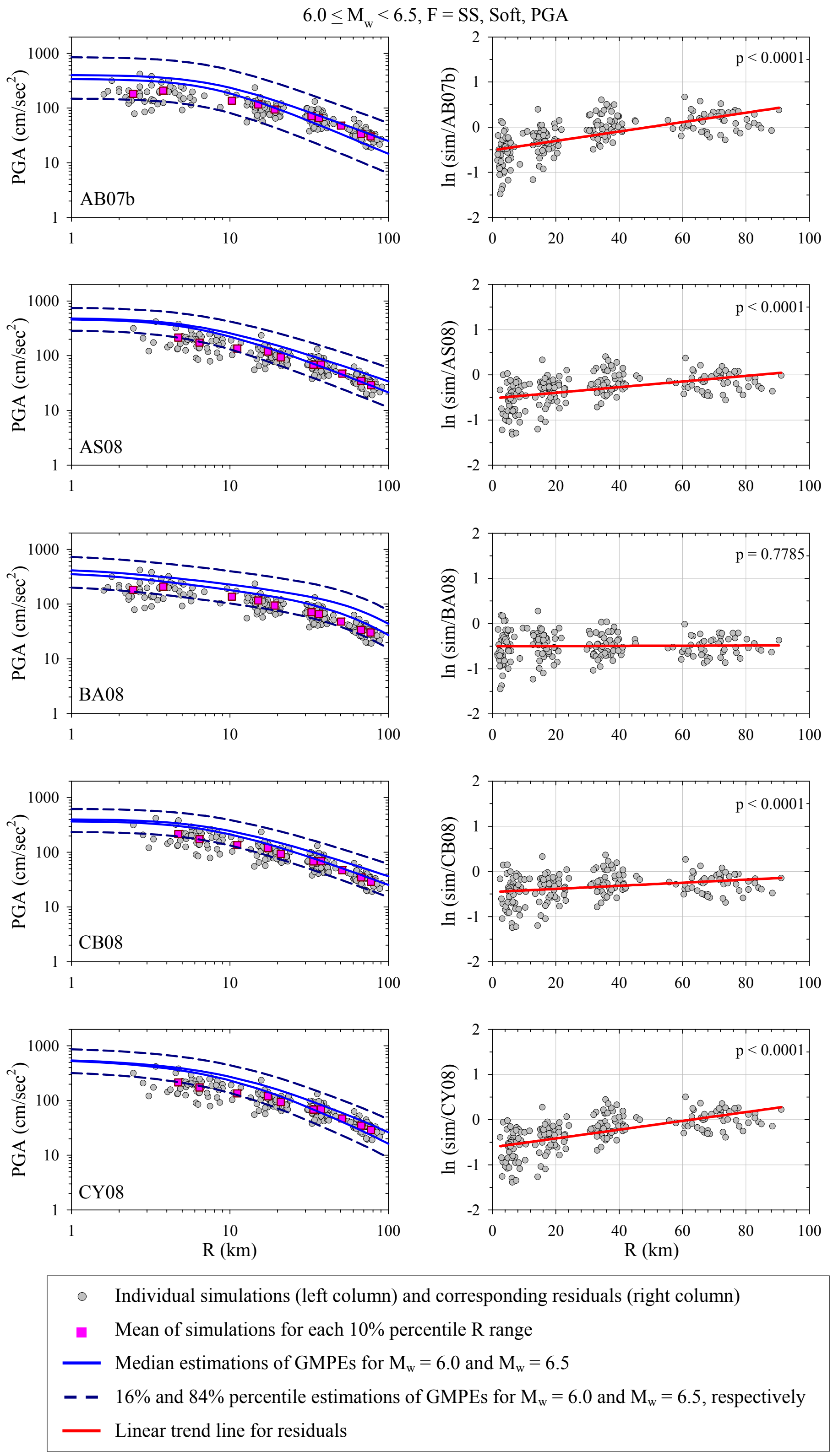

Figure C.6 Distance-dependent comparisons of soft site simulations and GMPEs in terms of PGA for strike-slip (SS) faults

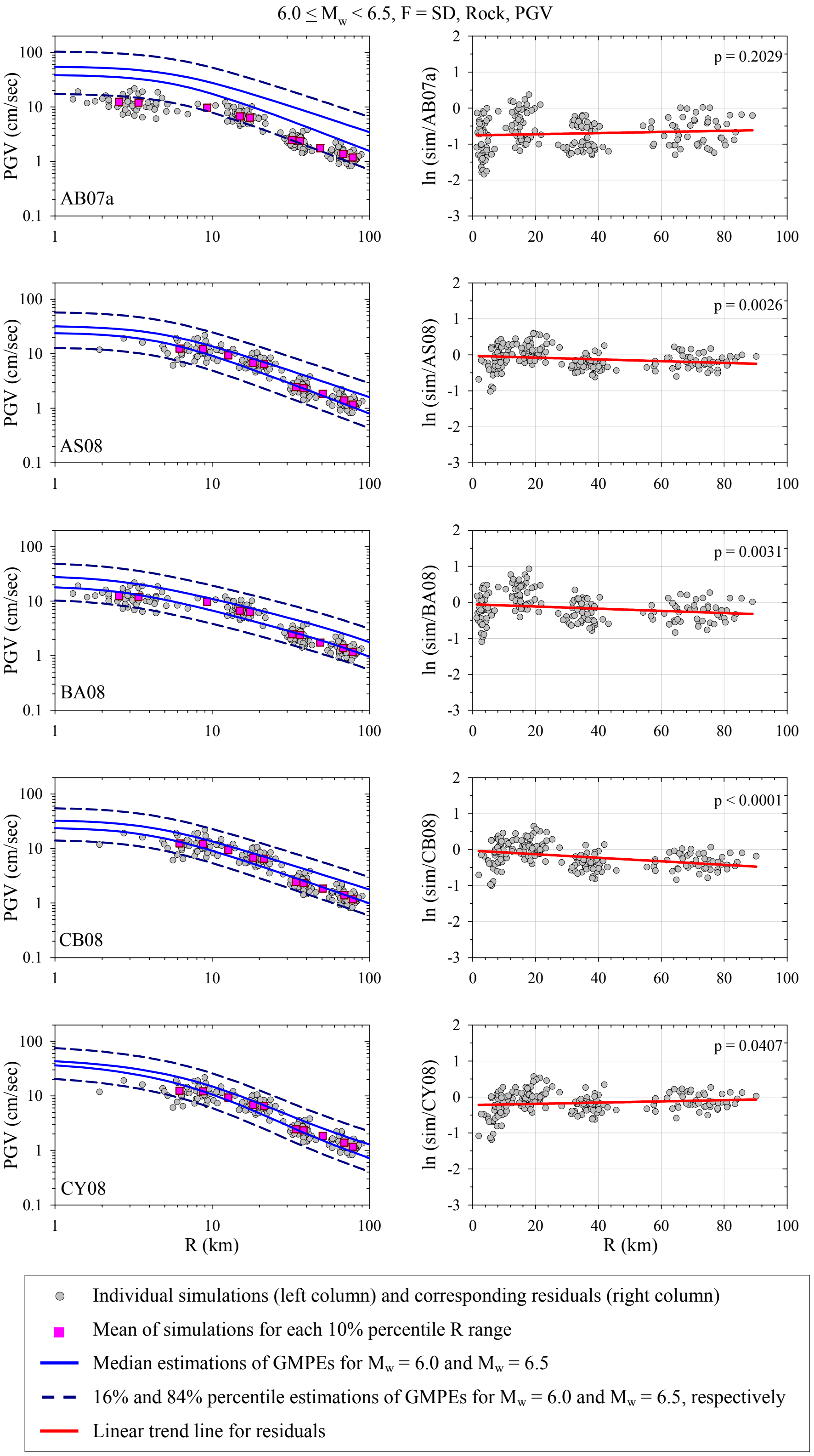

Figure C.7 Distance-dependent comparisons of rock site simulations and GMPEs in terms of PGV for shallow dipping (SD) faults

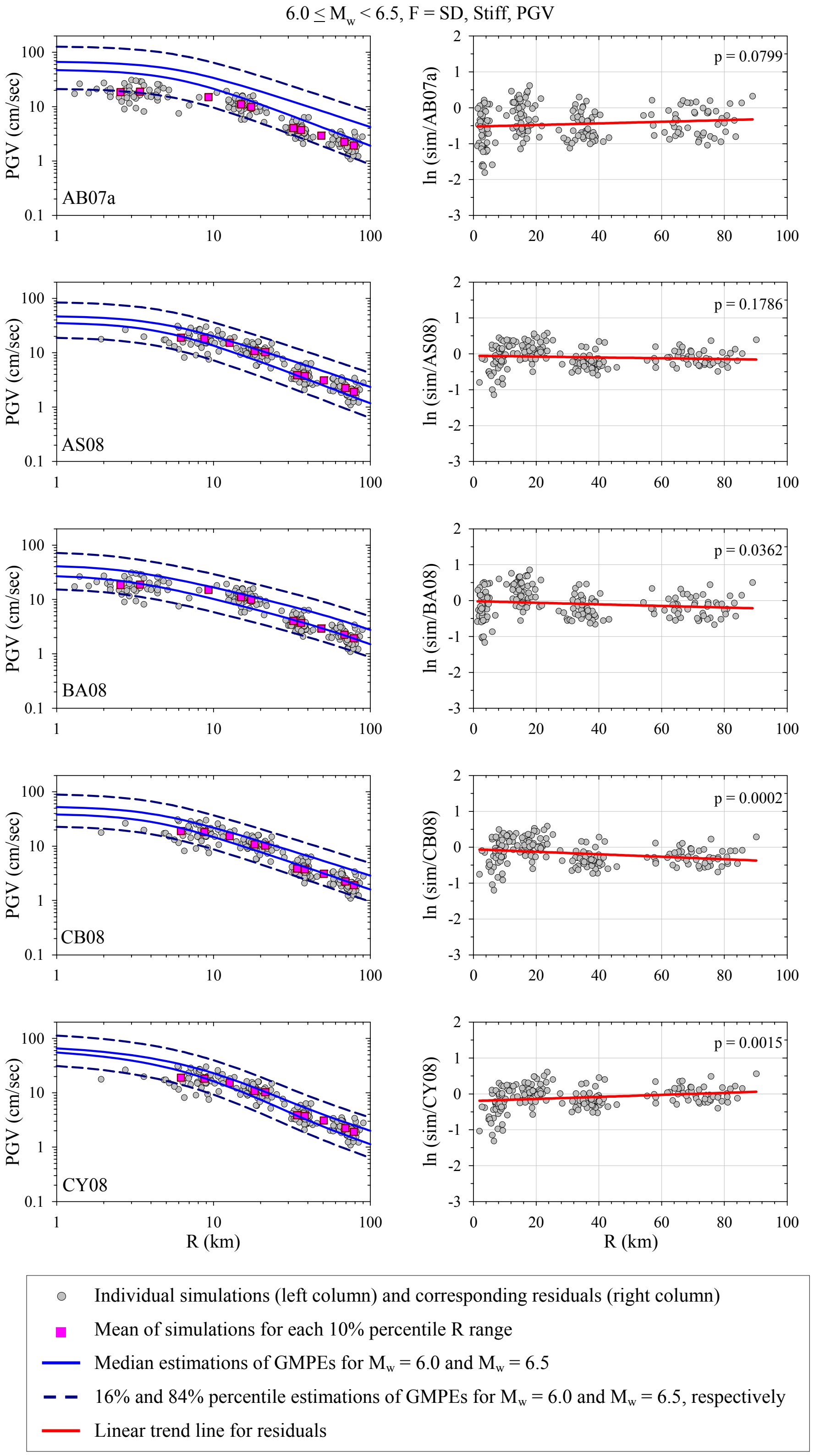

Figure C.8 Distance-dependent comparisons of stiff site simulations and GMPEs in terms of PGV for shallow dipping (SD) faults

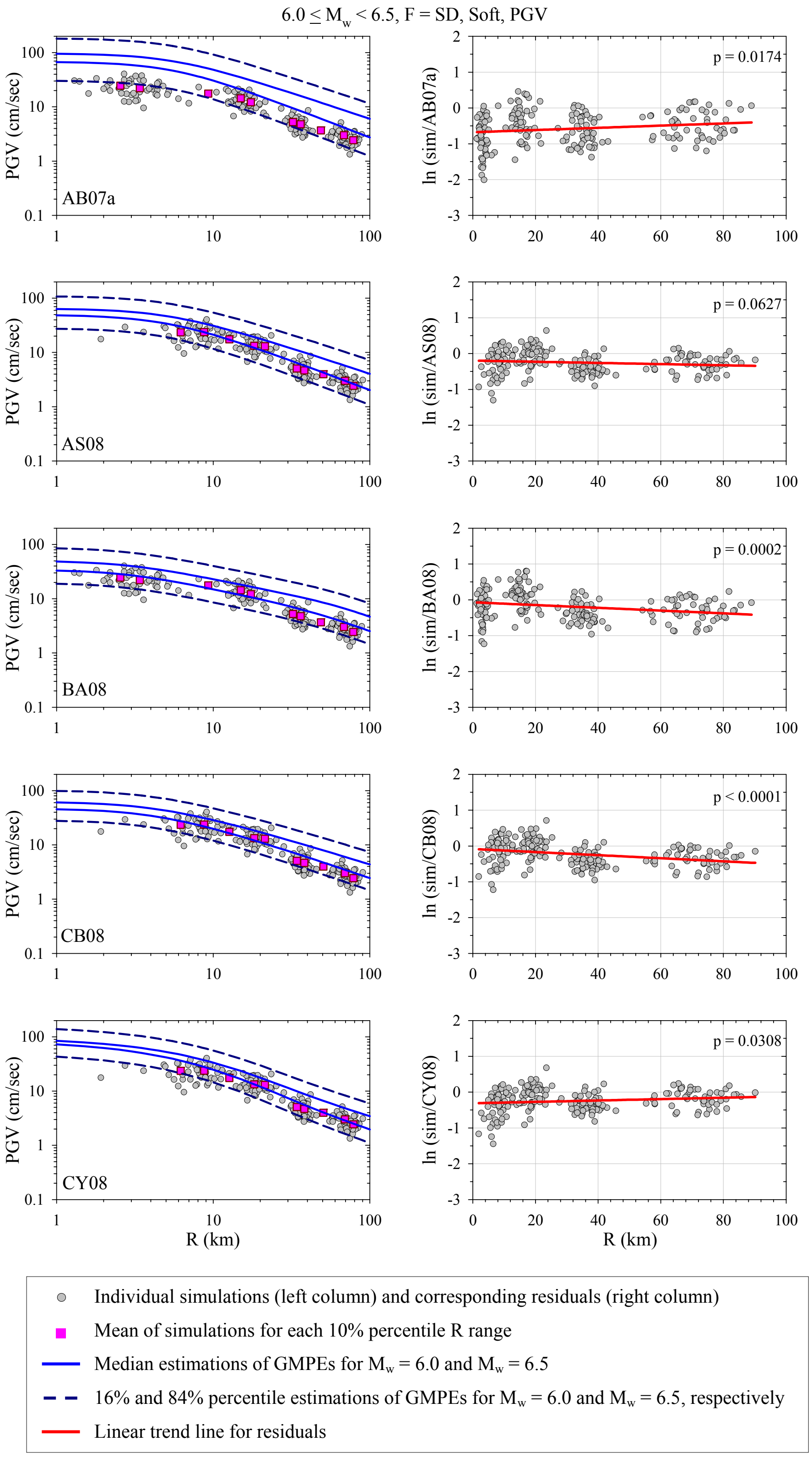

Figure C.9 Distance-dependent comparisons of soft site simulations and GMPEs in terms of PGV for shallow dipping (SD) faults

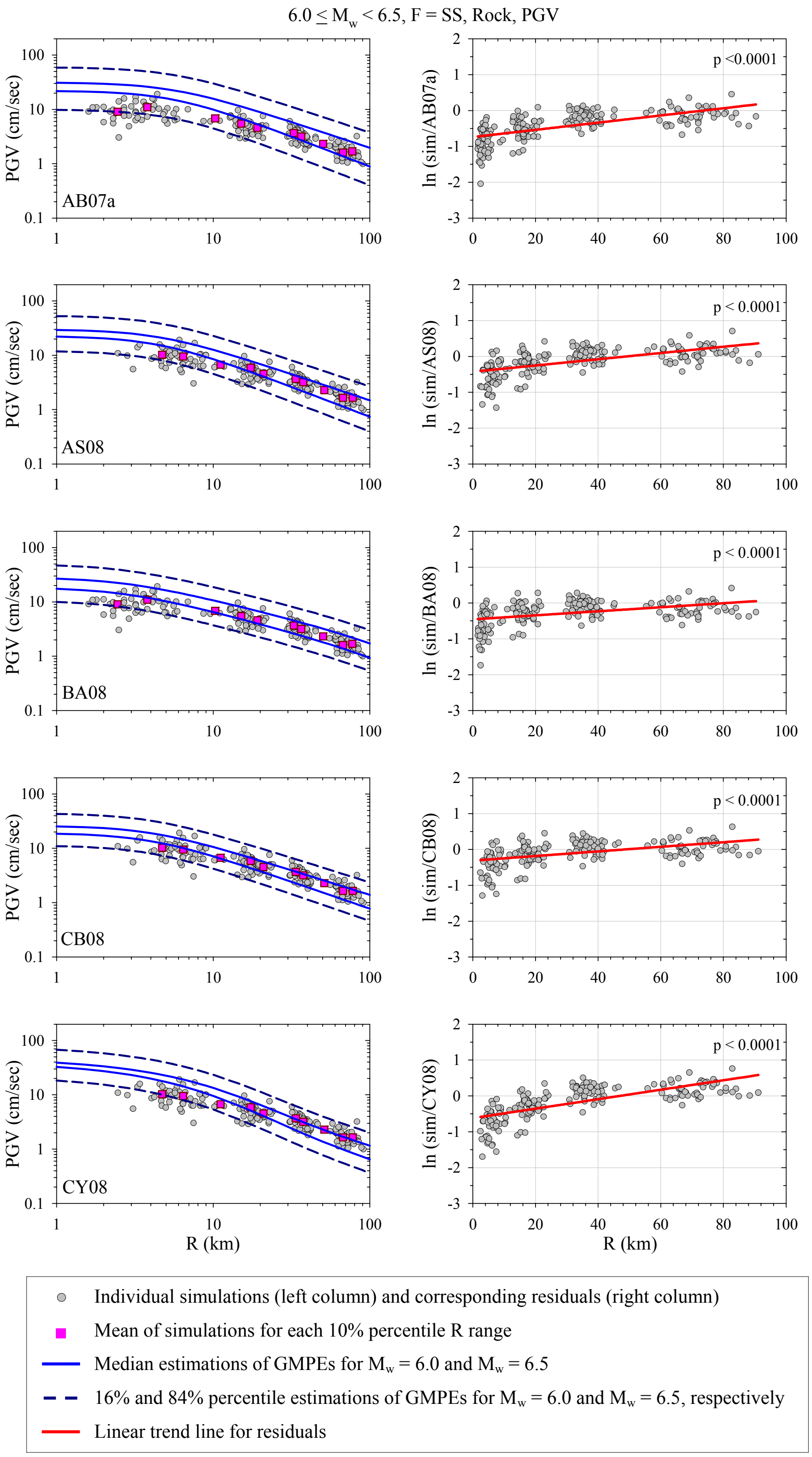

Figure C.10 Distance-dependent comparisons of rock site simulations and GMPEs in terms of PGV for strike-slip (SS) faults

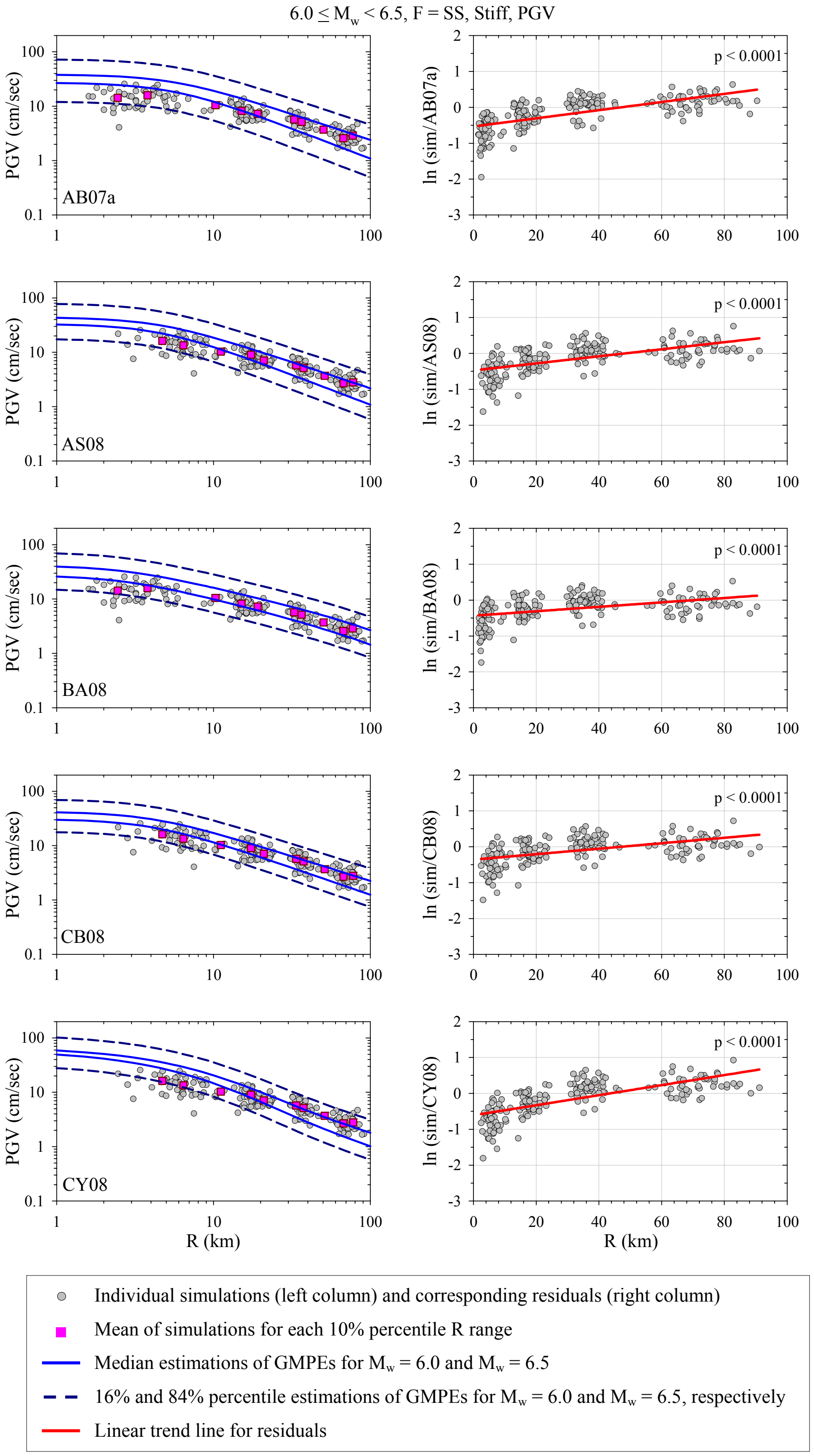

Figure C.11 Distance-dependent comparisons of stiff site simulations and GMPEs in terms of PGV for strike-slip (SS) faults

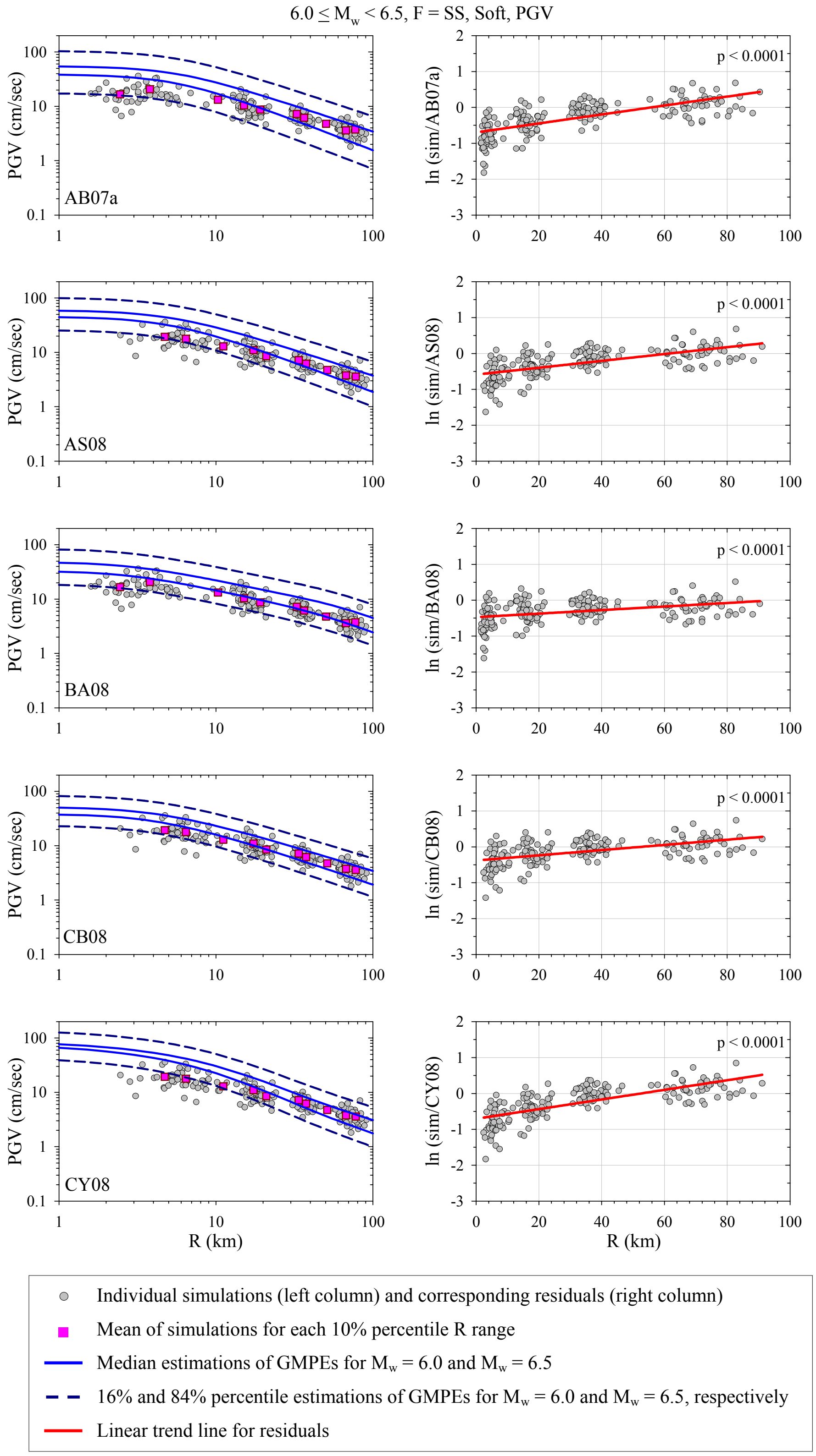

Figure C.12 Distance-dependent comparisons of soft site simulations and GMPEs in terms of PGV for strike-slip (SS) faults

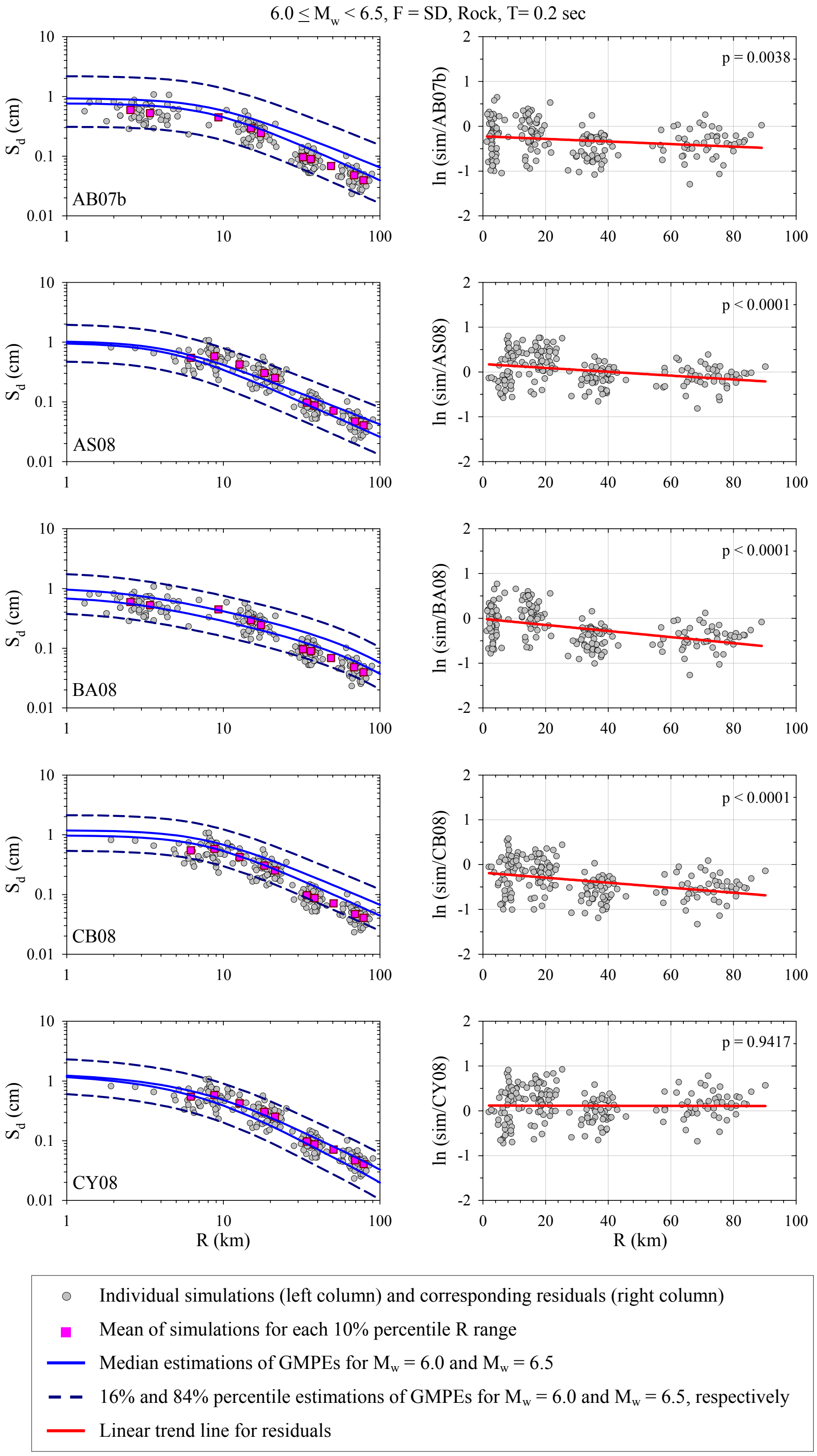

Figure C.13 Distance-dependent comparisons of rock site simulations and GMPEs in terms of S_d ($\xi = 5\%$) at T = 0.2 sec for shallow dipping (SD) faults

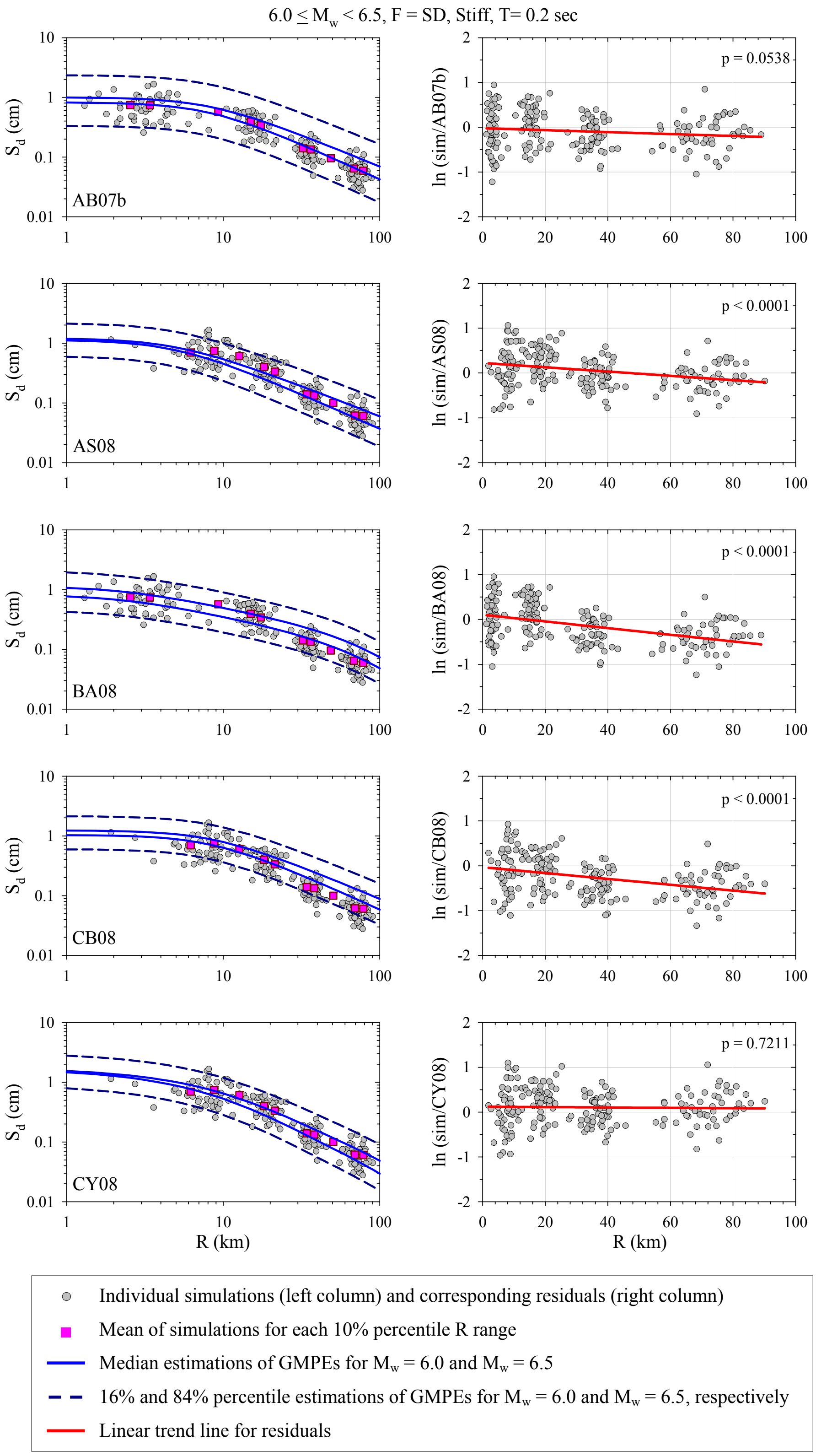

Figure C.14 Distance-dependent comparisons of stiff site simulations and GMPEs in terms of S_d ($\xi = 5\%$) at T = 0.2 sec for shallow dipping (SD) faults

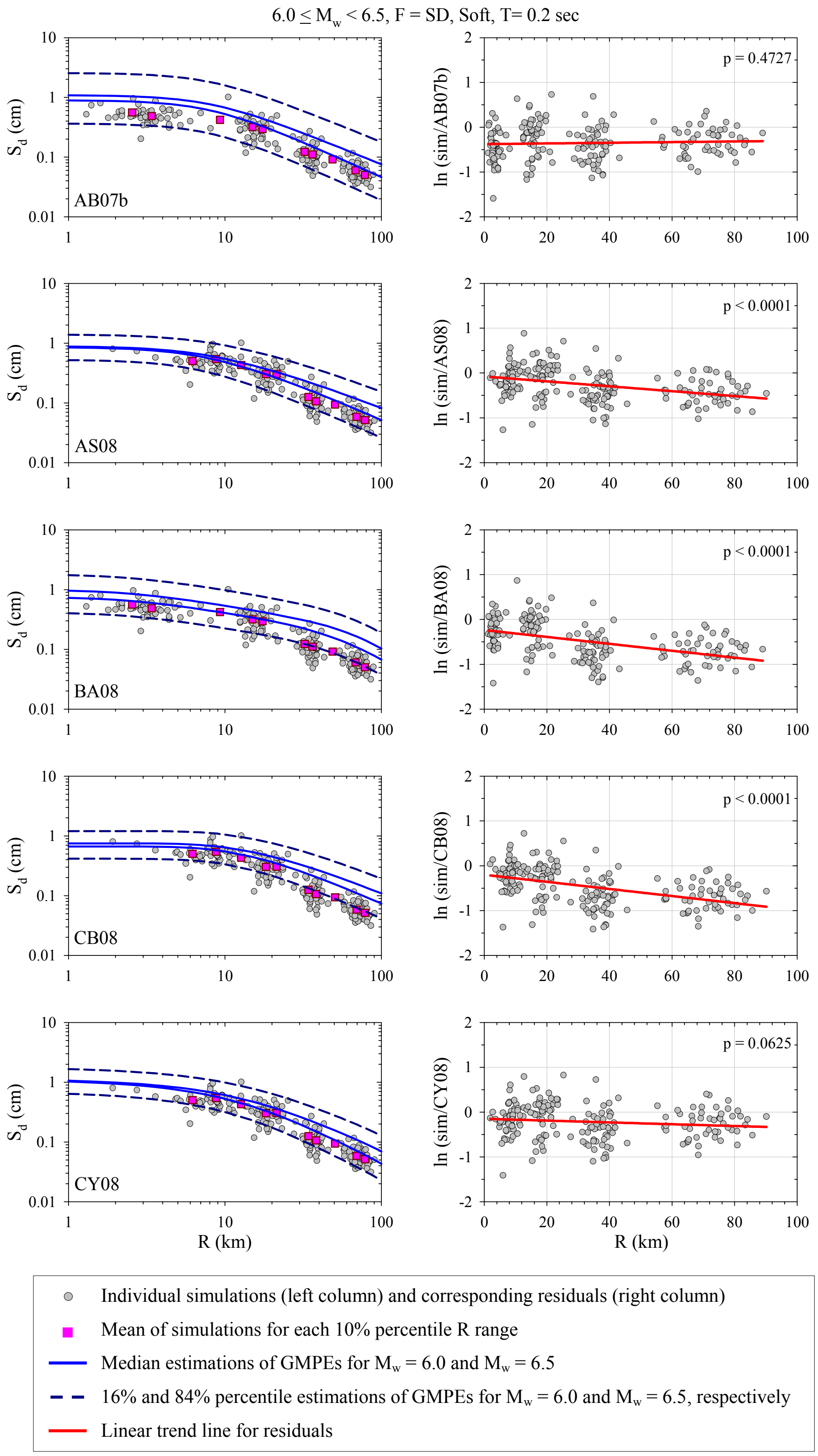

Figure C.15 Distance-dependent comparisons of soft site simulations and GMPEs in terms of S_d ($\xi = 5\%$) at T = 0.2 sec for shallow dipping (SD) faults

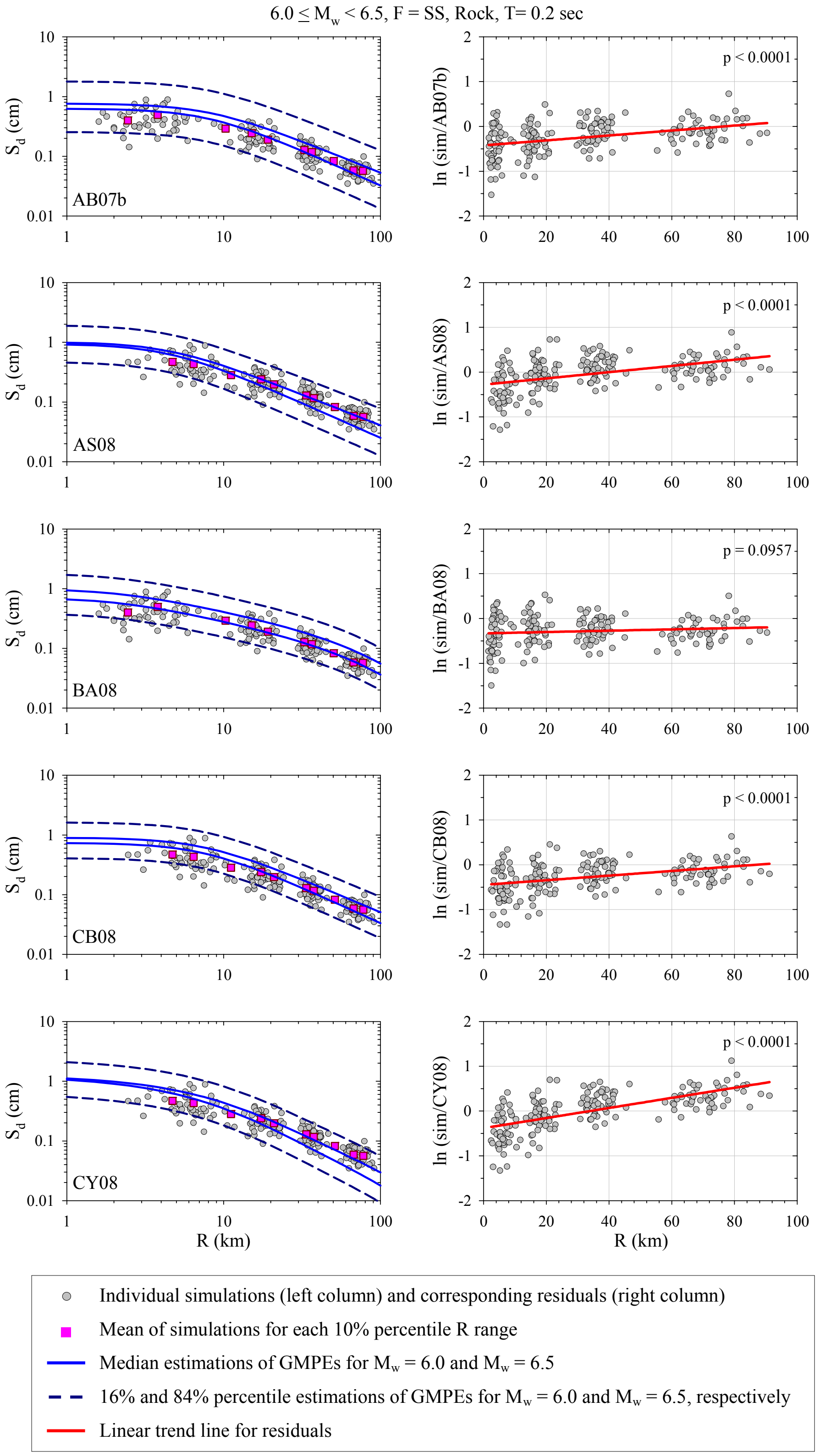

Figure C.16 Distance-dependent comparisons of rock site simulations and GMPEs in terms of S_d ($\xi = 5\%$) at T = 0.2 sec for strike-slip (SS) faults

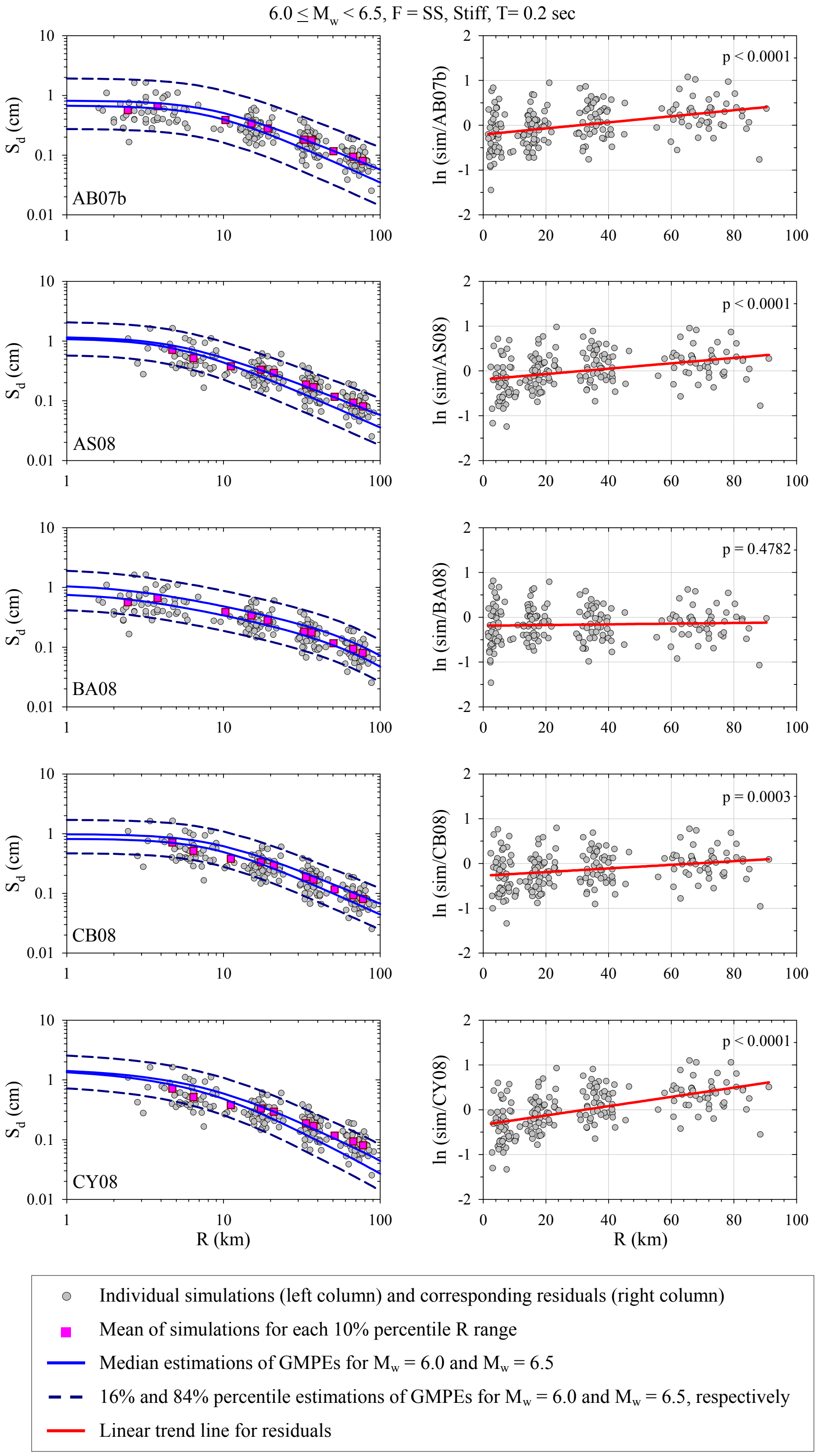

Figure C.17 Distance-dependent comparisons of stiff site simulations and GMPEs in terms of S_d ($\xi = 5\%$) at T = 0.2 sec for strike-slip (SS) faults

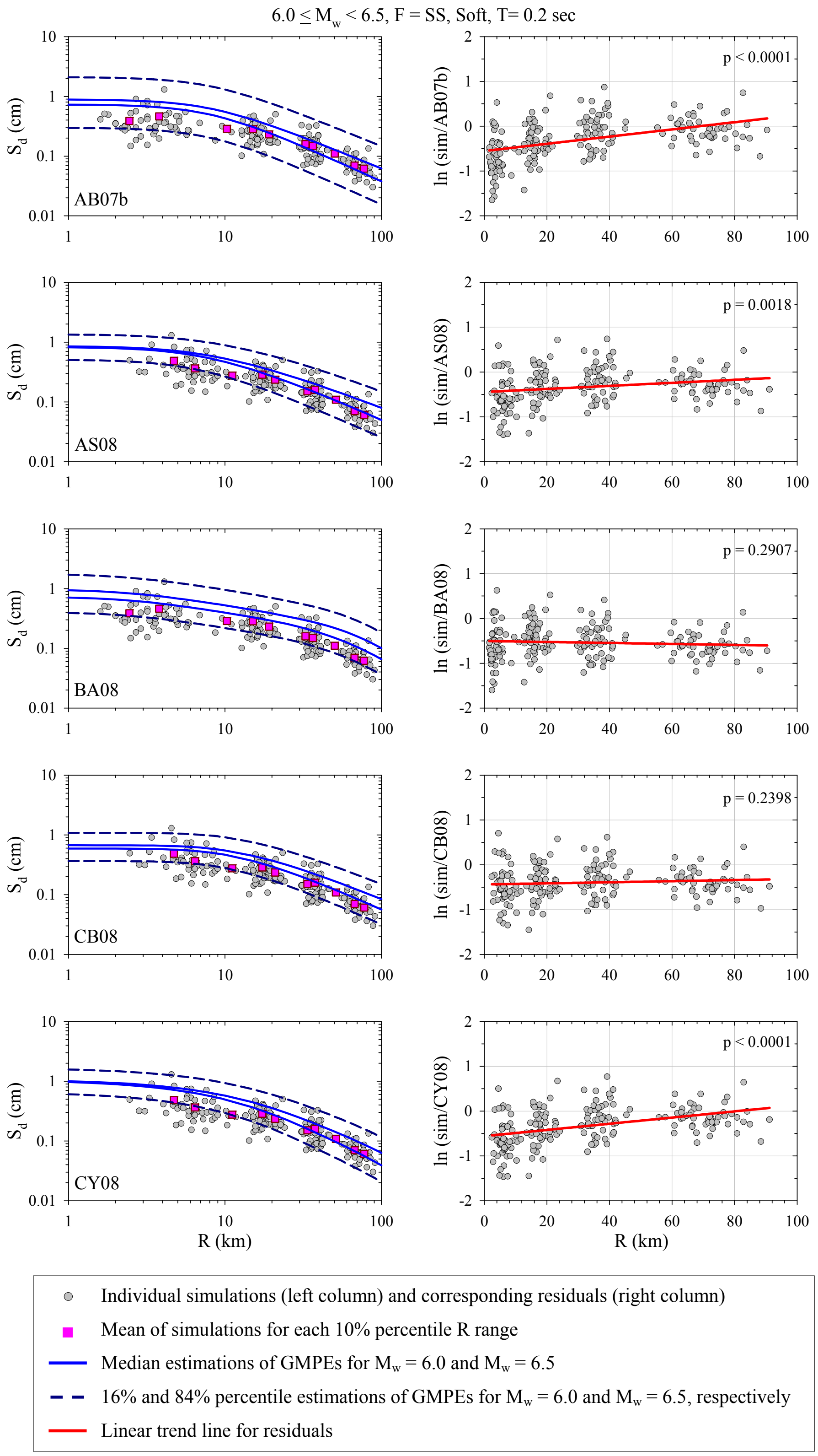

Figure C.18 Distance-dependent comparisons of soft site simulations and GMPEs in terms of S_d ($\xi = 5\%$) at T = 0.2 sec for strike-slip (SS) faults

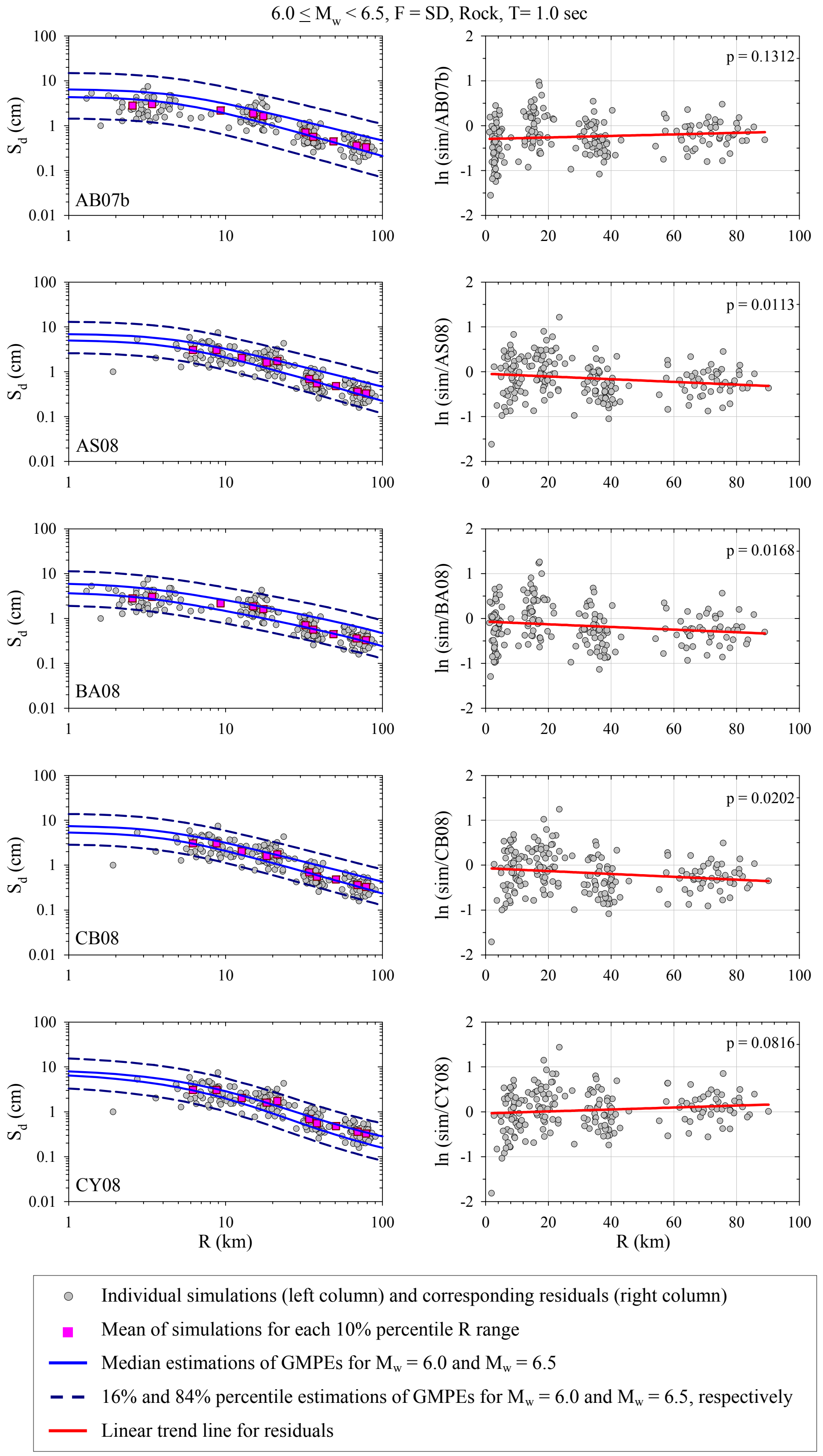

Figure C.19 Distance-dependent comparisons of rock site simulations and GMPEs in terms of S_d ($\xi = 5\%$) at T = 1.0 sec for shallow dipping (SD) faults

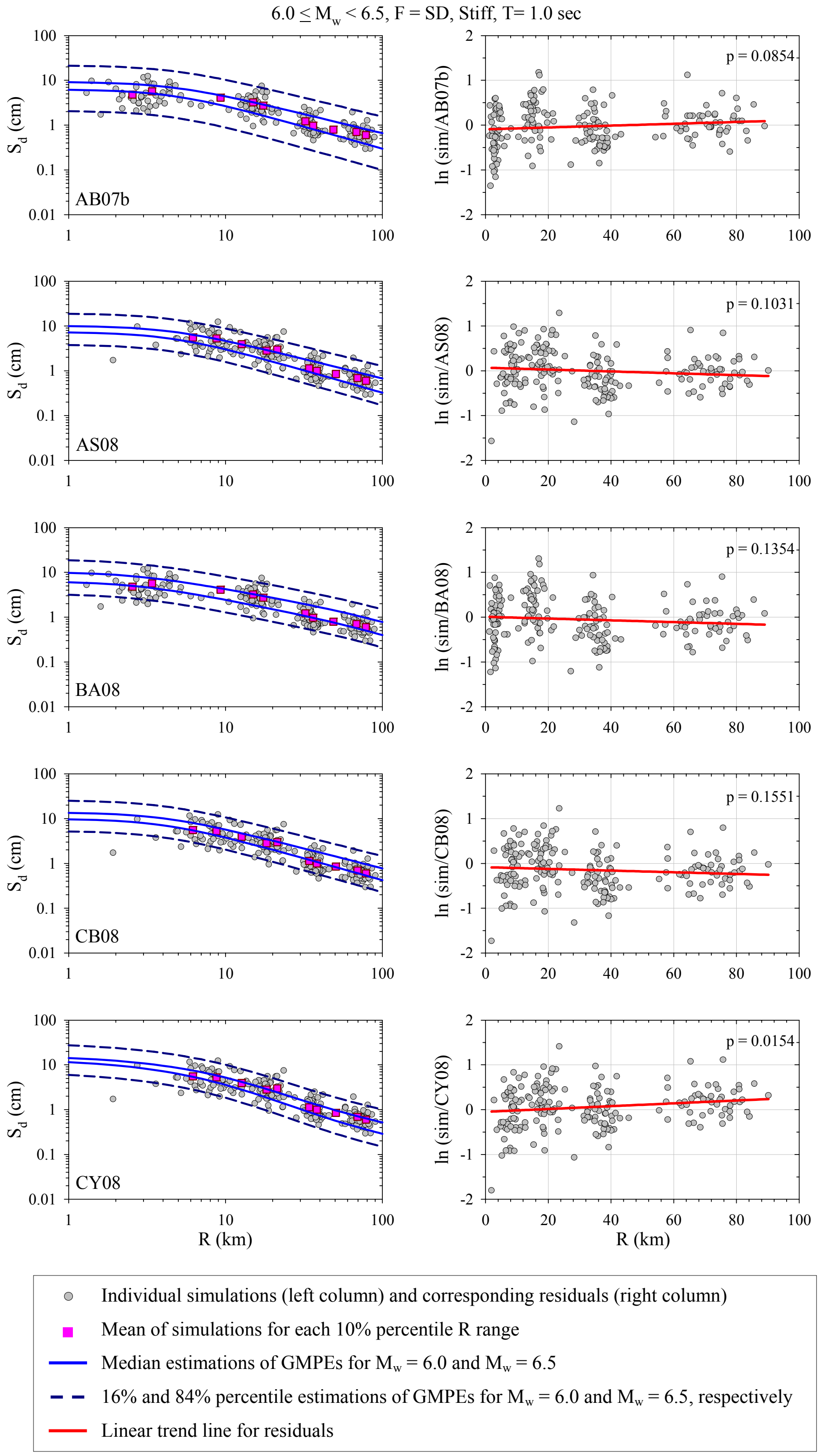

Figure C.20 Distance-dependent comparisons of stiff site simulations and GMPEs in terms of S_d ($\xi = 5\%$) at T = 1.0 sec for shallow dipping (SD) faults

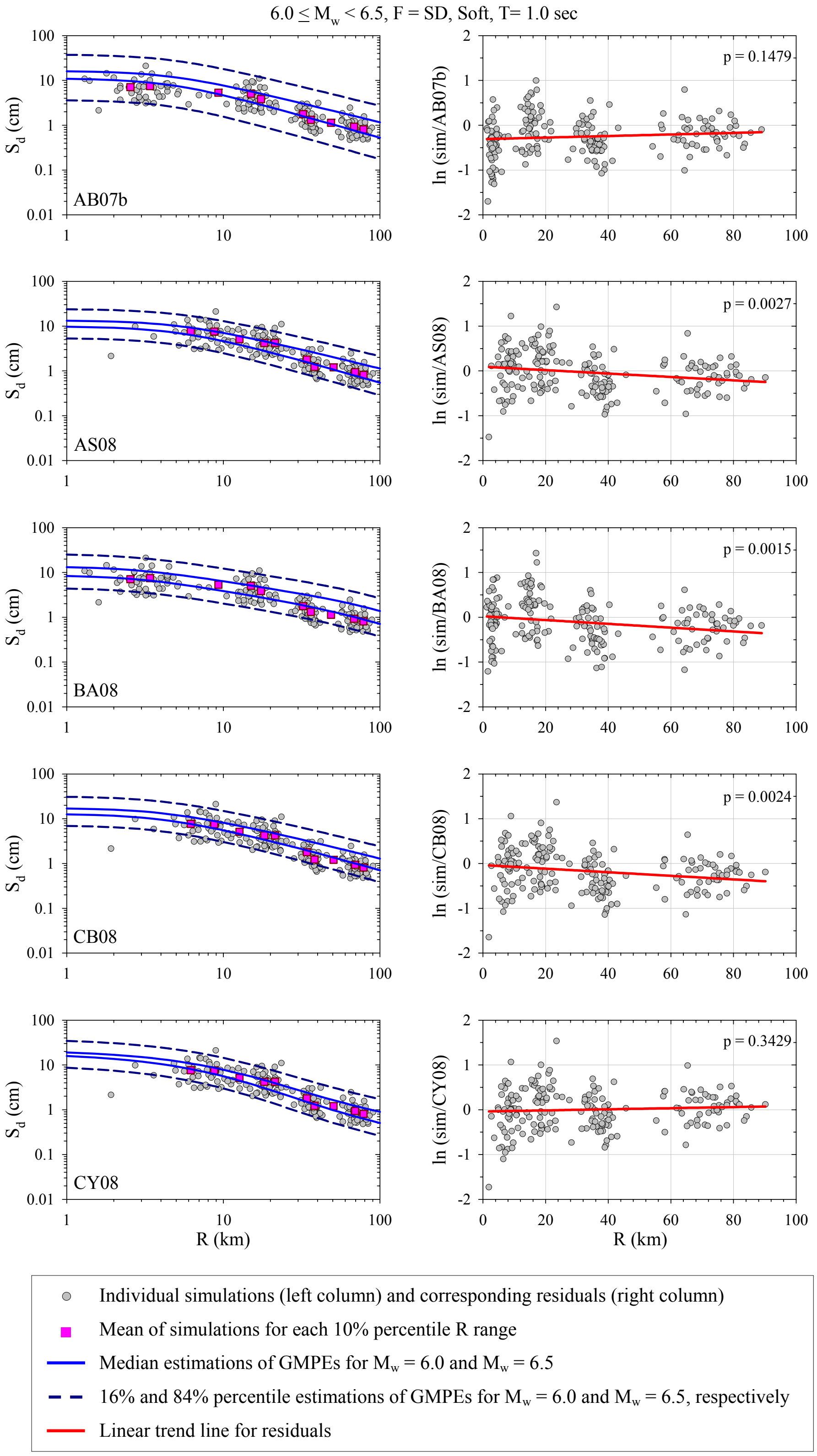

Figure C.21 Distance-dependent comparisons of soft site simulations and GMPEs in terms of S_d ($\xi = 5\%$) at T = 1.0 sec for shallow dipping (SD) faults

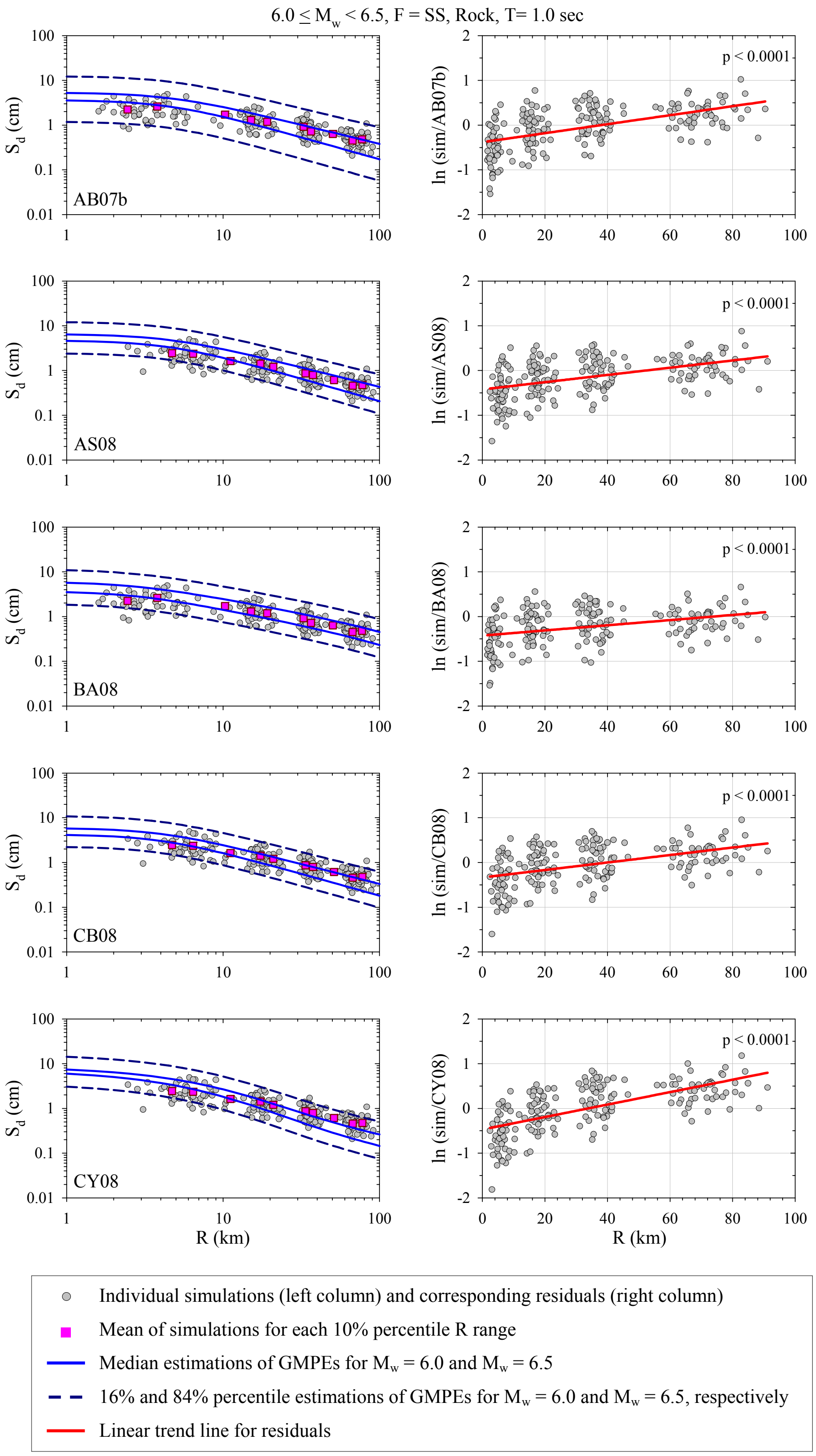

Figure C.22 Distance-dependent comparisons of rock site simulations and GMPEs in terms of S_d ($\xi = 5\%$) at T = 1.0 sec for strike-slip (SS) faults

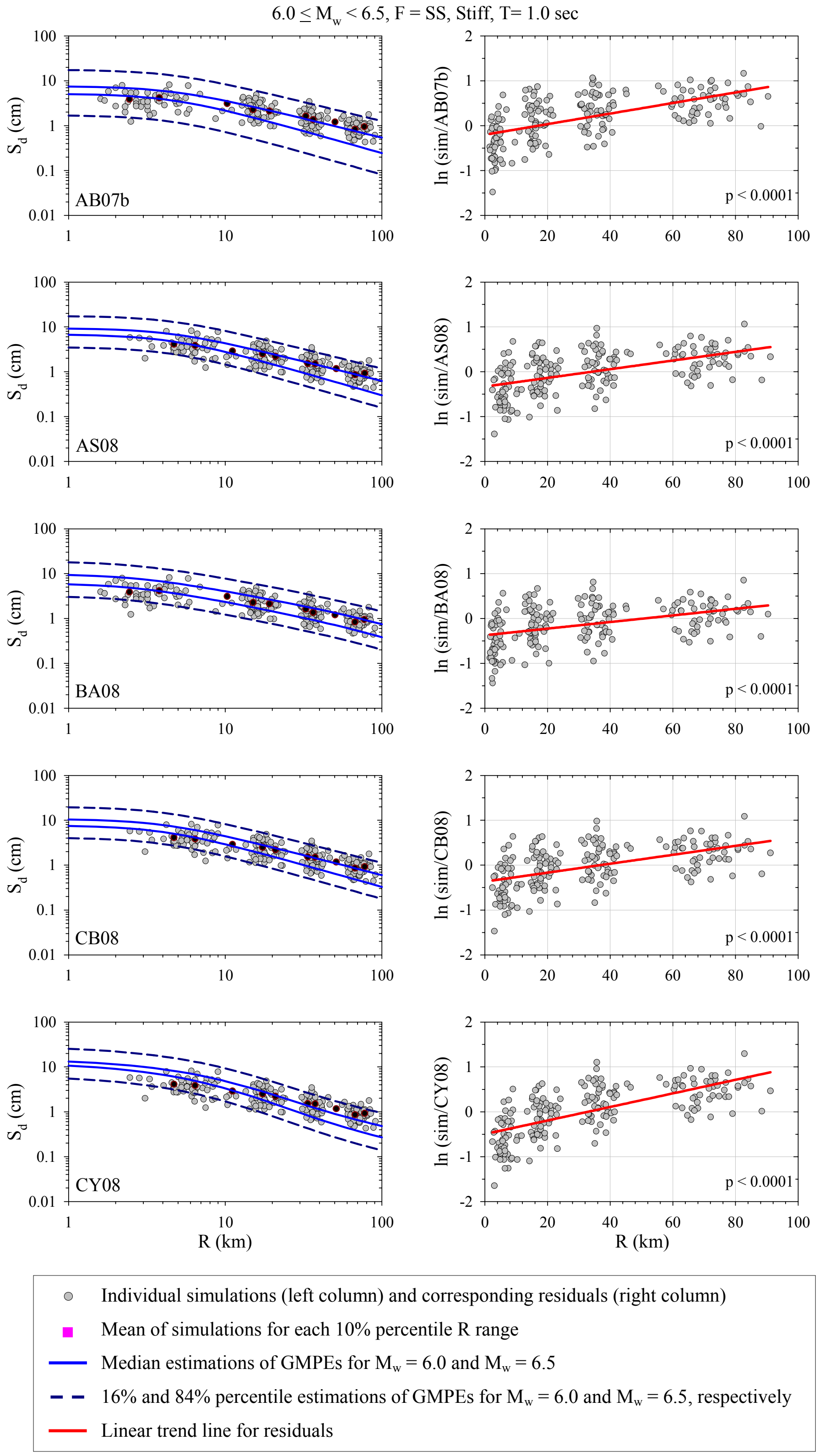

Figure C.23 Distance-dependent comparisons of stiff site simulations and GMPEs in terms of S_d ($\xi = 5\%$) at T = 1.0 sec for strike-slip (SS) faults

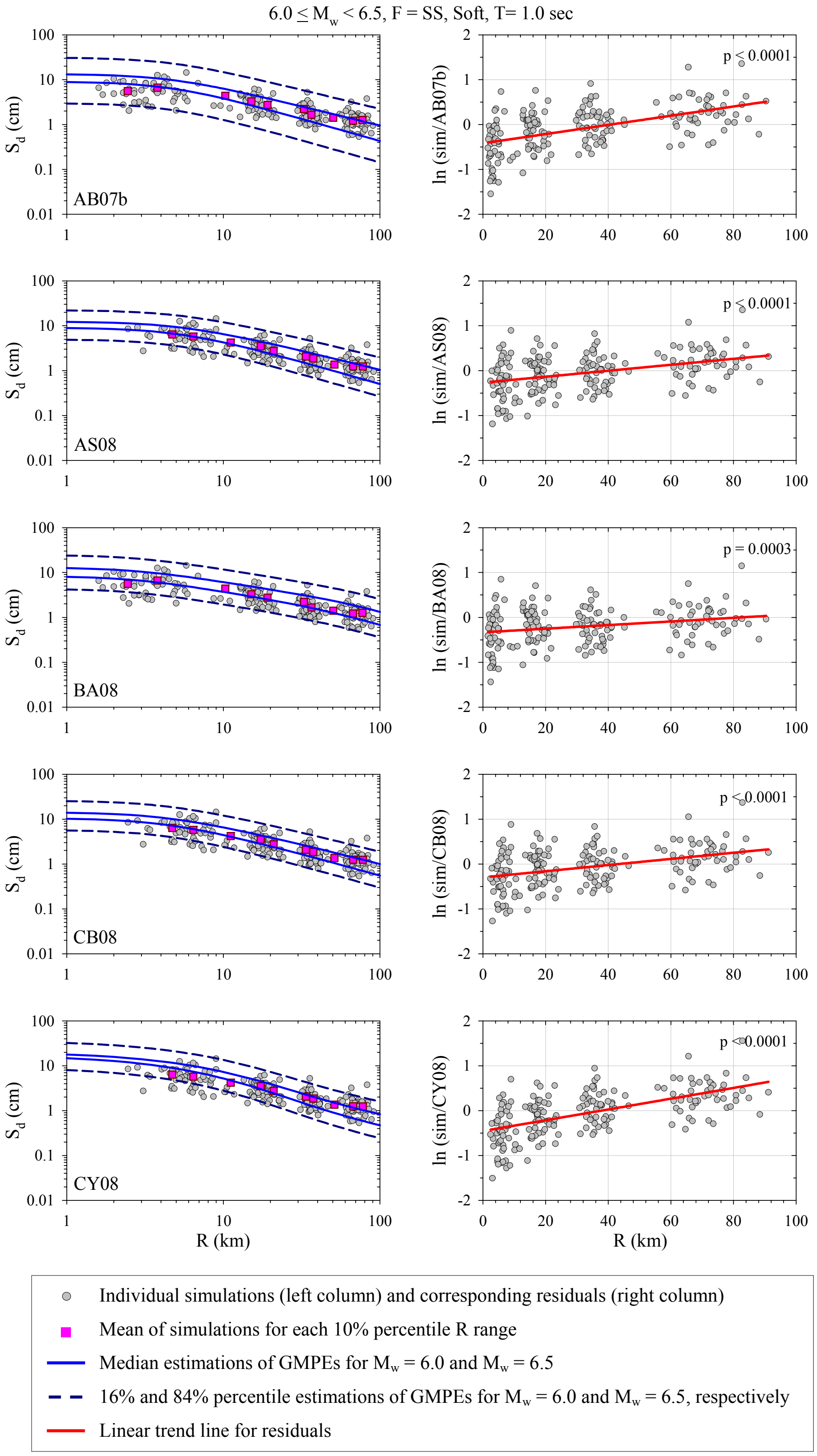

Figure C.24 Distance-dependent comparisons of soft site simulations and GMPEs in terms of S_d ($\xi = 5\%$) at T = 1.0 sec for strike-slip (SS) faults

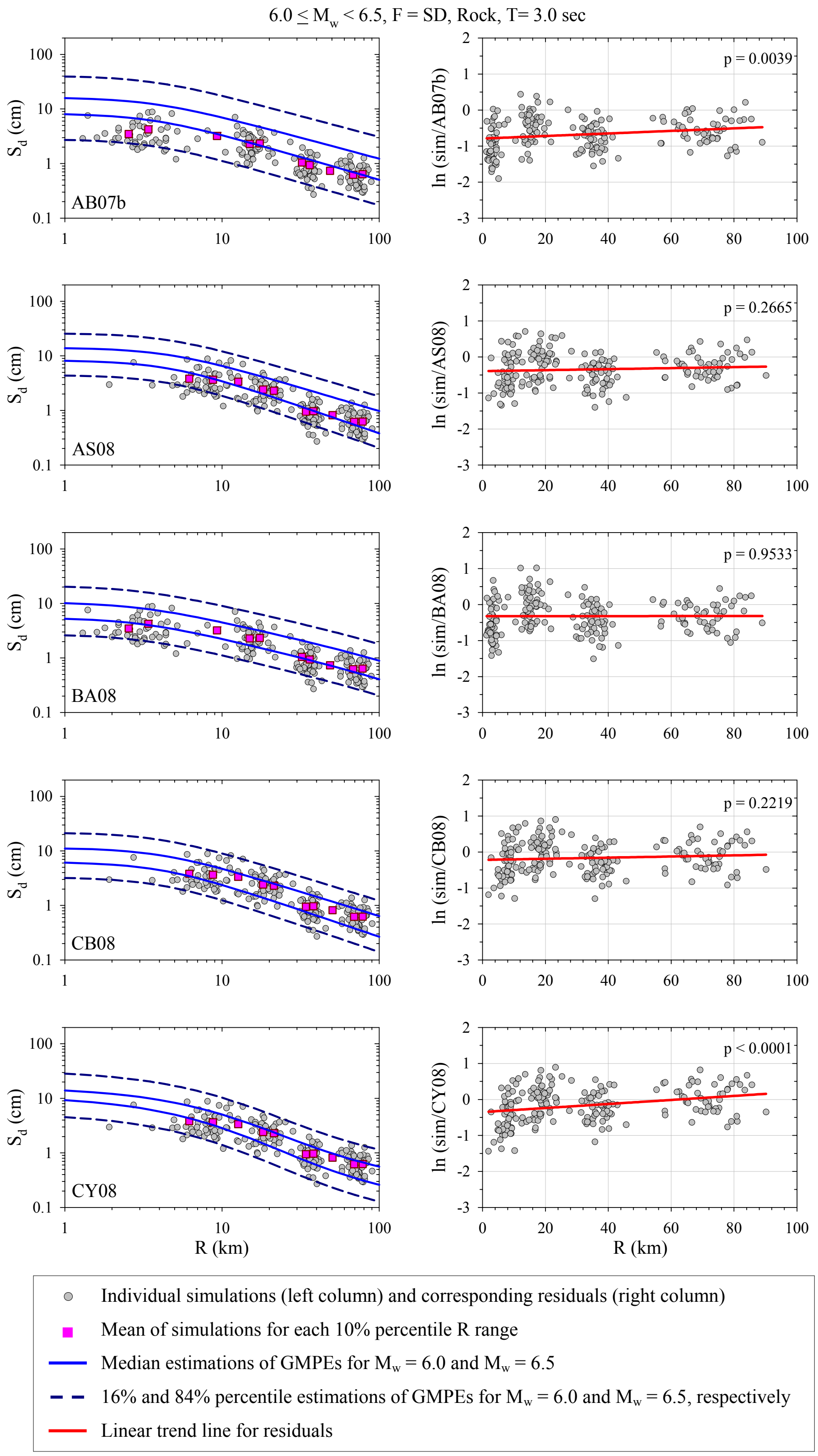

Figure C.25 Distance-dependent comparisons of rock site simulations and GMPEs in terms of S_d ($\xi = 5\%$) at T = 3.0 sec for shallow dipping (SD) faults

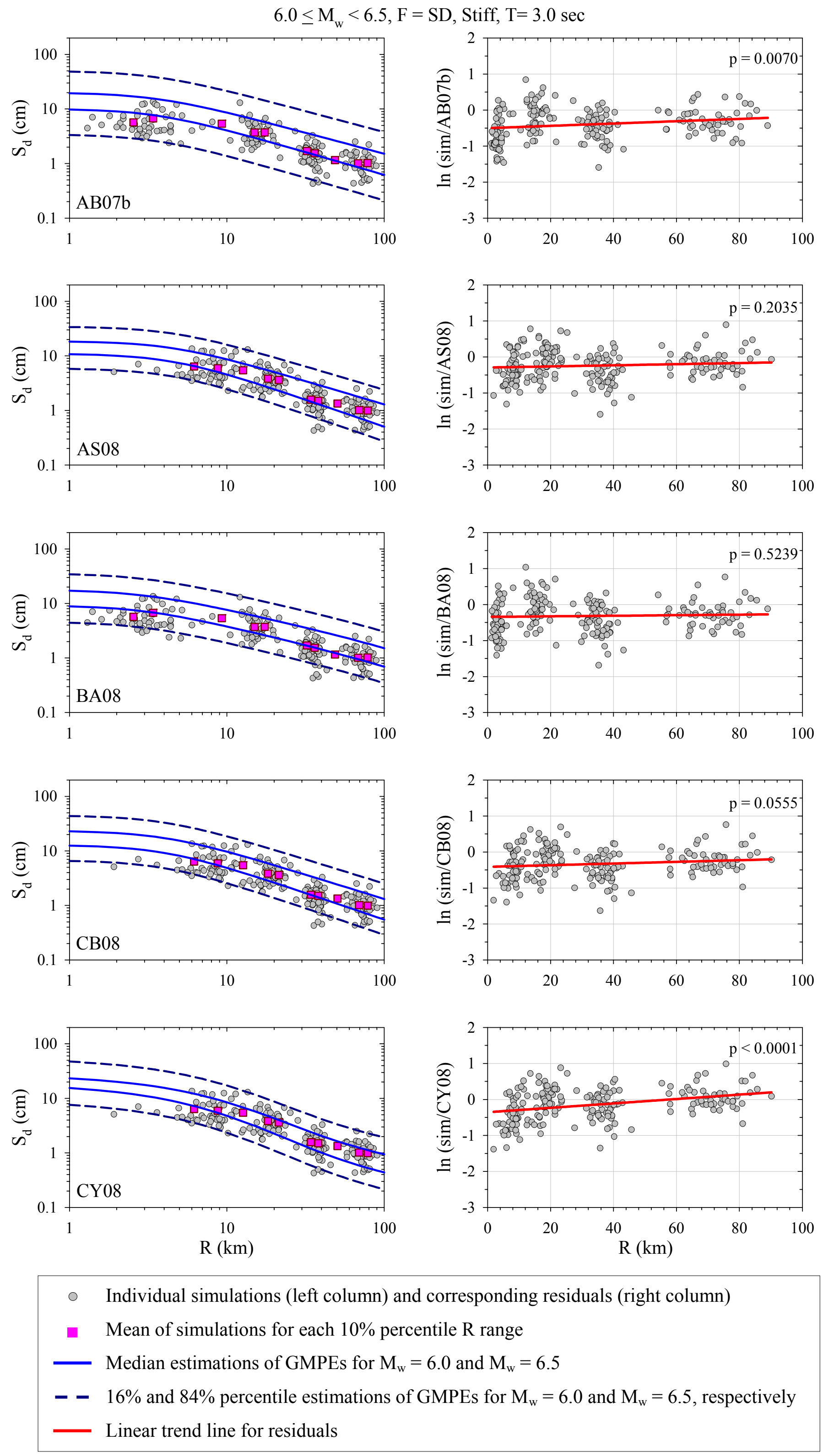

Figure C.26 Distance-dependent comparisons of stiff site simulations and GMPEs in terms of S_d ($\xi = 5\%$) at T = 3.0 sec for shallow dipping (SD) faults

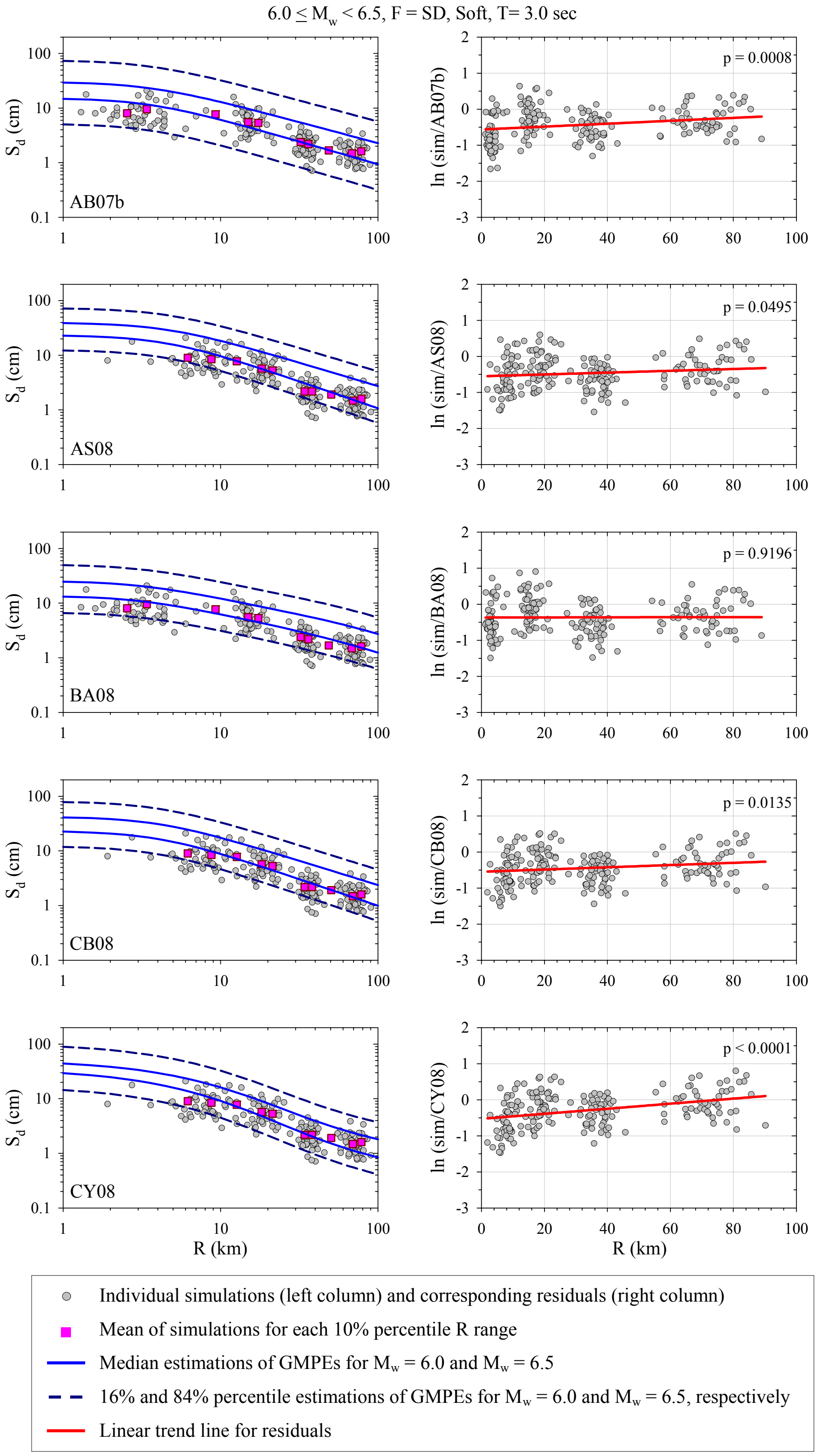

Figure C.27 Distance-dependent comparisons of soft site simulations and GMPEs in terms of S_d ($\xi = 5\%$) at T = 3.0 sec for shallow dipping (SD) faults

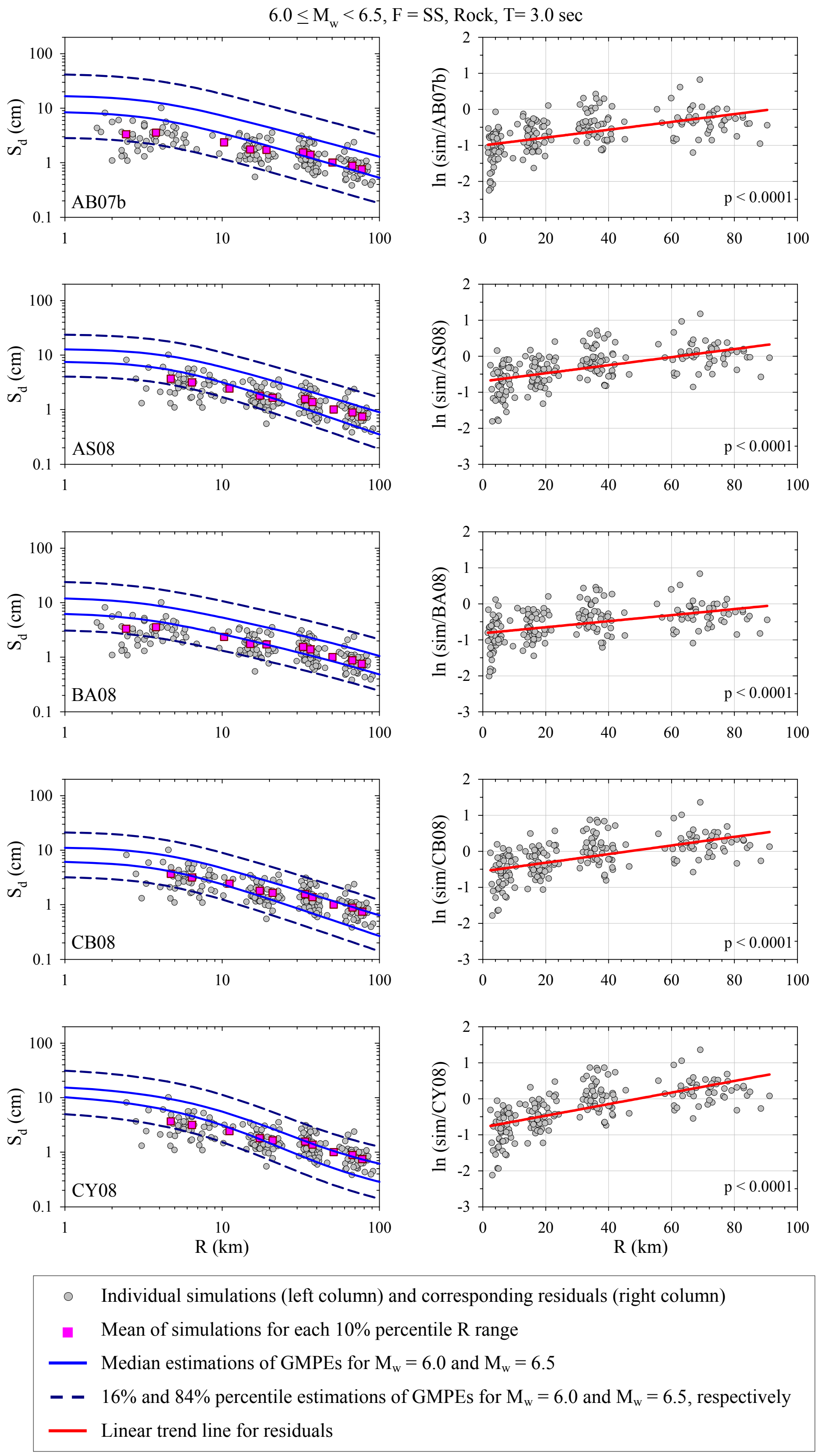

Figure C.28 Distance-dependent comparisons of rock site simulations and GMPEs in terms of S_d ($\xi = 5\%$) at T = 3.0 sec for strike-slip (SS) faults

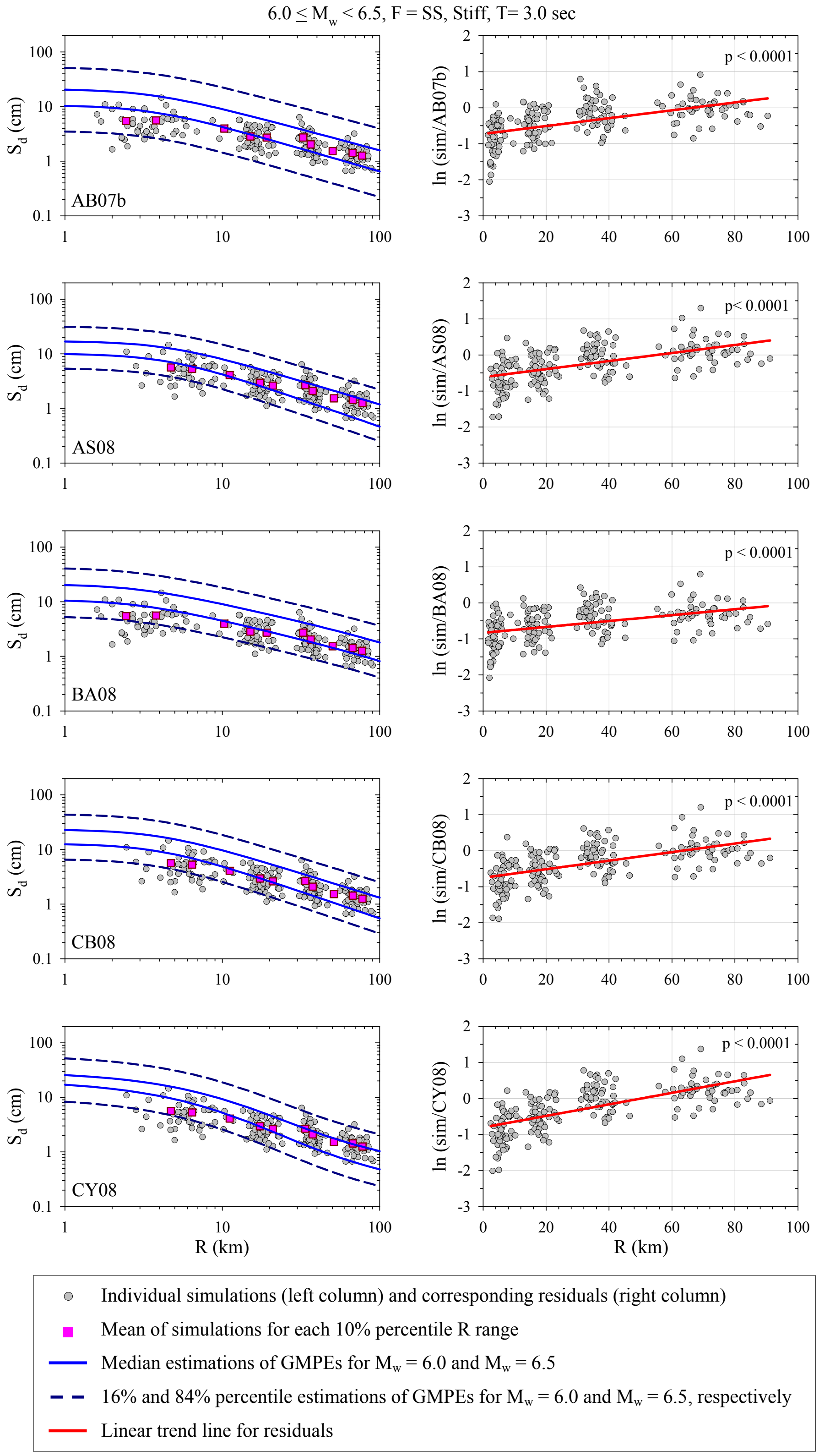

Figure C.29 Distance-dependent comparisons of stiff site simulations and GMPEs in terms of S_d ($\xi = 5\%$) at T = 3.0 sec for strike-slip (SS) faults

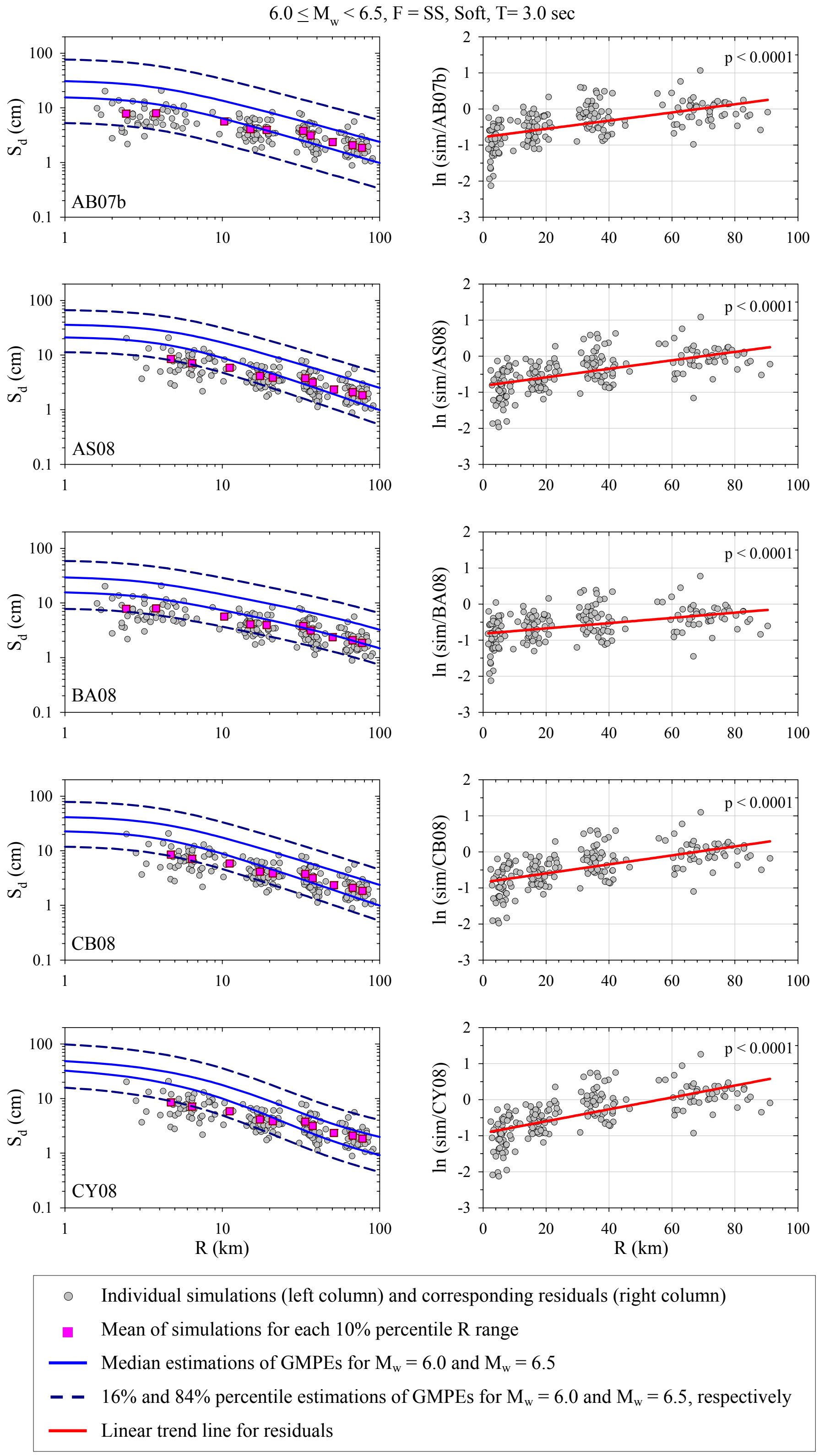

Figure C.30 Distance-dependent comparisons of soft site simulations and GMPEs in terms of S_d ($\xi = 5\%$) at T = 3.0 sec for strike-slip (SS) faults

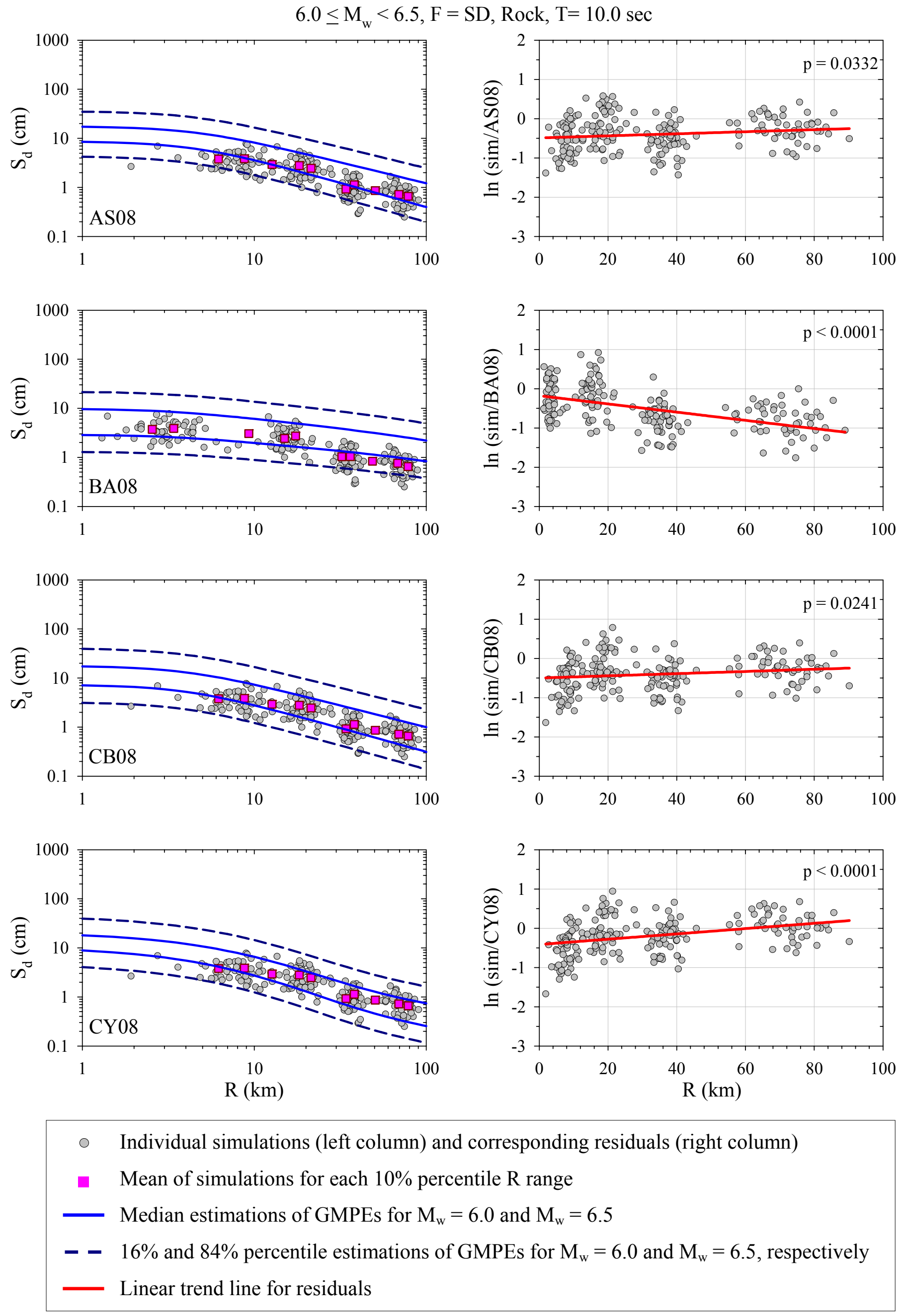

Figure C.31 Distance-dependent comparisons of rock site simulations and GMPEs in terms of S_d ($\xi = 5\%$) at T = 10.0 sec for shallow dipping (SD) faults

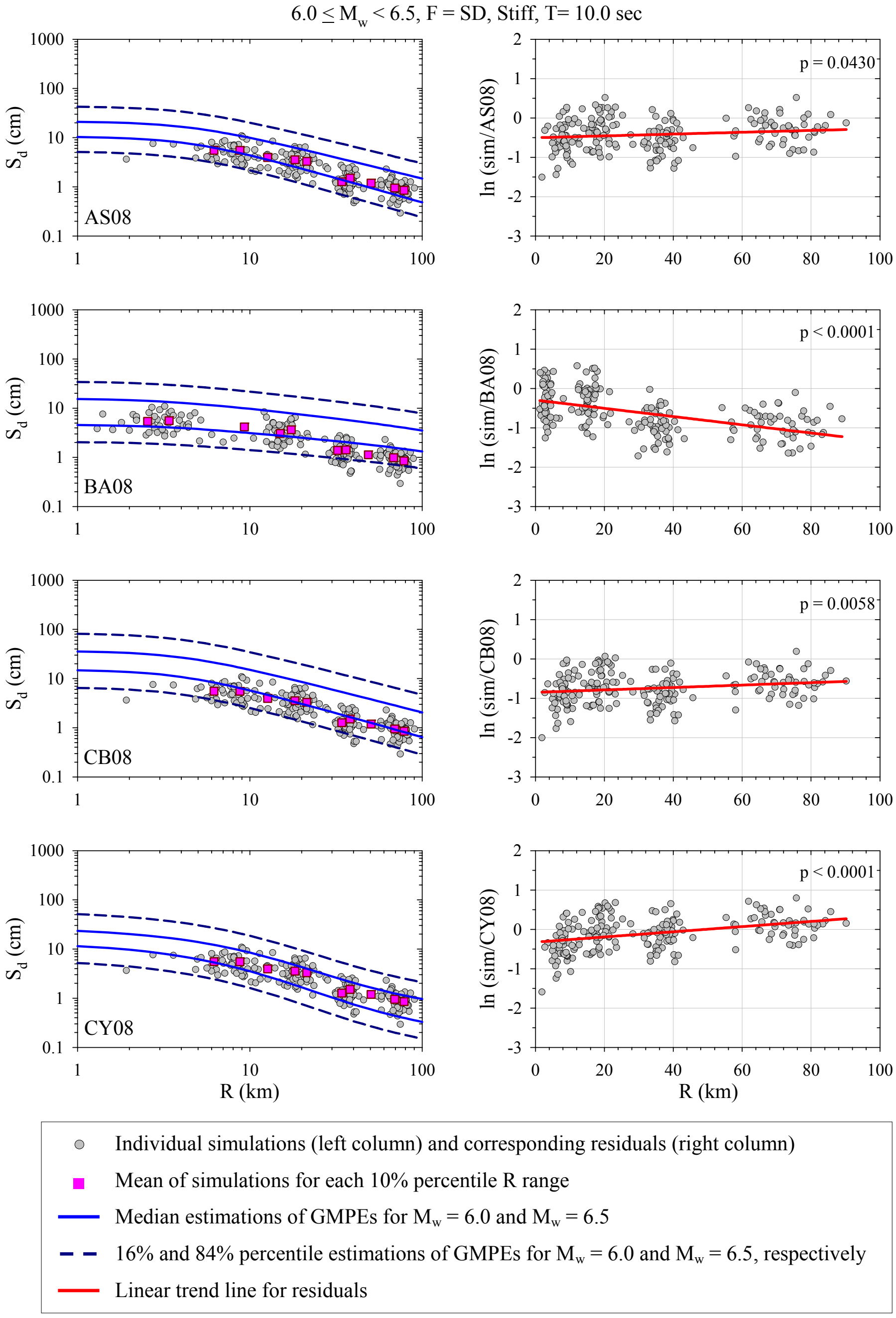

Figure C.32 Distance-dependent comparisons of stiff site simulations and GMPEs in terms of S_d ($\xi = 5\%$) at T = 10.0 sec for shallow dipping (SD) faults

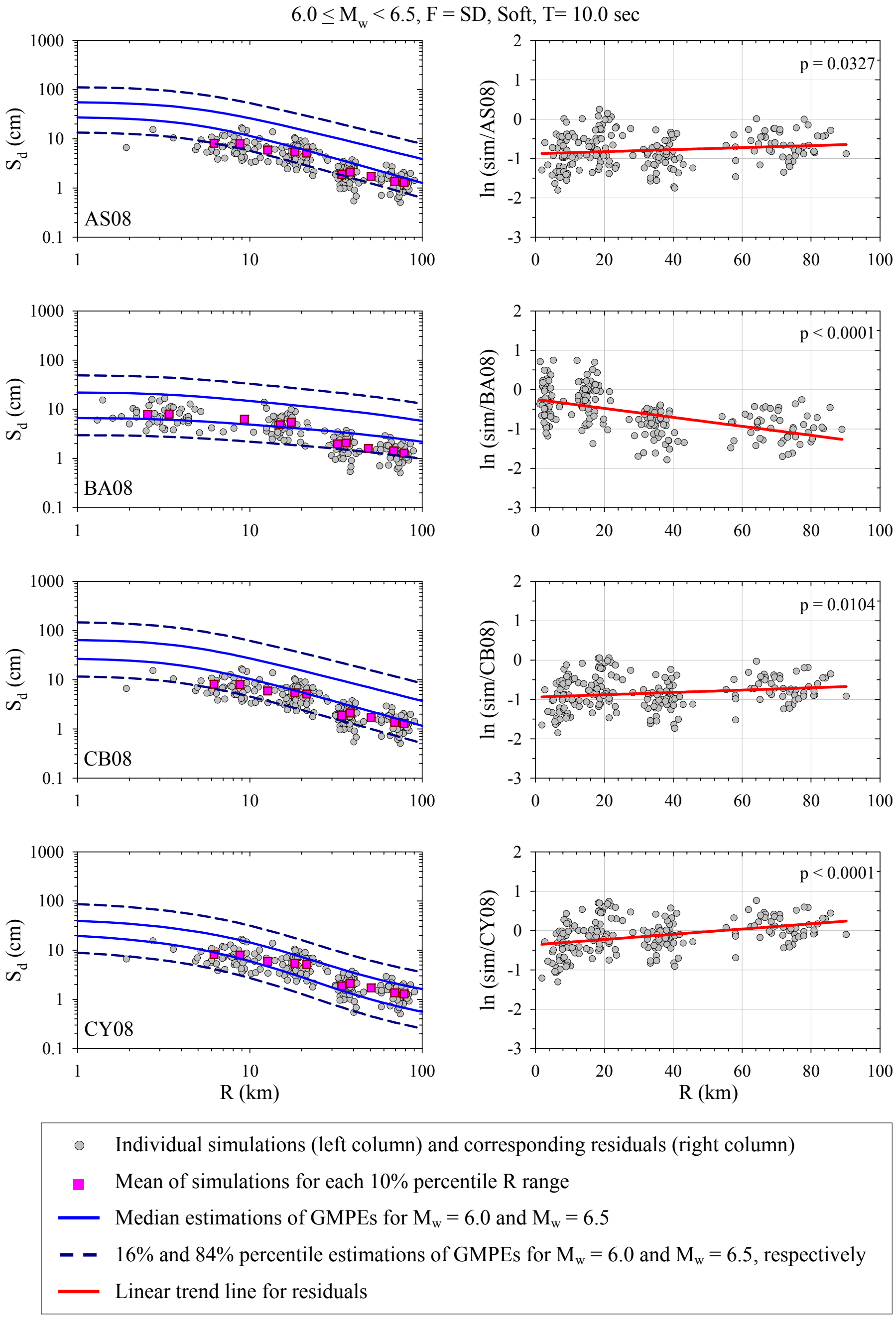

Figure C.33 Distance-dependent comparisons of soft site simulations and GMPEs in terms of S_d ($\xi = 5\%$) at T = 10.0 sec for shallow dipping (SD) faults

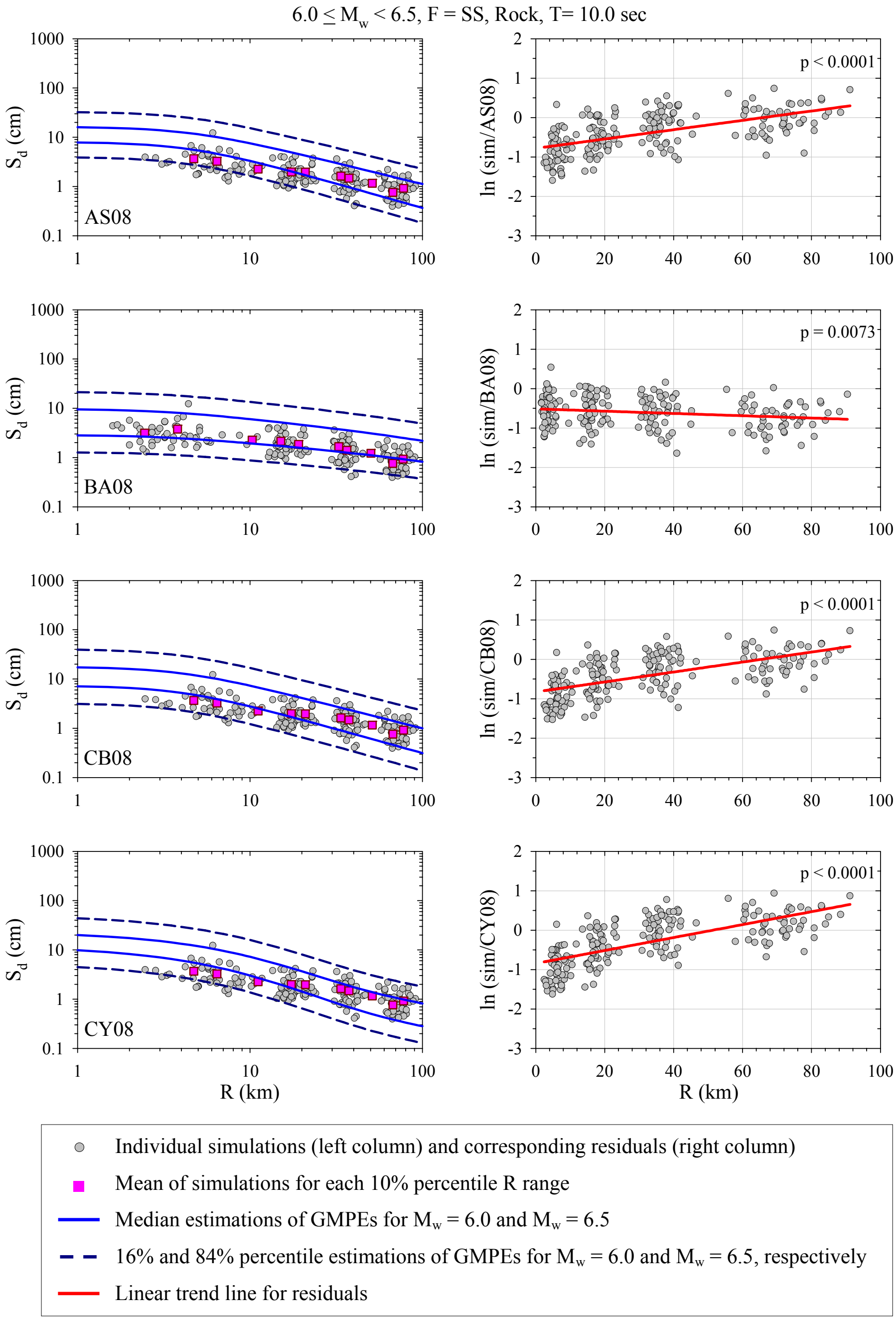

Figure C.34 Distance-dependent comparisons of rock site simulations and GMPEs in terms of S_d ($\xi = 5\%$) at T = 10.0 sec for strike-slip (SS) faults

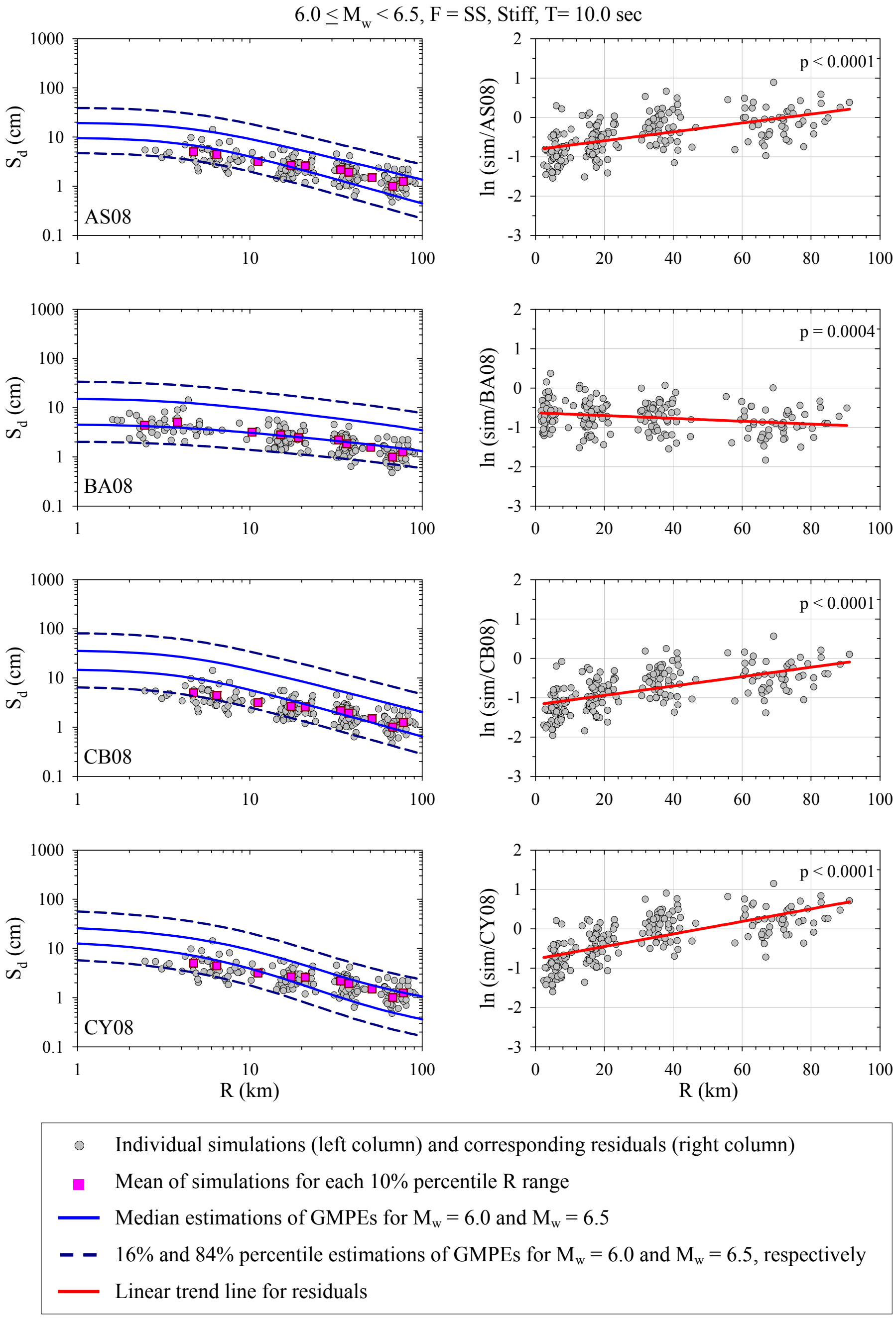

Figure C.35 Distance-dependent comparisons of stiff site simulations and GMPEs in terms of S_d ($\xi = 5\%$) at T = 10.0 sec for strike-slip (SS) faults

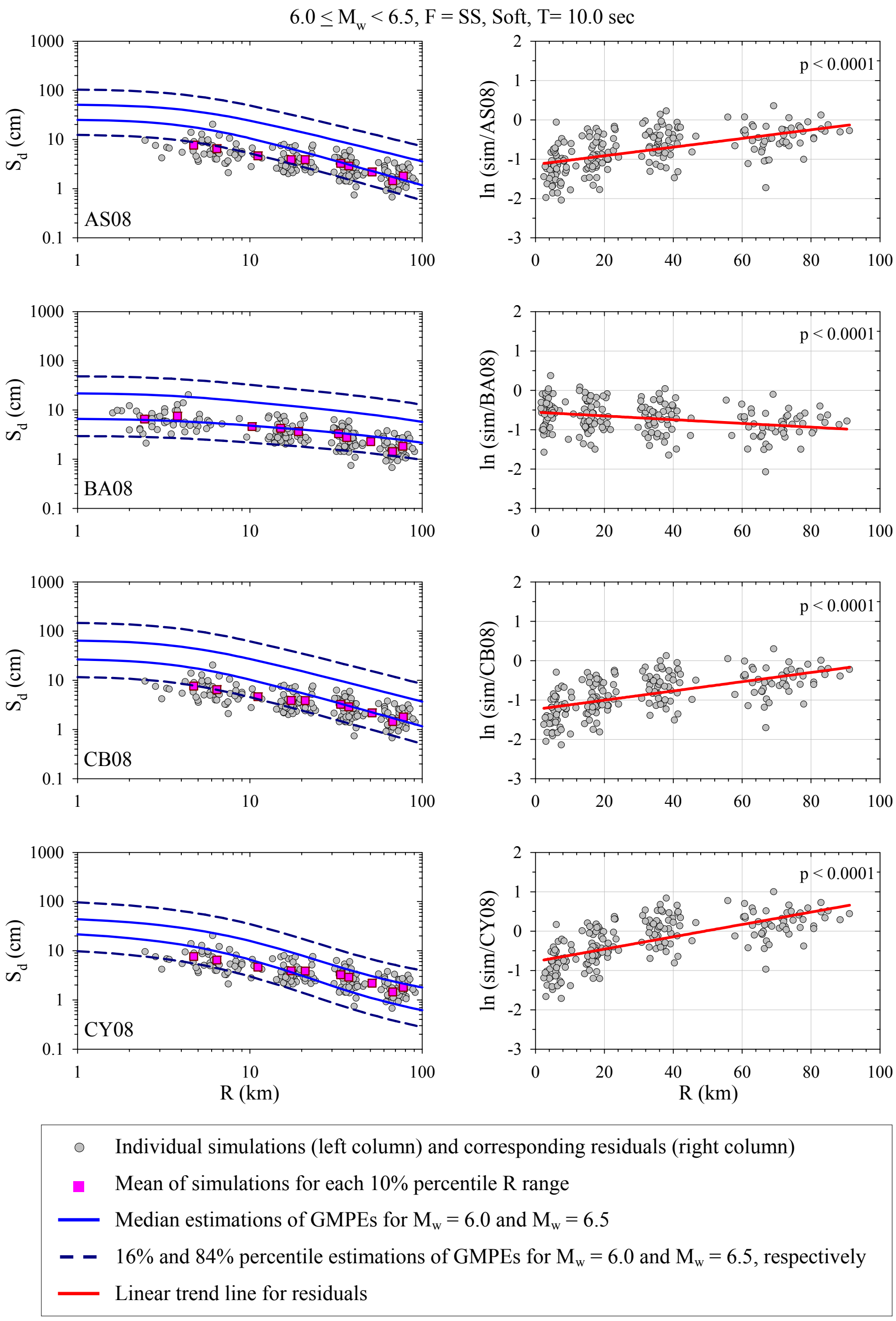

Figure C.36 Distance-dependent comparisons of soft site simulations and GMPEs in terms of S_d ($\xi = 5\%$) at T = 10.0 sec for strike-slip (SS) faults

APPENDIX D

COMPARISON OF DISTANCE-DEPENDENT RESIDUALS OBTAINED FROM SYNTHETIC GROUND MOTIONS GENERATED BY USING R_{hyp} AND R_{rup}

The comparison of distance-dependent residuals obtained from the synthetics that are generated by using R_{hyp} and R_{rup} for shallow dipping (SD) and strike-slip (SS) events at soft sites (180 m/sec $\leq V_{S,30} \leq$ 360 m/sec) are presented. The magnitude range for the comparative plots is $6.0 \leq M_w < 6.5$.

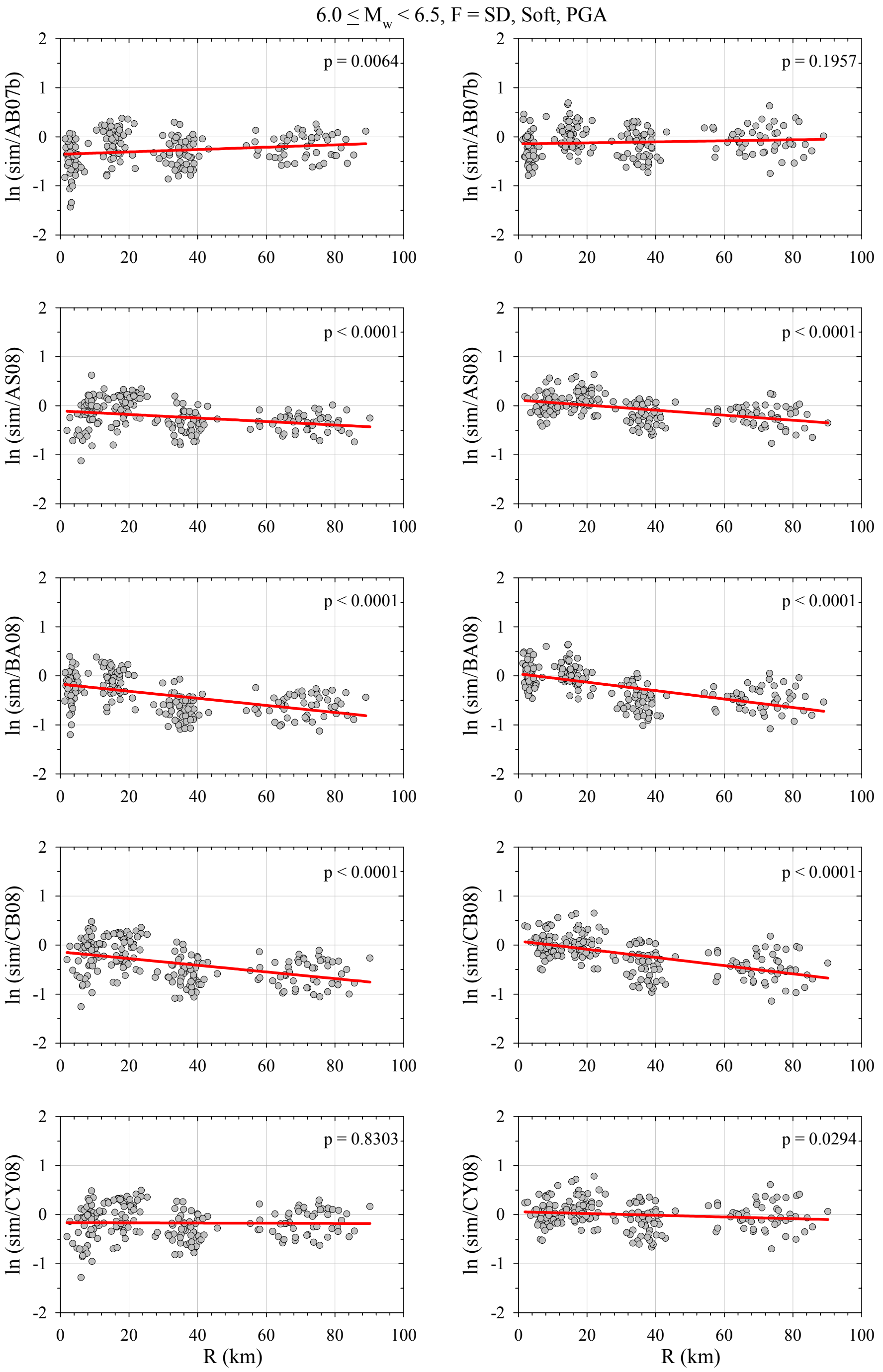

Figure D.1 Distance-dependent comparisons of PGA residuals obtained from synthetic ground motions generated by using R_{hyp} (left column) and R_{rup} (right column) for shallow dipping (SD) faults

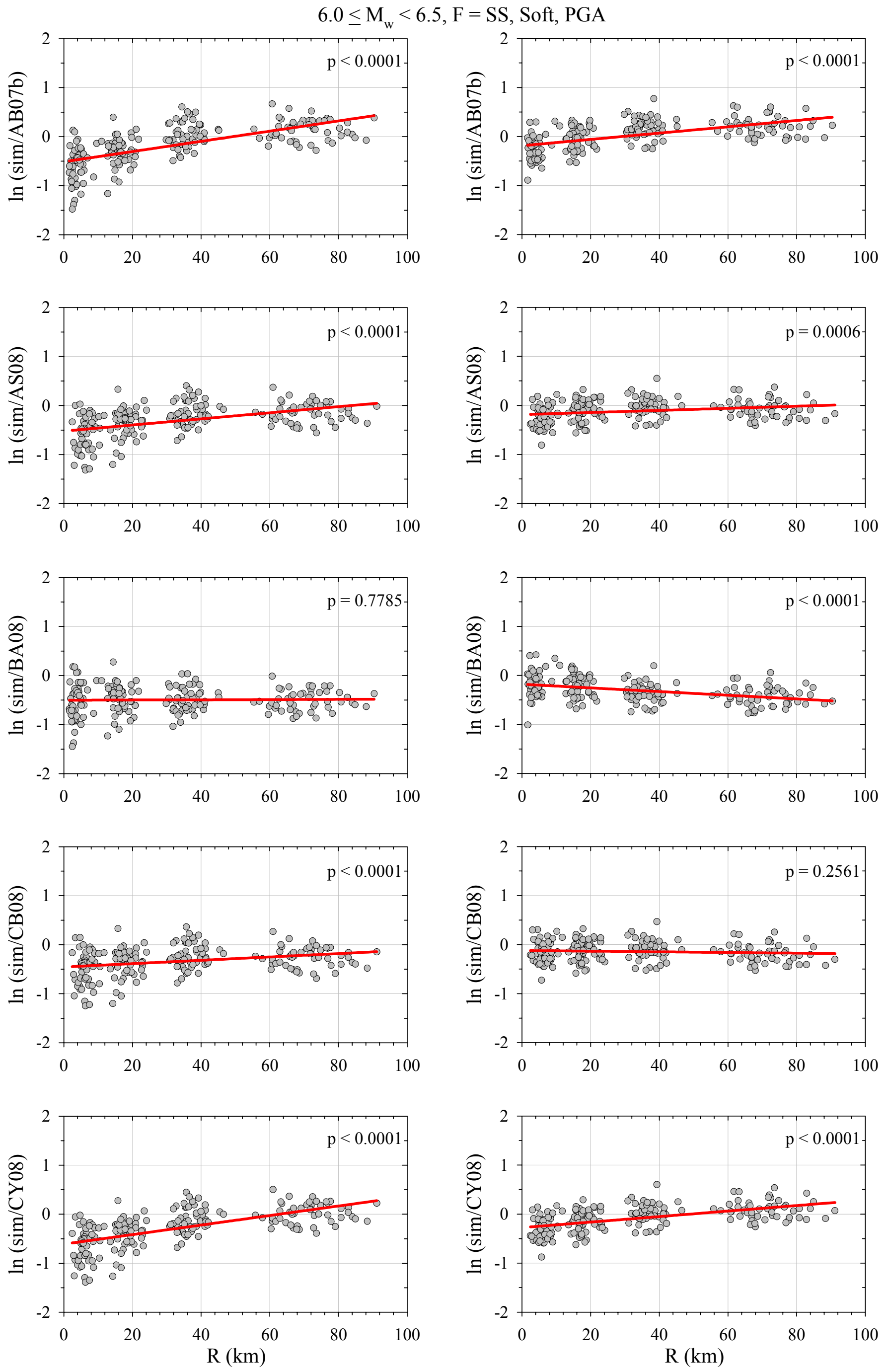

Figure D.2 Distance-dependent comparisons of PGA residuals obtained from synthetic ground motions generated by using R_{hyp} (left column) and R_{rup} (right column) for strike-slip (SS) faults

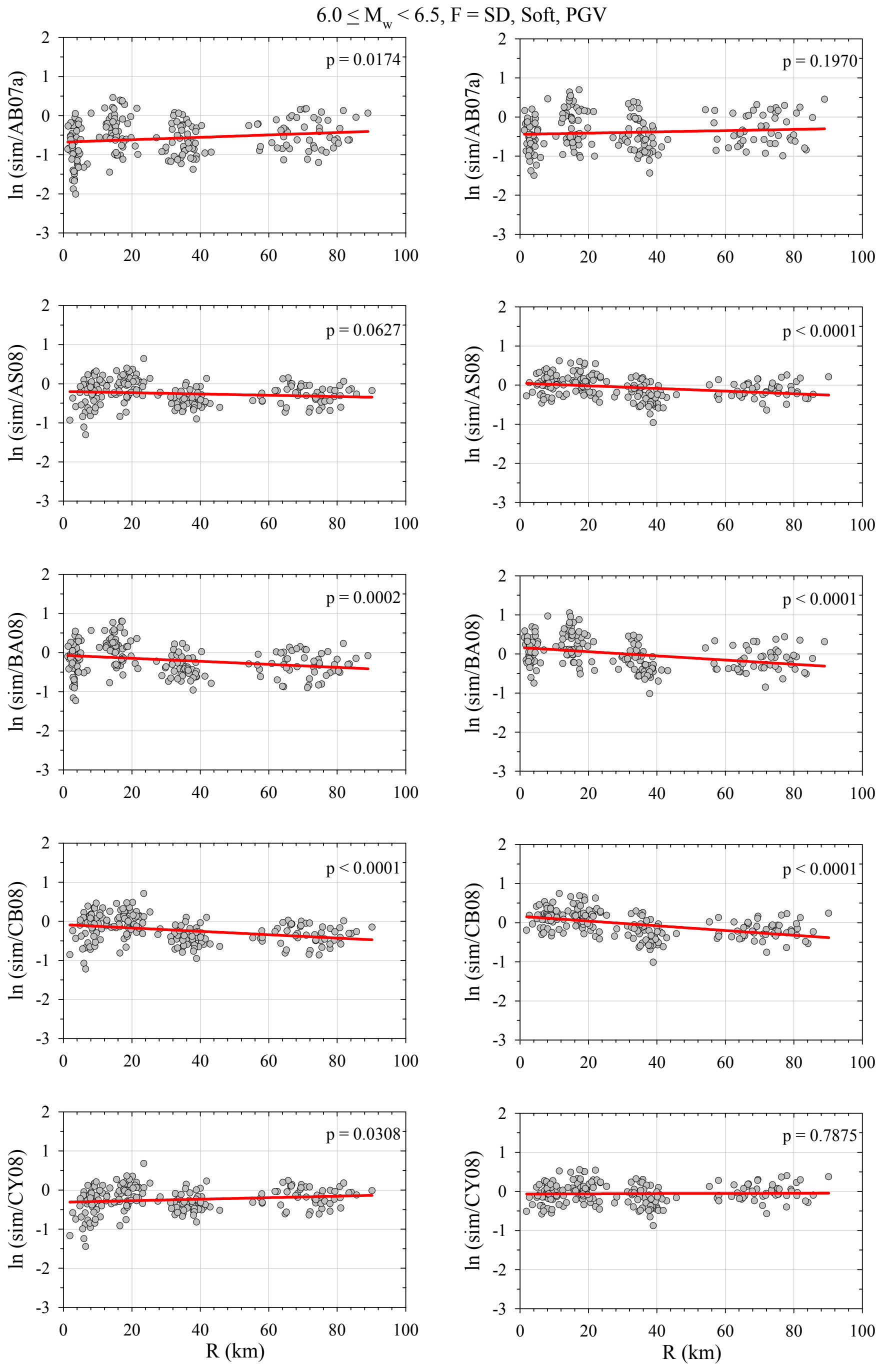

Figure D.3 Distance-dependent comparisons of PGV residuals obtained from synthetic ground motions generated by using R_{hyp} (left column) and R_{rup} (right column) for shallow dipping (SD) faults

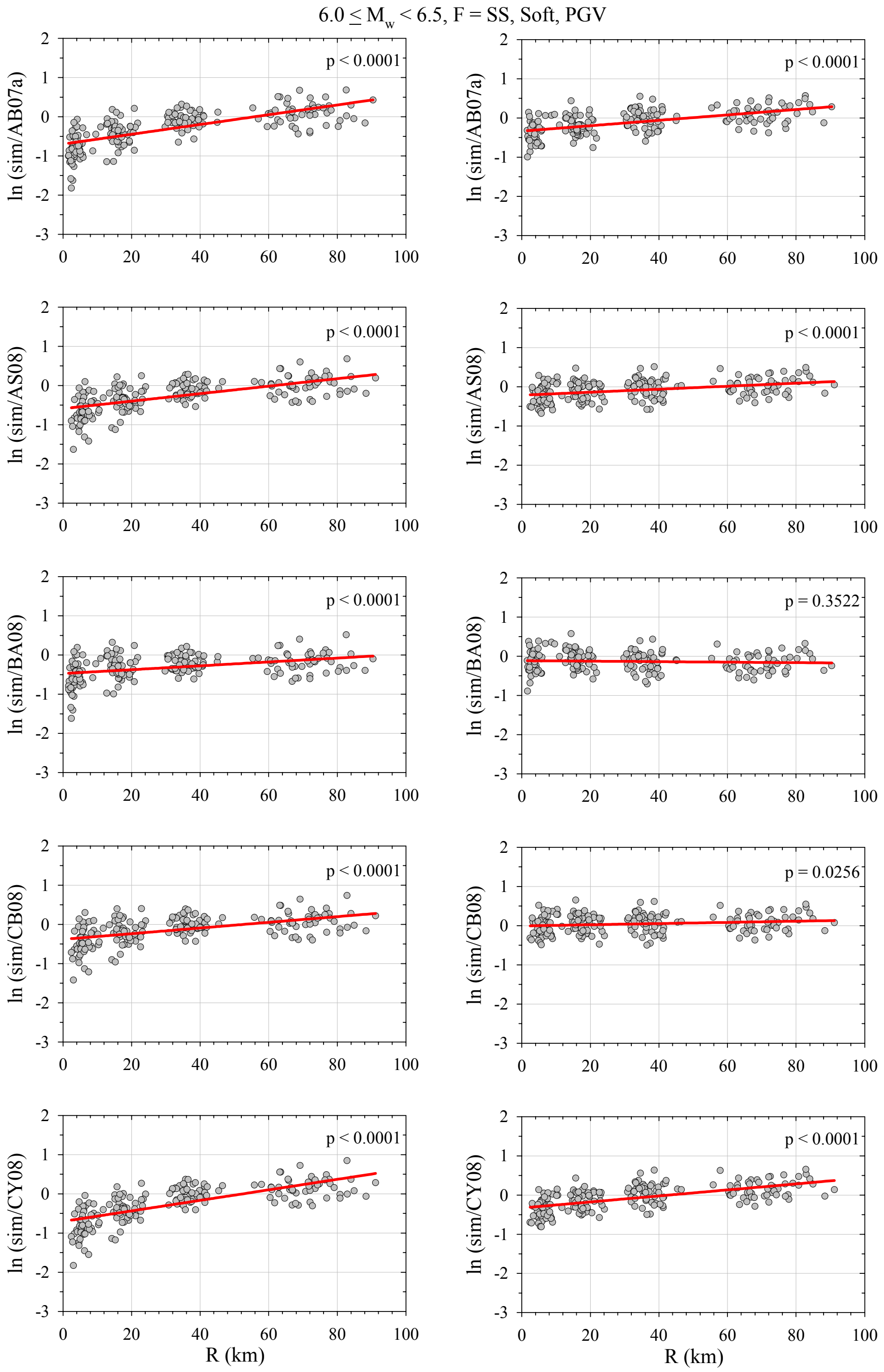

Figure D.4 Distance-dependent comparisons of PGV residuals obtained from synthetic ground motions generated by using R_{hyp} (left column) and R_{rup} (right column) for strike-slip (SS) faults

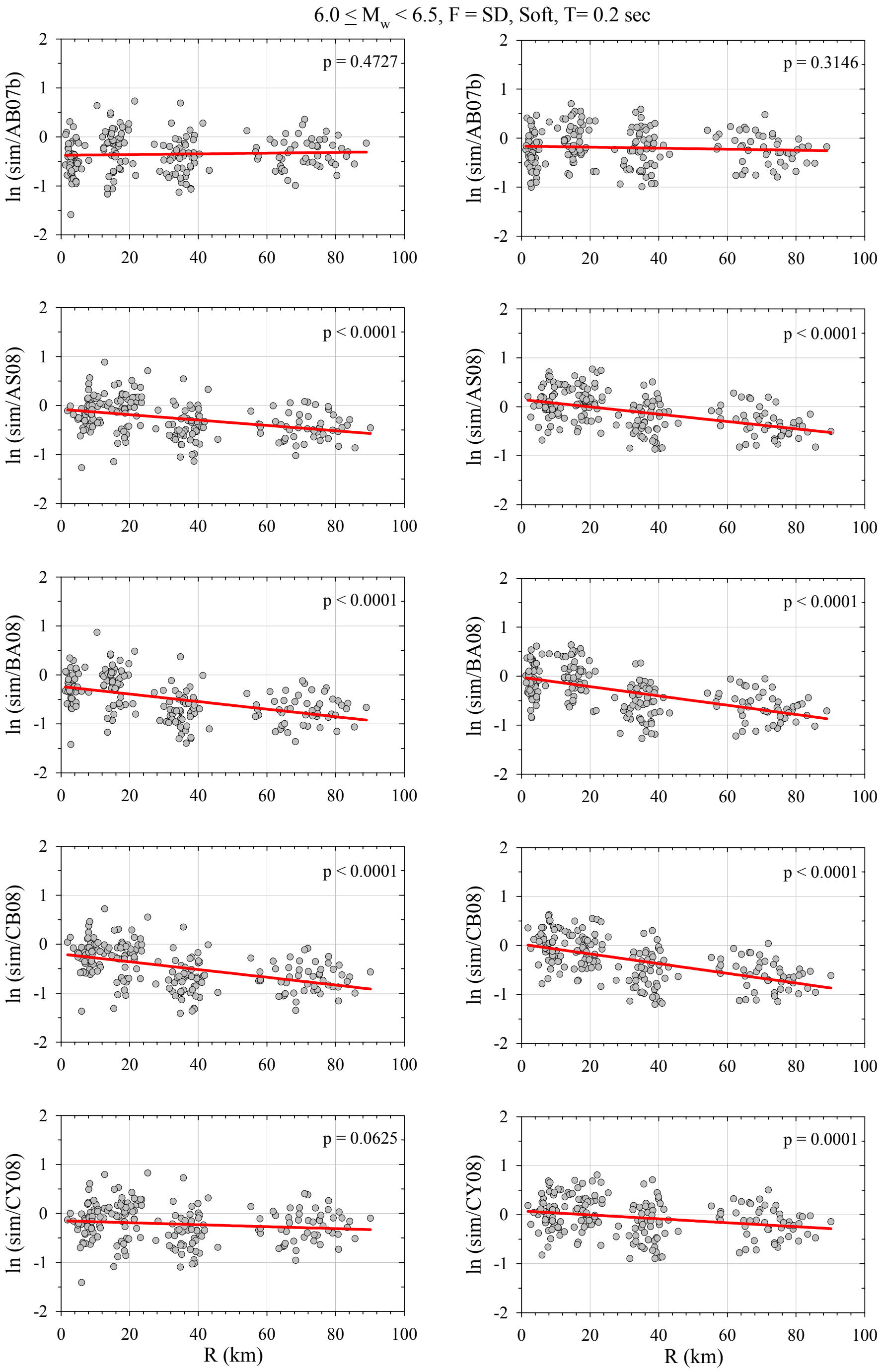

Figure D.5 Distance-dependent comparisons of residuals for S_d (ξ = 5%) at T = 0.2 sec obtained from synthetic ground motions generated by using R_{hyp} (left column) and R_{rup} (right column) for shallow dipping (SD) faults

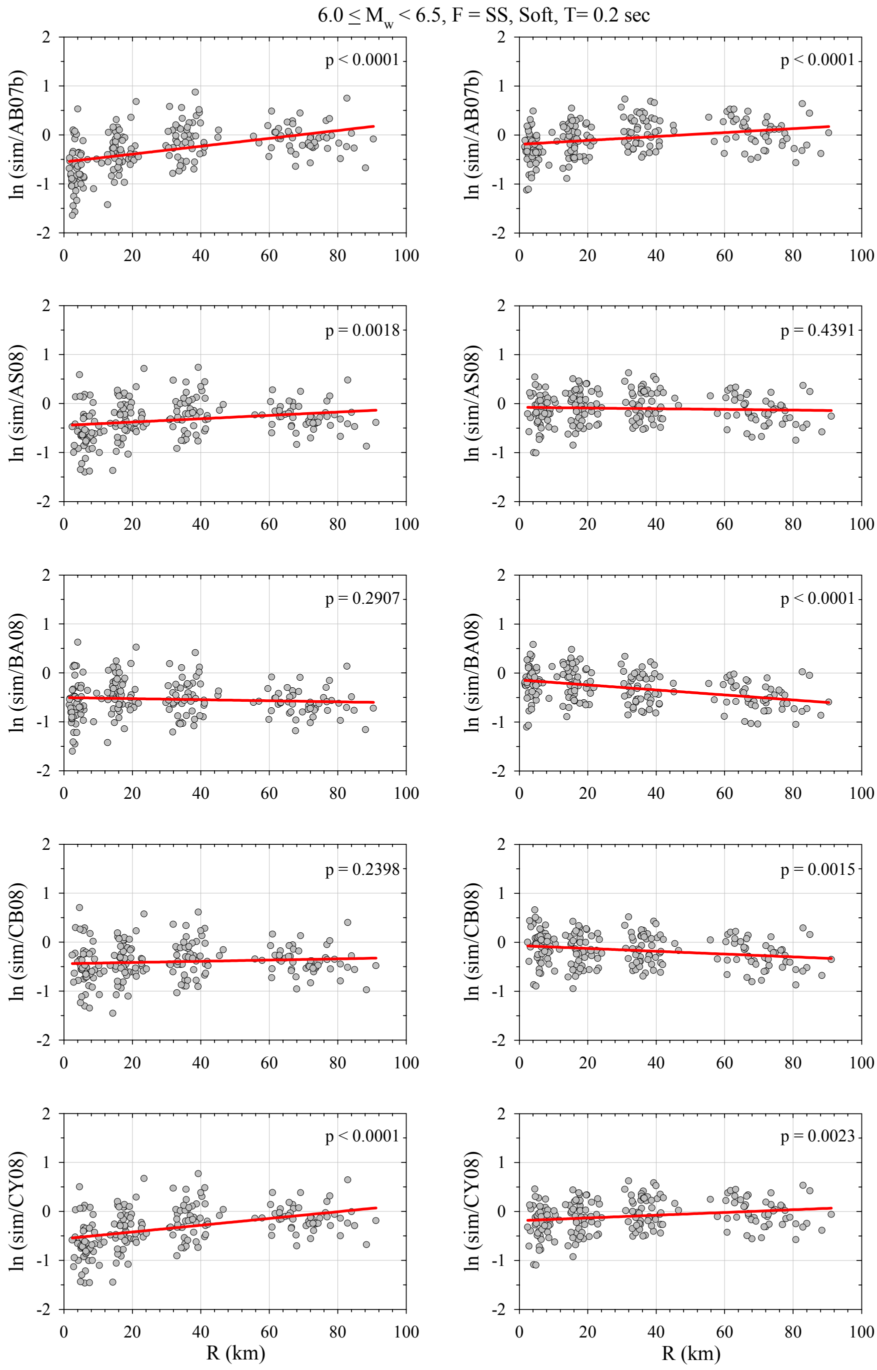

Figure D.6 Distance-dependent comparisons of residuals for S_d ($\xi = 5\%$) at T = 0.2 sec obtained from synthetic ground motions generated by using R_{hyp} (left column) and R_{rup} (right column) for strike-slip (SS) faults

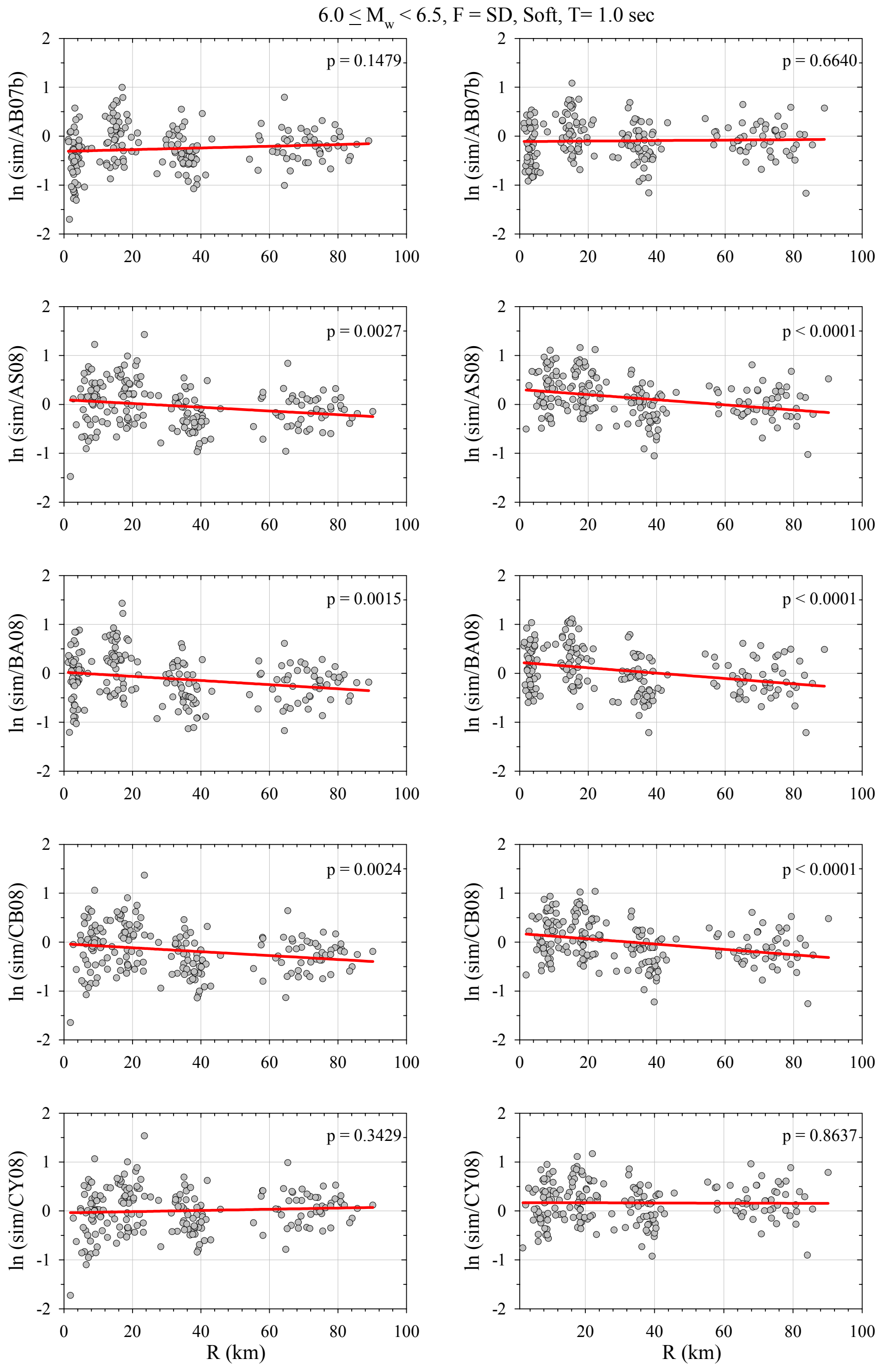

Figure D.7 Distance-dependent comparisons of residuals for S_d (ξ = 5%) at T = 1.0 sec obtained from synthetic ground motions generated by using R_{hyp} (left column) and R_{rup} (right column) for shallow dipping (SD) faults

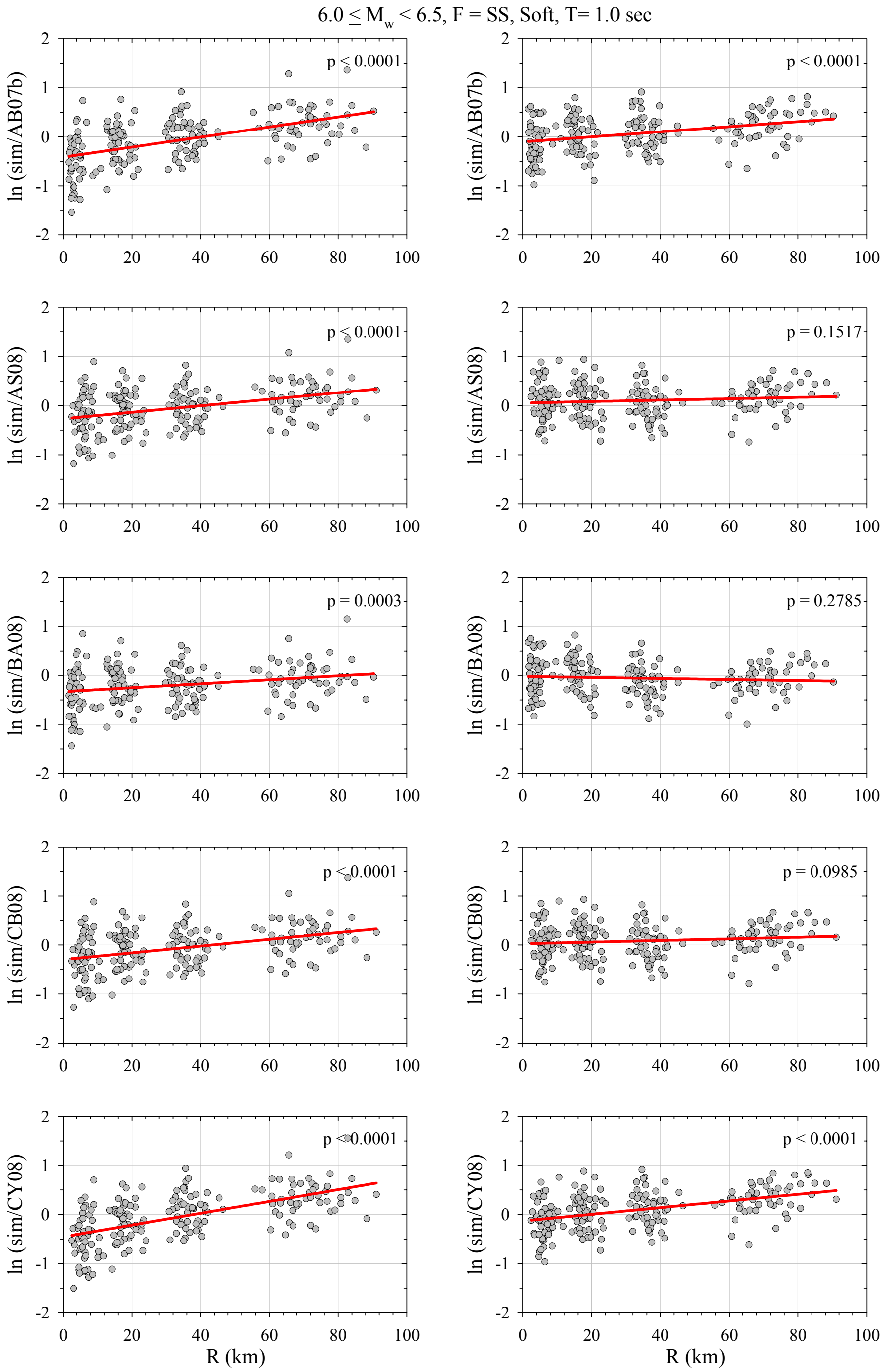

Figure D.8 Distance-dependent comparisons of residuals for S_d ($\xi = 5\%$) at T = 1.0 sec obtained from synthetic ground motions generated by using R_{hyp} (left column) and R_{rup} (right column) for strike-slip (SS) faults

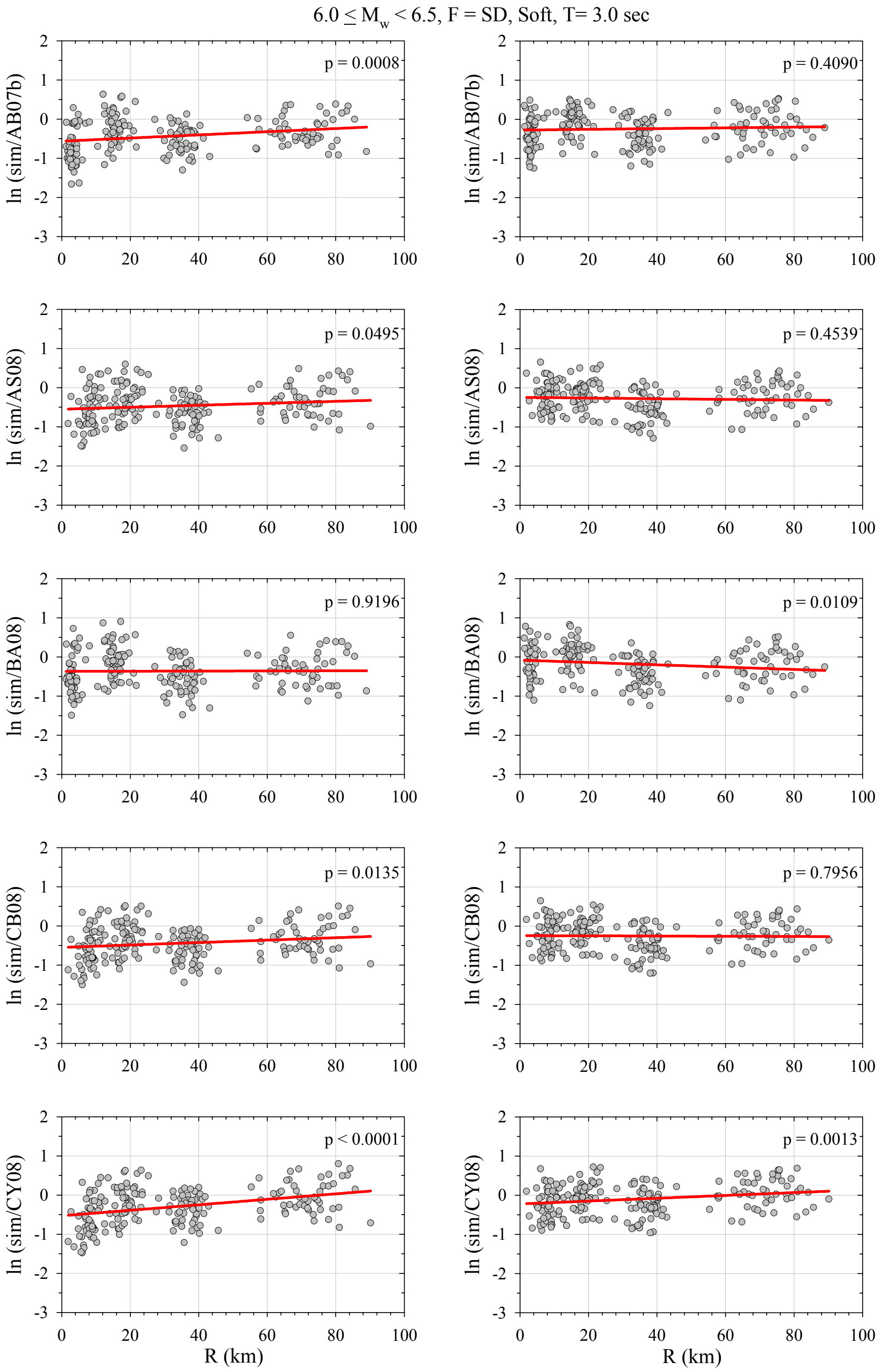

Figure D.9 Distance-dependent comparisons of residuals for S_d ($\xi = 5\%$) at T = 3.0 sec obtained from synthetic ground motions generated by using R_{hyp} (left column) and R_{rup} (right column) for shallow dipping (SD) faults

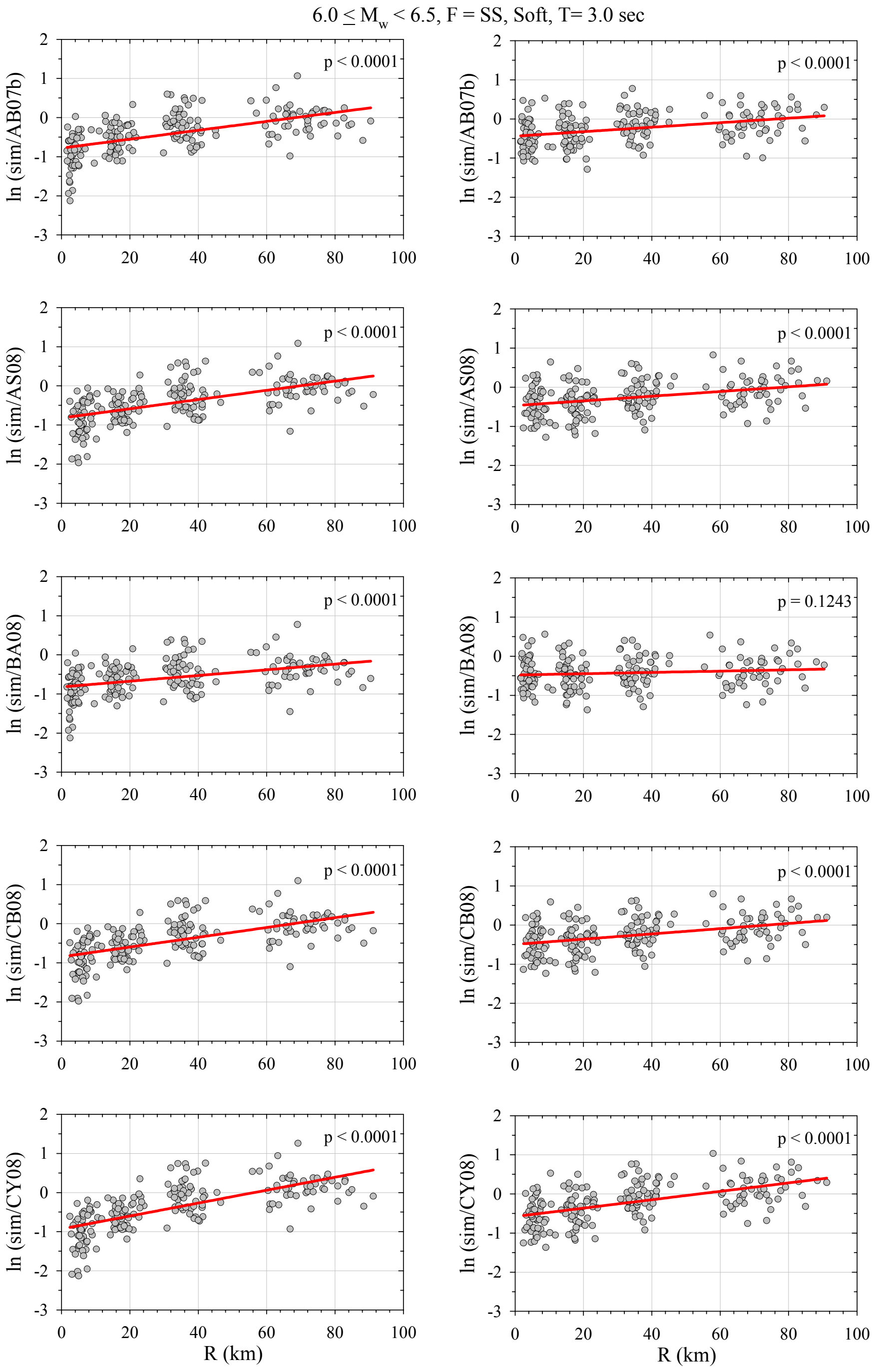

Figure D.10 Distance-dependent comparisons of residuals for S_d ($\xi = 5\%$) at T = 3.0 sec obtained from synthetic ground motions generated by using R_{hyp} (left column) and R_{rup} (right column) for strike-slip (SS) faults

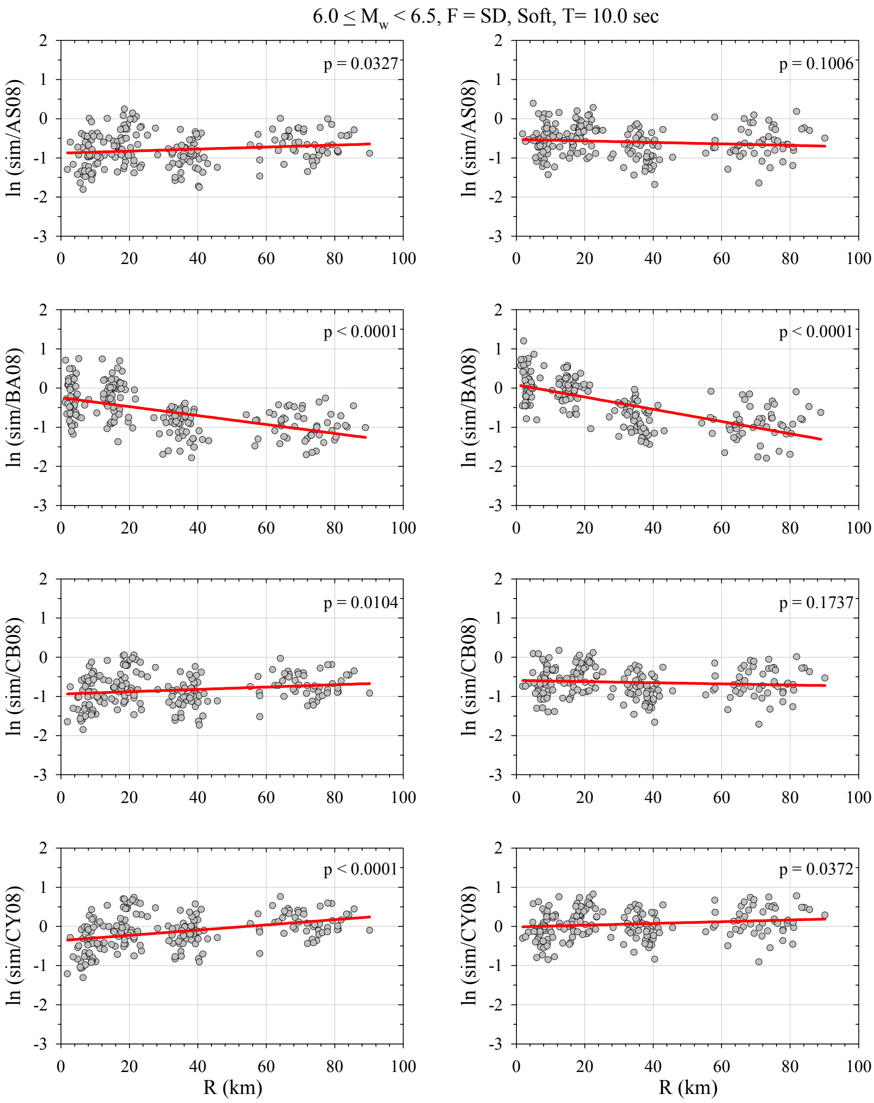

Figure D.11 Distance-dependent comparisons of residuals for S_d ($\xi = 5\%$) at T = 10.0 sec obtained from synthetic ground motions generated by using R_{hyp} (left column) and R_{rup} (right column) for shallow dipping (SD) faults

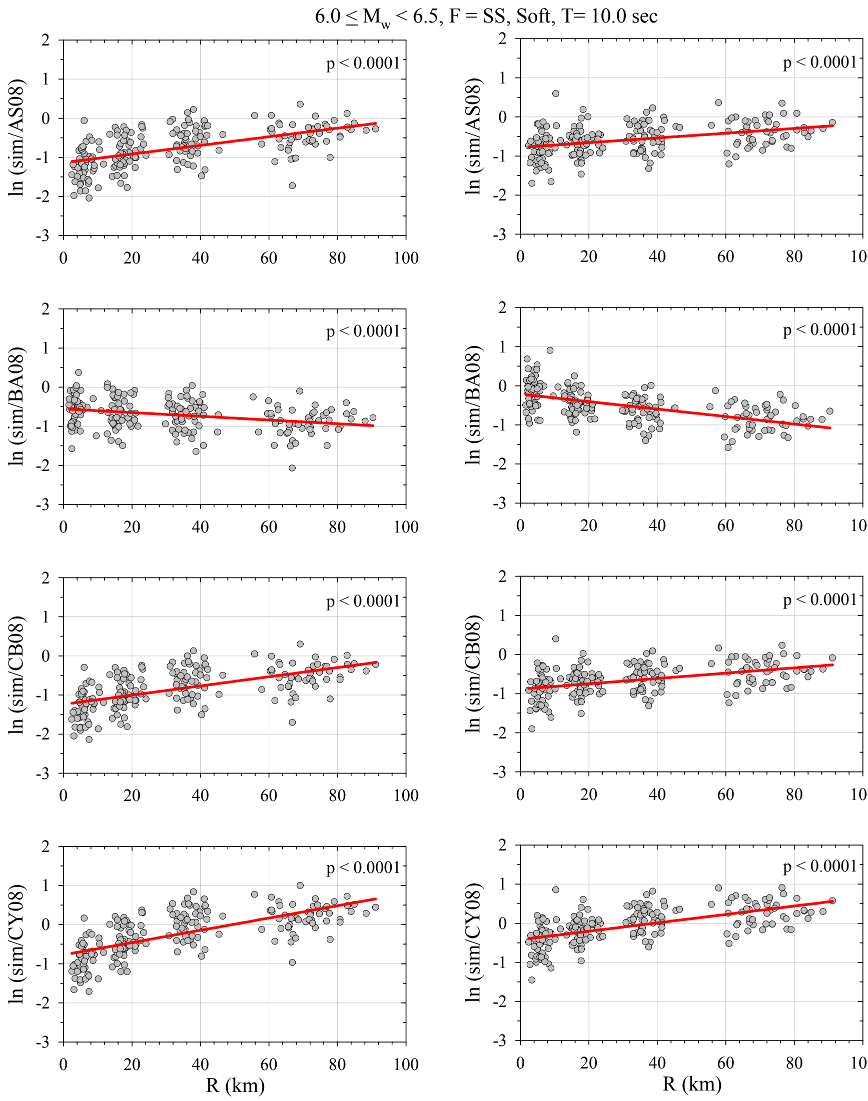

Figure D.12 Distance-dependent comparisons of residuals for S_d ($\xi = 5\%$) at T = 10.0 sec obtained from synthetic ground motions generated by using R_{hyp} (left column) and R_{rup} (right column) for strike-slip (SS) faults